AD-A186 113 THE NUMERICAL AND ANALYTICAL STUDY OF BIFURCATION AND MULTICELLULAR FLOW.. (U) AIR FORCE INST OF TECH WRIGHT-PATTERSON AFB OH D B FANT 1987 1/3

UNCLASSIFIED AFIT/CI/NR-87-134D F/G 20/13 NL

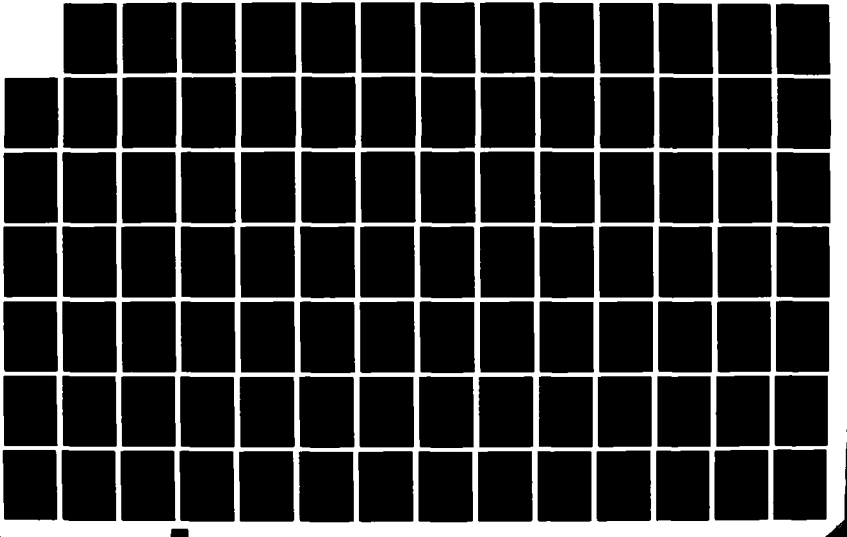

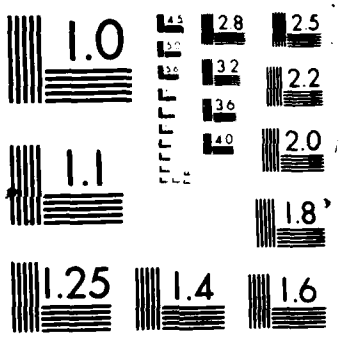
1.0
1.1
1.25
1.4
1.6
2.8
3.2
3.6
4.0
2.5
2.2
2.0
1.8

REPORT DOCUMENTATION PAGE

READ INSTRUCTIONS BEFORE COMPLETING FORM

1. REPORT NUMBER: AFIT/CI/NR 87-134D
2. GOVT ACCESSION NO.:
3. RECIPIENT'S CATALOG NUMBER:

4. TITLE (and Subtitle): The Numerical and Analytical Study of Bifurcation and Multicellular Flow Instability Due to Natural Convection Between Narrow Horizontal Isothermal Cylindrical Annuli at High Rayleigh Numbers

5. TYPE OF REPORT & PERIOD COVERED: THESIS/DISSERTATION

6. PERFORMING ORG. REPORT NUMBER:

7. AUTHOR(s): Daniel Bartholemew Fant

8. CONTRACT OR GRANT NUMBER(s):

9. PERFORMING ORGANIZATION NAME AND ADDRESS: AFIT STUDENT AT: Iowa State University

10. PROGRAM ELEMENT, PROJECT, TASK AREA & WORK UNIT NUMBERS:

11. CONTROLLING OFFICE NAME AND ADDRESS: AFIT/NR, WPAFB OH 45433-6583

12. REPORT DATE: 1987

13. NUMBER OF PAGES: 251

14. MONITORING AGENCY NAME & ADDRESS (if different from Controlling Office):

15. SECURITY CLASS. (of this report): UNCLASSIFIED

15a. DECLASSIFICATION/DOWNGRADING SCHEDULE:

16. DISTRIBUTION STATEMENT (of this Report): APPROVED FOR PUBLIC RELEASE; DISTRIBUTION UNLIMITED

17. DISTRIBUTION STATEMENT (of the abstract entered in Block 20, if different from Report):

18. SUPPLEMENTARY NOTES: APPROVED FOR PUBLIC RELEASE: IAW AFR 190-1

LYNN E. WOLAVER 26 Oct 87
Dean for Research and Professional Development
AFIT/NR

19. KEY WORDS (Continue on reverse side if necessary and identify by block number):

20. ABSTRACT (Continue on reverse side if necessary and identify by block number): ATTACHED

DD FORM 1 JAN 73 1473 EDITION OF 1 NOV 65 IS OBSOLETE

The numerical and analytical study of bifurcation and multicellular flow instability due to natural convection between narrow horizontal isothermal cylindrical annuli at high Rayleigh numbers

Daniel Bartholemew Fant

Under the supervision of Joseph M. Prusa
From the Department of Mechanical Engineering
Iowa State University

This ~~research~~ effort deals with a numerical and analytical study of multicellular flow instability due to natural convection between narrow horizontal isothermal cylindrical annuli.

Buoyancy-induced steady or unsteady flow fields between the annuli are determined using the Boussinesq approximated two-dimensional (2-D) Navier-Stokes equations and the viscous-dissipation neglected thermal-energy equation. The vorticity-stream function formulation of the Navier-Stokes equations is adopted.

Both thermal and hydrodynamic instabilities are explored. An asymptotic expansion theory is applied to the Navier-Stokes equations in the double-limit of Rayleigh number approaching infinity and gap width approaching zero. This double-limiting condition reduces the governing equations to a set of Cartesian-like boundary-layer equations. These equations are further simplified by considering the extreme limits of $Pr \to \infty$ and $Pr \to 0$. The former limit yields an energy equation which retains the nonlinear convective terms, while the vorticity equation reduces to a Stokes-flow equation, signifying the potential for thermal instability. In the latter limit, the nonlinear terms in the vorticity

equation remain, while the energy equation collapses to a one-dimensional conduction equation, signifying the potential for hydrodynamic instability.

Thermal instability of air near the top portions of narrow annuli is considered for various size small gap widths. For these narrow gaps, the Rayleigh numbers corresponding to the onset of steady multicellular flow are predicted. Numerical solutions of the 2-D Navier-Stokes equations also yield hysteresis behavior for the two-to-six and two-to-four cellular states, with respect to diameter ratios of 1.100 and 1.200. In contrast, an unsteady hydrodynamic multicellular instability is experienced near the vertical sections of narrow annuli when the $Pr \to 0$ boundary-layer equations are solved numerically.

In addition, analytical steady-state perturbative solutions to the boundary-layer equations are obtained. These results compare favorably to related numerical solutions of both the Navier-Stokes and the $Pr \to 0$ simplified equations.

In all cases, finite-differenced solutions to the governing equations are obtained using a stable second-order, fully-implicit time-accurate Gauss-Seidel iterative procedure.

TABLE OF CONTENTS

NOMENCLATURE

a	Inner cylinder radius
b	Outer cylinder radius
c	Specific heat
$\hat{e}_r$	Unit vector in radial direction
$\hat{e}_\psi$	Unit vector in angular direction
f	$\frac{\bar{f}}{\nu}$, dimensionless stream function in Navier-Stokes equations
$\tilde{f}$	Dimensionless stream function in finite-Pr boundary-layer equations
g	$\bar{g}$, acceleration of gravity
h	Heat transfer coefficient
h_b, h_f	Variable radial increments
k	Thermal conductivity
k_b, k_{bl}, k_f, k_{fl}	Variable angular increments
k_{eq}	Equivalent thermal conductivity (actual heat flux divided by conductive heat flux)
p	Pressure
q	Local heat flux
r	$\frac{\bar{r}-a}{b-a}$, dimensionless radial coordinate
t	$\bar{t}\,\frac{\nu}{a^2}$, dimensionless time in Navier-Stokes equations
$\tilde{t}$	$Ra^{1/2}\,t$, dimensionless scaled time in finite-Pr boundary-layer equations
$\hat{t}$	$(\frac{Ra}{Pr})^{1/2}\,t$, dimensionless scaled time in zero-Pr boundary-layer equations

u	$\bar{u}(\frac{a}{\nu}) = \frac{-1}{G(r + \frac{1}{G})} \frac{\partial f}{\partial \psi}$, dimensionless radial velocity in Navier-Stokes equations
$\tilde{u}$	Dimensionless radial velocity in finite-Pr boundary-layer equations
v	$\bar{v}(\frac{a}{\nu}) = \frac{1}{G} \frac{\partial f}{\partial r}$, dimensionless angular velocity in Navier-Stokes equations
$\tilde{v}$	Dimensionless angular velocity in finite-Pr boundary-layer equations
w	$\bar{w}\ (\frac{a^2}{\nu})$, dimensionless vorticity in Navier-Stokes equations
$\tilde{w}$	Dimensionless vorticity in finite-Pr boundary-layer equations
A1,A2,...,H4	Coefficients in asymptotic expansion solution
F	Dimensionless stream function in zero-Pr boundary-layer equations
$\bar{F}$	Dimensional body force term
G	$\frac{b-a}{a}$, dimensionless gap number in Navier-Stokes equations
$\tilde{G}$	$Ra^{1/4}\ G$, dimensionless scaled gap number in finite-Pr boundary-layer equations
$\hat{G}$	$(\frac{Ra}{Pr})^{1/4} G$, dimensionless scaled gap number in zero-Pr boundary-layer equations
Gr, Gr_a	$\frac{g\beta a^3(T_i-T_o)}{\nu^2}$, Grashof number
Gr_{b-a}	$\frac{g\beta(b-a)^3(T_i-T_o)}{\nu^2}$, Grashof number based on gap width
H	h_f/h_b, radial increment ratio
K	k_f/k_b, angular increment ratio

NR	Number of nodes in radial direction
NS	Number of nodes in angular direction
Nu	$qa/\{k(T_i-T_o)\}$, local Nusselt number
$\overline{Nu}$	Mean Nusselt number
Nu_{COND}	$\{\ell n\ (\frac{b}{a})\}^{-1}$, conductive Nusselt number
P, Q	Dummy variables
Pr	ν/α, Prandtl number
R	$\bar{r}-a/\delta$, stretched inner radial coordinate
Ra	$\frac{g\beta a^3(T_i-T_o)}{\nu\ \alpha}$, Rayleigh number
Ra_{TR}	Rayleigh number characterizing the onset of multicellular transition
Ra_{b-a}	$\frac{g\beta(b-a)^3(T_i-T_o)}{\nu\ \alpha}$, Rayleigh number based on gap width
S	Source term in numerical method
T	$\frac{\bar{T}\ -\ T_o}{T_i\ -\ T_o}$, dimensionless temperature in Navier-Stokes equations
$\tilde{T}$	Dimensionless temperature in finite-Pr boundary-layer equations
T_i	Inner cylinder temperature
T_o	Outer cylinder temperature
W	Dimensionless vorticity in zero-Pr boundary-layer equations
$D/D\bar{t}$	Total time derivative

Greek symbols

α	$\frac{k}{\rho c}$, thermal diffusivity
β	Coefficient of thermal expansion
δ	Boundary-layer thickness
ε	Convergence criterion, or dimensionless eccentricity variable
γ	$\frac{\tau a^2}{\mu \nu}$, dimensionless local shear-stress
$\bar{\gamma}$	Dimensionless average shear-stress
λ	Parameter in finite-difference equations
μ	Dynamic viscosity, or parameter in finite-difference equation
ν	$\frac{\mu}{\rho}$, momentum diffusivity
ψ	$\bar{\psi}$, dimensionless angular coordinate
ρ	Density
τ	Local shear-stress, or time increment in numerical method
ϕ	Arbitrary dependent variable
Γ	Parameter in finite-difference equations
Ω_1, Ω_2	Relaxation parameters in numerical method
$\bar{\nabla}$	Gradient differential operator
$\nabla 1, \nabla 2, \tilde{\nabla}$	Parameters in finite-difference equations
∇^2, ∇_2^2	Second-order differential operators

Superscripts

m	Iteration number
n	Time level

Subscripts

BL	Boundary-layer
c	Inviscid-core
i	Radial position, or heated inner cylinder surface
j	Angular position
o	Cooled outer cylinder surface
0,1,,,8,10,12	Node position in computational molecule
0,1,2,3,4	Order of expansion term in asymptotic analysis

1. INTRODUCTION

From a practical standpoint, the study of natural convection between horizontal isothermal concentric cylinders has a wide variety of technological applications, ranging from nuclear reactors and thermal storage systems to cooling of electronic components, aircraft fuselage insulation, underground electrical transmission lines and even the flow in the cooling passages of turbine blades (Tsui and Tremblay, 1984).

However, in a different perspective, the work set forth in this research effort was undertaken to gain a more practical understanding of the effects of nonlinearity with regard to natural convective flow instabilities. Still not well understood is the influence of Prandtl number variations on the nonlinear processes involved in triggering either thermal or hydrodynamic types of instabilities. Also of relevance is the aspect of nonuniqueness, which allows the possibility of hysteresis behavior associated with thermal-convective instabilities. These important issues and concerns are addressed and studied in this thesis.

In light of the above, the work in this thesis is separated into three main areas.

First, a stable second-order finite-difference solution to the 2-D Navier-Stokes equations is implemented in order to investigate possible hysteresis behavior in relation to multicellular thermal instability near the top of narrow horizontal annuli for air.

The second area of work involves an asymptotic expansion theory applied to the 2-D Navier-Stokes equations in the double-limit of Rayleigh number approaching infinity and gap width approaching zero. In this double-limit, the Navier-Stokes equations are reduced to Cartesian-like boundary-layer equations. Analytical steady-state solutions to these simplified equations are also obtained, and the results are compared to related 2-D Navier-Stokes numerical data. Moreover, in order to obtain further insight into the nonlinearity associated with extreme Prandtl number variations, limiting boundary-layer equations for $Pr \to 0$ and $Pr \to \infty$ are derived.

Thirdly, the $Pr \to 0$ simplified boundary-layer equations are solved numerically to investigate the full effects of nonlinearity, which were believed to cause an unsteady hydrodynamic multicellular instability between the vertical portions of narrow horizontal annuli.

Before delving into deep analysis and discussion of these topics, an intensive literature review and derivation of the applicable governing equations are presented in Chapters 2 and 3, respectively. Finally, the key results and conclusions of this work are given in Chapters 6 and 7.

2. LITERATURE REVIEW

Natural convection phenomena between horizontal isothermal concentric cylinders have been scrutinized experimentally, analytically, and numerically throughout the past few decades. In the 1960s, most work was experimental in nature. In the '70s and '80s, many numerical studies dominated the literature due to the advent of the modern computer. Analytical studies, in general, have been much more limited.

This thesis concentrates on the high Rayleigh number/small-gap flow regime. It has been found that while numerical studies in the low to moderate Rayleigh number range are quite abundant and agree rather favorably with related experimental work, the numerical work in the high Rayleigh number multicellular flow regime (usually associated with narrow gaps) has been much less exhaustive. This is due to the fact that many computational schemes either could not resolve the transition to the laminar multicellular flow field, or they became unstable just prior to it. Analytical approaches, especially with regard to the high Rayleigh number/small-gap flow regime, have been virtually unexplored.

To better understand how the various studies were conducted and evolved, this literature survey will be essentially divided into three main categories; namely, the analytical analyses, the experimental approaches, and the numerical studies. In addition, three sections will be included near the end of this chapter to further support some of the assumptions and findings relevant to this present study. These

sections will touch upon variable fluid property effects, flow bifurcation, and natural convective flow between vertical slots. Although many of the reviews will relate to the pretransition, non-multicellular flow studies, their inclusion is necessary to fully appreciate some of the follow-up work described in this thesis.

The basic flow field normally encountered between horizontal isothermal concentric cylinders (see Figure 6.3a) is the bicellular kidney-shaped pattern that results strictly from buoyancy effects: density differences occur due to the inner cylinder being hotter than the outer one. The lighter, hotter fluid begins to rise in a boundary-layer manner near the warmer inner cylinder while ascending more uniformly in the inviscid core region near the center of the annulus. Finally, it separates and impinges upon the top of the outer cylinder via the thermal plume. The cooler, more dense fluid, then, descends along the outer cylinder and regains its upward cyclic ascent near the lower portion of the annulus. A similar kidney-shaped flow pattern will also occur when the inner cylinder is cooled and the outer one heated. Other interesting flow patterns are possible and will be discussed in the sections that follow. Symbols will be either directly defined or their meaning may be found in the Nomenclature.

2.1. Analytical Studies

Eight analytical studies pertaining to natural convective flow between horizontal concentric cylinders were found in the literature search. Of the eight, seven involved perturbation methods and only

one dealt with linearized stability theory. All but one related to the relatively small Rayleigh number domain.

Mack and Bishop (1968) used a Rayleigh number power series expansion to obtain a steady-state solution for natural convection between 2-D horizontal isothermal cylinders. The dimensionless vorticity-transport and energy equations were assumed to govern the flow field in this analysis. They expanded temperature (T) and the stream function (ψ) in the following manner:

$$T = \sum_{j=0}^{\infty} A^j T_j(r,\theta) \tag{2.1a}$$

$$\psi = \sum_{j=1}^{\infty} A^j \psi_j(r,\theta) \tag{2.1b}$$

where A signified the Rayleigh number and θ the angular coordinate. The first term in their expansion represented the creeping-flow solution and was in agreement with that obtained by Crawford and Lemlich (1962). The expansions for temperature and stream function were carried out to three terms. It was estimated that for Pr ~ 1, the convection terms were negligible in comparison to the conduction terms for Rayleigh numbers ranging up to approximately 10^4 and R (the radius ratio) in the range of 1.15 to 4.15. Vertical symmetry was assumed, and for Pr $\geq$ 1, the flow resulted in the single-cell kidney-shaped pattern for moderate Rayleigh numbers. But for A ~ 0 (10^4), the second and third terms in the stream function expansion started to outgrow the first term, so any resulting flow patterns were deemed

invalid. For the case of Pr = .02 (liquid mercury), A = 300 and R = 2.0, a multicellular flow was reported. Two weak secondary cells formed at the top and bottom, while a stronger primary cell formed near the center of the annulus. At the time though, experimental results for the larger gap low-Prandtl number range were unavailable; hence, their multicellular flow pattern could not be fully supported. Note that a similar perturbation analysis was performed for spherical annuli in Mack and Hardee (1968). Their flow field patterns were very similar to those obtained in the concentric cylinder geometry.

Rotem (1972) studied the conjugate problem of conduction within the inner cylinder coupled with convective motion in the gap. Through a trial-and-error procedure, he was able to obtain the following expansions for stream function and temperature:

$$\psi = G\,\psi_1 + G^2\psi_2^a + Pr\,G^2\psi_2^b + G^3\psi_3^a + Pr\,G^3\psi_3^b + Pr^2\,G^3\psi_3^c + \ldots. \quad (1 \leq r \leq R) \tag{2.2a}$$

$$T = To + R_A T_1 + R_A G T_2^a + R_A^2 T_2^b + R_A^2 G T_3^a + \ldots. \tag{2.2b}$$

where G was the Grashof number based on (R-1), R_A represented the Rayleigh number, and R the outer-to-inner radius ratio. The first term in these expansions corresponded to the creeping-flow solution. Rotem (1972) carried out the stream function expansion to two terms and calculated three terms for the temperature perturbation expansion.

Through his results, Rotem (1972) confirmed the basic single-cell solution and reinforced the idea that one should be careful in reporting counter-rotating cells with an asymptotic method, since this usually signifies that the expansions are starting to diverge. He did not investigate the extreme Prandtl number cases, but he did express the fact that further transformations were needed to eliminate Pr as an independent parameter and render the equations free from singularities in the limits of $Pr \to 0$ and $Pr \to \infty$. Such has been obtained, for example, in his analysis on natural convection above unconfined horizontal surfaces (Rotem and Claassen, 1969).

Hodnett (1973) used a perturbation method to analyze the same problem as Mack and Bishop (1968), except that his analysis was in terms of primitive variables. He extended his work in order to determine how large R could be, at a given value of Grashof number, for the problem to remain conduction dominated. He found that convection was negligible only when R satisified

$$R^3 \ln^{-1} R = O[(\varepsilon G)^{-1}] \tag{2.3}$$

where εG represented his Grashof number and ε was given by

$$\varepsilon = \frac{T_i - T_o}{T_o} ,$$

while G signified a natural convective type Reynolds number.

Huetz and Petit (1974) performed a theoretical study of free convection in a horizontal annulus for low values of Grashof number. Their governing equations were written in the same form as Mack and Bishop (1968), and vertical symmetry was also assumed. They expanded stream function and temperature in a power series with respect to Grashof number (Gr), where Gr was based on the inner cylinder radius. Two case studies were investigated. Case I related to a constant heat flux imposed on the inner wall and constant temperature on the outer wall, and vice-versa for case II. For Pr ~ 1, only monocellular flow was obtained in both cases I and II, regardless of the radius ratio for Grashof numbers less than 1,000. However, for Pr = .02, R = 2.0, and Gr = 15,000 (or Ra = 300), a multicellular flow was observed. Secondary cells formed at the top and bottom of the annulus with the primary cell in the center, but the secondary cells did not appear simultaneously. In case II, the bottom cell appeared first, and in case I, the upper cell appeared first. Thus, the results of this study further support the multicellular flow recognized by Mack and Bishop (1968).

Custer and Shaughnessy (1977a) investigated natural convection within a horizontal annuli for very low Prandtl numbers by solving the dimensionless thermal energy and vorticity equations with a double perturbation expansion in powers of Grashof and Prandtl numbers. The stream function and temperature expansions were written as:

$$\Psi(r,\theta) = \sum_{n=o}^{\infty} \sum_{m=0}^{\infty} Pr^n \, Gr_{r_o}^m \, \Psi_{nm}(r,\theta) \qquad (2.4a)$$

$$T(r,\theta) = \sum_{j=0}^{\infty} \sum_{k=0}^{\infty} Pr^{j} \, Gr_{r_o}^{k} \, T_{jk}(r,\theta) \quad . \tag{2.4b}$$

For a fairly large gap of R = 5 and Pr → 0, they reported that the center eddy fell downward as the Grashof number increased, which was contrary to the behavior of fluids for Pr $\geq$ .7. For this same size gap, at Gr_{r_o} = 12,000, they observed the formation of a weak eddy near the top of the inner cylinder. For R = 2, at Gr_{r_o} = 120,000, two weak eddies formed near the top and bottom of the annulus while the stronger kidney-shaped one remained in the center. Vertical symmetry was again assumed for this problem. These conclusions also help to confirm the multicellular flow pattern observed by Mack and Bishop (1968). Custer and Shaughnessy also stressed that only numerical solutions to the full nonlinear equations, or experiments, could actually establish the true existence of this multicellular flow field.

Custer and Shaughnessy (1977b) continued to study the problem described in the above review. In this analysis, the dependent variables in the governing equations were represented by the following partial spectral expansions:

$$\Psi(r,\theta) = \sum_{n=1}^{\infty} f_n(r) \sin n\theta \tag{2.5a}$$

$$T(r,\theta) = \sum_{n=0}^{\infty} g_n(r) \cos n\theta \quad . \tag{2.5b}$$

The use of these expansions resulted in ordinary differential equations governing $f_n(r)$ and $g_n(r)$. The equations were solved numerically and their results were based on the series being truncated after three terms. For Pr = .01 and Ra < 50 (or Gr < 5,000), they obtained the following correlation for their heat transfer data (note that Ra and Gr were based on the inner cylinder radius):

$$\text{at } R = 2.00, \qquad \bar{k}_{eq} = 1 + 5 \times 10^{-8}\, Ra^{2.014} \tag{2.6a}$$

$$\text{at } R = 4.00, \qquad \bar{k}_{eq} = 1 + 1 \times 10^{-4}\, Ra^{1.935}\ , \tag{2.6b}$$

where $\bar{k}_{eq}$ signifies the average equivalent thermal conductivity and represents the actual mean heat flux divided by the heat flux for pure conduction. For a radius ratio of 1.1, they found that $\bar{k}_{eq}$ was equal to 1 out to a Grashof number of approximately 10^6. Also, for all the cases studied, only the single-cell flow field resulted in the vertical half of the annulus.

Walton (1980) utilized a multiple-scales linearized stability theory to study the instability of natural convective flow between narrow cylindrical annuli. First, he represented the basic flow by expanding the stream function (Ψ) and temperature (T) in terms of the dimensionless gap width, ε:

$$(\Psi,T) = (\Psi_o,T_o) + \varepsilon(\Psi_1,T_1) + \varepsilon^2(\Psi_2,T_2) \tag{2.7a}$$

where

$$\varepsilon = \frac{r_o - r_i}{r_i} \quad \text{and} \quad \varepsilon << 1 \quad . \tag{2.7b}$$

He then let ψ' and T' represent small perturbations to ψ and T given in Eq. (2.7a). By using the dimensionless forms of the vorticity and energy equations, he was able to consider the stability of the basic flow to small disturbances, via linearized stability theory. He determined that the convective flow became unstable at a critical value of the Rayleigh number, R, (associated with a particular wavenumber) given by:

$$R = R_c + \varepsilon R_1 + ... \tag{2.8}$$

where, for Pr = .7, R_c = 1707.762 and R_1 = 258.4. Thus, as $\varepsilon \to 0$, $R \to 1707.762$. According to his results, the narrow-gap annulus collapsed to the horizontal flat plate Bénard problem as the gap width tended to zero. Hence, for Pr ~ 1, a thermal-type instability should arise near the top of the annulus.

Jischke and Farshchi (1980) studied the boundary-layer regime for laminar free convection between 2-D horizontal annuli at the large Rayleigh number limit. They divided the flow field into five physically distinct regions, valid for the high Rayleigh number limiting condition. They assumed a stagnant regime for the bottom part of the annulus; a boundary-layer type behavior near the inner and outer cylinders; an inviscid core region in the center portion of the

annulus; plus a thermal plume section along the vertical line of symmetry above the inner cylinder, where the inner boundary-layer joins up with the outer boundary-layer. Their governing equations were written in terms of primitive variables, and they employed a zeroth-order asymptotic expansion to represent the velocity and temperature fields within the annulus. For the boundary-layer regime, they assumed (from free convective boundary-layer studies of a single horizontal cylinder) that the velocity and temperature fields would scale as:

$$u \sim Ra^{1/4} u_o + \ldots.$$

$$v \sim v_o + \ldots.$$

$$T \sim T_o + \ldots. \qquad (2.9)$$

where u signified the radial velocity and, v, the tangential velocity component. Their simplified equations, resulting from the $Ra \to \infty$ limit, were solved by means of an integral method in the limit of $Pr \to \infty$. They compared their heat transfer results to those of Kuehn and Goldstein (1976a) for a radius ratio of R = 2.6, Pr = .706 and $Ra = 4.7 \times 10^4$. Qualitatively, their basic flow field and results were very similar, but significant deviation was apparent in their plots of the variation of local Nusselt number with angular position on the inner cylinder. Their best agreement was achieved near the top of the inner cylinder, at $\theta = 180°$. They seemed to have captured the essential features of the flow field in their boundary-layer analysis,

although only bicellular-type flows were studied. The authors of this article did not investigate the narrow-gap limit of their $Ra \to \infty$ equations.

2.2. Experimental Studies

Most of the articles in this section relate to natural convection between either concentric cylinders or spheres. Various flow patterns have been investigated in the experimental work, ranging from the multicellular flow prevalent in the narrow gaps to the unsteady type flows originating in the larger gaps. Studies include both 2-D and 3-D phenomena over a range of fluids such as air, water, liquid mercury, oil and glycerin.

Liu et al. (1962) studied natural convection heat transfer for air, water and silicone oil ($0.7 \leq Pr \leq 3{,}500$) between horizontal cylindrical annuli. They considered five different geometries with radius ratios of R = 1.154, 1.5, 2.5, 3.75 and 7.5. For the larger radius ratios, all three fluids experienced a slow sideways oscillation near the top of the cylinders as the Rayleigh number (Ra_{b-a}) exceeded some limiting value, and this value decreased with gap size. For the smaller gap, R = 1.154, a multicellular type flow (near the top) was observed for air and silicone oil, at Ra_{b-a} of approximately 2,000 and 18,000, respectively. A kidney-shaped flow pattern was maintained below the counter-rotating cells that formed near the top of the annulus. They speculated that for gaps smaller than R = 1.154, the Bénard critical Rayleigh number ($Ra_{b-a} \approx 1700$) would be approached.

Bishop et al. (1964) investigated natural convective heat transfer between concentric spheres. They examined two radius ratios, R = 3.14 and R = 1.19. For the larger gap, only the kidney-shaped flow pattern, similar to that seen for concentric cylinders, was observed. No sideways oscillations were noticed. But in the smaller gap, R = 1.19, two counter-rotating cells appeared near the top at a Ra_{b-a} of about 3,600. However, due to the spherical geometry, the two secondary cells almost immediately began to coalesce into an elongated shape and soon became indistinguishable. Although the geometries are different, the multicellular flow observed in the narrow spherical annuli supports the same type of flow seen by Liu et al. (1962) in the narrow cylindrical annuli.

Grigull and Hauf (1966) used a Mach-Zehnder interferometer to measure the temperature field between horizontal cylindrical annuli filled with air. From these measurements, they were able to obtain the local Nusselt numbers for a particular gap size and Grashof number. They discussed three different regimes of convective flow:

1. A 2-D pseudo-conductive regime for $Gr_{b-a} < 2{,}400$. Here, conduction effects were dominant, although some convective motion was evident.
2. A transitional regime with 3-D convective motion, for $2{,}400 \leq Gr_{b-a} \leq 30{,}000$. For the intermediate-size gaps, $(1.2 < R < 2.0)$, the flow field transitioned to a form of 3-D vortices in unsteady oscillatory motion.

3. A 2-D fully-developed laminar convective motion regime for $30{,}000 \leq Gr_{b-a} \leq 716{,}000$. The 2-D motion was considered steady for the larger gap widths in this particular range of Grashof numbers. They did notice that as Grashof number increased, the centers of the kidney-shaped cells moved closer to the upper portion of the annulus.

Vivid flow pictures (observed by cigarette smoke) were included for all three convective flow regimes.

Bishop et al. (1966) extended their study of 1964 (Bishop et al., 1964) to include the effects of various radius ratios, ranging from R = 1.19 to R = 3.14. In their experiments, they confirmed the occurrence of counter-rotating cells previously observed in the smallest gap width, R = 1.19. For the relatively narrow gaps (slightly greater than R = 1.19) in the high Grashof number range, they observed a boundary-layer type flow near the walls of the annulus, coupled with a slower, more uniform type of fluid motion near the center. Also, from their measured heat-transfer data for four different radius ratios, they obtained two Nusselt-Grashof number correlations that fit their data to within 15.5 percent.

Lis (1966) studied the flow behavior in simple and obstructed annuli using the Schileren technique with both sulphur hexafluoride and nitrogen as the working fluid. The six axial spacers used in the obstructed annuli provided for enhanced heat transfer effects (compared to the simple annuli) due to more efficient mixing near the upper parts of the annulus. Also, for $2 \leq R \leq 4$, the flow pattern became unstable

at the higher Rayleigh numbers and random oscillations developed near the top of the gap (for the unobstructed annuli).

Bishop and Carley (1966) performed photographic studies of natural convective air patterns between concentric cylinders. They observed an oscillatory flow for R = 3.69, that started at $Ra_{b-a} \approx 270{,}000$ (a much larger value than that indicated by Liu et al. (1962) for the same size gap). They also tried to reproduce the multicellular flow field observed by Liu et al. (1962) for the small gap, R = 1.154. They used a gap width of .688 inches, and for Rayleigh numbers (Ra_{b-a}) up to 20,000, no type of multicellular flow occurred. Either the gap size was too large, or a much higher Rayleigh number was needed to observe the cells with their particular apparatus.

Bishop et al. (1968) re-examined experimentally, for air, the oscillatory flow in the larger size cylindrical annuli. For gap widths of R = 3.70, 2.46 and 1.846, they observed that the oscillations started at Rayleigh numbers (Ra_{b-a}) of approximately 240,000, 150,000 and 35,000, respectively. Using the data from these three gaps, they obtained empirical correlations for the period, wavelength and amplitude of the oscillations.

Powe et al. (1969) experimentally studied the natural convective flow of air between horizontal concentric cylinders for various radius ratios. They characterized the flow into three basic regimes:

I. 2-D multicellular flow for $R \leq 1.2$,

II. 3-D spiral flow for $1.2 < R \leq 1.7$, and

III. 2-D/3-D oscillatory flow for $R > 1.7$.

Regimes II and III were unsteady. The multicellular flow field in Regime I remained steady for a small number of cells, but as the Rayleigh number increased and the chain of cells near the top stopped forming, slight oscillations about the vertical center-line occurred.

Yin et al. (1973) experimentally investigated the natural convective flow patterns between isothermal concentric spheres for air and water. For air, with R = 1.4 and Ra_{b-a} = 5930, they observed two steady counter-rotating cells near the top of the annulus. With the larger gaps (R = 2.17 and 1.78), for both air and water, the familiar kidney-shaped pattern resulted for relatively small Rayleigh numbers. But as Rayleigh number increased, an unsteady flow behavior was initiated.

Kuehn and Goldstein (1976a) studied the natural convective flow of air and water between isothermal concentric cylinders both experimentally and numerically. A Mach-Zehnder interferometer was used to obtain temperature profiles for both air and water with an annulus of R = 2.6. Heat transfer correlations were found by using a least-squares regression analysis. For air,

$$\bar{k}_{eq} = .159\ Ra_{b-a}^{.272}\ ,\ 2.1 \times 10^4 < Ra_{b-a} < 9.6 \times 10^4 \qquad (2.10)$$

and for water,

$$\bar{k}_{eq} = .234\ Ra_{b-a}^{.238}\ ,\ 2.3 \times 10^4 < Ra_{b-a} < 9.8 \times 10^5\ . \qquad (2.11)$$

At similar Rayleigh numbers, the temperature distributions for air and water were essentially the same. The flow field remained steady and symmetric for all Rayleigh numbers investigated at R = 2.6. There was no sign of any type of multicellular flow behavior.

Kuehn and Goldstein (1978) studied the effects of eccentricity and Rayleigh number on natural convection heat transfer between horizontal annuli filled with pressurized nitrogen. A Mach-Zehnder interferometer was again used to obtain interferograms of the working fluid. For an eccentric geometry of $\epsilon_v/L \leq \frac{2}{3}$ (meaning the inner cylinder is set above the concentric center), the overall heat transfer rates were within ten percent of that for concentric cylinders at the same Rayleigh number. But local changes in the heat transfer rates were significant where the cylinder walls were nearly touching. When the inner cylinder was closest to the bottom of the outer cylinder ($\epsilon_v/L = -.623$), an unsteady thermal plume behavior was witnessed, with the flow eventually transitioning to turbulence upon further increase in Rayleigh number.

Warrington and Powe (1985) experimentally examined natural convection between concentrically located isothermal spherical, cylindrical and cubical inner bodies, surrounded by a cubical enclosure. To within 15 percent of their experimental data, mean Nusselt number correlations were obtained for all three configurations. In comparison to heat transfer data from spherical annuli, they found that cubical enclosures with a spherical inner body yielded larger Nusselt numbers for a given Rayleigh number and aspect ratio. Also, for the higher Rayleigh numbers, a

multicellular flow field was encountered for the cubical enclosures with cylindrical inner bodies.

2.2.1. Heat transfer correlations

Some basic correlations are presented in McAdams (1954) for natural convection from single horizontal cylinders. He observed that the heat transfer data for single cylinders should approach that obtained with concentric cylinders in the limit as $R \to \infty$. McAdams also presented expressions for natural convective heat transfer between horizontal and vertical enclosed air spaces. All of his correlations took on the form $Nu = a(Ra)^b$, where b was typically 1/4 for laminar flows and 1/3 for turbulent-type flows.

Itoh et al. (1970) proposed a new method for correlating heat transfer coefficients for natural convection between horizontal cylindrical annuli. They claimed that heat transfer coefficients ($\bar{h}_i$, $\bar{h}_o$) are well correlated by the mean Nusselt number, $\overline{Nu}$, and the mean Grashof number, Gr_m, defined as follows:

$$\overline{Nu} = \frac{\bar{h}_i \cdot [r_i \ell n(r_o/r_i)]}{k} = \frac{\bar{h}_o \cdot [r_o \ell n(r_o/r_i)]}{k} \tag{2.12}$$

$$Gr_m = \frac{g\beta(T_1 - T_2)[(\sqrt{r_i r_o})\ell n(r_o/r_i)]^3}{\nu^2} \quad . \tag{2.13}$$

With these definitions, any resulting heat transfer data (for laminar flow) could be represented by

$$\overline{Nu} = c_1 \, Gr_m^{1/4} \tag{2.14a}$$

where c_1 is a constant value.

Powe (1974) examined heat transfer correlations given by Liu et al. (1962) and Scanlan et al. (1970) to determine the bounding effects of heat loss by free convection from concentric cylinders and spheres, respectively. For various Rayleigh numbers, he calculated limiting bands at which the empirical equations were valid. Beyond these limits, the equations either collapsed to the conduction solution for small gap widths, or to natural convective flow of a single cylinder (or sphere) exposed to an infinite atmosphere, for the larger gap sizes.

Raithby and Hollands (1975) proposed a heat transfer correlation for isothermal concentric cylinders. Based on their experimental data for air, water and silicon oil, they obtained the following correlation (valid for the convection-dominated flow regime):

$$\bar{k}_{eq} = .386\,[Pr/(.861 + Pr)]^{1/4}\,Ra_{cc}^{1/4} \qquad (2.14b)$$

where

$$Ra_{cc} = \frac{[\ell n\,(D_o/D_i)]^4}{(b-a)^3\,(1/D_i^{3/5} + 1/D_o^{3/5})^5}\,Ra_{b-a} \qquad (2.14c)$$

and b-a = annulus gap-width. They mentioned that the correlation worsened as the annular gap spacing increased, but appeared to be highly satisfactory for the relatively narrow and intermediate size gaps.

Kuehn and Goldstein (1976b) obtained correlating equations for heat transfer between horizontal concentric cylinders. For R = 2.6 and $.01 \leq Pr \leq 1{,}000$, the following expression (for the mean inner-diameter Nusselt number) represented their heat transfer data to within 2 percent:

$$\overline{Nu}_{D_i} = \frac{2}{\ell n \left\{ \dfrac{1 + \dfrac{2}{[(.518\ Ra_{D_i}^{1/4}[1+(\frac{.559}{Pr})^{3/5}]^{-5/12})^{15}+(.1\ Ra_{D_i}^{1/3})^{15}]^{1/15}}}{1 - \dfrac{2}{\{([(\frac{2}{1-e^{-.25}})^{5/3}+(.587\ G\ Ra_{D_o}^{1/4})^{5/3}]^{3/5})^{15}+(.1\ Ra_{D_o}^{1/3})^{15}\}^{1/15}}} \right\}} \tag{2.15}$$

where

$$G = [(1 + \frac{0.6}{Pr^{.7}})^{-5} + (.4 + 2.6\ Pr^{.7})^{-5}]^{-1/5}$$

and Ra_{D_i}, Ra_{D_o} signify the Rayleigh numbers evaluated at the inner and outer cylinder diameters. They also discussed that as the diameter of the outer cylinder increased, the heat transfer approached that of a single horizontal cylinder. They found that to have heat transfer within 5 percent of a free cylinder required $D_o/D_i > 360$ at $Ra_{D_i} = 10^7$ and $D_o/D_i > 700$ for $Ra_{D_i} = 10^{-1}$.

Boyd (1981) used a unified theory to correlate steady laminar natural convection heat transfer between horizontal annuli. His correlations were successfully extended to annuli with irregular boundaries. For isothermal concentric cylinders, he suggested the following relationship for the mean Nusselt number based on the gap width, Δ:

$$\overline{Nu}_{\Delta} = C_4 \, Pr^{n^*} \, Ra^{1/4} \tag{2.16}$$

where

$$n^* = C_5 + C_6 \, Pr^{-1/3}$$

and C_4, C_5 and C_6 were constants that depended on related heat transfer data. These constants were evaluated using data from Keuhn and Goldstein (1976a). The result is given by

$$\overline{Nu}_{\Delta} = .796 \, Pr^{n^*} \, Ra^{1/4} \tag{2.17}$$

where

$$n^* = .00663 - .0351 \, Pr^{-1/3} \, .$$

According to Boyd, this expression was valid for $10^1 < Ra < 10^7$, $.706 \leq Pr \leq 3100$, and $.125 \leq \frac{\Delta}{r_i} \leq 2.0$; where $\frac{\Delta}{r_i}$ represented the aspect ratio for the annulus.

2.3. Numerical Studies

As previously mentioned, most of the numerical studies for natural convection between horizontal annuli pertain to the bicellular solutions associated with the low to moderate Rayleigh numbers. Although the reviews in this section will be rather concise, particular attention will focus on the finite-differencing methods used, especially with regard to the numerical representation of the nonlinear convective terms.

Crawford and Lemlich (1962) studied natural convection of air between horizontal cylindrical annuli. They numerically examined three different radius ratios, R = 2, 8, and 57, and confined their study to extremely low Grashof numbers, the so-called creeping flow solution. In their numerical method, conventional central-differencing was used throughout, and the stream function and temperature were calculated using a Gauss-Seidel iterative procedure. Vertical symmetry was assumed and their results revealed the characteristic kidney-shaped circulation pattern.

Abbott (1964) discussed a numerical method for solving the same problem as Crawford and Lemlich (1962), except for very narrow annuli. He studied four types of narrow gaps, R = 1.0256, 1.0170, 1.0084 and 1.0040. Abbott began his solution process by first obtaining solutions to the conduction-dominated energy equation and the creeping-flow (negligible convective acceleration terms) momentum equation. He then used these results to approximate the convective terms in the full set of governing equations. Thus, by linearizing the equations in terms

of the unknowns, he was able to obtain successive approximations to the nonlinear terms. He solved for the unknown temperatures and stream functions by using a matrix inversion technique. His results represent only slight convective perturbations to the creeping-flow solution. For all cases, he obtained the basic kidney-shaped flow pattern.

Powe et al. (1971) obtained the first semblance of a secondary air flow captured numerically in narrow horizontal annuli. They assumed vertical symmetry and used a complete central-difference representation for the nonlinear convective terms in the governing energy and vorticity-transport equations. Their equations were formulated for the steady-state case. Moreover, their numerical solutions could only capture the flow field up to the point where the stream function changed its sign (signifying counter-rotating flow). After this point, their code would no longer converge. Thus, they could not fully resolve the multicellular flow field for the narrow gaps, but they were able to make estimates of the transitional Rayleigh numbers. Using this approach, they estimated a transitional Rayleigh number of $Ra = 452{,}000$ for $R = 1.2$. Their mean Nusselt numbers were not at all affected by the appearance of these unresolved secondary flows.

Charrier-Motjtabi et al. (1979) used an ADI scheme to numerically solve for the natural convective flow field between horizontal annuli. Coupled with the energy equation, they used the stream function-vorticity approach to analyze the flow. Also, a fictitious time was defined so as to more readily achieve the steady-state condition. They did not mention what type of finite-differencing was employed for the

nonlinear convective terms. For the narrow gap of R = 1.2 and Rayleigh numbers up to Ra = 875,000, no multicellular flow field was observed for air. However, for Pr = .02 and R = 2.0, they obtained a multicellular flow similar to that described by Mack and Bishop (1968).

Astill et al. (1979) obtained numerical solutions for natural convection in concentric spherical annuli. They considered fluids with Prandtl numbers between .7 and 5.00, and radius ratios from 1.03 to 2.00. Pure central-differencing was used to obtain approximations to the steady-state stream function and energy equations. The system of equations was solved using a Gauss-Seidel iterative procedure with under-relaxation, and vertical symmetry was again assumed. They mainly observed the typical kidney-shaped pattern for all fluids and gaps studied. However, for air and R = 1.1 and 1.2, they resolved a second vortex formation occurring at Ra_{b-a} = 25,000 and 8,000, respectively. These counter-rotating cells were seen experimentally by Bishop et al. (1964), but at a much lower Rayleigh number for R = 1.2.

Caltagirone et al. (1979) also performed a numerical study of natural convection between spherical annuli filled with air. They used an ADI scheme to solve for the stream function, temperature and vorticity fields. They considered vertical symmetry and radius ratios between 1.15 and 3.00. Using "zero" initial conditions, only bicellular solutions were found for Rayleigh numbers up to 10^5. But upon using an initial temperature distribution of the form

$$T \propto a \sin(\pi r) \cos(b\theta) \qquad (2.18)$$

(where 'a' was an amplitude value and 'b' a characteristic wavenumber), the converged flow field for R = 2 and Ra = 50,000 experienced a counter-rotating cell near the top of the half-annulus. Associated with this secondary flow was a rise in the mean Nusselt number. But, this multicellular flow field was probably unrealistic, since this type of flow has only been observed experimentally for the very narrow spherical annuli, $R \leq 1.4$.

Kuehn and Goldstein (1980b) studied the effects of Prandtl number and diameter ratio on natural convection between horizontal cylindrical annuli. They employed an explicit finite-difference scheme to solve the energy, stream function and vorticity equations for steady laminar flow. They used a hybrid technique for the nonlinear terms, which switched from central to upwind differencing when the mesh Reynolds number constraint was exceeded. For large Prandtl numbers, a fully-developed boundary-layer with an impinging thermal plume resulted, whereas, as $Pr \to 0$, the temperature distribution approached the pure conduction limit. Also, the mean Nusselt number asymptotically approached the single horizontal cylinder value as $R \to \infty$. The authors derived a correlation valid for laminar flow over $.001 \leq Pr \leq 1{,}000$ and $1.0 \leq R \leq \infty$ (although the correlation fit best for Pr = .7):

$$\overline{Nu}_{D_i}_{CONV} = \frac{2}{1 + \frac{2}{.518\ Ra_{D_i}^{1/4}\left[1 + \left(\frac{.559}{Pr}\right)^{3/5}\right]^{-5/12}} \ell n \left\{ \frac{}{1 - \frac{2}{.587\ Ra_{D_o}^{1/4}}} \right\}} \qquad (2.19a)$$

$$\overline{Nu}_{D_i}_{COND} = \frac{2}{\ell n\ (D_o/D_i)} \qquad (2.19b)$$

$$\overline{Nu}_{D_i} = \left(Nu_{D_i}^{15}{}_{COND} + Nu_{D_i}^{15}{}_{CONV}\right)^{1/15} \qquad (2.19c)$$

where Ra_{D_i} and Ra_{D_o} are the same as those described in Eq. (2.15). Over their range of data, they reported a maximum deviation of 13 percent occurring for Prandtl numbers near .02.

Projahn et al. (1981) solved the energy and the vorticity-stream function equations numerically by using a strongly implicit method as described by Weinstein et al. (1970). The convective terms were written in divergence form and were differenced using a corrected upwind scheme obtained from Jacobs (1973). In their analysis of natural convection between concentric and eccentric cylinders, they reported that for a negative (downward) vertical displacement of the inner cylinder, the

mean Nusselt number was always greater than that in the concentric case. Also, for Pr = .7 and R = 2.6, they obtained a counter-rotating cell near Ra = 12,000, but attributed this cell formation to their assumption of symmetrical boundary conditions.

Ingham (1981) solved a set of equations similar to that described by Projahn et al. (1981), but Ingham's equations were formulated in a more general fashion to account for either the concentric spherical or cylindrical geometry. He assumed steady-state and vertical symmetry and used central-differencing throughout, except for the nonlinear terms where he employed a cleverly weighted second-order upwind-differencing scheme. He tested for steady multicellular flows by considering a spherical radius ratio of R = 1.19 with Pr = .7, and for a range of values of Ra up to 2.5×10^7, he did not obtain any sign of a multicellular structure.

Farouk and Güceri (1982) were the first to study turbulent natural convection numerically between 2-D horizontal concentric cylinders. They used a k - ε turbulence model and obtained steady-state results that were in good agreement with experimental data. All of their test cases pertained to R = 2.6 with vertical symmetry assumed, and they considered Rayleigh numbers (based on gap width) up to 10^6 - 10^7.

Cho et al. (1982) studied the natural convection of air in eccentric horizontal isothermal cylindrical annuli. They solved the problem using bipolar coordinates with the assumption of vertical symmetry. Central-differencing was employed for all the derivatives, including the nonlinear terms. They numerically investigated a

radius ratio of R = 2.6 with varying degrees of eccentricity, for Raleigh numbers (based on gap width) less than 5.0×10^4. Their numerical results agreed rather well with experimentally obtained interferograms. It was observed that the average heat transfer increased as the inner cylinder moved downward along the vertical center-line.

Prusa and Yao (1983) numerically examined natural convection between eccentric horizontal cylinders, similar to that described in the above with Cho et al. (1982). However, they employed a unique radial transformation method that allowed them to study various eccentricities while avoiding any type of singular behavior in the limit of zero eccentricity. They also developed a convenient variable mesh routine which provided the flexibility of concentrating grid nodes within the boundary-layer and thermal plume regions. Central-differencing was used throughout, along with a stable corrected second-order central difference scheme to represent the nonlinear terms. They obtained very good agreement with experimental and analytical data, and confirmed the fact that the overall heat transfer could be reduced or enhanced with respect to the upward or downward shift of the inner cylinder about the vertical center-line. In addition, they appeared to be the first to determine the critical eccentricity associated with minimum heat transfer for various Grashof numbers.

Chandrashekar et al. (1984) studied natural convective flow of a Boussinesq heat-generating fluid between two horizontal concentric cylinders. They investigated the effects of two driving mechanisms -

an externally imposed temperature gradient across the annulus, coupled with a uniform internal heat generation. The parameter that represented the ratio of the internal heating to the applied temperature difference was denoted by S, where the S = 0 limit corresponded to the isothermal concentric cylinder case. They assumed vertical symmetry and marched numerically in time to achieve the steady-state condition. The governing equations were solved with an ADI scheme on a uniform mesh, and central-differencing was used throughout. They found that as S increased from zero, a transition took place (for Pr = .7) from a unicellular to a bicellular circulation in each half-cavity. For this transition, the critical value of S depended on both the Rayleigh number and the radius ratio.

Tsui and Tremblay (1984) used an unsteady code to obtain steady-state solutions for natural convective air flow between horizontal annuli. They employed an ADI scheme to solve the energy and vorticity-stream function equations. They assumed vertical symmetry and used a relatively coarse mesh of 16 radial nodes together with 21 angular nodes. For moderate size Rayleigh numbers, they achieved steady-state results for three radius ratios, R = 1.2, 1.5 and 2.0. In all of these cases, they obtained the steady-state kidney-shaped flow pattern.

Lee (1984) studied laminar convection of air between concentric and eccentric heated rotating cylinders. His numerical method involved a mesh transformation technique coupled with the introduction of false transient time terms that facilitated steady-state solutions

to the problem. He studied a radius ratio of 2.6 at different Rayleigh numbers, Reynolds numbers, and eccentricities. His governing equations were solved with an ADI method and all spatial derivatives were approximated by second-order central-differences. Second-order upwind-differencing was used on the convective terms. For Ra = 25,000, he obtained a multicellular type flow when the inner cylinder was shifted upward next to the outer cylinder (ε = 2/3). When the inner cylinder was rotated, various patterns of skewed cells resulted.

Rao et al. (1985) investigated natural convective flow patterns in horizontal cylindrical annuli. They appear to be the first group of researchers that fully resolved numerically the counter-rotating cells for air, which are experienced at high Rayleigh numbers in the narrow type gaps. An unsteady formulation of the (2-D) energy and vorticity-stream function equations was used, and they solved the equations using an ADI scheme with central-differencing throughout. For R = 1.175 and a Rayleigh number (Ra) of approximately 750,000, they obtained two counter-rotating cells near the top of the half-annulus. They reported a jump in the steady-state mean Nusselt number when the flow made the transition from unicellular to multicellular flow. Numerically, they could not resolve any type of oscillatory flow for the larger gap widths, but they did experimentally verify the 3-D spiral flow associated with the intermediate size gaps.

Hessami et al. (1985) studied natural convection in a wide horizontal annulus with a radius ratio of R = 11.4. They obtained

experimental and numerical data for air, glycerin and liquid mercury in the ranges of $.023 \leq Pr \leq 10{,}000$ and $.03 \leq Gr_{D_i} \leq 3 \times 10^6$. The influence of variable versus constant fluid properties was also explored numerically.

Experimentally, they observed the regular kidney-shaped pattern for air, and a multicellular flow pattern for the liquid mercury case, similar to that described by Mack and Bishop (1968). Numerically, they assumed vertical symmetry and used a basic central-differencing scheme, except for the convective terms which were discretized by using a hybrid-differencing technique developed by Spalding (1972). This hybrid scheme collapsed to first-order accuracy upon exceeding the mesh Reynolds number constraint. Globally, the heat transfer computations for air, mercury and glycerin did not change with variation of fluid properties. However, local estimates of the Nusselt number did exhibit significant discrepancy for glycerin between the constant and variable fluid property cases.

Ozoe et al. (1985) performed a 3-D numerical analysis of natural convection in a spherical annulus for Pr = 1 and Ra = 500. By imposing a sinusoidal temperature field on the outer cylinder, they were able to obtain both symmetrical and unsymmetrical cell formation. They solved the governing equations with an ADI scheme, using central-difference approximations at all points.

2.4. Variable Fluid Properties

Since the mathematical model in this thesis is based upon the Boussinesq approximation, the effects of variable fluid properties and viscous dissipation on laminar natural convective flows should be addressed. The reviews in this section will consider some of these effects with regard to various surface geometries.

Sparrow and Gregg (1958) analyzed the influence to variable fluid properties on an isothermal vertical flat plate. They reported that laminar free convection heat transfer under variable property conditions could be accurately computed by using constant property results when evaluated at an adequate reference temperature, T_r. For air and liquid mercury, the film temperature, T_f, given by

$$T_f = (T_w + T_\infty)/2 \tag{2.20}$$

was valid for most applications. However, specific reference temperature relations were derived and are listed below.

For gases:

$$T_r = T_w - .38\ (T_w - T_\infty) \tag{2.21a}$$

and for liquid mercury:

$$T_r = T_w - .3\ (T_w - T_\infty)\ . \tag{2.21b}$$

Gebhart (1962) considered the effects of viscous dissipation on natural convective heat transfer for vertical surfaces subject to both isothermal and uniform-flux surface conditions. For such fluids as liquid sodium, gases and water, the standard practice of neglecting viscous dissipation for natural convective type flows was quite valid, especially in the laminar regime. But, he found that important viscous dissipation could result when the flow made the transition to turbulence. Also, he discussed the fact that significant viscous dissipation might occur for laminar flows subject to large decelerations or high rotative speeds.

Gray and Giorgini (1976) determined that for gases and most liquids, in geometries such as vertical plates and horizontal cylinders, the strict Boussinesq approximation was valid for Rayleigh numbers (based on the fluid layer depth) up to 10^{17}, nearly 13 decades above the transition point for turbulence (provided $\frac{\Delta\rho}{\rho} << 1$).

Clausing and Kempka (1981) experimentally investigated natural convective heat transfer from a vertical isothermal heated surface to gaseous nitrogen. They found that variable properties caused virtually no influence in heat transfer rates in the laminar regime, whereas dramatic increases were seen in the turbulent regime.

Hessami et al. (1984) studied the effects of variable fluid properties on natural convective heat transfer between horizontal concentric cylinders, for R = 2.6. They concluded that for air, the constant fluid property assumption was quite valid (for Rayleigh numbers based on gap up to 9×10^4), and could probably be extended to

all gases. In contrast, for glycerin, significant differences in the temperature field resulted between the constant and variable fluid property assumptions, although average values of the Nusselt number were very similar.

Mahony et al. (1985) investigated variable property effects on the laminar natural convection of air between horizontal cylindrical annuli. They numerically computed velocity and temperature profiles for R = 1.5, 2.28, 2.6 and 5.0, with Rayleigh numbers based on gap width up to 1.8×10^5. They claimed that the Boussinesq approximation was valid for a temperature difference ratio, θ_o, of less than .2, where θ_o was given as

$$\theta_o = \frac{T_H - T_c}{T_c} \quad . \tag{2.22}$$

But for all the numerical studies discussed in the previous section, θ_o was smaller than .1; hence any related heat transfer results were not affected by the constant property assumption. They also mentioned that since relatively low velocities are encountered in laminar natural convection, the variable property assumption should usually prove of little influence on calculated heat transfer rates.

2.5. Flow Bifurcation

Due to the tendency of multicellular flow to occur between narrow horizontal concentric cylinders at high Rayleigh numbers, flow bifurcation with related hysteresis behavior is definitely possible.

This section will briefly touch upon some articles that aid in the description of nonuniqueness and the bifurcation phenomena associated with various flows.

Coles (1965) experimentally studied flow transition between vertical concentric rotating cylinders. The so-called Taylor instability resulted when the inner cylinder achieved some critical speed. At certain speeds, Coles was able to observe both singly and doubly-periodic type motion. In this paper, Coles claims that "the property of nonuniqueness is most vividly demonstrated by the existence of a number of hysteresis loops, in which the flow changes from one state to another and back again as the speed of the inner cylinder is slowly increased and then decreased." He mentions that this same kind of behavior is possible with the cellular convection patterns that occur between horizontal heated surfaces.

In Benjamin (1978), some of the basic theory associated with bifurcation phenomena in steady flows is described. First, he points out that an instability phenomenon probably exists if a precise critical value of some parameter can be related to the onset of cellular motion. Then, a secondary mode of motion is usually realized after the primary flow becomes unstable due to some type of disruptive instability. He also stated that the Rayleigh number (in the Bénard problem) played a role similar to that corresponding to the Reynolds number in the Taylor problem.

Benjamin and Mullin (1982) observed fifteen different kinds of steady multicellular flow produced in a Taylor apparatus with the

outer wall stationary. They discussed various forms of bifurcation that might result due to sudden changes in the flow field induced by variations in the Reynolds number. And, they noted that depending on the particular cellular mode initiated at the outset, many different paths to turbulence could be followed.

Nandakumar and Masliyah (1982) investigated the occurrence of dual solutions in curved ducts through a numerical solution of the Navier-Stokes equations in a bipolar-toroidal coordinate system. The Dean number was the critical parameter used in this study, and was given by:

$$Dn = Re/R_c^{1/2} \tag{2.23}$$

where Re represented the Reynolds number and R_c the dimensionless radius of curvature of the duct. In addition to the Dean number, the shape of the duct was also varied systematically in order to study the bifurcation of a two-vortex solution into a two and four-vortex solution. They found that flow bifurcation was possible irrespective of the shape of the tube, but it was much easier to obtain a dual solution when the outer surface of the duct was nearly flat.

Cliffe (1983) numerically studied the flow in a Taylor apparatus where the length of the annulus was shortened so that only one or two Taylor cells would result. He solved the Navier-Stokes equations with a finite-element method and then, applied the methods of bifurcation theory (see Keller, 1977) to obtain multiple solutions of the equations as the Reynolds number and aspect ratio varied. At a

Reynolds number of 175, he obtained three distinct flows: a stable two-cell flow, an unstable asymmetric flow, and a stable single-cell flow. His numerical method was able to resolve the extremely delicate hysteresis effect, and he claimed that his method was powerful enough to capture the more complicated flows observed in the Taylor experiment for moderate aspect ratios.

Nandakumar et al. (1985) studied laminar mixed-convective flow in horizontal ducts of rectangular, circular and semicircular cross-sections. In all cases, dual solutions of two and four-vortex patterns were observed. The governing equations, subject to the Boussinesq approximation and an axially uniform heat-flux condition, were solved numerically with central-differencing used for both the diffusive and convective terms. For the case of the rectangular duct with a 21 x 21 uniform grid, flow hysteresis with respect to both average Nusselt number and friction-factor occurred when the flow made the transition from a two to a four-vortex steady solution. The fluid in this case was air, Pr = .73.

Kolodner et al. (1986) experimentally studied the flow patterns associated with Rayleigh-Bénard convection in rectangular containers having an intermediate aspect ratio of about 10 to 5, for Prandtl numbers between 2 and 20. In their experiments, they observed 2-D skewed-varicose and knot type instabilities, which were found to trigger successive transitions between time-independent flow patterns. In the larger Rayleigh number regime, for Pr < 10, the flow instabilities appeared to have an intrinsic oscillatory-like time

dependence.

Also related to flow bifurcation is the phenomena of strange attractors. In some systems that experience a bifurcation by way of a flow instability, an ordered route to chaos has been reported (see Ruelle and Takens, 1971; Newhouse et al., 1978; Giglio et al., 1981; Brandstäter et al., 1983; Grebogi et al., 1983; and Guckenheimer, 1986). A typical sequence of events is as follows. First, the system behaves in a time-periodic manner after the onset of the initial instability. Then, upon further increase of a system parameter (such as Reynolds or Rayleigh number), a cycle of periodic-doubling is usually observed, until finally, chaotic behavior sets in via small-scale spectral-broadening.

Some of these strange but ordered characteristics seem to have been numerically predicted in this present study. A description of the numerical technique and related results will be given in Chapters 5 and 6, respectively.

2.6. Natural Convection in Vertical Slots

Based upon the work set forth in this thesis, it appears that a multicellular instability may occur in the vertical sections of very narrow horizontal cylindrical annuli. Because of this likelihood, several papers dealing with laminar natural convection in vertical slots will be reviewed in order to shed more light on the manifestation of this unique type of hydrodynamic instability.

Elder (1965) performed an experimental study of natural convection for a liquid (Pr = 1,000) in a vertical slot with isothermal walls (the left wall being hottest). Unicellular flows resulted when the Rayleigh number based on gap width was less than 10^5. But for the larger aspect ratio (narrow gap) slots, with Rayleigh numbers slightly greater than 10^5, a steady 'cats-eye' patterned secondary flow became superimposed on the basic unicellular flow. And, upon further increasing Rayleigh number to above 10^6, Elder (1965) reported the emergence of a tertiary flow with counter-rotating type cells.

Elder (1966) numerically solved the same problem as described above, except in this case, he considered only the moderate-size vertical slots. He was able to duplicate the basic flow field obtained in his experiments, but was not able to resolve the secondary flow that was present in his previous work. Elder mentioned that the nonlinear terms began to dominate the motion as Rayleigh number increased, and he was able to numerically show the development of the boundary-layers and the fully-developed boundary-layer flow.

Vest and Arpaci (1969) analytically investigated the stability of natural convection in a narrow vertical slot. By using linearized hydrodynamic stability theory, they were able to obtain a neutral stability curve for the conduction-dominated flow regime. For $.01 \leq Pr \leq 10$, the variation of the critical Grashof number was found to be less than .7 percent. Hence, for Prandtl numbers in this range, they determined a single critical Grashof number of 7,880 at a wavenumber of 2.65. Also, their analytically obtained stream function plots for

the secondary flow qualitatively agreed with related flow pictures obtained experimentally.

Thomas and Vahl Davis (1970) numerically studied natural convection between vertical cylindrical annuli, with the inner cylinder being at a higher temperature than the outer. (Note that a similar study with more basic results can be found in Vahl Davis and Thomas, 1969.) They solved the unsteady vorticity and energy equations using an ADI scheme. For an aspect ratio of H = 25 (length of annulus to gap width), and a Rayleigh number of 22,500 (based on gap width), they observed an unsteady type of multicellular flow for Pr = 1.0. This phenomena was similar to that reported by Elder (1965), except that Elder's secondary flow maintained the steady-state condition.

Korpela et al. (1973) used linear stability theory to examine the stability of the conduction regime for natural convection in a vertical slot. For $Pr < 12.7$, they claimed that the instability set in as horizontal cells. They observed a critical Grashof number of 7,932, at a wavenumber of 2.65, for Pr = 0. This particular type of instability was thought to be hydrodynamic in origin, resulting from the vorticity distribution of the base flow.

Korpela (1974) studied a problem similar to that described above, except in this case, he assumed that the narrow slot was maintained at an angle δ with the vertical. For $Pr < 12.7$, he found that the instability set in as transverse travelling waves for small angles of inclination, and that longitudinal cells formed as δ reached a certain value. In the range of $.24 \leq Pr \leq 12.7$, he determined that the

instability would lead to horizontal cells for angles close to the vertical, whereas longitudinal cells would result as the slot was further inclined. For Pr < .24, he claimed that only horizontal cells were possible and that the stability of the flow was mainly a function of Pr tan δ.

Pepper and Harris (1977) numerically obtained 2-D natural convective flow patterns in rectangular and annular vertical cavities. The energy and vorticity equations were written in divergence form and were solved using central-differencing with a strongly implicit procedure. For the rectangular slot with an aspect ratio of 10, for Pr = 1,000, they obtained a weak multicellular flow pattern at a Rayleigh number (based on gap width) of approximately 5×10^5.

Seki et al. (1978) performed an in-depth experimental analysis of natural convection in narrow vertical rectangular cavities. They considered transformer oil, water and glycerin as the working fluids. All three fluids yielded a multicellular type of secondary flow at a certain Rayleigh number, Ra_H, based on the height of the slot. For oil, as the temperature difference was increased, they noticed a tertiary flow with counter-rotating cells, until finally, the flow near the upper region of the hot wall became unsteady and turbulent. For the oil, for an aspect ratio of 15, the secondary motion began at $Ra_H = 6 \times 10^8$ and the transition to turbulence took place at about $Ra_H = 1.5 \times 10^{10}$. They concluded that the flow field more easily shifted from laminar to transitional flow as the Prandtl number decreased and the cavity width increased. Another interesting

description of these secondary and tertiary motions can be found in Vahl Davis and Mallinson (1975).

Using linear theory, Choi and Korpela (1980) studied the stability of the conduction regime for natural convection in a vertical annulus. They found that for all Prandtl numbers, the instability set in as an upward travelling wave. Hence, stationary cells were no longer possible as with the vertical slot geometry. For low Prandtl numbers, the larger the curvature, the more stable the flow, while the reverse was true for the higher Prandtl number fluids. From experimental data, the measured wavelength of the cells was in good agreement with their linear analysis.

Orszag and Kells (1980) studied the role of two- and three-dimensional finite-amplitude disturbances in the breakdown of plane Poiseuille and plane Couette flows. To determine the evolution of these disturbances, they solved the 3-D time-dependent Navier-Stokes equations using spectral methods with Fourier and Chebyshev polynomial series. They claimed that the 3-D finite-amplitude effects produced strong inflexional velocity profiles that eventually caused the transition to turbulence; whereas the 2-D disturbances proved to be much less destabilizing, and seemed powerless for Reynolds numbers below 3,000. The contour velocity plots due to the 3-D disturbances evolved into a 'cats-eye' pattern very similar to that observed by Lee and Korpela (1983) and Elder (1965) in their study of multicellular natural convective flow in a vertical slot.

Lee and Korpela (1983) succeeded in numerically resolving multicellular natural convective flow in narrow vertical slots. They attributed their success to the 4th-order differencing method of Arakawa (1966), which was used in approximating the nonlinear convective terms. The important buoyancy term for the vertical slot geometry was represented by the single component, $\partial T/\partial x$, in the vorticity-transport equation. This resembled the buoyancy term obtained in the boundary-layer equations of Chapter 4 of this thesis, where the term reduced to simply $\partial T/\partial r$ at $\psi = 90°$ (see Figure 3.1 and Eq. (4.25b)). They were able to obtain steady multicellular flow for Prandtl numbers ranging from zero to 1,000. However, as the Prandtl number increased, the aspect ratio (H) had to be increased significantly in order to trigger the multicells. For Pr = 0, and H = 15, they obtained a secondary-flow transition to six cells at a Grashof number (based on gap width) of 8,000. This number agreed quite well with their analytical prediction of 7,932 derived in Korpela et al. (1973). The six cells formed in the vertical slot appeared fairly constant in strength. They were not sure whether a further transition to periodic flow was possible for this 2-D flow or whether the next physically important structure was a 3-D steady or periodic-type flow.

2.7. Concluding Remarks

This literature review discusses the various assumptions and solution methods employed by researchers in studying natural convection

between horizontal concentric cylinders. Some contradictory conclusions and results have been highlighted. Of particular importance, experimenters have verified that for air at high Rayleigh numbers, a multicellular flow is possible near the top of narrow horizontal cylindrical annuli. However, not all numerical investigators confirmed this fact. It seemed that the transition to multicells could not be captured due to either first-order upwind differencing of the convective terms, or a lack of numerical stability experienced when approaching high Rayleigh numbers. Thus, it appears that at least second-order accuracy is a prerequisite for resolving this multicellular type of instability. In addition, for this geometry there appears to be a void in the research regarding the possibility of related hysteresis behavior associated with the transition to multicells.

Also from this literature review, it can be seen that the potential multicellular flow in the vertical portions of narrow horizontal annuli, as described in this research effort, has not been examined.

3. MATHEMATICAL ANALYSIS

In this study, the Boussinesq approximated Navier-Stokes equations and the viscous-dissipation neglected thermal-energy equation will be used to determine the buoyancy-induced steady or unsteady flow fields between horizontal isothermal concentric cylinders. The Boussinesq approximation states that density perturbations are only felt in the body force terms and can be neglected in the acceleration and viscous components. Furthermore, the vorticity-stream function formulation of the Navier-Stokes equations will be adopted. Using this approach completely eliminates the pressure gradient terms and automatically satisfies the conservation of mass principle. An added advantage is that stream function and vorticity contours are well-suited for visualizing and analyzing the flow.

3.1. The Physical Model

a. The model is unsteady and two-dimensional (see Figure 3.1).

b. Initially, the fluid is at rest.

c. The cylinders are assumed horizontal and isothermal, with the inner cylinder temperature exceeding the outer.

d. Laminar fluid motion is induced by buoyancy effects. The fluid is Newtonian.

e. All material properties are assumed constant. Density variations are allowed to occur via the Boussinesq approximation.

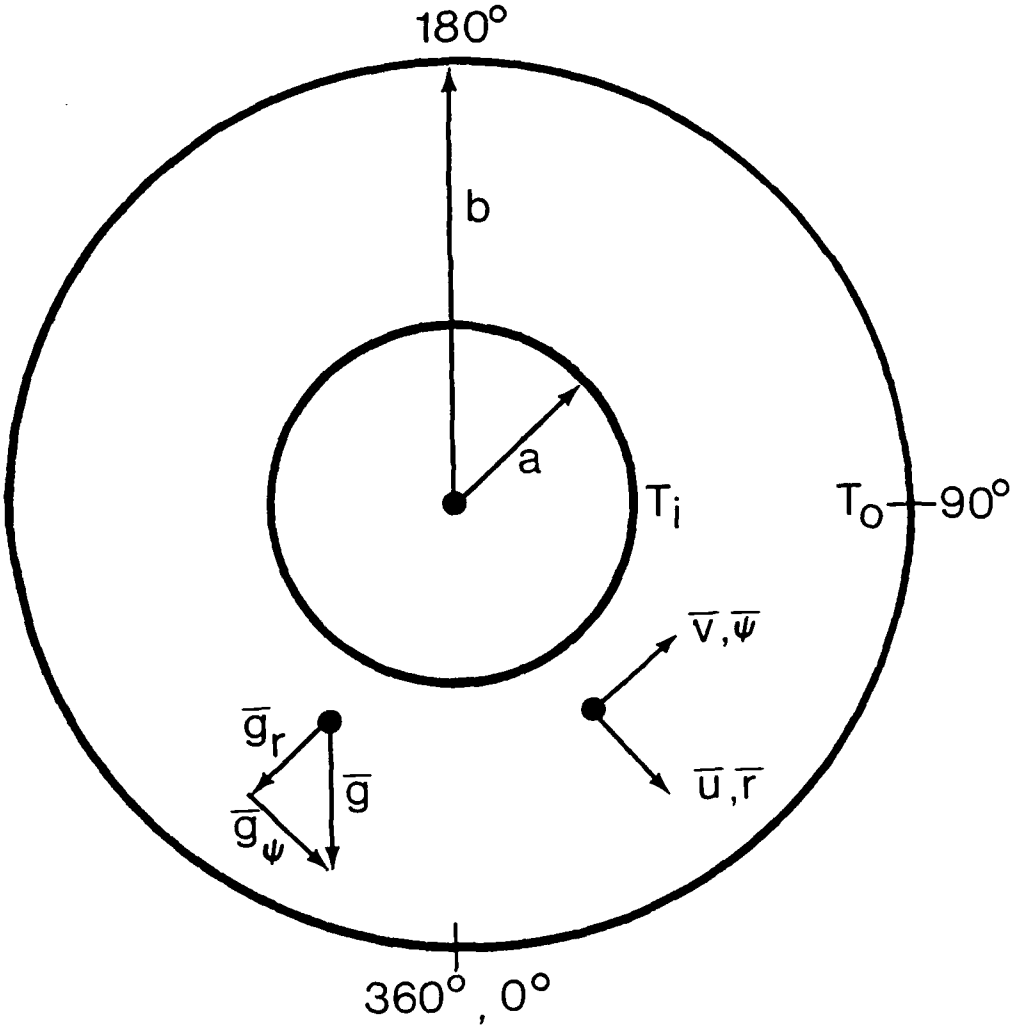

Figure 3.1. 2-D concentric cylinder geometry

3.2. The Complete Set of Governing Equations

Before formally deriving the dimensional and nondimensional forms of the governing equations, the complete system of equations will be given below. This is done to provide for easy access when the equations are numerically solved or referred to in subsequent chapters of this thesis. The dimensionless system of coupled partial differential equations is

Thermal-energy:

$$G^2 \frac{\partial T}{\partial t} + \left(r + \frac{1}{G}\right)^{-1} \left(\frac{\partial f}{\partial r}\frac{\partial T}{\partial \psi} - \frac{\partial f}{\partial \psi}\frac{\partial T}{\partial r}\right) = \frac{1}{Pr}\left\{\frac{\partial^2 T}{\partial r^2} + \left(r + \frac{1}{G}\right)^{-1}\frac{\partial T}{\partial r} + \left(r + \frac{1}{G}\right)^{-2}\frac{\partial^2 T}{\partial \psi^2}\right\} \tag{3.1a}$$

Vorticity:

$$Pr\left\{G^2 \frac{\partial w}{\partial t} + \left(r + \frac{1}{G}\right)^{-1}\left(\frac{\partial f}{\partial r}\frac{\partial w}{\partial \psi} - \frac{\partial f}{\partial \psi}\frac{\partial w}{\partial r}\right)\right\} = Pr\left\{\frac{\partial^2 w}{\partial r^2} + \left(r + \frac{1}{G}\right)^{-1}\frac{\partial w}{\partial r} + \left(r + \frac{1}{G}\right)^{-2}\frac{\partial^2 w}{\partial \psi^2}\right\} + G(Ra)\left\{\sin\psi\,\frac{\partial T}{\partial r} + \frac{\cos\psi}{\left(r + \frac{1}{G}\right)}\frac{\partial T}{\partial \psi}\right\} \tag{3.1b}$$

Stream function:

$$\frac{\partial^2 f}{\partial r^2} + \left(r + \frac{1}{G}\right)^{-1}\frac{\partial f}{\partial r} + \left(r + \frac{1}{G}\right)^{-2}\frac{\partial^2 f}{\partial \psi^2} = G^2 w \quad , \tag{3.1c}$$

while the related boundary conditions are

at r = 0 (inner cylinder):

$$T = 1$$

$$w = \frac{1}{G^2} \frac{\partial^2 f}{\partial r^2}$$

$$f = 0 \qquad (3.1d)$$

at r = 1 (outer cylinder):

$$T = 0$$

$$w = \frac{1}{G^2} \frac{\partial^2 f}{\partial r^2}$$

$$f = 0 \; . \qquad (3.1e)$$

The derivation and explanation of important terms and symbols, together with the boundary and initial conditions, follow in the next two sections.

3.3. The Dimensional Formulation

3.3.1. Governing equations in primitive variables

Four governing equations are needed in order to describe the transport of mass, momentum and energy between the horizontal concentric cylinder geometry. These equations are written in terms of primitive variables using polar coordinates $(\bar{r},\bar{\psi})$ (see Figure 3.1). The bar over the variable signifies a dimensional quantity. The radial and angular coordinates are given by $\bar{r}$ and $\bar{\psi}$, respectively. $\bar{T}$ is the

temperature and $\bar{t}$ denotes time. The radial velocity is represented by $\bar{u}$ and the angular or tangential velocity is given by $\bar{v}$. $\bar{P}$ is the pressure term, while ν and α are the momentum and thermal diffusivities, respectively. Lastly, ρ is the density and $\bar{F}$ is the body force term in the equations of motion. The 2-D governing equations in primitive variables are

Equation of continuity:

$$\frac{\partial \bar{u}}{\partial \bar{r}} + \frac{\bar{u}}{\bar{r}} + \frac{1}{\bar{r}} \frac{\partial \bar{v}}{\partial \psi} = 0 \tag{3.2a}$$

Equations of motion:

$$\frac{D\bar{u}}{D\bar{t}} - \frac{\bar{v}^2}{\bar{r}} = \frac{-1}{\rho} \frac{\partial \bar{p}}{\partial \bar{r}} + \nu(\nabla^2 \bar{u} - \frac{\bar{u}}{\bar{r}^2} - \frac{2}{\bar{r}^2} \frac{\partial \bar{v}}{\partial \psi}) + \bar{F}_r \tag{3.2b}$$

$$\frac{D\bar{v}}{D\bar{t}} + \frac{\bar{u}\bar{v}}{\bar{r}} = \frac{-1}{\rho \bar{r}} \frac{\partial \bar{p}}{\partial \psi} + \nu(\nabla^2 \bar{v} - \frac{\bar{v}}{\bar{r}^2} + \frac{2}{\bar{r}^2} \frac{\partial \bar{u}}{\partial \psi}) + \bar{F}_\psi \tag{3.2c}$$

Equation of thermal-energy:

$$\frac{D\bar{T}}{D\bar{t}} = \alpha \nabla^2 \bar{T} \tag{3.2d}$$

where $D/D\bar{t}$, the substantial or material derivative, represents a combination of the local and convective changes of a particular property (usually associated with the acceleration terms), and is given by

$$\frac{D}{D\bar{t}} = \frac{\partial}{\partial \bar{t}} + \bar{u} \frac{\partial}{\partial \bar{r}} + \frac{\bar{v}}{\bar{r}} \frac{\partial}{\partial \psi} \quad .$$

Also, ∇^2 (the 2-D cylindrical Laplacian) is given by

$$\nabla^2 = \frac{\partial^2}{\partial \bar{r}^2} + \frac{1}{\bar{r}} \frac{\partial}{\partial \bar{r}} + \frac{1}{\bar{r}^2} \frac{\partial^2}{\partial \psi^2} \quad . \tag{3.3}$$

The centrifugal acceleration term, $\bar{v}^2/\bar{r}$, in Eq. (3.2b), represents the effective force per unit mass and volume in the radial direction, resulting from fluid motion in the angular direction. Whereas, $\bar{u}\bar{v}/\bar{r}$ in Eq. (3.2c) designates the Coriolis acceleration, and represents the effective force (per unit mass and volume) in the angular direction when fluid motion occurs in both the radial and angular directions. It should be noted that these two terms arise automatically upon transformation from rectangular to cylindrical coordinates (Bird et al., 1960). The $\bar{F}$ terms in Eqs. (3.2b) and (3.2c) are due to the buoyancy force. They can be evaluated with the aid of the Boussinesq approximation, which allows density to be variable only in the body force terms of the momentum equation. The corresponding change in fluid density with temperature is related by

$$\rho' = \rho - \rho_o = -\rho_o \beta \, (\bar{T} - T_o)$$

where ρ_o, T_o represent property values evaluated at some known reference state (e.g., the initial density and temperature of the fluid within the annulus), and β is the coefficient of thermal expansivity, which becomes the negative reciprocal of absolute

temperature for an ideal gas. One can regard the expression for ρ as the first two terms of a Taylor-series expansion about T_o. The net body force term, $\frac{-\rho'}{\rho_o} \bar{g}\, \hat{j}$, can now be broken down into its radial and angular components:

$$-g\beta(\bar{T} - T_o)\hat{j} = -g\beta(\bar{T} - T_o)\cos\psi\ \hat{e}_r + g\beta(\bar{T} - T_o)\sin\psi\ \hat{e}_\psi \qquad (3.4)$$

where g is the acceleration of gravity.

The Boussinesq approximation is normally considered quite accurate when dealing with laminar-type flows, especially for Prandtl numbers ranging from near zero to one and for small ΔT ($\Delta T \sim 0$ (15°C) or less) (Gray and Giorgini, 1976; Hessami et al., 1984; Mahony et al., 1985). As a final note, the viscous dissipation term has not been included in the thermal-energy equation. This term is usually only significant in high-speed flow applications, or for laminar flows subject to large decelerations (Gebhart, 1962).

3.3.2. Governing equations using the stream function-vorticity approach

The stream function ($\bar{f}$) is defined in such a way so as to automatically satisfy the continuity equation. It is valid for all two-dimensional flows, both rotational and irrotational, and can be defined as:

$$\bar{u} = \frac{-1}{\bar{r}} \frac{\partial \bar{f}}{\partial \psi} \quad \text{and} \quad \bar{v} = \frac{\partial \bar{f}}{\partial \bar{r}} \ . \qquad (3.5)$$

The number of dependent velocity variables has now been reduced by one. Physically, for 2-D incompressible flows, the volumetric flow rate between two streamlines is given by the difference in $\bar{f}$.

To further simplify the remaining governing equations, the vorticity-transport equation will be derived by taking the curl of the Navier-Stokes equations. To begin, the equations of motion for a Newtonian fluid of constant density and viscosity will be written in vector form (which is valid for any coordinate system):

$$\frac{\partial \bar{v}}{\partial t} + (\bar{v} \cdot \bar{\nabla})\bar{v} = -\frac{\bar{\nabla}p}{\rho} + \nu\nabla^2 \bar{v} + \bar{F}_B \quad . \tag{3.6}$$

Note that $\bar{\nabla} = \frac{\partial}{\partial \bar{r}} \hat{e}_r + \frac{1}{\bar{r}} \frac{\partial}{\partial \bar{\psi}} \hat{e}_\psi$ in 2-D cylindrical coordinates, and $\bar{v}$ represents the velocity vector. Next, the convective term in Eq. (3.6) is expanded using the following vector identity:

$$(\bar{v} \cdot \bar{\nabla})\bar{v} = \frac{1}{2} \bar{\nabla}(\bar{v} \cdot \bar{v}) - \bar{v} \times (\bar{\nabla} \times \bar{v}) \quad .$$

Then, since vorticity (which physically represents the rotation of an infinitesimal fluid particle) is given by

$$\bar{w} = \bar{\nabla} \times \bar{v} \ ,$$

and by utilizing other appropriate vector identities along with the continuity equation, one obtains the following result:

$$\frac{\partial \bar{w}}{\partial t} + (\bar{v} \cdot \bar{\nabla})\bar{w} = (\bar{w} \cdot \bar{\nabla})\bar{v} + \nu\bar{\nabla}^2\bar{w} + \bar{\nabla} \times \bar{F}_B \quad . \tag{3.7}$$

The left side on Eq. (3.7) describes the total rate change of particle vorticity. $(\bar{w} \cdot \bar{\nabla})\bar{v}$, which represents the rate of stretching of vortex lines, is identically zero for 2-D flows since the vorticity vector in the 2-D case is always perpendicular to the plane of flow. $\nu\bar{\nabla}^2\bar{w}$ signifies the net rate of vorticity diffusion due to viscous effects. The last term, $\bar{\nabla} \times \bar{F}_B$, represents the rate of internal vorticity generation due to body forces, which result from significant density perturbations in natural convective flows (Panton, 1984). Note the fact that the pressure term does not appear explicitly in the vorticity equation. Thus, the vorticity and stream function (velocity) fields can be determined without any prior knowledge of the pressure distribution (Currie, 1974).

Using the result of Eq. (3.4) to evaluate $\bar{\nabla} \times \bar{F}_B$, and upon substituting the stream function for the velocity terms, the final form of the vorticity-transport equation is obtained, namely:

$$\frac{\partial \bar{w}}{\partial \bar{t}} + \frac{1}{\bar{r}} \frac{\partial(\bar{f},\bar{w})}{\partial(\bar{r},\bar{\psi})} = g\beta\left(\sin\bar{\psi} \frac{\partial \bar{T}}{\partial \bar{r}} + \frac{\cos\bar{\psi}}{\bar{r}} \frac{\partial \bar{T}}{\partial \bar{\psi}}\right) + \nu\bar{\nabla}^2\bar{w} \tag{3.8a}$$

and likewise, the thermal-energy and stream function equations simplify to:

$$\frac{\partial \bar{T}}{\partial \bar{t}} + \frac{1}{\bar{r}} \frac{\partial(\bar{f},\bar{T})}{\partial(\bar{r},\bar{\psi})} = \alpha\bar{\nabla}^2\bar{T} \tag{3.8b}$$

$$\bar{w} = \nabla^2 \bar{f} \ , \tag{3.8c}$$

where ∇^2 is the same as in Eq. (3.3), and the Jacobian, $\partial(P,Q)/\partial(x,y)$, is defined as

$$\frac{\partial(P,Q)}{\partial(x,y)} = \frac{\partial P}{\partial x}\frac{\partial Q}{\partial y} - \frac{\partial P}{\partial y}\frac{\partial Q}{\partial x} \ .$$

Equations (3.8a, b, and c) are the three coupled governing equations that describe the dependent variables $\bar{w}$, $\bar{T}$, and $\bar{f}$ for the horizontal annulus.

3.3.3. Boundary conditions

The energy, vorticity, and stream function equations are all second-order partial differential equations. Therefore, two boundary conditions (in each spatial coordinate) for each equation are needed to properly define a well-posed mathematical problem. For temperature, isothermal cylinders are assumed, with the inner cylinder being hotter than the outer one. Thus,

$$\bar{T} = T_i \quad \text{at} \quad \bar{r} = a$$

and

$$\bar{T} = T_o \quad \text{at} \quad \bar{r} = b \ , \tag{3.9a}$$

where T_i is greater than T_o.

Since both $\bar{u}$ and $\bar{v}$ are identically zero at the stationary cylinder walls due to the no-slip condition, the vorticity boundary condition

becomes:

$$\bar{w} = \frac{\partial^2 \bar{f}}{\partial \bar{r}^2} \quad \text{at } \bar{r} = a \text{ and } \bar{r} = b \quad . \tag{3.9b}$$

Again, because of no-slip at the walls, the stream function must remain constant and can be taken as:

$$\bar{f} = 0 \quad \text{at } \bar{r} = a \text{ and } \bar{r} = b \quad . \tag{3.9c}$$

Since the complete annular cylindrical space (0-2π) is being analyzed, the following boundary conditions (in $\bar{\psi}$) are needed because of continuity at zero and 2π radians:

$$\phi_o = \phi_{2\pi}$$

$$\text{and} \qquad \left.\frac{\partial \phi}{\partial \bar{\psi}}\right|_o = \left.\frac{\partial \phi}{\partial \bar{\psi}}\right|_{2\pi} \quad \text{for any given } \bar{r},\ a \leq \bar{r} \leq b \ , \tag{3.9d}$$

where ϕ takes on values of either temperature, vorticity, or stream function.

For certain cases (as will be described in the numerical analysis of Chapter 5), symmetry about the vertical axis will be assumed. In these cases, the condition defined by Eq. (3.9d) will be replaced by the following symmetrical boundary conditions:

$$\bar{f} = \bar{w} = 0 \text{ and } \frac{\partial \bar{T}}{\partial \bar{\psi}} = 0 \text{ at } \bar{\psi} = 0 \text{ and } \pi \text{ radians} \quad . \tag{3.10}$$

3.3.4. Initial conditions

Since initially there is no fluid motion, the initial conditions for this problem are straightforward. Thus,

$$\bar{f} = \bar{w} = 0 \text{ and } \bar{T} = T_o \tag{3.11a}$$

throughout the annulus, except at the walls where:

$$\bar{T} = T_i \text{ and } \bar{T} = T_o \tag{3.11b}$$

at $\bar{r} = a$ and $\bar{r} = b$, respectively.

Prescribed initial conditions, other than "zero" fluid motion, will be used in this study when checking for hysteresis loops. These conditions will be briefly discussed after the nondimensional formulation is derived in the next section.

3.4. The Dimensionless Formulation

The advantages of casting equations in dimensionless format are that first, it helps transform the mathematical or numerical results into a simpler (normalized) form, thus allowing for better graphical interpretation. Second, measurement scales are no longer an intrinsic part of the physical quantities, so that any laws governing physical variables are valid for all different measurement systems (Panton, 1984). Most importantly, when a problem is nondimensionalized, fewer variables are used and the number of dimensionless groups needed to specify a particular system is kept to a minimum.

3.4.1. Coordinate transformation

The radial coordinate is nondimensionalized so that the outer boundary at $\bar{r} = b$ is transformed into the unit circle $r = 1$ (see Figure 3.2). The inner boundary, $\bar{r} = a$, is transformed into the pole, $r = 0$. The following is then obtained:

$$r = \frac{\bar{r} - a}{b - a} \, , \quad \psi = \bar{\psi} \qquad \text{(coordinate transformation)} \tag{3.12a}$$

and the other independent variable, time, is scaled as

$$t = \bar{t} \, \frac{\nu}{a^2} \quad . \tag{3.12b}$$

3.4.2. Governing equations

The remaining dependent variables are now scaled to produce the following dimensionless set of dependent variables:

$$T = \frac{\bar{T} - T_o}{T_i - T_o} \qquad \text{(temperature)} \tag{3.12c}$$

$$w = \bar{w} \, \frac{a^2}{\nu} \qquad \text{(vorticity)} \tag{3.12d}$$

$$f = \frac{\bar{f}}{\nu} \qquad \text{(stream function)} \quad . \tag{3.12e}$$

Equations (3.12) can now be substituted into Eqs. (3.8a-c), yielding the following nondimensional governing equations:

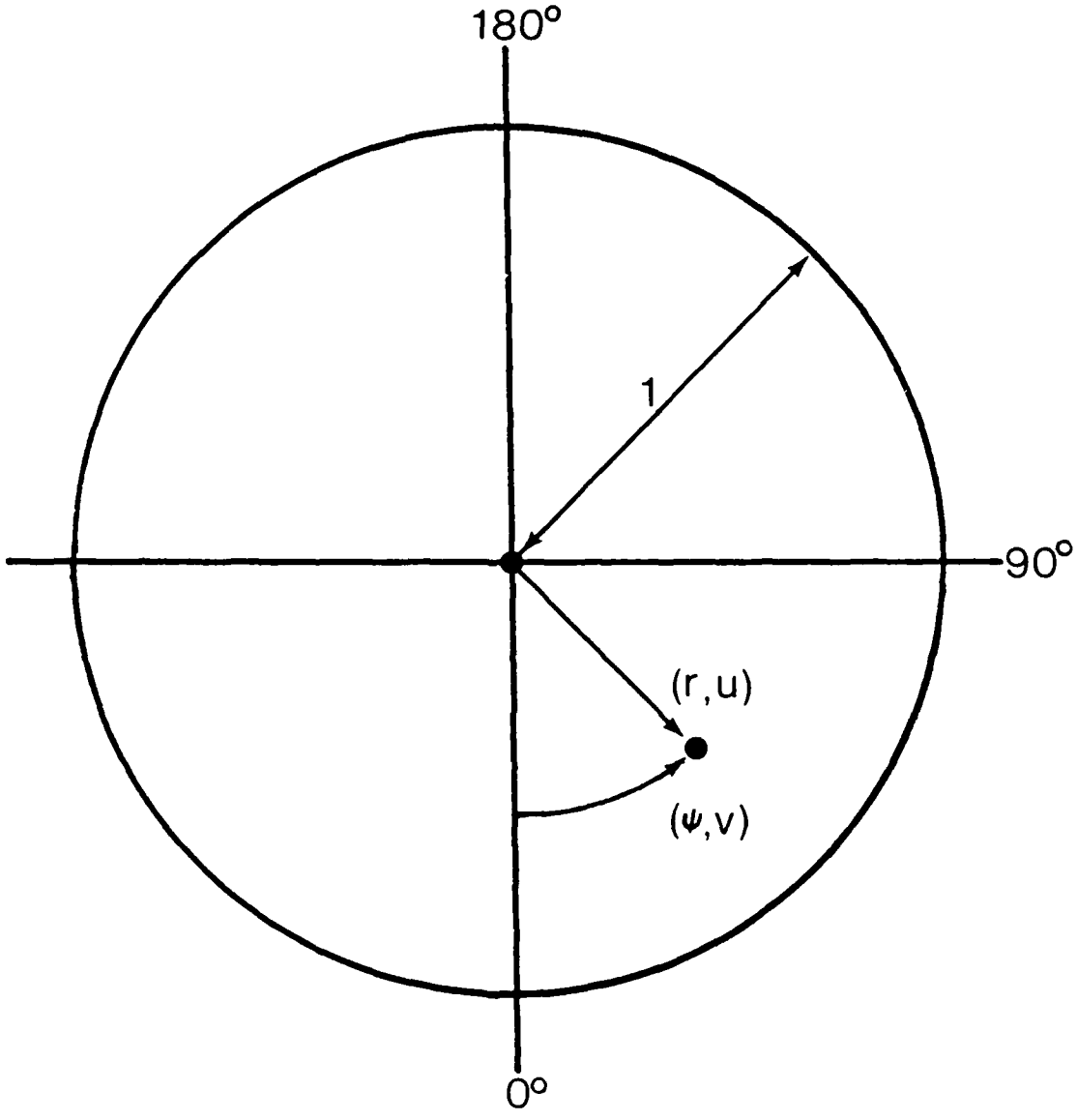

Figure 3.2. Dimensionless coordinate system for the concentric cylinder geometry

$$Pr\ \{G^2\ \frac{\partial w}{\partial t} + (r + \frac{1}{G})^{-1}\ \frac{\partial(f,w)}{\partial(r,\psi)}\ \} = Pr \cdot \nabla_2^2 w$$

$$+ G \cdot Ra\ \{\sin\psi\ \frac{\partial T}{\partial r} + \frac{\cos\psi}{(r + \frac{1}{G})}\ \frac{\partial T}{\partial \psi}\ \} \qquad (3.13a)$$

$$G^2\ \frac{\partial T}{\partial t} + (r + \frac{1}{G})^{-1}\ \frac{\partial(f,T)}{\partial(r,\psi)} = \frac{1}{Pr}\ (\nabla_2^2\ T) \qquad (3.13b)$$

$$\nabla_2^2\ f = G^2 w \qquad (3.13c)$$

where

$$\nabla_2^2 = \frac{\partial^2}{\partial r^2} + (r + \frac{1}{G})^{-1}\ \frac{\partial}{\partial r} + (r + \frac{1}{G})^{-2}\ \frac{\partial^2}{\partial \psi^2}$$

and again,

$$\frac{\partial(P,Q)}{\partial(x,y)} = \frac{\partial P}{\partial x}\ \frac{\partial Q}{\partial y} - \frac{\partial P}{\partial y}\ \frac{\partial Q}{\partial x} \quad .$$

Also,

$$Pr = \frac{\nu}{\alpha} \qquad \text{(Prandtl number)} \qquad (3.13d)$$

$$Ra = \frac{g\beta a^3 (T_i - T_o)}{\nu\ \alpha} \qquad \text{(Rayleigh number based on the inner radius, a)} \qquad (3.13e)$$

and $$G = \frac{b - a}{a} \qquad \text{(gap number)} \quad . \qquad (3.13f)$$

G was chosen such that as the inner radius (a) approached the outer radius (b), the gap number would tend to zero.

Therefore, the three dimensionless groups brought forth from this analysis are G, Pr, and Ra. These three variables will be used to simulate the various flow conditions and geometries under consideration. The Rayleigh number alone is normally considered the critical parameter which predicts the onset of thermal and/or hydrodynamic instability (variations of this will be discussed in Chapter 4), and can be interpreted as the ratio of the destabilizing buoyant forces to the stabilizing viscous forces. The Prandtl number characterizes the fluid, and the gap number identifies the geometry.

In the formulation of Eqs. (3.13), the variables w, f, and t were nondimensionalized with ν instead of α. This was done in the hope that for $Pr \leq 1$, the numerical stability of the problem would be enhanced. For these low range Prandtl numbers, investigated in this study, the flow field should be thermal-diffusion dominated. This is consistent with the thermal-energy equation (Eq. 3.13b); that is, as Pr decreases from one, the diffusion-side of Eq. (3.13b) increases. Representing the equations in this nondimensional form better supports diagonal dominance when the equations are solved numerically, since less emphasis is given to the left-hand side (off-diagonal contributing) nonlinear terms.

The Jacobian terms in Eqs. (3.13a and b) can also be written in terms of the velocity variables, where u and v are:

$$u = \frac{-1}{G(r + \frac{1}{G})} \frac{\partial f}{\partial \psi} = \bar{u} \left(\frac{a}{\nu}\right) \qquad \text{(radial velocity)} \qquad (3.14a)$$

and

$$v = \frac{1}{G}\frac{\partial f}{\partial r} = \bar{v}\ (\frac{a}{\nu}) \qquad \text{(tangential velocity).} \qquad (3.14b)$$

With these substitutions, the dimensionless governing equations in (3.13) become:

Energy:

$$G^2\frac{\partial T}{\partial t} + uG\frac{\partial T}{\partial r} + \frac{vG}{(r+\frac{1}{G})}\frac{\partial T}{\partial \psi}$$

$$= \frac{1}{Pr}\{\frac{\partial^2 T}{\partial r^2} + \frac{1}{(r+\frac{1}{G})}\frac{\partial T}{\partial r} + \frac{1}{(r+\frac{1}{G})^2}\frac{\partial^2 T}{\partial \psi^2}\} \qquad (3.15a)$$

Vorticity:

$$Pr\{G^2\frac{\partial w}{\partial t} + uG\frac{\partial w}{\partial r} + \frac{vG}{(r+\frac{1}{G})}\frac{\partial w}{\partial \psi}\}$$

$$= Pr\{\frac{\partial^2 w}{\partial r^2} + \frac{1}{(r+\frac{1}{G})}\frac{\partial w}{\partial r} + \frac{1}{(r+\frac{1}{G})^2}\frac{\partial^2 w}{\partial \psi^2}\}$$

$$+ G(Ra)\{\sin\psi\frac{\partial T}{\partial r} + \frac{\cos\psi}{(r+\frac{1}{G})}\frac{\partial T}{\partial \psi}\} \qquad (3.15b)$$

Stream function:

$$\frac{\partial^2 f}{\partial r^2} + \frac{1}{(r+\frac{1}{G})}\frac{\partial f}{\partial r} + \frac{1}{(r+\frac{1}{G})^2}\frac{\partial^2 f}{\partial \psi^2} = G^2 w \quad . \qquad (3.15c)$$

Equations (3.15a-c) were written in the above form so as to facilitate the asymptotic analysis that will follow in Chapter 4, in which the double-limit of $Ra \to \infty$ and $G \to 0$ is examined.

3.4.3. Boundary conditions

The nondimensional boundary conditions for this problem are obtained by substituting Eqs. (3.12) into Eqs. (3.9). They are given in Eqs. (3.1d) and (3.1e) for $r = 0$ and 1, respectively.

The continuity boundary condition applies at zero and 2π radians, and is similar to that described in Eq. (3.9d), except that dimensional variables are now nondimensionalized. Likewise, if vertical symmetry is assumed, one gets:

$$f = w = 0, \frac{\partial T}{\partial \psi} = 0 \text{ at } \psi = 0 \text{ and } \pi \text{ radians} \quad . \tag{3.15d}$$

3.4.4. Initial conditions

The dimensionless initial conditions are essentially the same as those listed in Eqs. (3.11). That is, for the entire annulus,

$$T = f = w = 0 \ , \tag{3.16a}$$

except at the isothermal walls, where:

$$T = 1 \text{ at } r = 0$$

and

$$T = 0 \text{ at } r = 1 \quad . \tag{3.16b}$$

Again, these initial conditions arise by assuming that initially the fluid is motionless, or Ra = 0. Thus, the problem initially reduces to the 1-D steady-state conduction case for a cylindrical annulus. However, when numerically searching for transitional Rayleigh numbers and hysteresis behavior, initial conditions other than "zero" are used. These procedures will be outlined in detail in Chapter 5.

4. ASYMPTOTIC ANALYSIS

In this chapter, a high Rayleigh number/small-gap asymptotic expansion theory is described in which the 2-D Navier-Stokes (N-S)[1] equations collapse into cartesian-like boundary-layer equations.

The purpose of this analysis was to gain a deeper understanding of the transitional tendency toward multicellular flow in narrow gaps, especially with regard to the mechanism that triggers the multicells. To understand this mechanism, key points had to be resolved: (1) does the source of instability originate from thermal or hydrodynamic effects, and (2) once determined, do these effects ever coexist or does one always outweigh the other?

Also from this asymptotic analysis, results were obtained which serve as convenient checks for the pretransitional numerical results generated in the flow bifurcation study of this research effort.

At the high Rayleigh number limit, the annular flow field can be divided into an inner and outer boundary-layer with an inviscid core in the center. In general, the boundary-layers are noninteracting, which disallows an inviscid core solution to be arbitrarily set. Also, since inviscid flows are nonunique, the correct core solution must be chosen in order to avoid a singularity at separation (Goldstein, 1948). Since the correct inviscid solution is usually not known a priori, one needs a type of interactive boundary-layer theory which

---

[1] Throughout this chapter, the 2-D N-S equations refer to those outlined in Eq. (3.15).

supports separation. A good way of devising such a theory for this particular geometry is to look for the point where the boundary-layers merge. Then, the inviscid core can be asymptotically matched with the boundary-layer to verify the small-gap boundary-layer structure.

Work begins with the construction of inviscid core expansions for $Ra \to \infty$ and $G \to 0$. This construction is necessary to facilitate a valid match of the core and boundary-layer tangential velocities, which, in turn, provides for the correct scaling of the boundary-layer variables.

4.1. The Inviscid Core

For finite values of the coordinates, the viscous terms in the 2-D N-S vorticity equation can be neglected in the limit as $Ra \to \infty$. This results in an inviscid vorticity equation in which the buoyancy forces are balanced by the convective acceleration forces at steady state. Since vorticity is represented as the curl of the velocity field, and because the gap scaling has been taken care of in the nondimensionalization, one can assume that velocity expands like vorticity, which gives

$$w_c \sim u_c \sim v_c \sim Ra^{1/2}$$

by inspection of the inviscid vorticity equation. More formally, the following expansions can be substituted into the inviscid vorticity equation to provide the same result to leading order, namely,

$$
\begin{aligned}
u_c &= \delta_o u_o + \delta_1 u_1 + \ldots . \\
v_c &= \delta_o v_o + \delta_1 v_1 + \ldots . \\
w_c &= \delta_o w_o + \delta_1 w_1 + \ldots . \\
f_c &= \eta_o f_o + \eta_1 f_1 + \ldots . \\
T_c &= \gamma_o T_o + \gamma_1 T_1 + \ldots .
\end{aligned} \tag{4.1}
$$

where $\delta_o \sim Ra^{1/2}$. Likewise, upon substituting the expansions for f and w into the stream function equation, one gets

$$\eta_o \sim \delta_o \sim Ra^{1/2} \quad .$$

Similarly, because velocity scales become large as $Ra \to \infty$, the viscous terms in the energy equation can also be neglected. Assuming that temperature is of order one in the core, from the anticipated match with the wall boundary-layers, $\gamma_o \sim 1$. Thus, to first order, the inviscid core expansions become:

$$
\begin{aligned}
u_c &= Ra^{1/2}\, u_o + O(1) \\
v_c &= Ra^{1/2}\, v_o + O(1) \\
w_c &= Ra^{1/2}\, w_o + O(1) \\
f_c &= Ra^{1/2}\, f_o + O(1) \\
T_c &= T_o + O(Ra^{-1/2}) \quad .
\end{aligned} \tag{4.2}
$$

With these expansions, the inviscid governing equations, for a finite-

gap inviscid core, take on the following form (to first order in the limit as $Ra \to \infty$):

Energy:

$$G^2 \frac{\partial T_o}{\partial t^*} + G\, u_o \frac{\partial T_o}{\partial r} + \frac{G}{r + \frac{1}{G}} v_o \frac{\partial T_o}{\partial \psi} = 0 \tag{4.3}$$

Vorticity:

$$Pr \left\{G^2 \frac{\partial w_o}{\partial t^*} + u_o\, G \frac{\partial w_o}{\partial r} + \frac{G}{r + \frac{1}{G}} v_o \frac{\partial w_o}{\partial \psi}\right\}$$
$$= G \left\{\sin\psi \frac{\partial T_o}{\partial r} + \frac{\cos\psi}{r + \frac{1}{G}} \frac{\partial T_o}{\partial \psi}\right\} \tag{4.4}$$

Stream Function:

$$\frac{\partial^2 f_o}{\partial r^2} + \frac{1}{r + \frac{1}{G}} \frac{\partial f_o}{\partial r} + \frac{1}{(r + \frac{1}{G})^2} \frac{\partial^2 f_o}{\partial \psi^2} = G^2\, w_o \tag{4.5}$$

where $t^* = Ra^{1/2} t$.

With the above time-scaling factor, the local acceleration terms are retained in the governing equations. Although steady-state analytical solutions are sought, the unsteady terms enable one to solve the equations numerically by marching in a time-accurate fashion. Thus, the capability exists for resolving either steady or unsteady effects within the resulting flow field. Also of importance, the Rayleigh number dependence, which was one of the key dimensionless parameters in the 2-D N-S equations, has been completely factored out in Eqs. (4.3) and (4.4).

Considering the limit as $G \to 0$, the curvilinear metrics drop out and new scales are obtained in order to retain all the nonlinear convective terms while satisfying the stream function equation:

$$
\begin{aligned}
u_o &\sim G\,\tilde{u}_o + O(G^2) \\
v_o &\sim \tilde{v}_o + O(G) \\
w_o &\sim G^{-1}\,\tilde{w}_o + O(1) \\
f_o &\sim G\,\tilde{f}_o + O(G^2) \\
T_o &\sim \tilde{T}_o + O(G^2)
\end{aligned}
\tag{4.6}
$$

Neglecting terms of $O(G^2)$ and higher, relative to terms of $O(G)$, Eqs. (4.3) through (4.5) become:

Energy:

$$
\frac{\partial \tilde{T}_o}{\partial t^*} + \tilde{u}_o \frac{\partial \tilde{T}_o}{\partial r} + \tilde{v}_o \frac{\partial \tilde{T}_o}{\partial \psi} = 0 \tag{4.7}
$$

Vorticity:

$$
Pr \left\{ \frac{\partial \tilde{w}_o}{\partial t^*} + \tilde{u}_o \frac{\partial \tilde{w}_o}{\partial r} + \tilde{v}_o \frac{\partial \tilde{w}_o}{\partial \psi} \right\} = \sin\psi \frac{\partial \tilde{T}_o}{\partial r} \tag{4.8}
$$

Stream Function:

$$
\frac{\partial^2 \tilde{f}_o}{\partial r^2} = \tilde{w}_o \quad . \tag{4.9}
$$

In these equations, the G dependency, which was again important in the 2-D N-S equations, has also vanished. The stream function equation appears to be in boundary-layer format, as should also be the case for the energy and vorticity equations when the viscous terms are included. The inviscid core equations can satisfy the flow tangency condition, but cannot satisfy the physical no-slip condition that must be met at the walls, where the viscous terms play their important role. At this point, one gathers from Eq. (4.8) that the gravitational terms have reduced to simply $\sin\psi\ \partial\tilde{T}_o/\partial r$, as $G \to 0$. This first-order term is essential in driving the buoyancy-induced flow field, and its effect seems just as significant in the adjacent boundary-layers, as will be shown in the next section. Note, however, that the gravitational term proportional to $\cos\psi\ \partial\tilde{T}_o/\partial\psi$ comes in as a second-order effect within the small-gap inviscid core solution. But its effect should prove negligible (or of much less importance) within the boundary-layers since being consistent with boundary-layer theory, $\partial T/\partial\psi << \partial T/\partial r$.

4.2. The Boundary-Layer Expansion

To incorporate the higher order viscous derivatives, the inner radial coordinate is stretched as

$$R = \frac{\bar{r} - a}{\delta} = \frac{r\ G\ a}{\delta} \qquad (4.10)$$

where δ is the inner boundary-layer thickness. Then, in its transformed

state, the tangential velocity ($v = \frac{1}{G} \frac{\partial f}{\partial r}$) within the boundary-layer, v_{BL}, becomes (for a finite-gap size):

$$v_{BL} = \frac{1}{\delta} \frac{\partial f}{\partial R} \tag{4.11}$$

and due to asymptotic matching principles, one must have

$$v_{BL} \sim v_c \sim O(Ra^{1/2}) \quad . \tag{4.12}$$

For this condition to hold, the stream function variable within the boundary-layer must scale as

$$f_{BL} \sim O(\delta \, Ra^{1/2}) \quad . \tag{4.13}$$

The radial velocity ($u = \frac{-1}{G(r + \frac{1}{G})} \frac{\partial f}{\partial \psi}$) then goes as f (for finite-gap), or

$$u_{BL} \sim O(\delta \, Ra^{1/2}) \quad . \tag{4.14}$$

From the definition of vorticity, one gets

$$w_{BL} \sim O(Ra^{1/2}/\delta) \quad . \tag{4.15}$$

Lastly, since temperature is of $O(1)$ in the core, it must also match and be $O(1)$ in the boundary-layer. Thus, the boundary-layer

expansions are:

$$u_{BL} = \delta\, Ra^{1/2}\, U_o + \ldots.$$

$$v_{BL} = Ra^{1/2}\, V_o + \ldots.$$

$$w_{BL} = \frac{Ra^{1/2}}{\delta}\, W_o + \ldots.$$

$$f_{BL} = \delta\, Ra^{1/2}\, F_o + \ldots.$$

$$T_{BL} = T_o + \ldots. \qquad (4.16)$$

Using the above boundary-layer expansions together with the fact that $\delta \to 0$ in the limit as $Ra \to \infty$, one can reduce the 2-D N-S equations to the following form.

Energy:

$$Ra^{1/2} \left\{ \frac{1}{a} \frac{\partial T_o}{\partial t^*} + U_o \frac{\partial T_o}{\partial R} + \frac{V}{a} \frac{\partial T_o}{\partial \Psi} \right\} = \frac{a}{Pr\delta^2} \frac{\partial^2 T}{\partial R^2}$$

Vorticity:

$$Pr \left\{ \frac{1}{a} \frac{\partial W_o}{\partial t^*} + U_o \frac{\partial W_o}{\partial R} + \frac{V_o}{a} \frac{\partial W_o}{\partial \Psi} \right\} = \frac{Pr \cdot a}{\delta^2\, Ra^{1/2}} \frac{\partial^2 W_o}{\partial R^2} + \sin \Psi \frac{\partial T_o}{\partial R}$$

Stream Function:

$$\frac{\partial^2 F_o}{\partial R^2} = \frac{1}{a^2} W_o \qquad (4.17)$$

and again, $t^* = Ra^{1/2}t$.

These equations clearly bring forth the scaling required for the boundary-layer thickness, that is

$$\delta \sim Ra^{-1/4} \tag{4.18}$$

where the 1/4 power is typical for natural convective laminar-type flows. Using Eq. (4.18), the boundary-layer expansions become:

$$\begin{aligned} u_{BL} &= Ra^{1/4}\, U_o + O(Ra^{-1/4}) \\ v_{BL} &= Ra^{1/2}\, V_o + O(1) \\ w_{BL} &= Ra^{3/4}\, W_o + O(Ra^{1/4}) \\ f_{BL} &= Ra^{1/4}\, F_o + O(Ra^{-1/4}) \\ T_{BL} &= T_o + O(Ra^{-1/2}) \quad . \end{aligned} \tag{4.19}$$

Physically these expansions make sense, since within the boundary-layer, vorticity should be much larger than the stream function or velocity components, and the tangential velocities should be greater than the radial velocities for this particular flow geometry. Also, following the same aforementioned steps, the outer boundary-layer thickness can be shown to scale in the same manner as the inner one.

Now, as $G \to 0$, the boundary-layers must merge at some point giving

$$2\delta = G\,a \quad . \tag{4.20}$$

Knowing this relation, G must then scale as δ or

$$G \sim Ra^{-1/4} \quad . \tag{4.21}$$

Substituting Eq. (4.21) into Eq. (4.6) and placing the result into Eq. (4.2), yields the inviscid core expansions as

$$\begin{aligned} u_c &= Ra^{1/4}\,\tilde{u}_o + \ldots. \\ v_c &= Ra^{1/2}\,\tilde{v}_o + \ldots. \\ w_c &= Ra^{3/4}\,\tilde{w}_o + \ldots. \\ f_c &= Ra^{1/4}\,\tilde{f}_o + \ldots. \\ T_c &= T_o + \ldots. \end{aligned} \tag{4.22}$$

Comparing Eq. (4.22) with (4.19), one can claim that at the point where the boundary-layers merge, the 'outer' or core expansions do indeed match the 'inner' or boundary-layer expansions.

4.3. The Analytical Cell-Development Regime

Since the radius ratio b/a is of O(1) for narrow gaps and Eqs. (4.17) are independent of G, the boundary-layer expansions do not have to be rescaled to avoid losing any nonlinear physics as $G \to 0$.

Therefore, it can now be inferred that the dependent variables in the governing N-S equations will scale the same as in the boundary-layer for the double limit of $Ra \to \infty$ and $G \to 0$. Thus, we take

$$G = Ra^{-1/4}\,\tilde{G} \tag{4.23}$$

and the expansions

$$\begin{aligned} u &= Ra^{1/4}\,\tilde{u} + O(Ra^{-1/4}) \\ v &= Ra^{1/2}\,\tilde{v} + O(1) \\ w &= Ra^{3/4}\,\tilde{w} + O(Ra^{1/4}) \\ f &= Ra^{1/4}\,\tilde{f} + O(Ra^{-1/4}) \\ T &= \tilde{T} + O(Ra^{-1/2}) \quad . \end{aligned} \tag{4.24}$$

With Eqs. (4.23) and (4.24) in-hand, the 2-D N-S equations collapse into Cartesian-like, boundary-layer type equations. In final form, they become:

Energy:

$$\tilde{G}^2\,\frac{\partial\tilde{T}}{\partial\tilde{t}} + \tilde{G}\left\{-\frac{\partial\tilde{f}}{\partial\psi}\,\frac{\partial\tilde{T}}{\partial r} + \frac{\partial\tilde{f}}{\partial r}\,\frac{\partial\tilde{T}}{\partial\psi}\right\} = \frac{1}{Pr}\,\frac{\partial^2\tilde{T}}{\partial r^2} \tag{4.25a}$$

Vorticity:

$$\tilde{G}^2 \cdot Pr \frac{\partial \tilde{w}}{\partial \tilde{t}} + \tilde{G} \cdot Pr \{ - \frac{\partial \tilde{f}}{\partial \psi} \frac{\partial \tilde{w}}{\partial r} + \frac{\partial \tilde{f}}{\partial r} \frac{\partial \tilde{w}}{\partial \psi} \}$$

$$= Pr \frac{\partial^2 \tilde{w}}{\partial r^2} + \tilde{G} \sin \psi \frac{\partial \tilde{T}}{\partial r} \qquad (4.25b)$$

Stream Function:

$$\frac{\partial^2 \tilde{f}}{\partial r^2} = \tilde{G}^2 \tilde{w} \qquad (4.25c)$$

with related boundary conditions of:

$$\tilde{T}(0,\psi) = 1, \ \tilde{T}(1,\psi) = 0 \qquad (4.25d)$$

$$\tilde{f}(0,\psi) = \tilde{f}(1,\psi) = 0 \qquad (4.25e)$$

$$\tilde{w}(0,\psi) = \tilde{w}(1,\psi) = \frac{1}{G^2} \frac{\partial^2 \tilde{f}}{\partial r^2} \Big|_{r=0,1} \qquad (4.25f)$$

where again, $\tilde{G}$, the scaled gap, is defined as

$$\tilde{G} = Ra^{1/4} G \qquad (4.26a)$$

and the time-term is also scaled the same as in the boundary-layer, or

$$\tilde{t} = Ra^{1/2} t \quad . \qquad (4.26b)$$

Equations (4.25) represent the key governing equations for arbitrary Prandtl number in the double limit of $Ra \to \infty$ and $G \to 0$. The numerical method used to solve these equations will be described in Chapter 5. These equations can be further simplified under certain limiting conditions. Three limiting cases will be investigated; namely, the $\tilde{G} \to 0$ limit, plus the vanishingly small and infinite Prandtl number limits.

To leading-order, in the limit as $\tilde{G} \to 0$, Eqs. (4.25) reduce to:

Energy:

$$\frac{\partial^2 \tilde{T}}{\partial r^2} = 0$$

Vorticity:

$$\frac{\partial^2 \tilde{w}}{\partial r^2} = 0$$

Stream Function:

$$\frac{\partial^2 \tilde{f}}{\partial r^2} = 0 \quad . \tag{4.27}$$

Thus, the energy equation simplifies to the steady-state 1-D conduction equation, which integrates to

$$\tilde{T} = 1 - r \tag{4.28}$$

for the isothermal boundary conditions of this problem. Also, from the no-slip condition, the vorticity and velocity components become identically zero. Hence, convective effects are discarded, and the temperature field becomes completely determined by the linear relationship of Eq. (4.28).

From the above analysis, one can conclude that a Stokes-layer or a conductive/viscous dominated flow field prevails as $\tilde{G} \to 0$. Therefore, the multicellular regime that is associated with the narrow type gaps (at high Rayleigh number) most likely reverts back to two cells and then, finally to a pure conductive mode when the velocities tend to zero as $\tilde{G} \to 0$ (or $G \to 0$ for a specified Rayleigh number). Contrary to this result, many investigators (Walton, 1980; Powe et al., 1971; Liu et al., 1962) believed that as the gap approached zero, a true Bénard type instability would evolve, where the typical critical Rayleigh number (Ra_{b-a}) of about 1,700 is approached. Instead, it appears that after a certain point, the transitional Rayleigh number increases with decreasing gap size (to well above 1,700), until eventually, a conduction-dominated flow results as the gap approaches zero (see Chapter 6).

4.4. The Perturbative Solution to the Steady-State Finite-Prandtl Number Equations

From numerical results obtained in this study, and results discussed in Powe et al. (1971) and Rao et al. (1985), it can be seen that the narrow-gap solutions for flows prior to multicellular transition (and even beyond to a certain extent) behave in a

seemingly steady-state manner. Assuming the steady-state condition and using the leading-order solution of Eq. (4.27), the convective terms in the vorticity equation of (4.25) become zero. From this, $\tilde{w}$ must then scale as $\tilde{G}$ in order to balance viscous and buoyancy effects, and upon entering the stream function equation of (4.25), one sees that $\tilde{f} \sim \tilde{G}^3$. This logic can be repeated in a successive manner (without neglecting cross terms) until the following asymptotic expansions are obtained for the steady-state case:

$$\tilde{T} = (1-r) + \tilde{G}^4 T_1 + \tilde{G}^8 T_2 + \tilde{G}^{12} T_3 + O(\tilde{G}^{16})$$

$$\tilde{w} = \tilde{G}\, w_1 + \tilde{G}^5 w_2 + \tilde{G}^9 w_3 + \tilde{G}^{13} w_4 + O(\tilde{G}^{17})$$

$$\tilde{f} = \tilde{G}^3 f_1 + \tilde{G}^7 f_2 + \tilde{G}^{11} f_3 + \tilde{G}^{15} f_4 + O(\tilde{G}^{19}) \qquad (4.29a)$$

while the related boundary conditions are:

$$\tilde{T}(0,\psi) = 1,\ \tilde{T}(1,\psi) = 0$$

$$\tilde{f}(0,\psi) = \tilde{f}(1,\psi) = 0$$

$$\frac{\partial \tilde{f}}{\partial r}(0,\psi) = \frac{\partial \tilde{f}}{\partial r}(1,\psi) = 0 \quad . \qquad (4.29b)$$

All of the important physics are included in the first two terms of the expansions in Eq. (4.29a); that is, the gravitational, viscous and convective effects are accounted for.

Substituting Eq. (4.29a) into Eq. (4.25) and matching terms of like coefficients, yields an infinite set of steady uncoupled linear partial differential equations. These equations take on the following form:

Energy:

$$\tilde{G}^4: \quad \frac{\partial f_1}{\partial \psi} = \frac{1}{Pr} \frac{\partial^2 T_1}{\partial r^2} \tag{4.30}$$

$$\tilde{G}^8: \quad \frac{\partial f_2}{\partial \psi} + - \frac{\partial f_1}{\partial \psi} \frac{\partial T_1}{\partial r} + \frac{\partial f_1}{\partial r} \frac{\partial T_1}{\partial \psi} = \frac{1}{Pr} \frac{\partial^2 T_2}{\partial r^2} \tag{4.31}$$

$$\tilde{G}^{12}: \quad \frac{\partial f_3}{\partial \psi} + - \frac{\partial f_2}{\partial r} \frac{\partial T_1}{\partial r} + - \frac{\partial f_1}{\partial \psi} \frac{\partial T_2}{\partial r} + \frac{\partial f_2}{\partial r} \frac{\partial T_1}{\partial \psi} + \frac{\partial f_1}{\partial r} \frac{\partial T_2}{\partial \psi} = \frac{1}{Pr} \frac{\partial^2 T_3}{\partial r^2} \tag{4.32}$$

Vorticity:

$$\tilde{G}: \quad \frac{\partial^2 w_1}{\partial r^2} = \frac{\sin \psi}{Pr} \tag{4.33}$$

$$\tilde{G}^5: \quad -Pr \frac{\partial f_1}{\partial \psi} \frac{\partial w_1}{\partial r} + Pr \frac{\partial f_1}{\partial r} \frac{\partial w_1}{\partial \psi} = Pr \frac{\partial^2 w_2}{\partial r^2} + \sin \psi \frac{\partial T_1}{\partial r} \tag{4.34}$$

$$\tilde{G}^9: \quad -Pr \frac{\partial f_1}{\partial \psi} \frac{\partial w_2}{\partial r} + -Pr \frac{\partial f_2}{\partial \psi} \frac{\partial w_1}{\partial r} + Pr \frac{\partial f_1}{\partial r} \frac{\partial w_2}{\partial \psi} + Pr \frac{\partial f_2}{\partial r} \frac{\partial w_1}{\partial \psi} = Pr \frac{\partial^2 w_3}{\partial r^2} + \sin \psi \frac{\partial T_2}{\partial r} \tag{4.35}$$

Stream Function:

$$\tilde{G}^3: \quad \frac{\partial^2 f_1}{\partial r^2} = w_1 \tag{4.36}$$

$$\tilde{G}^7: \quad \frac{\partial^2 f_2}{\partial r^2} = w_2 \tag{4.37}$$

$$\tilde{G}^{11}: \quad \frac{\partial^2 f_3}{\partial r^2} = w_3 \quad . \tag{4.38}$$

Equations (4.30) - (4.38) were solved analytically with the following result (note: vorticity, temperature and stream function were carried out to the first three nonzero terms):

$$f_1 = \frac{\sin \psi}{24\ Pr}\ (A1) \tag{4.39}$$

$$w_1 = \frac{\sin \psi}{2\ Pr}\ (B1) \tag{4.40}$$

$$T_1 = \frac{\cos \psi}{1440}\ (C1) \tag{4.41}$$

$$f_2 = \frac{\sin 2\psi}{96\ Pr}\ \left(A2 + \frac{B2}{Pr}\right) \tag{4.42}$$

$$w_2 = \frac{\sin 2\psi}{96\ Pr}\ \left(C2 + \frac{D2}{Pr}\right) \tag{4.43}$$

$$T_2 = \frac{\cos 2\psi}{96\ Pr}\left(E2 + \frac{F2}{Pr}\right) + \frac{\cos^2 \psi}{34560}\ (G2) + \frac{\sin^2 \psi}{34560}\ (H2) \tag{4.44}$$

$$f_3 = \frac{\sin 2\psi \cos \psi}{2304\ Pr^2}\left(A3 + \frac{B3}{Pr}\right) + \frac{\cos 2\psi \sin \psi}{96\ Pr^2}\left(C3 + \frac{D3}{Pr}\right)$$

$$+ \frac{\cos 2\psi \sin \psi}{96\ Pr}\left(E3 + \frac{F3}{Pr}\right) + \frac{\cos^2\psi \sin \psi}{34560\ Pr}(G3)$$

$$+ \frac{\sin^3\psi}{34560\ Pr}(H3) \qquad (4.45)$$

$$w_3 = \frac{\sin 2\psi \cos \psi}{2304\ Pr^2}\left(A4 + \frac{B4}{Pr}\right) + \frac{\cos 2\psi \sin \psi}{96\ Pr^2}\left(C4 + \frac{D4}{Pr}\right)$$

$$+ \frac{\cos 2\psi \sin \psi}{96\ Pr}\left(E4 + \frac{F4}{Pr}\right) + \frac{\cos^2\psi \sin \psi}{34560\ Pr}(G4$$

$$+ \frac{\sin^3\psi}{34560\ Pr}(H4) \qquad (4.46)$$

where

$$A1 = r^2(r-1)^2 \qquad (4.47)$$

$$B1 = r(r-1) + \frac{1}{6} \qquad (4.48)$$

$$C1 = r(2r^5 - 6r^4 + 5r^3 - 1) \qquad (4.49)$$

and A2 through H4, which are also functions of r only, are given in Appendix A.

In Equations (4.39) - (4.46), the stream function and vorticity expansions have the same angular dependence, and to leading-order, are inversely proportional to Prandtl number. For temperature, however,

the conductive term $(1 - r)$ and T_1 are completely independent of the Prandtl number.

From Eq. (4.39), it can be seen that, to leading-order, the stream function is positive for all ψ at a given value of r (for the half annulus), and becomes zero at $\psi = 0, \pi$. Therefore, the primary basic flow does indeed consist of two counter-rotating kidney-shaped cells as discussed in the literature survey of Chapter 2. It is interesting to note that the second and third terms of the stream function expansion are proportional to sin 2ψ; thus, the basic flow has the potential of obtaining more than two cells in the complete annulus - especially when the Prandtl number is sufficiently small (Mack and Bishop, 1968; Walton, 1980).

Before completing this section, the asymptotic expansions of Eq. (4.29) will be placed in a compact recursive notation:

$$\tilde{T} = (1 - r) + \sum_{n=1}^{\infty} \tilde{G}^{4n} T_n$$

$$\tilde{w} = \sum_{n=1}^{\infty} \tilde{G}^{4n-3} w_n$$

$$\tilde{f} = \sum_{n=1}^{\infty} \tilde{G}^{4n-1} f_n \quad . \tag{4.50}$$

The angular dependent coefficients (to be denoted by F, W and T) in Eqs. (4.39) - (4.46) can also be written in the following revealing notation:

$$F_1 = W_1 = \sin \Psi$$

$$F_m = W_m = \sin \Psi \frac{\partial F_{m-1}}{\partial \Psi} \; ; \; m=2 \text{ to } \infty$$

$$T_n = \frac{\partial F_n}{\partial \Psi} \; ; \; n=1 \text{ to } \infty \; . \qquad (4.51)$$

Since the T_n terms are always functions of cos Ψ or squared powers of sin Ψ and cos Ψ, the isotherms must remain symmetric on either half of the annulus. Similarly, since F_m and W_m are functions of sin Ψ, sin 2Ψ or a combination thereof, the angular dependent coefficients will always be equal in magnitude, but opposite in sign for each half annulus. Thus, due to the above trigonometric arguments (and since symmetry is likely enforced by the concentric cylinder geometry), symmetric (bi-cellular or multicellular) solutions are implied for either temperature, vorticity or stream function. This observation is further supported by the analytical and numerical steady-state calculations obtained in this study (see Chapter 6), along with the experimental results of Kuehn and Goldstein (1976a) and Powe et al. (1969). Although this analysis supports the result of symmetric solutions, especially at very small gaps, the introduction of full nonlinear effects (from either the thermal-energy or vorticity equation) may allow asymmetric solutions to come into play. Therefore, even though subsequent numerical solutions will concentrate on the symmetric case, the asymmetric possibility should not be entirely ruled out.

4.4.1 Heat transfer relations

To better compare heat transfer predictions of the asymptotic method to the 2-D N-S numerical results, analytical expressions for Nusselt number were determined. First, inner and outer Nusselt numbers are defined as:

$$Nu_i = \frac{-Ra^{1/4}}{G} \left.\frac{\partial T}{\partial r}\right|_{r=0} \tag{4.52}$$

$$Nu_o = \frac{-Ra^{1/4}}{G} \left.\frac{\partial T}{\partial r}\right|_{r=1} . \tag{4.53}$$

Then, using the asymptotic expansion result for temperature (Eq. 4.29), the following equations for finite Prandtl number can be written:

$$Nu_i^* = \frac{Nu_i}{Ra^{1/4}} = \tilde{G}^{-1} + \tilde{G}^3 \left(\frac{\cos\psi}{1440}\right)$$

$$+ \tilde{G}^7 \left\{\frac{\cos 2\psi}{96}\left[\frac{1}{387701} + \frac{1}{Pr}\left(\frac{1}{997934}\right)\right]\right\}$$

$$+ \tilde{G}^7 \left\{\frac{\cos^2\psi}{34560}\left(\frac{1}{277}\right)\right\} + \tilde{G}^7 \left\{\frac{\sin^2\psi}{34560}\left(\frac{1}{171}\right)\right\} + O(\tilde{G}^{11}) \tag{4.54}$$

$$Nu_o^* = \frac{Nu_o}{Ra^{1/4}} = \tilde{G}^{-1} - \tilde{G}^3 \left(\frac{\cos\psi}{1440}\right)$$

$$+ \tilde{G}^7 \left\{\frac{\cos 2\psi}{96}\left[\frac{-1}{3374633} + \frac{1}{Pr}\left(\frac{1}{998521}\right)\right]\right\}$$

$$+ \tilde{G}^7 \left\{\frac{\cos^2\psi}{34560}\left(\frac{1}{277}\right)\right\} + \tilde{G}^7 \left\{\frac{\sin^2\psi}{34560}\left(\frac{1}{171}\right)\right\} + O(\tilde{G}^{11}) . \tag{4.55}$$

AD-A186 113 THE NUMERICAL AND ANALYTICAL STUDY OF BIFURCATION AND MULTICELLULAR FLOW..(U) AIR FORCE INST OF TECH WRIGHT-PATTERSON AFB OH D B FANT 1987 2/3

UNCLASSIFIED AFIT/CI/NR-87-134D F/G 20/13 NL

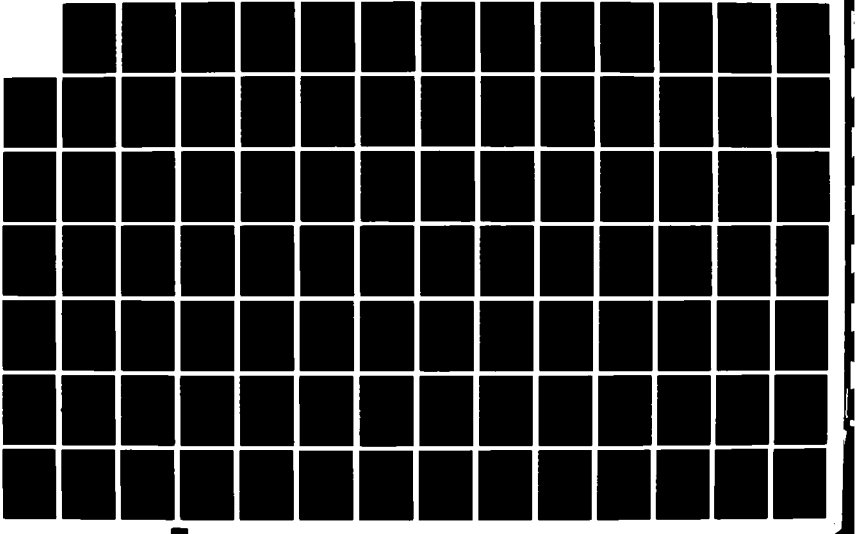

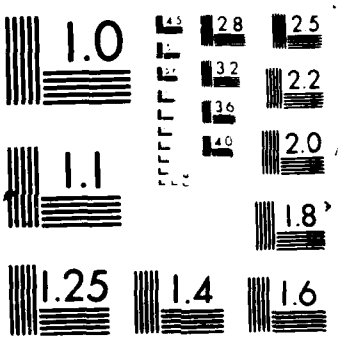
1.0
1.1
1.25
1.4
1.6
2.8
3.2
3.6
4.0
2.5
2.2
2.0
1.8

The first term in Eqs. (4.54) and (4.55), $\tilde{G}^{-1}$, represents the purely conductive contribution to heat transfer. The convective influence is provided by the remaining two terms of order $\tilde{G}^3$ and $\tilde{G}^7$.

In the limits as $Pr \to 0$ and $Pr \to \infty$ (see Sections 4.5 and 4.7), analytical expressions for the inner and outer Nusselt numbers can also be obtained. Hence, from forthcoming equations (4.76) and (4.106), one gets:

For $Pr \to 0$:

$$Nu_i^* = Nu_o^* = \hat{G}^{-1} \tag{4.56}$$

where $\hat{G}$ is given by Eq. (4.67), or

$$\hat{G} = \tilde{G}\, Pr^{-1/4} \quad .$$

For $Pr \to \infty$:

$$Nu_i^* = \tilde{G}^{-1} + \tilde{G}^3 \left(\frac{\cos\psi}{1440}\right) + \tilde{G}^7 \left\{\frac{\cos 2\psi}{96}\left(\frac{1}{387701}\right)\right\}$$
$$+ \tilde{G}^7 \left\{\frac{\cos^2\psi}{34560}\left(\frac{1}{277}\right)\right\} + \tilde{G}^7 \left\{\frac{\sin^2\psi}{34560}\left(\frac{1}{171}\right)\right\}$$
$$+ O(\tilde{G}^{11}) \tag{4.57}$$

$$Nu_o^* = \tilde{G}^{-1} - \tilde{G}^3 \left(\frac{\cos\psi}{1440}\right) + \tilde{G}^7 \left\{\frac{\cos 2\psi}{96}\left(\frac{-1}{3374633}\right)\right\}$$
$$+ \tilde{G}^7 \left\{\frac{\cos^2\psi}{34560}\left(\frac{1}{277}\right)\right\} + \tilde{G}^7 \left\{\frac{\sin^2\psi}{34560}\left(\frac{1}{171}\right)\right\} + O(\tilde{G}^{11}) \tag{4.58}$$

Equation (4.56) signifies the pure conduction result for $Pr \to 0$, and thus, does not retain any convective influence to heat transfer. Equations (4.57) and (4.58) are similar to those for finite Prandtl number, except terms proportional to Pr^{-1} have vanished.

4.5. The Zero Prandtl Number Limit

In this section, the previously derived small-gap (finite-Prandtl number) equations will be used to analyze the theoretical effects as $Pr \to 0$. From a practical standpoint, the behavior of liquid metals should fall within this low-Prandtl number approximation, and this analysis has application to the study of liquid metal-cooled nuclear reactors. It appears from the literature that $Pr \to 0$ limits have not been studied either numerically, analytically or experimentally for the horizontal narrow-gap concentric cylinder geometry. Lee and Korpela (1983) have studied a similar type of natural convective flow between vertical slots, where the left wall is heated. They demonstrated that in the narrow (high aspect-ratio) slots, a stationary multicellular flow resembling an hour-glass configuration is initiated near the center of the slot, and appears strongest for the near-zero Prandtl number cases. But the source of this unique instability is hydrodynamic rather than thermal, because for $Pr \to 0$, the large thermal diffusitives that result most probably rule out any type of thermal perturbations. Realizing this, one can speculate that in the vertical portions of a narrow horizontal annulus, the same type of hour-glass shaped hydrodynamic instability is possible. Furthermore, Korpela (1974) and

Walton (1980) discuss the fact (for flow due to natural convection in an inclined channel, see Chapter 2) that for $Pr \geq .24$, a true Bénard-type thermal instability prevails, whereas for $0 < Pr < .24$, a mixture of thermal and hydrodynamic instabilities result, until finally at $Pr = 0$, the instability is purely hydrodynamic. Thus, one might now look upon the narrow horizontal annulus geometry as a combination of horizontal, inclined and vertical channels. Both types of instability appear to have a definite role in the cellular patterns that develop in this geometry, as a function of Prandtl number. Therefore, the small-gap/finite-Prandtl number equations derived in Eq. (4.25) may prove useful in studying the cellular-structure variation with Prandtl number. But, since the limiting equations for $Pr \to 0$ have not yet been obtained, the following analytical analysis was conducted.

To begin, let $Pr \to 0$, and assume again that temperature is of $O(1)$ from the boundary conditions. Then, assume that

$$\tilde{w} = \lambda_1 W + ... \tag{4.59}$$

$$\tilde{f} = \lambda_2 F + ... \tag{4.60}$$

and consider the stream function equation in (4.25) to get

$$\lambda_2 \sim \tilde{G}^2 \lambda_1 \quad . \tag{4.61}$$

Using Eqs. (4.59) and (4.60), the vorticity equation in (4.25) becomes:

$$\tilde{G}^2 Pr\lambda_1 \frac{\partial W}{\partial \tilde{t}} + Pr\ \tilde{G}\ \lambda_2\lambda_1 \{- \frac{\partial F}{\partial \Psi} \frac{\partial W}{\partial r} + \frac{\partial F}{\partial r} \frac{\partial W}{\partial \Psi}\}$$

$$= Pr\ \lambda_1 \frac{\partial^2 W}{\partial r^2} + \tilde{G} \sin \Psi \frac{\partial T}{\partial r} \qquad (4.62)$$

or

$$\frac{\tilde{G}^2 Pr\lambda_1}{\tilde{t}} \sim Pr\ \tilde{G}\ \lambda_2\lambda_1 \sim Pr\ \lambda_1 \sim \tilde{G} \quad , \qquad (4.63)$$

and in order to retain the viscous term,

$$\lambda_1 \sim \frac{\tilde{G}}{Pr} \quad , \qquad (4.64)$$

then from Eq. (4.61),

$$\lambda_2 \sim \frac{\tilde{G}^3}{Pr} \quad . \qquad (4.65)$$

Equations (4.64) and (4.65) are then used in Eq. (4.63) to obtain

$$\tilde{G} \sim O(Pr^{1/4}) \qquad (4.66a)$$

and $\tilde{t} \sim \tilde{G}^2$, which yields from Eq. (4.66a)

$$\tilde{t} \sim O(Pr^{1/2}) \quad . \qquad (4.66b)$$

Thus, let

$$\tilde{G} = \hat{G}\, Pr^{1/4} \tag{4.67a}$$

and

$$\tilde{t} = \hat{t}\, Pr^{1/2} \quad . \tag{4.67b}$$

Hence,

$$\lambda_1 \sim Pr^{-3/4} \tag{4.68}$$

and

$$\lambda_2 \sim Pr^{-1/4} \quad . \tag{4.69}$$

With these results, the following expansions can be written:

$$\tilde{w} \sim Pr^{-3/4}\, W + O(Pr^{1/4}) \tag{4.70}$$

$$\tilde{f} \sim Pr^{-1/4}\, F + O(Pr^{3/4}) \tag{4.71}$$

$$\tilde{T} \sim T + O(Pr) \quad . \tag{4.72}$$

Also, Eqs. (4.67a) and (4.67b) can be expressed in terms of the key dimensionless variables, namely:

$$\hat{G} = Pr^{-1/4}\, \tilde{G} = \left(\frac{Ra}{Pr}\right)^{1/4} G$$

$$\hat{t} = Pr^{-1/2}\, \tilde{t} = \left(\frac{Ra}{Pr}\right)^{1/2} t \quad .$$

These new scales, when written in the above form, clearly display their unique dependency on Ra, Pr, G and t. Upon substituting Eqs. (4.70), (4.71) and (4.72), Eqs. (4.25) reduce to the following set in the limit as $Pr \to 0$:

Energy:

$$\frac{\partial^2 T}{\partial r^2} = 0 \tag{4.73}$$

Vorticity:

$$\hat{G}^2 \frac{\partial W}{\partial \hat{t}} + \hat{G} \left\{ - \frac{\partial F}{\partial \psi} \frac{\partial W}{\partial r} + \frac{\partial F}{\partial r} \frac{\partial W}{\partial \psi} \right\} = \frac{\partial^2 W}{\partial r^2} + \hat{G} \sin \psi \frac{\partial T}{\partial r} \tag{4.74}$$

Stream Function:

$$\frac{\partial^2 F}{\partial r^2} = \hat{G}^2 W \quad . \tag{4.75}$$

The energy equation in this case also reduces to the steady-state conduction equation. For the boundary conditions considered, the linear temperature distribution across the gap takes on the following simple solution:

$$T = 1 - r \quad . \tag{4.76}$$

Thus, as $Pr \to 0$, only concentric isotherms should result, regardless of the flow field that develops. The energy equation has now completely uncoupled itself from the vorticity equation, and since

Eq. (4.76) gives $\partial T/\partial r = -1$, the final two governing equations, which are directly independent of Prandtl number, become:

Vorticity:

$$\hat{G}^2 \frac{\partial W}{\partial \hat{t}} + \hat{G} \{- \frac{\partial F}{\partial \psi} \frac{\partial W}{\partial r} + \frac{\partial F}{\partial r} \frac{\partial W}{\partial \psi}\} = \frac{\partial^2 W}{\partial r^2} - \hat{G} \sin \psi \qquad (4.77)$$

Stream Function:

$$\frac{\partial^2 F}{\partial r^2} = \hat{G}^2 W \qquad (4.78)$$

with boundary conditions

$$F(0,\psi) = F(1,\psi) = 0 \qquad (4.79)$$

$$\frac{\partial F}{\partial r}(0,\psi) = \frac{\partial F}{\partial r}(1,\psi) = 0 \quad . \qquad (4.80)$$

These equations will be solved numerically in order to determine if a hydrodynamic-type instability (similar to that previously described) does indeed exist for this flow geometry (see Chapter 6 for a discussion of these results).

4.6. The Perturbation Solution to the Steady-State Zero Prandtl Number Equations

Assuming steady-state and upon eliminating W, one gets

$$W = \hat{G}^{-2} \frac{\partial^2 F}{\partial r^2} \qquad (4.81)$$

and

$$\hat{G}\left\{-\frac{\partial F}{\partial \Psi}\frac{\partial^3 F}{\partial r^3}+\frac{\partial F}{\partial r}\frac{\partial^3 F}{\partial r^2}\right\}=\frac{\partial^4 F}{\partial r^4}-\hat{G}^3\sin\Psi \quad . \tag{4.82}$$

The logic used to derive the expansions in Eq. (4.29) when $\tilde{G} \to 0$ can again be used to derive the expansions for the $\hat{G} \to 0$ limit. Thus, considering Eq. (4.82), the stream function expansion should behave as

$$F = \hat{G}^3 F_1 + \hat{G}^7 F_2 + \hat{G}^{11} F_3 + O(\hat{G}^{15}) \tag{4.83}$$

and from Eq. (4.78), the vorticity expansion becomes

$$W = \hat{G}\, W_1 + \hat{G}^5 W_2 + \hat{G}^9 W_3 + O(\hat{G}^{13}) \quad . \tag{4.84}$$

Notice that the power of the coefficients in the above expansions is identical with those in Eqs. (4.29), as should be the case. However, in deriving the asymptotic expansions of Eqs. (4.29), the buoyancy term, $\tilde{G} \sin \Psi \frac{\partial T}{\partial r}$ (in Eq. 4.25b), maintained the same order as the viscous term for all orders of the vorticity expansion. But for the $Pr \to 0$ limit, the buoyancy term comes directly into play only in the leading order W_1 term, where the viscous term is balanced by the buoyancy force; while in the other terms of the vorticity expansion, the convective forces are equated with the viscous ones and the buoyancy effects contribute only indirectly through F_1 and W_1.

Substituting expansion (4.83) into Eq. (4.82), and matching terms of like coefficients, yields the following steady-state result:

$$\hat{G}^3: \quad \frac{\partial^4 F_1}{\partial r^4} = \sin \psi \tag{4.85}$$

$$\hat{G}^7: \quad \frac{\partial^4 F_2}{\partial r^4} = - \frac{\partial F_1}{\partial \psi} \frac{\partial^3 F_1}{\partial r^3} + \frac{\partial F_1}{\partial r} \frac{\partial^3 F_1}{\partial r^2 \partial \psi} \quad . \tag{4.86}$$

Integrating Eq. (4.85), one gets

$$F_1 = \frac{r^4}{4!} \sin \psi + c_1 \frac{r^3}{3!} + c_2 \frac{r^2}{2} + c_3 r + c_4 \quad , \tag{4.87}$$

while the constants of integration are obtained from the boundary conditions of Eqs. (4.79) and (4.80) to give:

$$F_1 = r^2 (r-1)^2 \frac{\sin \psi}{24} \quad . \tag{4.88}$$

Differentiating Eq. (4.88) twice with respect to r gives

$$W_1 = \{r(r-1) + \frac{1}{6}\} \frac{\sin \psi}{2} \quad . \tag{4.89}$$

Using Eq. (4.88), Eq. (4.86) becomes

$$\frac{\partial^4 F_2}{\partial r^4} = \{6r^5 - 15 r^4 + 14 r^3 - 6 r^2 + r\} \frac{2 \sin 2\psi}{24^2} \quad . \tag{4.90}$$

Integrating Eq. (4.90) and applying boundary conditions (Eq. 4.79) and (Eq. 4.80) yields

$$F_2 = \frac{\sin 2\psi}{96} (B2) \tag{4.91}$$

and W_2 follows as

$$W_2 = \frac{\sin 2\psi}{96} (D2) \tag{4.92}$$

where B2 and D2 are the same as those in Eqs. (4.42) and (4.43), and again, are given in Appendix A.

The equations for F_1, W_1 and F_2, W_2 take on forms similar to those in Eqs. (4.39) through (4.43), except that in the former, the Prandtl number dependency and the coefficients A2 and C2 completely vanish for the limit of $Pr \to 0$. Then, by neglecting terms A3, C3, E3 in Eq. (4.45) and A4, C4, E4 in Eq. (4.46) for the limit as $Pr \to 0$, one easily obtains solutions for F_3 and W_3, respectively.

Since F_2, F_3 and W_2, W_3 involve terms proportional to sin 2ψ, it can be reasoned that these terms must contribute to the potential multicellular transition of the flow field occurring at some critical value of $\hat{G}$. By performing a simple order-of-magnitude analysis, one can estimate when these terms become of equal importance with the leading order expansion terms. From this result, the onset of multicellular flow can be approximately predicted. Carrying out this analysis, one finds that the sum of $\hat{G}^7 F_2$ and $\hat{G}^{11} F_3$ achieves the same order as $\hat{G}^3 F_1$, when $\hat{G} = 7.2$. Similarly, for vorticity, $\hat{G}^5 W_2$ and $\hat{G}^9 W_3$ achieve the same order as $\hat{G} W_1$ at $\hat{G} = 7.5$. Hence, the critical value of $\hat{G}$ appears to be about 7.

For the pretransitional cases, the first-order expansions of Eqs. (4.83) and (4.84) provide good approximations in describing the behavior of stream function and vorticity (respectively) for the limit as $Pr \to 0$. Since it is likely that terms beyond F_3 and W_3 play dominating roles in triggering the instability, the critical value of $\hat{G}$ might be lower than that predicted by the above order-of-magnitude analysis. To properly estimate this value, the full effects of nonlinearity must be taken into account. This will be done in Chapter 6 when the equations are solved numerically. Considering the above discussion, one obtains the following relations:

$$F = \hat{G}^3 r^2 (r-1)^2 \frac{\sin \psi}{24} \tag{4.93}$$

$$W = \hat{G} \{r (r-1) + \frac{1}{6}\} \frac{\sin \psi}{2} \quad . \tag{4.94}$$

Equations (4.93) and (4.94) represent analytical profiles for the steady-state pretransitional stream function and vorticity, which are valid throughout the annulus ($0 - 2\pi$). Comparisons to related numerical results will be given in Chapter 6. From these relations, it can be seen (for the half-annulus) that the vorticity given by Eq. (4.94) takes on positive values within the boundary-layers (for r near zero and one), and negative values within the inviscid core. The stream function (from Eq. 4.93) always remains non-negative, since the r terms are squared. This reasoning can be extended throughout the entire flow field, at least for the bicellular case.

Referring to Eqs. (4.93) and (4.94), it can be seen that any resulting bicellular profiles must be symmetric with respect to both the vertical and horizontal centerlines, or at ψ=0, $\frac{\pi}{2}$, π and $\frac{3\pi}{2}$. This suggests that for the Pr $\rightarrow$ 0 limit, the pretransitional flow fields are completely symmetric, although the possibility exists for the occurrence of asymmetric solutions due to nonlinearity, especially after the onset of instability. In addition, for the half-annulus basic cell-structure, the stream function achieves its maximum, and vorticity its maximum or minimum (depending on r), at $\psi = \frac{\pi}{2}$ for any particular r location.

Furthermore, because the extremum stream function location occurs at (or very near) $\psi = \frac{\pi}{2}, \frac{3\pi}{2}$ for Pr $\rightarrow$ 0, and since the buoyancy term $\sin \psi \frac{\partial T}{\partial r}$ reduces to $-\sin \psi$ for this case, one can speculate that the upward or downward shift in the stream function's position (caused by an increase in Rayleigh number) is probably dependent upon the magnitude of $\frac{\partial T}{\partial r}$ and the type of fluid used - or the value of Prandtl number.

4.7. The Infinite Prandtl Number Limit

To properly complete the analytical analysis of this particular flow geometry, the other end of the Prandtl number spectrum will be considered. Thus, simplified governing equations are sought for the Pr $\rightarrow \infty$ limit. Many important fluids (such as glycerin and most oils) possess a large Prandtl number and should be fairly accurately described by the infinite Prandtl number approximation.

Let $Pr \to \infty$ and assume again that temperature is of O(1); then let

$$\tilde{w} = \eta_1 \bar{w} + \ldots.$$

$$\tilde{f} = \eta_2 \bar{f} + \ldots.$$

$$\tilde{T} = \bar{T} + \ldots. \tag{4.95}$$

Substituting the above into the finite-Prandtl number equations of (4.25) gives

Energy:

$$\tilde{G}^2 \cdot Pr \frac{\partial \bar{T}}{\partial \tilde{t}} + \eta_2 \cdot Pr \tilde{G}[- \frac{\partial \bar{f}}{\partial \psi} \frac{\partial \bar{T}}{\partial r} + \frac{\partial \bar{f}}{\partial r} \frac{\partial \bar{T}}{\partial \psi}] = \frac{\partial^2 \bar{T}}{\partial r^2} \tag{4.96}$$

Vorticity:

$$\tilde{G}^2 \cdot Pr \, \eta_1 \frac{\partial \bar{T}}{\partial \tilde{t}} + \eta_2 \eta_1 \cdot Pr \tilde{G}[- \frac{\partial \bar{f}}{\partial \psi} \frac{\partial \bar{w}}{\partial r} + \frac{\partial \bar{f}}{\partial r} \frac{\partial \bar{w}}{\partial \psi}]$$

$$= \eta_1 Pr \frac{\partial^2 \bar{w}}{\partial r^2} + \tilde{G} \sin \psi \frac{\partial \bar{T}}{\partial r} \tag{4.97}$$

Stream Function:

$$\eta_2 \frac{\partial^2 \bar{f}}{\partial r^2} = \eta_1 \tilde{G}^2 \bar{w} \quad . \tag{4.98}$$

In the limit as $Pr \to \infty$, for $\tilde{G}$ and $\bar{T}$ of O(1), η_1 in the viscous term of the vorticity equation must go as $\frac{1}{Pr}$ so as to maintain the same order as the buoyancy term, which is also regarded as O(1). Now the

stream function equation must be satisfied; thus from Eq. (4.98), one obtains

$$\eta_2 \sim \eta_1 \sim \frac{1}{Pr} \tag{4.99}$$

and this expression for η_2 also satisfies the energy equation of (4.96) at steady-state. However, the unsteady time term in the energy equation can be retained by scaling $\tilde{t}$ as

$$\tilde{t} = Pr\ \bar{t} \tag{4.100}$$

or from Eq. (4.26b) one gets

$$\bar{t} = \frac{1}{Pr}\ \tilde{t} = \left(\frac{Ra^{1/2}}{Pr}\right)t \quad . \tag{4.101}$$

Hence, for the $Pr \to \infty$ limit, the following expansions result:

$$\begin{aligned} \tilde{w} &= Pr^{-1}\ \bar{w} + O(Pr^{-2}) \\ \tilde{f} &= Pr^{-1}\ \bar{f} + O(Pr^{-2}) \\ \tilde{T} &= \bar{T} + O(Pr^{-1}) \quad . \end{aligned} \tag{4.102}$$

With Eqs (4.100) and (4.102) in-hand, the governing equations become (in the limit as $Pr \to \infty$):

Energy:

$$\tilde{G}^2 \frac{\partial \bar{T}}{\partial \bar{t}} + \tilde{G}\left[-\frac{\partial \bar{f}}{\partial \psi}\frac{\partial \bar{T}}{\partial r} + \frac{\partial \bar{f}}{\partial r}\frac{\partial \bar{T}}{\partial \psi}\right] = \frac{\partial^2 \bar{T}}{\partial r^2} \tag{4.103}$$

Vorticity:

$$\frac{\partial^2 \bar{w}}{\partial r^2} + \tilde{G} \sin \psi \frac{\partial \bar{T}}{\partial r} = 0 \tag{4.104}$$

Stream Function:

$$\frac{\partial^2 \bar{f}}{\partial r^2} = \tilde{G}^2 \bar{w} \tag{4.105a}$$

with boundary conditions

$$\bar{T}(0,\psi) = 1, \ \bar{T}(1,\psi) = 0$$

$$\bar{f}(0,\psi) = \bar{f}(1,\psi) = 0$$

and

$$\frac{\partial \bar{f}}{\partial r}(0,\psi) = \frac{\partial \bar{f}}{\partial r}(1,\psi) = 0 \quad . \tag{4.105b}$$

By letting $Pr \to \infty$, the nonlinear convective terms in the vorticity equation have completely dropped out. However, since the nonlinear terms in the energy equation still remain, the decoupling effect between the energy and vorticity equations is no longer possible, as it was with the $Pr \to 0$ limiting solution. Also in the above equations, the Prandtl number dependency has again been eliminated.

Similar to the finite-Prandtl number equations, the $\tilde{G} \to 0$ limit yields a purely conductive-dominated flow field, where again, the temperature profile reduces to the 1-D steady-state conduction case. Hence, steady-state expansions can once again be found by proceeding with the $\tilde{G} \to 0$ solution. As expected, the expansions that result take on the same form as those in Eq. (4.29a):

$$\bar{T} = (1-r) + \tilde{G}^4 \bar{T}_1 + \tilde{G}^8 \bar{T}_2 + O(\tilde{G}^{12})$$

$$\bar{w} = \tilde{G} \bar{w}_1 + \tilde{G}^5 \bar{w}_2 + O(\tilde{G}^9)$$

$$\bar{f} = \tilde{G}^3 \bar{f}_1 + \tilde{G}^7 \bar{f}_2 + O(\tilde{G}^{11}) \quad . \tag{4.106}$$

Perturbative solutions to the infinite Prandtl number equations are readily found by neglecting the Prandtl number dependency and the coefficients of $O(\frac{1}{Pr})$ relative to those of $O(1)$, in Eqs. (4.39) through (4.46). This approach is similar to that used in the $Pr \to 0$ limit, but with opposite terms neglected.

Finally, then, in the limits of small and very large Prandtl number, the governing equations for the narrow-gap limit have become much simpler. In the former, the nonlinear terms in the vorticity equation (which could give rise to hydrodynamic instabilities) dominate, whereas in the latter case, the nonlinear terms in the energy equation (which should give rise to thermal-type instabilities) dominate. Thus, by examining these two limiting conditions, the crucial mechanism for causing potential natural convective instabilities between narrow

concentric horizontal isothermal cylinders is clearly set forth.

Simplified governing equations for $Pr \to 0$ and $Pr \to \infty$ can also be obtained from the 2-D N-S equations, which include both buoyancy terms and are valid for arbitrary gap size and Rayleigh number. These limiting conditions are explored and discussed in Appendix B.

Although the material in this chapter is very analytical in nature, many of the equations derived (with the exception of those relating to the infinite Prandtl number limit) will also be solved numerically in Chapter 6. Hence, useful comparisons to the analytical results can be made, and the critical effects of the nonlinear terms can be interpreted.

5. NUMERICAL ANALYSIS

This chapter is divided into two sections. The first describes the finite-differencing method used in solving the coupled set of governing partial differential equations. Two systems of equations will be considered: the 2-D unsteady elliptic Navier-Stokes equations derived in Chapter 3, and the 2-D unsteady boundary-layer equations developed in Chapter 4. The second section deals mainly with describing the numerical procedure employed in determining the onset of an instability, either thermal or hydrodynamic, for both the 2-D Navier-Stokes and boundary-layer equations. Procedures for capturing related hysteresis behavior will also be discussed. In addition, important computational details will be provided at the end of this section.

The essential features of the numerical method were adopted from Prusa (1983). However, several important modifications were incorporated into his scheme in order to enhance numerical stability and efficiency when solving the system of equations in the high Rayleigh number/small-gap multicellular flow regime. Of particular importance was the handling of the nonlinear convective terms, in which two types of representations were employed: a corrected second-order central difference scheme for the 2-D Navier-Stokes equations, and a corrected second-order upwind scheme for the boundary-layer-like equations. Also, the unsteady form of the equations was used to take advantage of achieving steady-state in a more stable manner and

allowing the opportunity to capture unsteady behavior when solved in a time-accurate fashion.

5.1. The Numerical Method of Solution

The 2-D Navier-Stokes equations outlined in Eq. (3.1) are discretized using finite-differencing techniques. This converts the equations into an algebraic system that is well-suited for computation on a high-speed computer. In the transformed plane, the computational domain was divided into a number of cells. This cellular mesh was formed by the intersection of a set of radial lines with a set of circular arcs concentric with the boundary, $r = 1$. The grid nodes are variably spaced and are defined by the intersection of these radial lines and concentric arcs. The variable increment nodes are depicted in Figure 5.1 by using an extended version of Southwell's (1946) notation in the immediate neighborhood of a typical node. Initially, the complete annular flow field (0 to 2π) was resolved numerically. However, if symmetric cellular patterns resulted, vertical symmetry was assumed and only the half-annulus (0 - π) was computed for subsequent calculations.

The use of variable increments allowed for the concentration of grid nodes in areas of large gradients within the computational domain, such as the inner and outer boundary-layers and the thermal plume region near the top of the inner cylinder. However, it should be noted that the use of variable increments may result in a loss of formal truncation error (Roache, 1976), where the loss becomes less

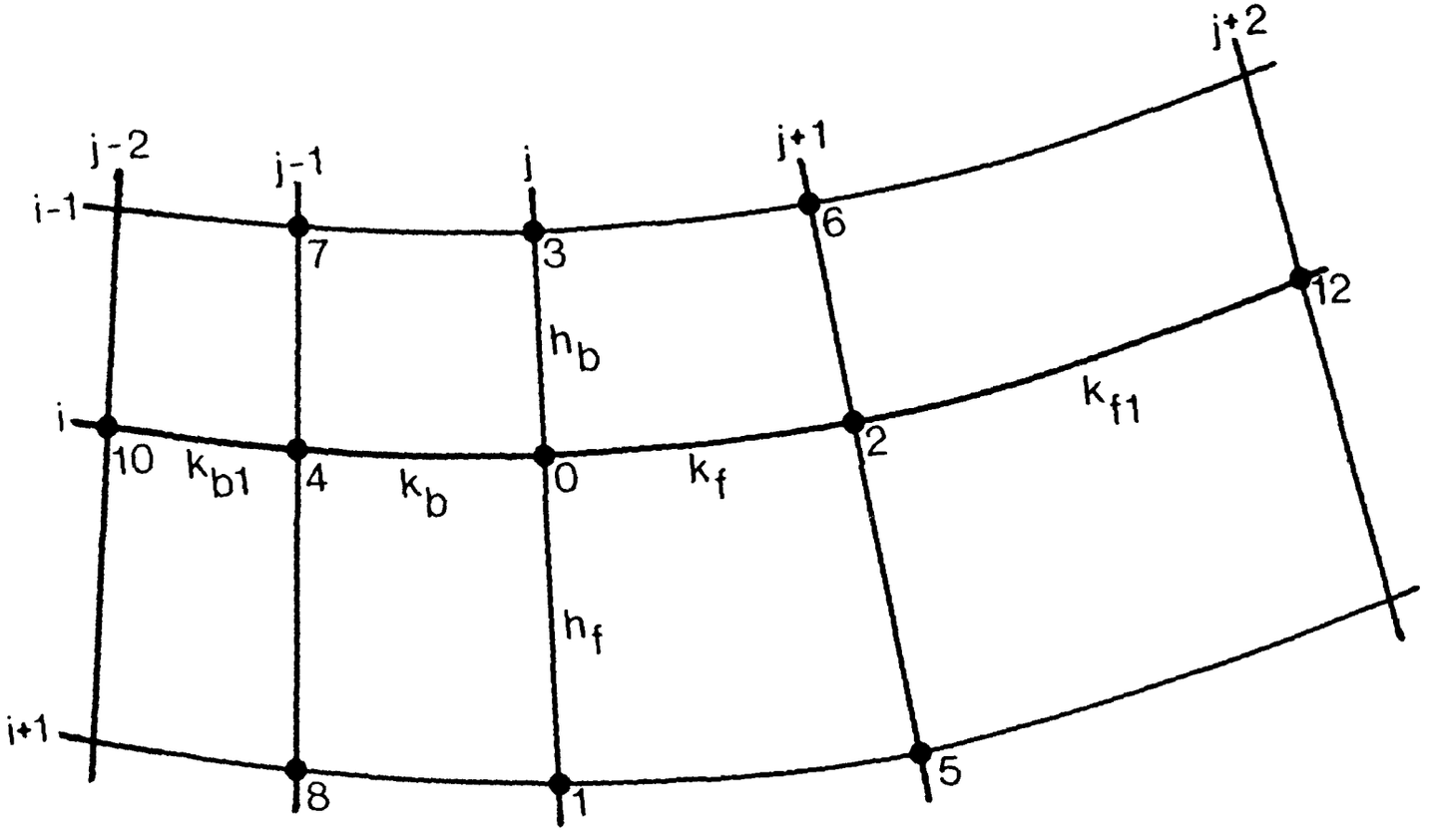

Figure 5.1. Computational mesh with variable increments

severe in the finer portions of the mesh and more severe in the coarser areas (this result is discussed further in subsection 5.1.2). A convenient 2-D coordinate variable mesh routine was developed in Prusa (1983), in which the variable nodal positions were computed by using a smooth fourth-order polynomial stretch that imposed a zero gradient increment variation at the edges of the mesh. This routine, with minor changes to accommodate the complete (0 - 2π) annulus, was used in this study to generate the various computational meshes. The program was relatively simple to use and proved quite valuable in resolving the multicellular flow field.

5.1.1. Variable increment finite-difference formulas

The formal Taylor series approach will be used to develop variable increment finite-difference approximations of the derivatives in the governing equations. The dependent variables T, w and f will be denoted by ϕ; k_f and k_b denote the increments in the directions of increasing and decreasing angular variation, from a given discrete point (r_i, ψ_j) (see Figure 5.1). Using Southwell's notation, the Taylor series expansions of ϕ_2 and ϕ_4 (r_i, ψ_j) are:

$$\phi_2 = \phi_0 + \frac{\partial\phi}{\partial\psi}\bigg|_0 k_f + \frac{1}{2}\frac{\partial^2\phi}{\partial\psi^2}\bigg|_0 k_f^2 + \frac{1}{6}\frac{\partial^3\phi}{\partial\psi^3}\bigg|_0 k_f^3 + \ldots. \qquad (5.1a)$$

$$\phi_4 = \phi_0 - \frac{\partial\phi}{\partial\psi}\bigg|_0 k_b + \frac{1}{2}\frac{\partial^2\phi}{\partial\psi^2}\bigg|_0 k_b^2 - \frac{1}{6}\frac{\partial^3\phi}{\partial\psi^3}\bigg|_0 k_b^3 + \ldots \qquad (5.1b)$$

Equation (5.1a) can now be solved explicitly to give a forward-difference representation of $\partial\phi_0/\partial\psi$:

$$\left.\frac{\partial\phi}{\partial\psi}\right|_0 = \frac{\phi_2 - \phi_0}{k_f} + O(k_f) \ , \tag{5.1c}$$

while Eq. (5.1b) yields the backward-difference form:

$$\left.\frac{\partial\phi}{\partial\psi}\right|_0 = \frac{\phi_0 - \phi_4}{k_b} + O(k_b) \ . \tag{5.1d}$$

Subtraction of Eq. (5.1b) from Eq. (5.1a) gives the (second-order-like) centered-difference result:

$$\left.\frac{\partial\phi}{\partial\psi}\right|_0 = \frac{\phi_2 - \phi_4}{k_f + k_b} + O(k_f - k_b) + O(k_f^2, k_f k_b, k_b^2) \ . \tag{5.1e}$$

A second linear combination of Eqs. (5.1a) and (5.1b) gives the centered second derivative:

$$\left.\frac{\partial^2\phi}{\partial\psi^2}\right|_0 = \frac{k_b\phi_2 - (k_f + k_b)\phi_0 + k_f\phi_4}{\frac{1}{2}(k_f + k_b)k_f k_b}$$

$$+ O(k_f - k_b) + O(k_f^2, k_f k_b, k_b^2) \ . \tag{5.1f}$$

The counterpart radial expressions for Eqs. (5.1c) through (5.1f) are easily obtained by substituting r for ψ, and ϕ_1, ϕ_3 and h_f, h_b for

ϕ_2, ϕ_4 and k_f, k_b, respectively.

Finite-difference formulas for the unsteady terms are found by using the standard, but generally stable, forward-difference molecule:

$$\left.\frac{\partial \phi}{\partial t}\right|_0 = \frac{\phi_0^{n+1} - \phi_0^n}{\Delta t} + O(\Delta t) \qquad (5.2)$$

where n designates the time level at which the dependent variable ϕ is evaluated. When marching in time to steady-state, the first-order truncation error should not influence the final result; hence, time steps as large as possible should be considered. However, when unsteady behavior had to be resolved (as with the $Pr \to 0$ case in this study), very small time steps should be used to avoid large truncation error, thus obtaining a time-accurate solution.

5.1.2. Finite-difference equations for the dependent variables

All spatial derivatives in the governing equations are second-order centrally (or upwind) differenced. This includes the convective terms which are represented by a first-order upwind expression together with a correction term for second-order-like accuracy. The convective terms are split in order to maintain diagonal dominance of the coefficient matrix at high Rayleigh numbers (as with pure upwind differencing), thus providing stable convergence toward the desired centrally differenced (or second-order upwind differenced) representation.

5.1.2.1. 2-D Navier-Stokes equations The nonlinear convective terms in the 2-D Navier-Stokes equations can be expressed as:

$$2\lambda \left.\frac{\partial \phi}{\partial r}\right|_0 = (\lambda - |\lambda|) \left\{\frac{\phi_0 - \phi_3}{h_b} + \frac{\phi_1 + H\phi_3 - (1 + H)\phi_0}{h_b + h_f}\right\}$$

$$+ (\lambda + |\lambda|) \left\{\frac{\phi_1 - \phi_0}{h_f} - \frac{\frac{\phi_1}{H} + \phi_3 - (1 + \frac{1}{H})\phi_0}{h_b + h_f}\right\} \qquad (5.3a)$$

and

$$2\mu \left.\frac{\partial \phi}{\partial \psi}\right|_0 = (\mu - |\mu|) \left\{\frac{\phi_0 - \phi_4}{k_b} + \frac{\phi_2 + k\phi_4 - (1 + k)\phi_0}{k_f + k_b}\right\}$$

$$+ (\mu + |\mu|) \left\{\frac{\phi_2 - \phi_0}{k_f} - \frac{\phi_2/k + \phi_4 - (1 + \frac{1}{k})\phi_0}{k_f + k_b}\right\} \qquad (5.3b)$$

where ϕ represents the dependent variables T, w, or f, and

$$H = \frac{h_f}{h_b}, \quad k = \frac{k_f}{k_b} .$$

The first terms within the brackets are the first-order upwind-difference components and the second terms are the added corrections which bring the differencing up to second-order accuracy. The terms within the parentheses (outside of the brackets) ensure that stable differencing 'into-the-wind' is enforced.

Using the above relations, Eqs. (3.1a, b, or c) can be manipulated into the following general form:

$$\Delta 2 \left\{- \tilde{\Delta} G^2 \frac{\partial \phi}{\partial t} + \frac{\partial^2 \phi}{\partial r^2} + (r + \frac{1}{G})^{-2} \frac{\partial^2 \phi}{\partial \psi^2}\right\} + 2\lambda \frac{\partial \phi}{\partial r} + 2\mu \frac{\partial \phi}{\partial \psi} + S = 0 \qquad (5.4)$$

where

$$2\lambda = \left(r + \frac{1}{G}\right)^{-1} \left\{\Delta 2 + \Delta 1 \frac{\partial f}{\partial \psi}\right\} \tag{5.5a}$$

$$2\mu = \frac{-\Delta 1}{r + \frac{1}{G}} \frac{\partial f}{\partial r} \tag{5.5b}$$

and

$$\Delta 1 = \begin{cases} Pr, & \phi = T \\ Pr, & \phi = w \\ 0, & \phi = f \end{cases} \qquad \Delta 2 = \begin{cases} 1, & \phi = T \\ Pr, & \phi = w \\ 1, & \phi = f \end{cases}$$

while

$$\tilde{\Delta} = \begin{cases} Pr, & \phi = T \\ 1, & \phi = w \\ 0, & \phi = f \end{cases} .$$

The derivatives in Eqs. (5.5a) and (5.5b) are represented by standard central-difference expressions, as in Eq. (5.1e).

Employing Eqs. (5.3a and 5.3b) and substituting the appropriate differences of Eqs. (5.1c-f), results in a general finite-difference equation for ϕ = T, w, or f:

$$C_0 \phi_0^{n+1} = \frac{(\Delta 2)\, \tilde{\Delta}\, G^2}{\tau} \phi_0^n + C_1 \phi_1^{n+1} + C_2 \phi_2^{n+1}$$

$$+ C_3 \phi_3^{n+1} + C_4 \phi_4^{n+1} + E^n + S^{n+1} \tag{5.6a}$$

where

$$C_0 = \frac{(\Delta 2)\ \tilde{\Delta}\ G^2}{\tau} + 2\ [\frac{\Delta 2}{h_f h_b} + \frac{\Delta 2}{k_f k_b\ (r + \frac{1}{G})^2}]$$

$$+ \lambda(\frac{1}{h_f} - \frac{1}{h_b}) + |\lambda|\ (\frac{1}{h_b} + \frac{1}{h_f}) + \Gamma\mu\ (\frac{1}{k_f} - \frac{1}{k_b})$$

$$+ \Gamma|\mu|\ (\frac{1}{k_b} + \frac{1}{k_f}) \qquad (5.6b)$$

$$C_1 = \frac{2(\Delta 2)}{h_f(h_f + h_b)} + \frac{(\lambda + |\lambda|)}{h_f} \qquad (5.6c)$$

$$C_2 = \frac{2\ (\Delta 2)}{(r + \frac{1}{G})^2\ (k_f + k_b)k_f} + \Gamma(\frac{\mu + |\mu|}{k_f}) \qquad (5.6d)$$

$$C_3 = \frac{2(\Delta 2)}{h_b(h_f + h_b)} - \frac{(\lambda - |\lambda|)}{h_b} \qquad (5.6e)$$

$$C_4 = \frac{2(\Delta 2)}{(r + \frac{1}{G})^2\ (k_f + k_b)k_b} - \frac{\Gamma(\mu - |\mu|)}{k_b}\ . \qquad (5.6f)$$

Note that a negative contribution to C_0 is possible if h_f/h_b or k_f/k_b departs too far from 1. Thus, unstable calculations may result if diagonal dominance is lost as C_o gets smaller in magnitude.

$$E^n = \left(\frac{\lambda}{h_f + h_b}\right) \{\phi_1^n \left(1 - \frac{1}{H}\right) + \phi_3^n (H - 1) - \phi_0^n \left(H - \frac{1}{H}\right)\}$$

$$- \left(\frac{|\lambda|}{h_f + h_b}\right) \{\phi_1^n \left(1 + \frac{1}{H}\right) + \phi_3^n (1 + H) - \phi_0^n \left(2 + H + \frac{1}{H}\right)\}$$

$$+ \left(\frac{\Gamma\, \mu}{k_f + k_b}\right) \{\phi_2^n \left(1 - \frac{1}{K}\right) + \phi_4^n (k - 1) - \phi_0^n \left(k - \frac{1}{k}\right)\}$$

$$- \left(\frac{\Gamma\, |\mu|}{k_f + k_b}\right) \{\phi_2^n \left(1 + \frac{1}{k}\right) + \phi_4^n (1 + k) - \phi_0^n \left(2 + k + \frac{1}{k}\right)\} \qquad (5.6g)$$

$$S^{n+1} = \begin{cases} 0 & , \ \phi = T \\ G \cdot Ra \left(\sin \psi \left.\frac{\partial T}{\partial r}\right|_0 + \frac{\cos \psi}{r + \frac{1}{G}} \left.\frac{\partial T}{\partial \psi}\right|_0\right)^{n+1} & , \ \phi = w \\ -G^2 \, w_0^{n+1} & , \ \phi = f \end{cases} \qquad (5.6h)$$

and

$$\Gamma = \begin{cases} 1, & \phi = T \\ 1, & \phi = w \\ 0, & \phi = f \end{cases} . \qquad (5.6i)$$

The derivatives $\left.\frac{\partial T}{\partial r}\right|_0$ and $\left.\frac{\partial T}{\partial \psi}\right|_0$ in Eq. (5.6h) are evaluated by using standard central-difference formulas. τ denotes the time increment,

while the superscripts, n, n+1, are as discussed in Eq. (5.2).

For a fully-implicit method, the correction term E, should be evaluated at the new-time level, E^{n+1}. However, as seen in Eq. (5.6g), the correction term for the 2-D Navier-Stokes equations was evaluated at the old-time level, E^n. Although the E^n method introduced a time truncation error of $O(\Delta t)$, it still remained consistent with the rest of the formulation. Also, since E^n uses known information from the previous time level, its contribution to the off-diagonal terms (ϕ_1^n, ϕ_2^n, ϕ_3^n and ϕ_4^n) was kept constant when evaluating flow properties at the new-time level. This factor apparently helped to enhance numerical stability, which in turn, improved the convergence rate and accuracy of the numerical method when compared to the E^{n+1} formulation. This was especially true for the highly convective flows associated with multicellular development (see Appendix C). In comparing to E^{n+1}, a truncation error analysis demonstrated that the E^n method preserved the formal accuracy of the system of equations. A description of this analysis and a tabular comparison of the two approaches is given in Appendix C.

5.1.2.2. Finite-Prandtl number boundary-layer equations The boundary-layer equations of (4.25) are numerically treated in a manner similar to that used on the 2-D Navier-Stokes equations. But since Eqs. (4.25a-c) are only first-order in ψ, a slightly modified version of Eq. (5.4) results:

$$\Delta 2 \left\{ - \tilde{\Delta}\, \tilde{G}^2 \frac{\partial \phi}{\partial t} + \frac{\partial^2 \phi}{\partial r^2} \right\} + 2\lambda \frac{\partial \phi}{\partial r} + 2\mu \frac{\partial \phi}{\partial \psi} + S = 0 \qquad (5.7)$$

where

$$2\lambda = \Delta 1 \cdot \frac{\partial \tilde{f}}{\partial \Psi} \tag{5.8a}$$

$$2\mu = - \Delta 1 \cdot \frac{\partial \tilde{f}}{\partial r} \quad . \tag{5.8b}$$

The first-order derivatives in the 2μ and 2λ coefficients are approximated by central-differences. Also,

$$\Delta 1 = \begin{cases} Pr \cdot \tilde{G}, & \phi = \tilde{T} \\ Pr \cdot \tilde{G}, & \phi = \tilde{w} \\ 0, & \phi = \tilde{f} \end{cases} \qquad \Delta 2 = \begin{cases} 1, & \phi = \tilde{T} \\ Pr, & \phi = \tilde{w} \\ 1, & \phi = \tilde{f} \end{cases}$$

while

$$\tilde{\Delta} = \begin{cases} Pr, & \phi = \tilde{T} \\ 1, & \phi = \tilde{w} \\ 0, & \phi = \tilde{f} \end{cases} \quad .$$

Except for the definition of λ, the convective term $2\lambda \frac{\partial \phi}{\partial r}$ is represented as in Eq. (5.3a). However, because of the parabolic nature of these boundary-layer equations, which are first-order in Ψ, a central-difference representation of the streamwise convective terms is no longer valid. Instead, a stable corrected second-order upwind-differenced scheme is employed. Namely,

$$2\mu \left.\frac{\partial\phi}{\partial\psi}\right|_0 = (\mu - |\mu|)\left\{\frac{\phi_0 - \phi_4}{k_b} + \frac{\phi_0 - \phi_4 + \left(\frac{k_b}{k_{b_1}}\right)(\phi_{10} - \phi_4)}{k_b + k_{b_1}}\right\}$$

$$+ (\mu + |\mu|)\left\{\frac{\phi_2 - \phi_0}{k_f} + \frac{\phi_2 - \phi_1 + \left(\frac{k_f}{k_{f_1}}\right)(\phi_2 - \phi_{12})}{k_f + k_{f_1}}\right\} \qquad (5.9)$$

(see Figure 5.1 for related nodal positions). The second term within the brackets represents the added correction to the first-order differenced component needed to achieve a second-order upwind-differenced expression.

Using the above results, the boundary-layer equations of (4.25) can be cast into a finite-difference form similar to that of Eq. (5.6a):

$$C_0\phi_0^{n+1} = \frac{(\Delta 2)\tilde{\Delta}\,\tilde{G}^2}{\tau}\phi_o^n + C_1\phi_1^{n+1} + C_2\phi_2^{n+1} + C_3\phi_3^{n+1}$$

$$+ C_4\phi_4^{n+1} + E^{n+1} + S^{n+1} \qquad (5.10a)$$

where

$$C_0 = \frac{(\Delta 2)\tilde{\Delta}\,\tilde{G}^2}{\tau} + \frac{2(\Delta 2)}{h_f h_b} + \Gamma\lambda\left(\frac{1}{h_f} - \frac{1}{h_b}\right) + \Gamma|\lambda|\left(\frac{1}{h_b} + \frac{1}{h_f}\right)$$

$$+ \Gamma\mu\left(\frac{1}{k_f} - \frac{1}{k_b}\right) + \Gamma|\mu|\left(\frac{1}{k_b} + \frac{1}{k_f}\right) \qquad (5.10b)$$

$$C_1 = \frac{2(\Delta 2)}{h_f(h_f + h_b)} + \Gamma\left(\frac{\lambda + |\lambda|}{h_f}\right) \tag{5.10c}$$

$$C_2 = \Gamma\left(\frac{\mu + |\mu|}{k_f}\right) \tag{5.10d}$$

$$C_3 = \frac{2(\Delta 2)}{(h_f + h_b)h_b} - \frac{\Gamma(\lambda - |\lambda|)}{h_b} \tag{5.10e}$$

$$C_4 = \frac{-\Gamma(\mu - |\mu|)}{k_b} \tag{5.10f}$$

and Γ is defined as in Eq. (5.6i), with ϕ now denoting the boundary-layer dependent variables. Before defining the correction term E^{n+1}, let

$$k1 = \frac{a}{b}, \quad k2 = \frac{c}{d}$$

where $a = k_f$, $b = k_{f1}$, $c = k_b$, $d = k_{b1}$. Then:

$$E^{n+1} = \Gamma\left(\frac{\lambda}{h_f + h_b}\right) \{{\phi_1}^{n+1}(1 - \tfrac{1}{H}) + {\phi_3}^{n+1}(H - 1) - {\phi_0}^{n+1}(H - \tfrac{1}{H})\}$$

$$- \Gamma\left(\frac{|\lambda|}{h_f + h_b}\right) \{{\phi_1}^{n+1}(1 + \tfrac{1}{H}) + {\phi_3}^{n+1}(1 + H) - {\phi_0}^{n+1}(2 + H + \tfrac{1}{H})\}$$

$$+ \mu\Gamma \{{\phi_2}^{n+1}[(1 + k1)/(a + b)] - {\phi_4}^{n+1}[(1 + k2)/(c + d)]$$

$$+ \phi_0^{n+1} [1/(c + d) - 1/(a + b)]$$

$$+ \phi_{10}^{n+1} [k2/(c + d)] - \phi_{12}^{n+1} [k1/(a + b)]\}$$

$$+ |\mu|\Gamma\{\phi_2^{n+1} [(1 + k1)/(a + b)] + \phi_4^{n+1} [(1 + k2)/(c + d)]$$

$$- \phi_0^{n+1} [1/(c + d) + 1/(a + b)] - \phi_{10}^{n+1} [k2/(c + d)]$$

$$- \phi_{12}^{n+1} [k1/(a + b)]\} \qquad (5.10g)$$

and lastly,

$$S^{n+1} = \begin{cases} 0 & \phi = T \\ \tilde{G} \left(\sin \psi_o \left.\frac{\partial \tilde{T}}{\partial r}\right|_0\right)^{n+1}, & \phi = \tilde{w} \\ -\tilde{G}^2 \tilde{w}_0^{n+1}, & \phi = \tilde{f} \end{cases} \qquad (5.10h)$$

where $\left.\frac{\partial \tilde{T}}{\partial r}\right|_0$ is centrally-differenced.

The first two terms of Eq. (5.10g) represent the second-order corrections corresponding to central-differencing in the transverse or radial direction, whereas the last two terms signify the corrections

necessary to obtain second-order upwind differencing in the streamwise or angular direction. In contrast to the 2-D Navier-Stokes equations, the correction terms for the boundary-layer equations were evaluated at the new-time level, E^{n+1}. Since it is usually the central-differenced streamwise convective terms that cause stability problems at high Rayleigh numbers, the E^{n} approach was adopted to alleviate this predicament for the Navier-Stokes equations. However, since second-order upwind differencing is generally more stable than central-differencing, the E^{n+1} method worked fine and remained stable for the boundary-layer calculations. Note that the E^{n+1} method also converged for the Navier-Stokes calculations, but the E^{n} formulation proved to be more efficient (see Appendix C). Based on the literature review and work in this study, it was found that although first-order upwind differencing is extremely stable at high Rayleigh numbers, at least second-order accuracy is needed to resolve the multicells.

5.1.2.3. Zero-Prandtl number boundary-layer equations In the $Pr \to 0$ limit, the energy equation reduced to simply $T = 1 - r$, therefore decoupling itself from the vorticity equation. Hence, only the vorticity and stream function equations had to be solved numerically in a coupled manner. The following one-equation format, similar to Eq. (5.7), can again be used to represent these two coupled equations as derived in Chapter 4 (Eqs. 4.77 and 4.78):

$$\Delta 2 \left\{ - \tilde{\Delta}\hat{G}^2 \frac{\partial \phi}{\partial t} + \frac{\partial^2 \phi}{\partial r^2} \right\} + 2\lambda \frac{\partial \phi}{\partial r} + 2\mu \frac{\partial \phi}{\partial \psi} + S = 0 \qquad (5.11)$$

where

$$2\lambda = \Delta 1 \cdot \frac{\partial F}{\partial \psi} \tag{5.12a}$$

$$2\mu = -\Delta 1 \cdot \frac{\partial F}{\partial r} \tag{5.12b}$$

and

$$\Delta 1 = \begin{cases} \hat{G}, & \phi = W \\ 0, & \phi = F \end{cases} \qquad \Delta 2 = \begin{cases} 1, & \phi = W \\ 1, & \phi = F \end{cases}$$

while

$$\tilde{\Delta} = \begin{cases} 1, & \phi = W \\ 0, & \phi = F \end{cases} .$$

The finite-difference form of Eq. (5.11) is identical to Eq. (5.10a) for the finite-Prandtl number boundary-layer equations, except that $\tilde{G}$ is now replaced by $\hat{G}$. The same applies to the coefficient equations for C_0, C_1, C_2, C_3 and C_4 in Eqs. (5.10b) - (5.10f), but with λ and μ being defined by Eqs. (5.12a) and (5.12b), respectively. The E^{n+1} correction term is similarly represented by Eq. (5.10g), while again making the appropriate substitutions for λ and μ. Also,

$$S^{n+1} = \begin{cases} -\hat{G} \sin \psi_0, & \phi = W \\ -\hat{G}^2 W_0^{n+1}, & \phi = F \end{cases} . \tag{5.13}$$

5.1.3. Boundary conditions

5.1.3.1. 2-D Navier-Stokes equations Considering the complete annulus, the finite-difference form of the boundary conditions for the 2-D Navier-Stokes equations is:

Energy:

$$T_{1,j}^{n+1} = 1 \tag{5.14a}$$

$$T_{NR,j}^{n+1} = 0 \tag{5.14b}$$

Vorticity:

$$w_{1,j}^{n+1} = \frac{2f_{2,j}^{n+1}}{(Gh_1)^2} \tag{5.14c}$$

$$w_{NR,j}^{n+1} = \frac{2f_{NR-1,j}^{n+1}}{(Gh_{NR-1})^2} \tag{5.14d}$$

Stream Function:

$$f_{1,j}^{n+1} = 0.0 \tag{5.14e}$$

$$f_{NR,j}^{n+1} = 0.0 \quad . \tag{5.14f}$$

Because of continuity at zero and 2π radians, a computational continuous condition must be defined such that:

$$\phi_{i,1}^{n+1} = \phi_{i,NS1}^{n+1} \tag{5.14g}$$

where ϕ takes on values of either temperature, vorticity, or stream function.

When symmetry about the vertical center-line is considered, the conditions imposed by Eq. (5.14g) are replaced by:

$\psi = 0$:

$$T_{i,1}^{n+1} = T_{i,2}^{n+1} - A_{i,1}k_1 \tag{5.15a}$$

$$w_{i,1}^{n+1} = 0.0 \tag{5.15b}$$

$$f_{i,1}^{n+1} = 0.0 \tag{5.15c}$$

$\psi = \pi$:

$$T_{i,NS}^{n+1} = T_{i,NS-1}^{n+1} - A_{i,NS}k_{NS-1} \tag{5.15d}$$

$$w_{i,NS}^{n+1} = 0.0 \tag{5.15e}$$

$$f_{i,NS}^{n+1} = 0.0 \tag{5.15f}$$

where

$$A_{i,1} = \frac{k_2 T_{i,1}^{n+1} - (k_1 + k_2)T_{i,2}^{n+1} + k_1 T_{i,3}^{n+1}}{k_2(k_1 + k_2)}$$

$$A_{i,NS} = \frac{k_{NS-2}T^{n+1}_{i,NS} - (k_{NS-1} + k_{NS-2})T^{n+1}_{i,NS-1} + k_{NS-1}T^{n+1}_{i,NS-2}}{k_{NS-2}(k_{NS-1} + k_{NS-2})}$$

and for Eqs. (5.14) and (5.15), $h_i = r_{i+1} - r_i$, $k_j = \psi_{j+1} - \psi_j$. Also, the i index refers to the radial position with i = 1 corresponding to the inner cylinder, r = 0; and i = NR corresponding to the outer cylinder, r = 1. The j index signifies the angular position with j = 1 referring to $\psi = 0°$, j = NS referring to $\psi = 180°$, and j = NS1 referring to $\psi = 360°$.

The symmetry conditions for temperature were obtained from Taylor-series expansions about j = 1 and NS, namely (for $\psi = 0$):

$$T_{i,2} = T_{i,1} + \left.\frac{\partial T}{\partial \psi}\right|_{i,1} k_1 + \frac{1}{2}\left.\frac{\partial^2 T}{\partial \psi^2}\right|_{i,1} k_1^2 + \ldots .$$

and upon assuming symmetry, one gets:

$$\left.\frac{\partial T}{\partial \psi}\right|_{i,1} = 0 \quad .$$

Then, solving for $T_{i,1}$ and substituting the second-order difference expression for $\frac{\partial^2 T}{\partial \psi^2}$ (evaluated at j = 1), the final form of Eq. (5.15a) is obtained. Equation (5.15d) can also be approximated in a similar manner.

The formal Taylor-series approach is also used to derive the vorticity-wall boundary conditions. At the inner wall, r = 0, let:

$$f_{2,j} = \underbrace{f_{1,j}}_{0,\text{ at wall}} + \underbrace{\left.\frac{\partial f}{\partial r}\right|_{1,j}}_{0,\text{ no-slip}} h_1 + \frac{1}{2}\left.\frac{\partial^2 f}{\partial r^2}\right|_{1,j} h_1^2 + O(h_1)^3 \quad .$$

Then,

$$\left.\frac{\partial^2 f}{\partial r^2}\right|_{1,j} = \frac{2f_{2,j}}{h_1^2} + O(h_1)$$

and from the definition of vorticity, one obtains:

$$w_{1,j} = \frac{2f_{2,j}}{(Gh_1)^2} \quad .$$

Likewise, the condition for the outer wall can be derived. According to Roache (1976), this first-order difference form of the vorticity boundary condition is the safest and most stable, and in fact, is sometimes more accurate than other second-order approximations.

5.1.3.2. Finite-Prandtl and zero-Prandtl number equations The finite-difference expressions for the boundary conditions of the finite-Prandtl and zero-Prandtl number equations are similar to those of the 2-D Navier-Stokes equations. These expressions can be found by simply replacing G with $\tilde{G}$, $\hat{G}$, and f, w, T, t with $\tilde{f}$, $\tilde{w}$, $\tilde{T}$, $\tilde{t}$ and F, W, T, $\hat{t}$, in Eqs. (5.14) and (5.15), respectively. Note again that for the $Pr \to 0$ case, the energy equation reduced to $T = 1 - r$, thus decoupling itself from the vorticity equation. Therefore, if vertical

symmetry is assumed, the $\frac{\partial T}{\partial \psi} = 0$ constraint drops out of the boundary conditions at $\psi = 0$ and $\psi = \pi$.

Finite-difference expressions for Nusselt number and shear stress are derived and explained in Appendix D.

5.2. The Computational Procedure

The systems of coupled finite-difference equations (as described in the preceding section) were solved implicitly in time using a point iterative Gauss-Seidel method with underrelaxation. The dependent variables at a given time level were found by repeated iterations of the governing equations.

Except for the preset isothermal boundary conditions, the dependent variables were first initialized by setting them all to zero. (However, as will be explained later, initial conditions other than zero were used when searching for hysteresis loops.)

For the first several time steps, the iterative solution process was initiated as follows. First, the E correction terms were set to zero and a converged first-order upwind differenced solution was obtained. This converged result was then used as an initial condition for obtaining a solution to the corrected central differenced scheme. This two-step method allowed for an enhanced convergence rate when the flow field was diffusion-dominated--usually associated with the first few time steps of a developing flow. However, for subsequent time steps, when convective effects became more significant, the correction terms were always retained and previously converged old-time second-

order accurate results were used as an initial start-up for the next time level. The advantages of this procedure are more fully explained and discussed in Kassinos (1986). Using this approach allowed for numerical solutions to be efficiently computed to any arbitrary time.

5.2.1. Iteration sequence and convergence criterion

The governing finite-difference equations (both the 2-D Navier-Stokes and the boundary-layer equations) were numerically iterated in the following sequence:

i. energy equation

ii. vorticity equation

iii. stream function equation.

This sequence was repeated until the iterations converged to within a prescribed tolerance. The maximum modulus of the difference between temperature, vorticity and stream function for two successive iteration values was used as the relative convergence constraint, namely,

$$\max \left| \frac{\phi^{m+1,\, n+1} - \phi^{m,\, n+1}}{(\phi^{m+1,\, n+1})_{max}} \right| < 1 \times 10^{-6} \qquad (5.16)$$

where ϕ represents temperature, vorticity or stream function. The iterative process was terminated and the numerical solution was considered converged when the above criterion was satisfied. In Eq. (5.16), the m referred to the iteration number, while the time level index was denoted by n. The vorticity iterations usually

converged the slowest (about 10^3 times slower when compared to temperature), especially for highly convective or multicellular-type flows.

5.2.2. Relaxation parameters

Two independent relaxation parameters, Ω_1 and Ω_2, were incorporated into the equations in order to gain some control on the rate of convergence of the iterations. The first relaxation parameter, Ω_1, was used only with the vorticity boundary conditions for both the 2-D Navier-Stokes and the boundary-layer equations. Its use on the inner cylinder boundary can be illustrated as follows (for the Navier-Stokes equations):

$$w_{1,j}^{m+1,\,n+1} = \Omega_1 \{2f_{2,j}^{m,\,n+1}/(Gh_1)^2\}$$

$$+ (1 - \Omega_1) w_{1,j}^{m,\,n+1} \quad \text{along } r = 0 \quad . \tag{5.17}$$

If $\Omega_1 < 1$, then the m + 1 iterated value of w becomes a weighted average of the newly computed value and the old m iterated value of w. Generally, $.1 \leq \Omega_1 \leq .5$ was used to help stabilize the numerical computations. When multicellular flow was encountered, the relaxation parameter was usually reduced to the smaller values. The above procedure was also used for the boundary-layer equations.

Since the central differenced correction terms of the 2-D Navier-Stokes equations were based on the old-time level (E^n), an

underrelaxation procedure was not needed to aid in computational stability. However, for the finite-Prandtl and the zero-Prandtl number boundary-layer equations, a second relaxation parameter, Ω_2, was used with the second-order upwind (or central) differenced correction terms which were based on the new-time level (E^{n+1}). The interior point equations for the dependent variables $\phi = \tilde{T}$ and $\tilde{w}$ for the finite-Prandtl number equations, and $\phi = W$ for the zero-Prandtl number equations, were computed according to:

$$\phi_0^{m+1,\, n+1} = \frac{(\Delta 2)\tilde{\Delta}\, \tilde{G}^2 \text{ (or } \hat{G}^2)}{C_0 \tau}\, \phi_0^n + \{C_1 \phi_1^{m,\, n+1} + C_2 \phi_2^{m,\, n+1}$$

$$+ C_3 \phi_3^{m+1,\, n+1} + C_4 \phi_4^{m+1,\, n+1} + S^{m+1,\, n+1}\}/C_0$$

$$+ \{\Omega_2\, E^{m+1,\, n+1} + (1 - \Omega_2)\, E^{m,\, n+1}\}/C_0 \quad . \tag{5.18}$$

In Eq. (5.18), the E^m term uses ϕ_0, ϕ_1, and ϕ_2 evaluated at the m - 1 iteration and n + 1 time level, together with ϕ_3 and ϕ_4 evaluated at the m iteration and n + 1 time level. Also, ϕ_0^n does not require an iteration index since it represents the previously converged value at the old-time level. For $\Omega_2 < 1$, the differencing of the correction term becomes a weighted average of Gauss-Seidel (current level) and Jacobi (previous level) iterations. Generally, $.1 \leq \Omega_2 \leq .5$ was used in the numerical computations. For the highly convective flows, the relaxation parameter was decreased to .2 or .1.

5.2.3. Multicellular flow determination

In the 2-D Navier-Stokes equations, multicellular flow near the top of the annulus was investigated for Pr = .706. When searching for the transitional Rayleigh numbers associated with particular narrow gap widths (numbers which characterize the transition from bicellular to multicellular flow), "zero" initial conditions were used for only the first pretransitional Rayleigh number case. Then, for each successive slightly higher Rayleigh number (Ra) run, the previous converged Ra solution was used to start the new solution. This procedure was repeated until at some Ra a transition to multicells occurred. In order to find hysteresis loops, prescribed multicellular initial conditions (usually associated with the multicellular flow field characterized by the transitional Rayleigh number) were used for gradually backtracking the Ra (also in a successive manner) until the bicellular solution again became apparent. Different solutions, dependent upon the initial conditions, are possible as a result of nonuniqueness inherent in nonlinear-type problems.

For the boundary-layer equations, a multicellular flow occurring near the vertical portions of a narrow annulus was investigated for the small-Prandtl number cases. The values of $\tilde{G}$ or $\hat{G}$ (which are proportional to Rayleigh number) corresponding to multicellular transition were determined in a manner similar to that just described, but with $\tilde{G}$ or $\hat{G}$ replacing Ra in the above procedure.

5.2.4. Computational details and discussion

The majority of the calculations were carried out with 31 radial nodes and 102 angular nodes for either the 0 - π or the 0 - 2π test cases. Using the variable-mesh algorithm, the mesh spacing was slightly reduced (generally by a factor of 1.5 for the largest to smallest increment size) near the inner and outer boundary-layers and also in the thermal plume region (for air) near the top of the inner cylinder.

For the 2-D Navier-Stokes equations, steady-state pretransitional solutions were obtained by using a time step of 5×10^{-4}. Typically, 300 time steps (t = .15) were required to reach a convincing steady-state result. The program was generally more stable with smaller time steps. This was probably due to increased diagonal dominance, since the C_0 coefficient gets larger in magnitude as τ decreases (see Eq. 5.6b). For larger time steps (between .001 and .01), the solution would often diverge as the Rayleigh number increased; this was especially true for the multicellular flow calculations. Thus, a small constant time step was used for most of the computations.

A typical pretransitional steady-state result took approximately 5-10 CPU hours on the Perkin-Elmer 3242 computer system (where 1 unit of CRAY1 time corresponds to approximately 50-60 units of Perkin-Elmer time), or an average of 1-2 minutes per time step. The average number of iterations per time step was approximately 20-30. However, when the transition to multicells occurred (two-to-four or two-to-six cells), the time step was maintained at 5×10^{-4}, but the amount of

CPU time needed to achieve steady-state (t = .15) increased to approximately 30 hours or an average of six minutes (for approximately 100 iterations) per time step.

For two of the narrow gaps (G = .100 and G = .200) associated with hysteresis behavior (Pr = .706), the complete annular gap was determined numerically. This was done in order to ascertain if symmetric cell development ensued near the top of the annulus, as initially expected. In both of these cases, symmetric cellular patterns resulted. Based on this information, all other narrow gaps for air were numerically studied by considering only the half-annulus with symmetry boundary conditions imposed at ψ = 0 and 180°. A 31 x 102 mesh was again used for these symmetric cases, thus creating an extremely fine grid for the half-plane geometry. Aside from G = .100 and .200, the transitional Rayleigh numbers predicted for the narrow gap widths were calculated by assuming symmetry about the vertical center-line. Note that for G = .100 and .200 (where the complete annulus was used), a 31 x 102 mesh was still employed, but the grid points were significantly concentrated near the top portion of the annular gap (by factors of 2.1 and 1.7, respectively) in order to achieve the necessary accuracy to resolve the symmetric multicellular flow field. For the G = .100 case, an erroneous asymmetric cellular pattern actually resulted when using a mesh with nodes concentrated near the top by a factor of 1.7. However, a six-cellular symmetric pattern became evident when the nodes were further concentrated to a factor of 2.1.

For the $Pr \to 0$ boundary-layer equations, symmetry about the vertical center-line was assumed for a 31 x 102 size mesh (this assumption is discussed in detail in the latter part of this subsection). Prior to the point of multicellular instability in the vertical portion of the annulus ($\hat{G} \leq 5.1$), steady-state solutions were easily achieved within 50 time steps for a $\Delta\hat{t}$ of 1.0. This size time step was also relatively small since $\hat{t} = (Ra/Pr)^{1/2}\, t$. Hence, as the Rayleigh number increased, t, in turn, decreased in proportion to $Ra^{-1/2}$. The amount of CPU-time required to reach the steady-state condition was approximately three hours or an average of 3.6 minutes (for approximately 80 iterations) per time step. However, when the multicellular flow instability set in at $\hat{G} = 5.2$, the steady-state condition could no longer be achieved. In order to obtain an efficient and time-accurate response of the unsteady flow field, five different time steps were considered: $\Delta t = .1, .25, .5, 1.0$ and 2.0. The first four time steps provided time-responses of the stream function at $r = .5/\psi = 90°$ to within 1 percent error of each other. Also, all four of these time steps were able to resolve the small but sudden variations of the stream function with time. For $\Delta\hat{t} = 2.0$, a notable difference in the time-response was observed. That is, the small sudden variations of the stream function with time could no longer be resolved. Values of the stream function were in error by approximately 4-5 percent when compared to those corresponding to $\Delta\hat{t} = .10$. These differences are most likely due to increased time truncation error when using $\Delta\hat{t} = 2.0$. In addition, for $\Delta\hat{t} = 2.0$, the number of iterations required for

convergence at a particular time level was disproportionately larger when compared to that for $\Delta\hat{t} = 1.0$. For example, an increase in $\hat{t}$ from 35.0 to 36.0 ($\Delta\hat{t} = 1.0$) took approximately 550 iterations, whereas an increase in $\hat{t}$ from 35.0 to 37.0 ($\Delta\hat{t} = 2.0$) required about 1375 iterations for convergence. This was probably due to a slight loss in numerical stability as a result of a decrease in the C_0 coefficient (see Eq. 5.10b) when $\Delta\hat{t}$ increases from 1.0 to 2.0.

Thus, due to computational time and accuracy considerations, the time step of 1.0 was chosen to numerically predict the time-response of the multicellular flow at $\hat{G} = 5.2$. Therefore, for values of $\hat{G}$ slightly greater than 5.2, a time step of 1.0 or less should be employed.

For $\Delta\hat{t} = 1.0$, the average CPU-time per time step amounted to 12-14 minutes (for approximately 300 iterations) with $\hat{G} = 5.2$ and a half-annular mesh of 31 x 102 nodes. The number of nodes in the angular direction was based on the maximum possible to properly capture cellular development while considering computer power and time limitations. In Section 6.2, a grid study for four different size meshes showed that the 31 x 102 node mesh was fine enough to resolve the same number of initial cells (seven) as the finer mesh of 41 x 132. In further support of using the 31 x 102 mesh, Lee and Korpela (1983) indicated that 10 grid points per cell were adequate for properly resolving cellular development in multicellular natural convective flow between long and narrow vertical slots. Therefore, since the instability at $\hat{G} = 5.2$ resulted in 7-8 cells per half-annulus, 102 nodes in the angular direction satisfied their particular recommendation for

avoiding significant resolution problems.

The use of symmetry boundary conditions with regard to unsteady cellular behavior in the half-annulus can be supported by the nature of the cellular activity that occurred. The strongest cellular behavior took place near the 90°-point vertical section of the annulus, whereas near ψ = 0° and ψ = 180°, the flow field remained quiet and undisturbed, preserving the end portions of the familiar steady-state kidney-shaped flow pattern. In support of this claim, the analytical steady-state result derived in Chapter 4 (for the Pr → 0 limit) demonstrated that the steady-state solutions were completely symmetric about ψ = 0 and 180°. Moreover, the cellular development in the vertical section of the half-annulus was not counter-rotating, hence the fluid was retained within the outer kidney-shaped streamline. This tends to indicate that the cellular flow in each half-annulus develops simultaneously and independently of each other. Also, when negative ψ is substituted into the Pr → 0 governing equations, the original form of the equations is maintained--again implying symmetry about ψ = 0 and 180°.

However, in order to properly verify this salient symmetry assumption, the symmetry conditions were relaxed and the flow in the complete annular gap was determined. For the complete annulus (0 - 2π), a 31 x 202 mesh was used and the initial time-response behavior of the unsteady cellular motion was obtained with $\Delta\hat{t}$ = 1.0. The initial conditions used to start the run were provided by the half-annular 7-cell solution at $\hat{t}$ = 35.0 (a mirror-image of this solution was used

to incorporate the whole annulus). The initial time-response behavior (the first 832 time steps corresponding to one cycle) of the 0 - 2π run reproduced that of the 0 - π run within one percent error (see Figure 6.14). The important changes of the cellular pattern with time were also duplicated. For the complete annulus, the average CPU-time per time step was about 26 minutes (for approximately 400 iterations).

Based on this single test case and preceding relevant supportive discussion, the half-annular symmetry assumption was used throughout this research to predict the unsteady cellular behavior associated with the vertical portions of a narrow annulus (for $Pr \to 0$). Proceeding with this symmetry assumption substantially reduced the CPU-time necessary for a converged solution, thus rendering the problem at hand feasible to study on the Perkin-Elmer 3242 computer system.

The numerical handling of the finite-Prandtl number boundary-layer equations was very similar to that previously described for the $Pr \to 0$ equations. These equations were also solved assuming symmetry using a half-annular mesh of 31 x 102 nodes with $\Delta\tilde{t} = 1.0$. The finite-Prandtl number equations were usually solved numerically to determine the transitional values of $\tilde{G}$, for various low-Prandtl number fluids, corresponding to the onset of multicellular instability. These equations were not used to study any type of unsteady behavior relating to a finite-Prandtl number hydrodynamic instability.

Upon solving the equations, it was noticed that as Prandtl number increased, so did the computation time necessary to reach convergence

at a particular time level. This was because the governing equations were nondimensionalized with respect to momentum diffusivity as opposed to thermal diffusivity, thus allowing the energy equation to become diffusion dominated for small Prandtl numbers. To reverse this situation, the governing equations must be recast to allow the vorticity equation to become diffusion dominated as Prandtl number increases.

Lastly, it should be noted that for both the 2-D Navier-Stokes and finite-Prandtl number boundary-layer equations, another important measure of numerical accuracy can be determined for the steady-state cases. That is, the average inner Nusselt number ($\overline{Nu}_i$) should equal the average outer Nusselt number ($\overline{Nu}_0$) at steady-state. For all of the steady-state test results, the equality was in error by less than .1 percent. For the pretransitional results of the 2-D Navier-Stokes equations, $\overline{Nu}_0$ was slightly less than $\overline{Nu}_i$. However, for the multicellular flows, $\overline{Nu}_0$ was slightly greater than $\overline{Nu}_i$.

6. RESULTS AND DISCUSSION

This chapter consists of two sections. The first essentially describes the hysteresis behavior associated with steady multicellular flow occurring in narrow gaps for air. This type of multicellular flow apparently originates because of thermal instability, and develops near the top portion of a narrow horizontal annulus.

The second section mainly describes an unsteady multicellular flow that develops near the vertical portions of a narrow horizontal annulus for small-Prandtl number fluids. This particular type of instability appears to be hydrodynamic in origin.

Wherever possible, results pertinent to this study will be compared to related analytical, numerical and/or experimental work.

6.1. Thermal Instability

6.1.1. Hysteresis behavior

As described in Chapter 5, the complete annular flow field ($0 - 2\pi$) was determined numerically when searching for hysteresis behavior. A 31 x 102 mesh was employed with the grid points concentrated near the top horizontal portion of the annulus - where the multicellular flow field tended to develop for air.

The average Nusselt number and shear-stress results are presented in Figures 6.1a, 6.1b and 6.2, respectively, for a gap number $G = .200$ and $Pr = .706$ (note that these average dimensionless parameters are defined in Appendix D). The transition of the flow field from two

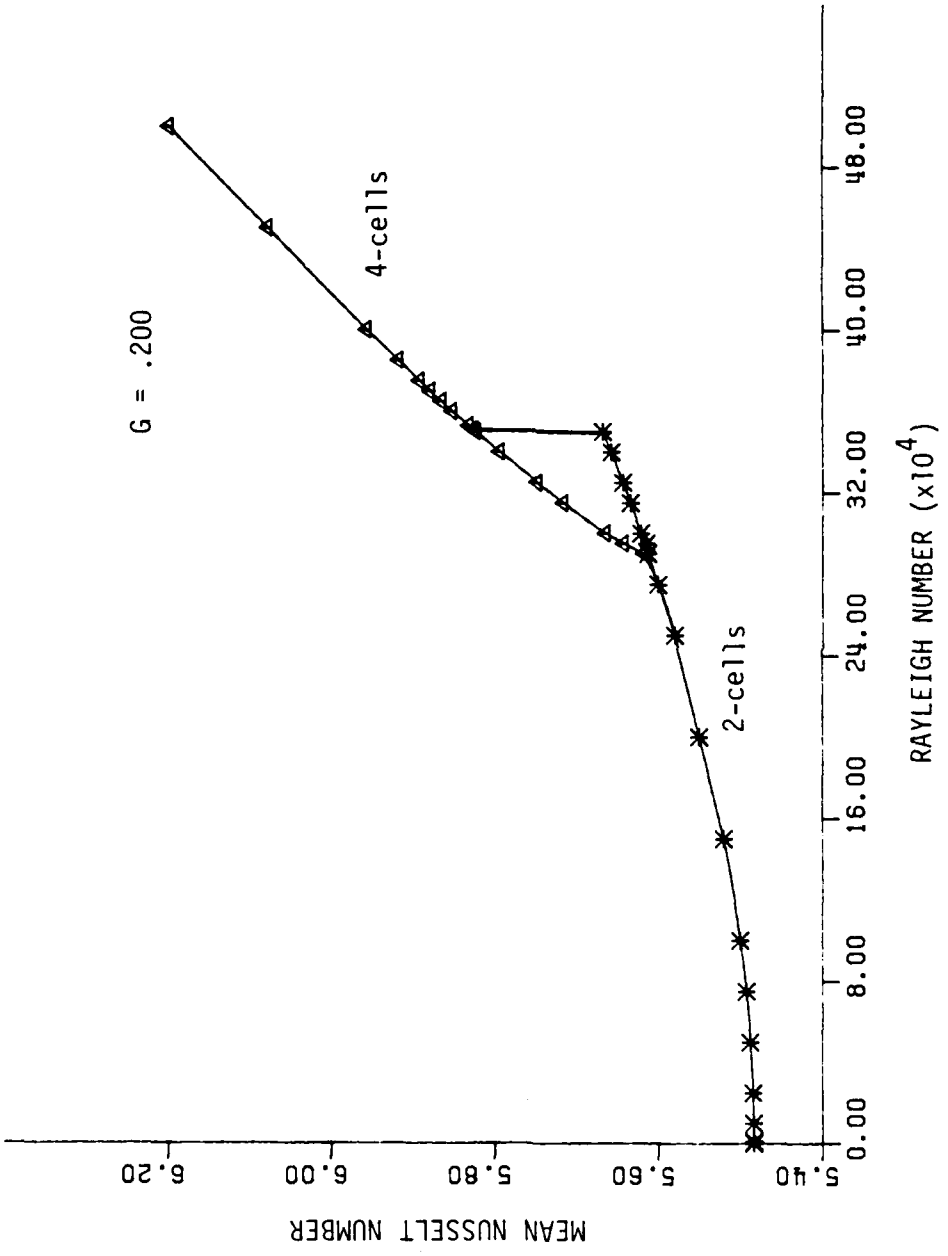

Figure 6.1a. Hysteresis behavior of the mean Nusselt number variation with Rayleigh number for G = .200 and Pr = .706 (Ra_{TR} = 351,000 and Nu_{COND} = 5.4836)

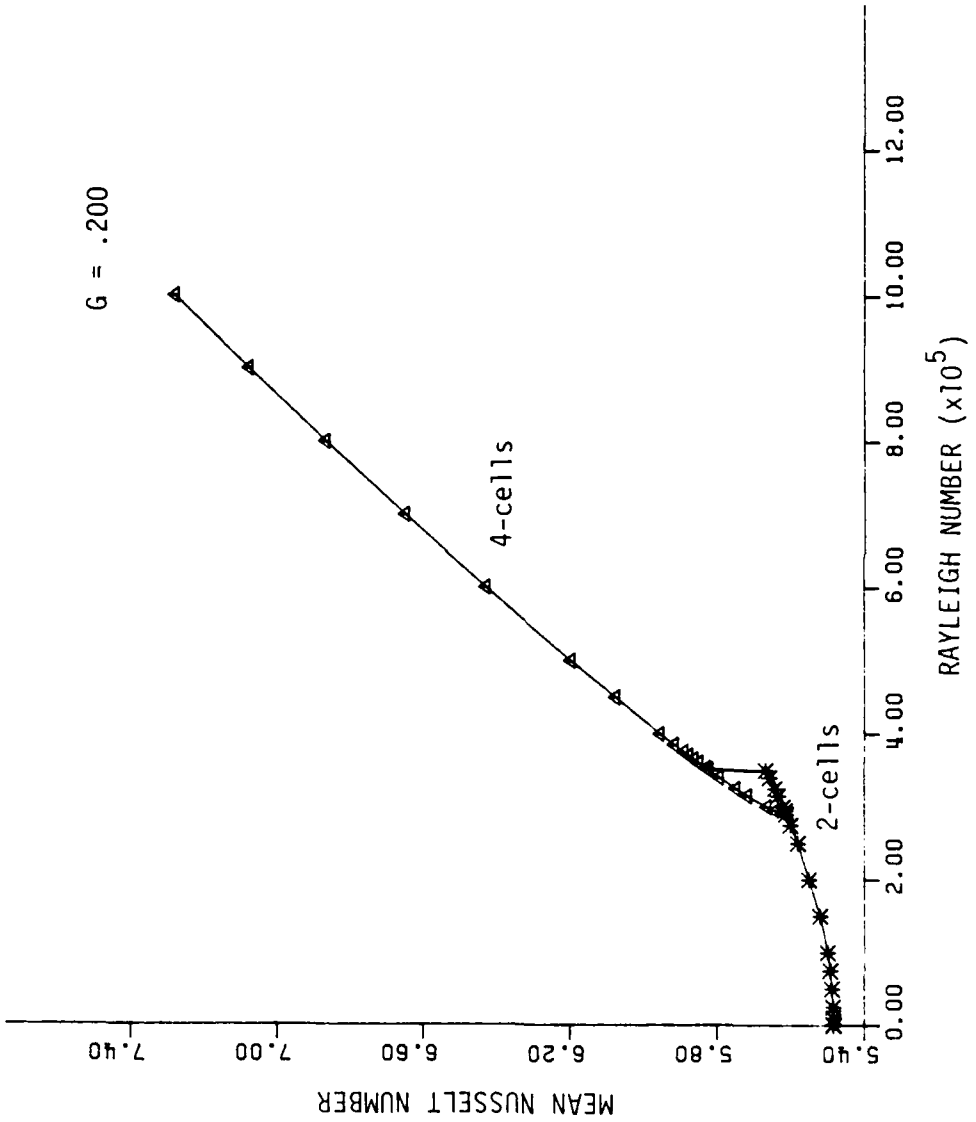

Figure 6.1b. Hysteresis loop of Figure 6.1a with an extended Rayleigh number variation

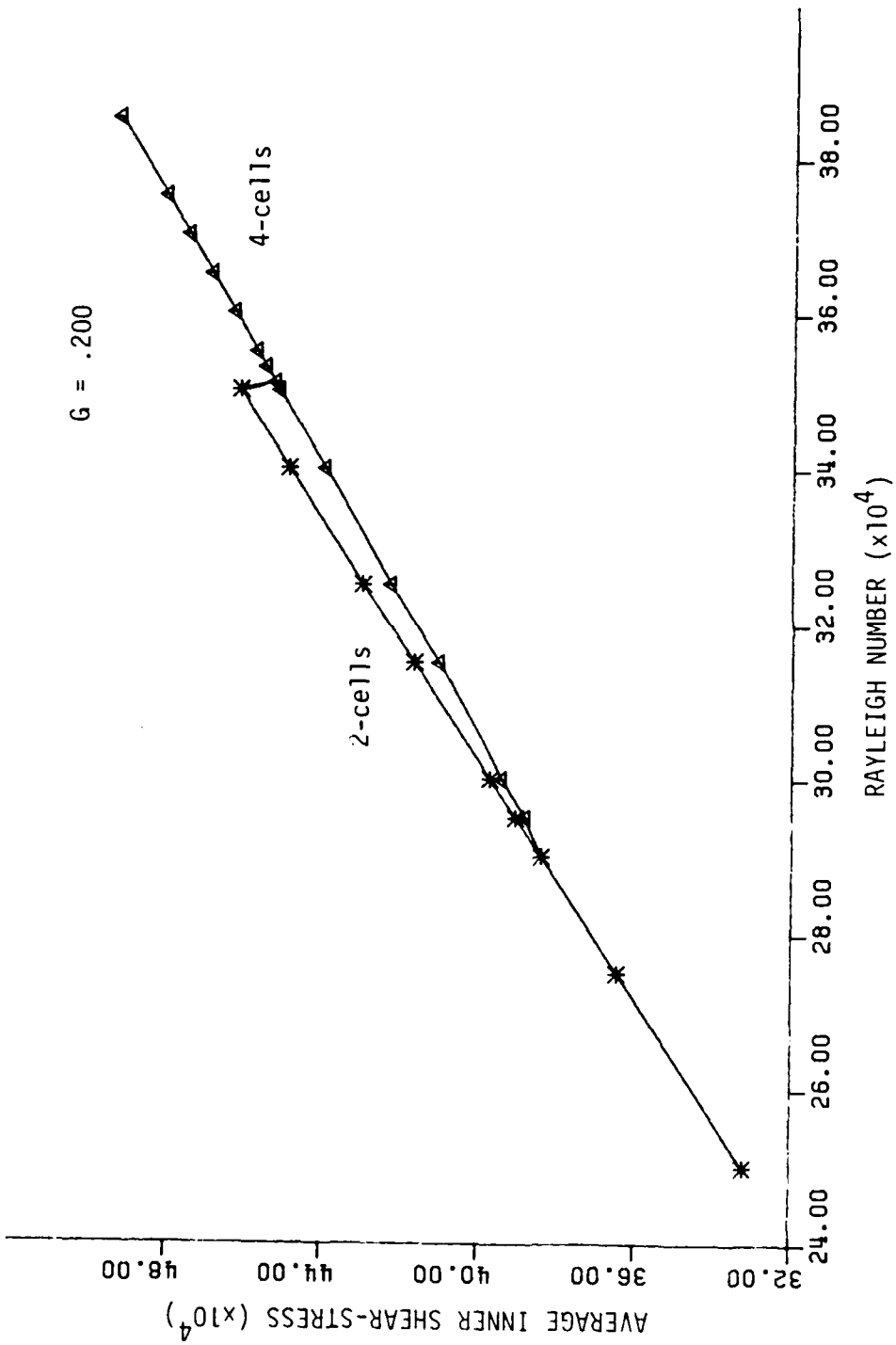

Figure 6.2. Hysteresis behavior of the average inner shear-stress variation with Rayleigh number for G = .200 and Pr = .706

to four cells occurred abruptly at a Rayleigh number of approximately 351,000 (or Ra_{b-a} = 2808). Associated with this transition was a sudden rise in the average Nusselt number (see Figure 6.1a) due mainly to more efficient fluid mixing created by the counter-rotating secondary cellular motion. This is analogous to the increase in heat transfer experienced when a flow makes the transition from laminar to turbulent fluid motion. Note that the above four-cell transition does not indicate the onset of turbulence, but rather signifies a more complex laminar multicellular flow condition. Also, because of the two smaller counter-rotating cells initiated near the top of the annulus, the local shear-stress in this region reversed its sign. Hence, a sudden decrease in the average inner shear-stress (for the half-annulus) occurred at the transition from two to four cells (see Figure 6.2). This particular phenomena bears resemblance to a similar occurrence in the Taylor-Instability problem of Coles (1965), for fluid flow between vertical concentric narrow rotating cylinders. In this problem, a hysteresis effect of the torque on the inner cylinder (which is directly proportional to shear-stress) was observed by Eagles (1974). He showed that at a certain Taylor number, the Taylor-vortex flow would change to a wavy-vortex flow; and associated with this change was a sudden lowering of the inner cylinder torque (as also discussed in Stuart, 1960), although the Taylor number had actually increased in magnitude.

Both the Nusselt number and the shear-stress data exhibited a hysteresis behavior as the Rayleigh number was gradually increased

and then decreased past the transition point. For Ra > 350,000, only a four-cell solution prevailed, while for Ra < 285,000, only a two-cell solution prevailed. However, between these two limits, both types of solutions were possible, thus forming a hysteresis loop. The numerical approach used to determine the transitional Rayleigh numbers and related hysteresis behavior was described in detail in Chapter 5.

Powe et al. (1971) numerically estimated a transitional Rayleigh number of 452,000 for G = .200 based upon the point at which the stream function changed its sign. However, they could not fully resolve the smaller counter-rotating cell with their particular method (see Chapter 2). They used a uniform increment mesh with 35 angular and 15 radial nodes for the half-annulus. The fact that they used a relatively coarse mesh in the angular direction may have caused resolution problems which delayed their transitional Rayleigh number to a value approximately 30 percent higher than the 351,000 value predicted in this study. A similar four-cellular flow pattern was experimentally observed by Bishop et al. (1964) in a concentric spherical geometry. For G = .19, they obtained a transitional Rayleigh number (based on gap width) of about 3600, which corresponds to approximately Ra = 525,000.

These earlier results agree with the present work in that a four-cell pattern predominates immediately after the thermal instability sets in for G = .200.

To improve the numerical prediction of the corresponding transitional Rayleigh number, grid nodes should be concentrated in the

thermal plume region where the smaller counter-rotating cells develop, as was properly done in this study (see Section 5.2.4 and Appendix E for further discussion).

Streamline plots of the cellular flow field development for G = .200 are depicted in Figures 6.3a-6.3c. Figure 6.3a corresponds to a pretransitional result, Ra = 350,000, and demonstrates the usual kidney-shaped flow pattern. Figure 6.3b shows the initial development of the two smaller counter-rotating cells for Ra = 351,000. Figure 6.3c depicts the secondary flow in a much stronger state beyond transition, at Ra = 900,000. A typical multicellular temperature profile is also given in Figure 6.3d for Ra = 900,000. The shape of the isotherms was responsive to the fluid motion for Pr = .706, resulting in an inverted thermal plume near the top portion of the annulus. In Figures 6.3a-d, the diameter ratio is shown as 1.5 times its actual size for ease of viewing.

Similarly, for G = .100, an abrupt rise in heat transfer occurred as the flow field made the transition from two to six cells at Ra_{TR} = 2,841,000 (or Ra_{b-a} = 2841), as shown in Figure 6.4. The hysteresis loop for this case expanded from Ra = 2,570,000 to Ra = 2,840,000, a change of approximately 270,000. Below this range, only the two-cell solution prevailed, while above this range, only the six-cell solution prevailed. For G = .200, the Rayleigh number change in the hysteresis loop amounted to approximately 65,000, considerably smaller than for G = .100. Furthermore, the rise in the average Nusselt number associated with the G = .200 multicellular transition was greater

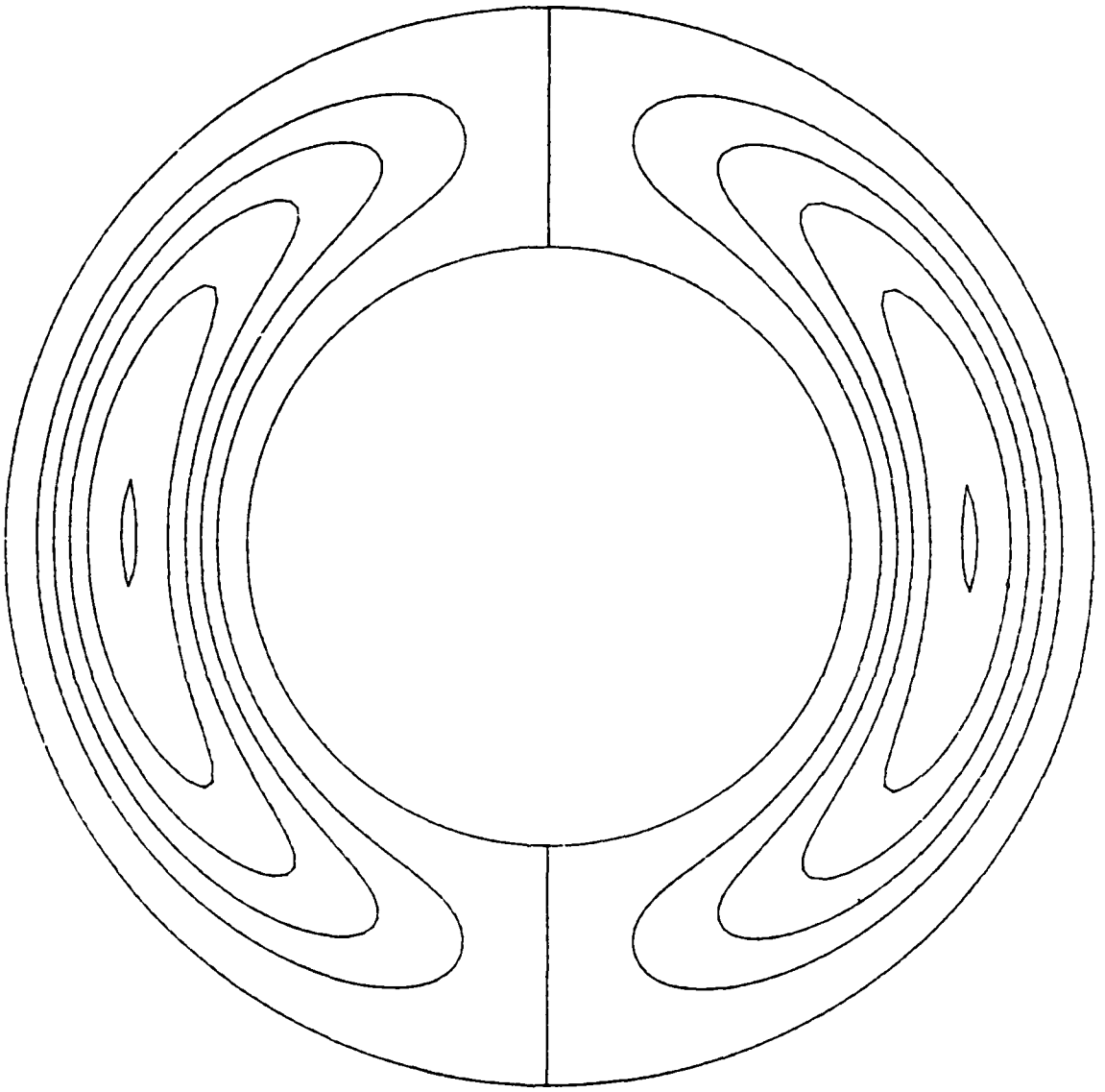

Figure 6.3a. Streamlines of a two-cellular flow field at Ra = 350,000 for G = .200 and Pr = .706 (diameter ratio shown as 1.5 times actual size)

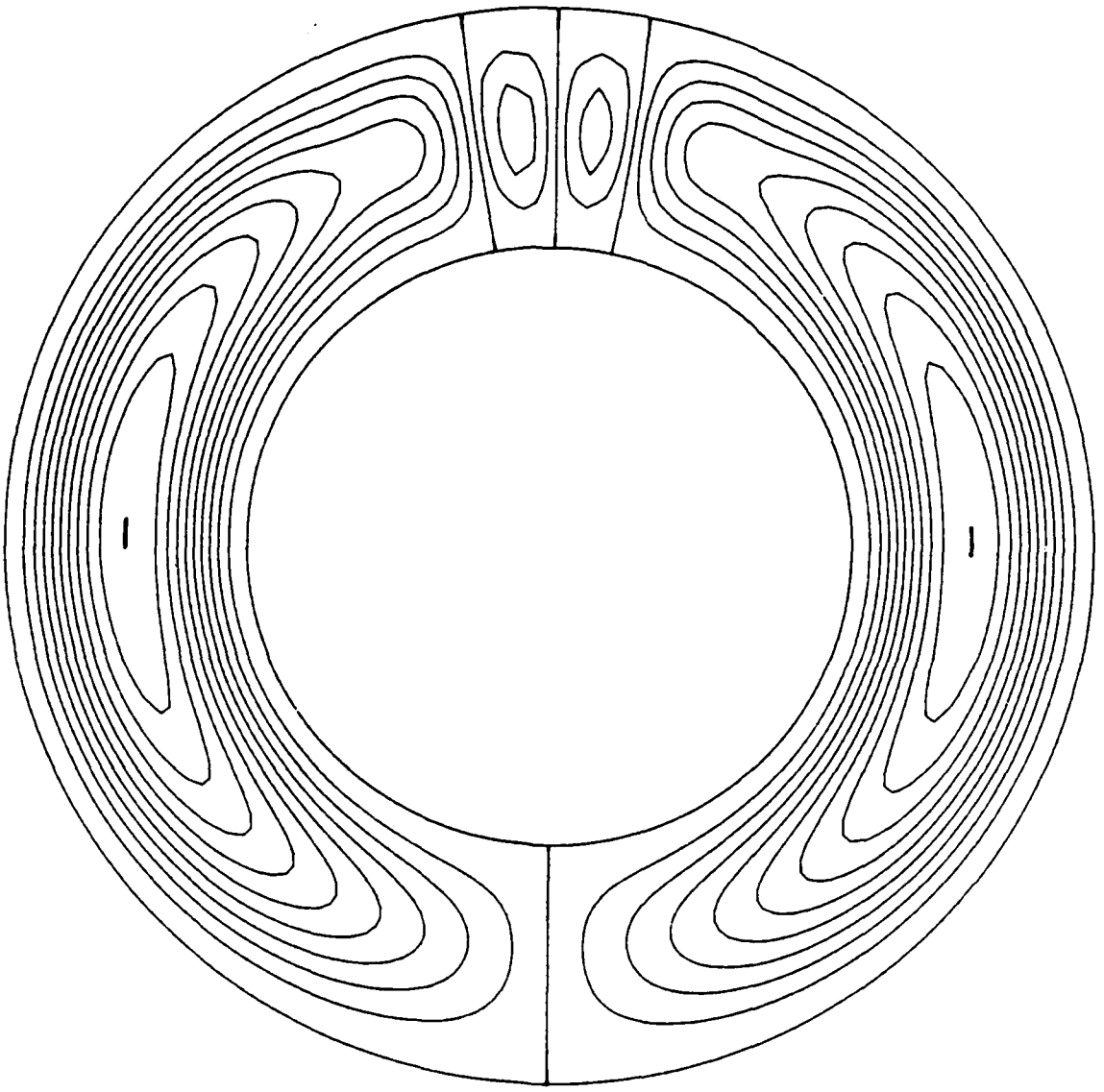

Figure 6.3b. Streamlines of an initial four-cellular flow field at Ra = 351,000 for G = .200 and Pr = .706 (diameter ratio shown as 1.5 times actual size)

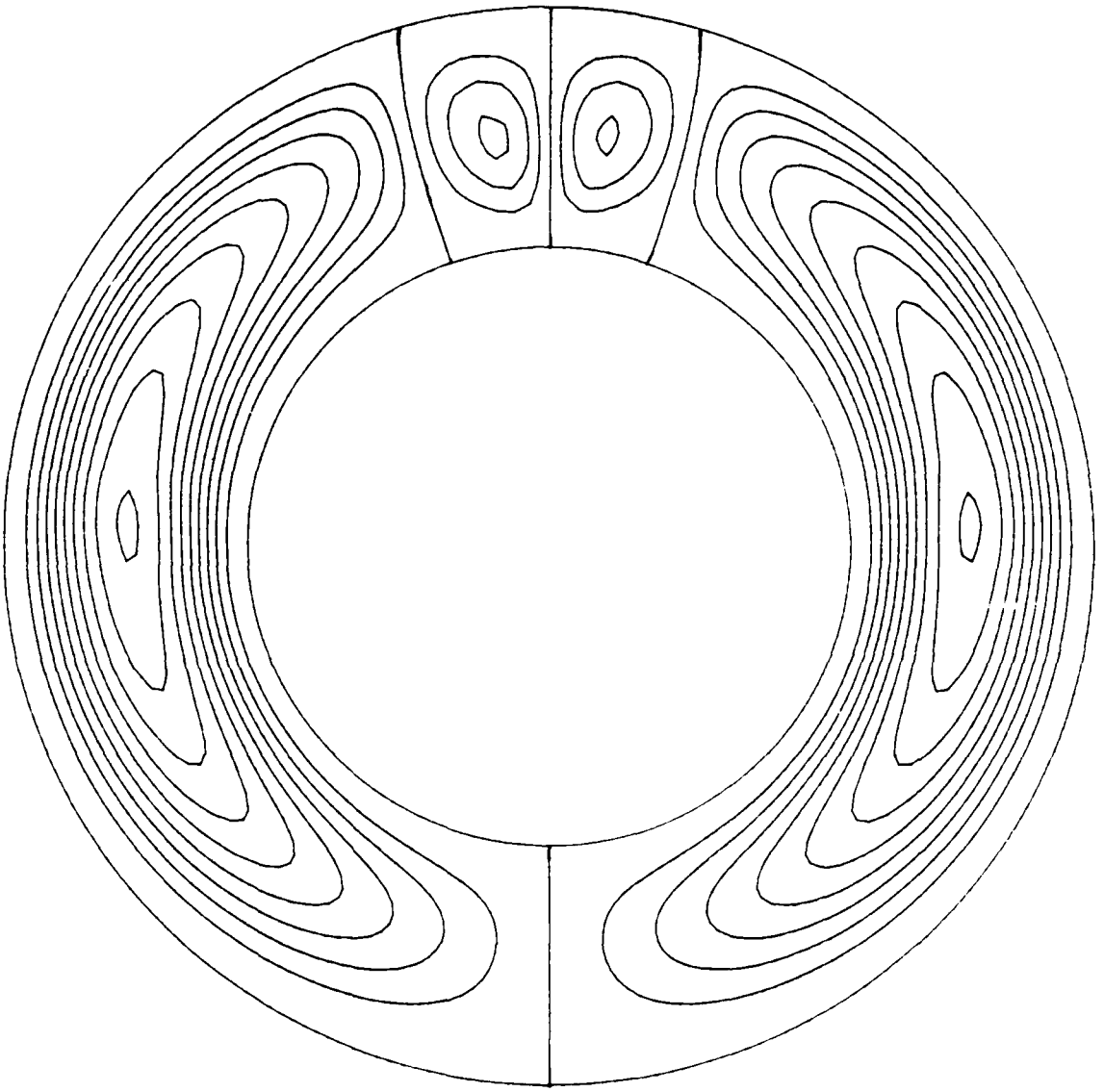

Figure 6.3c. Streamlines of a more developed four-cellular flow field at Ra = 900,000 for G = .200 and Pr = .706 (diameter ratio shown as 1.5 times actual size)

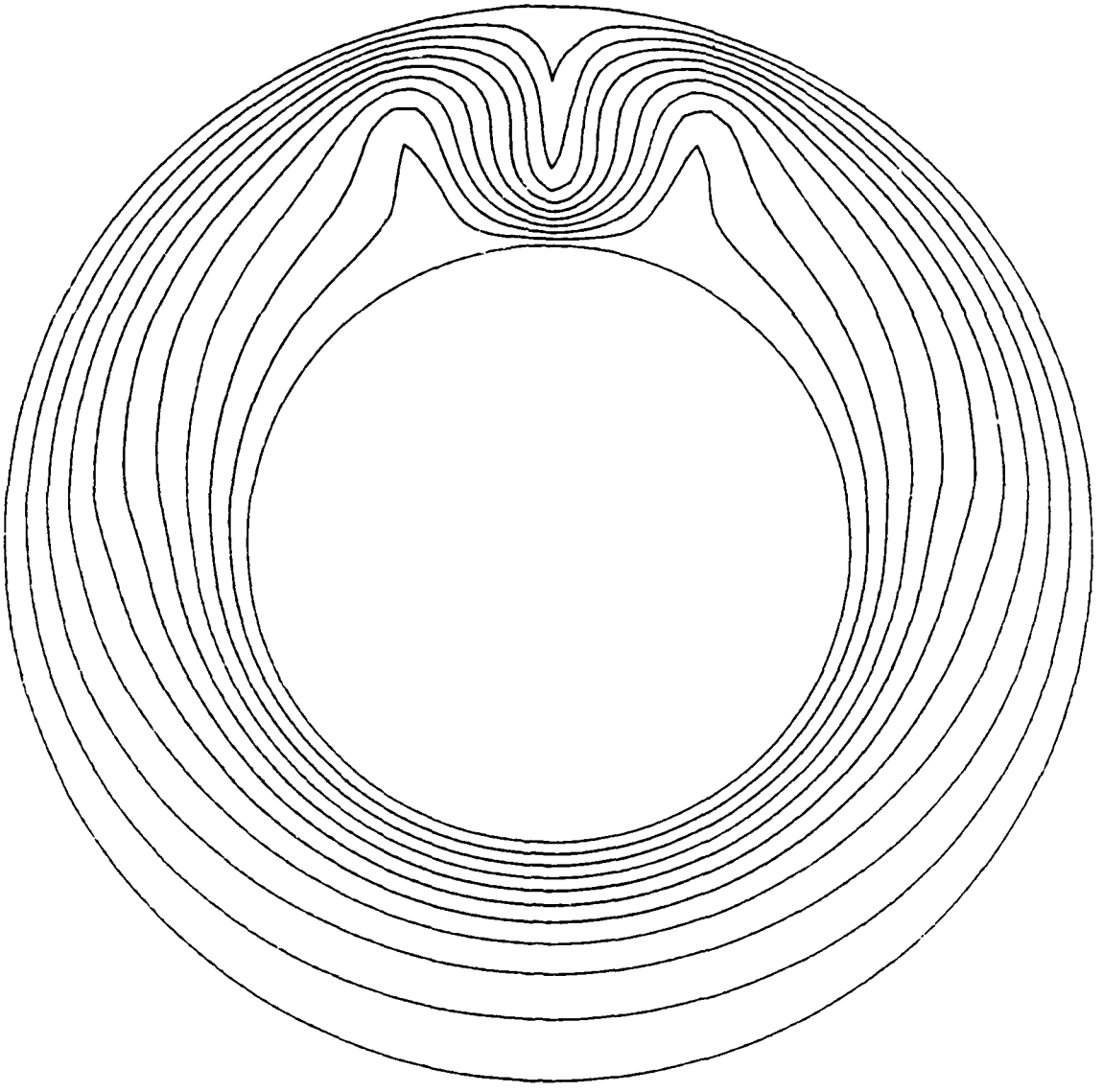

Figure 6.3d. Isotherms of a more developed four-cellular flow field at Ra = 900,000 for G = .200 and Pr = .706 (diameter ratio shown as 1.5 times actual size)

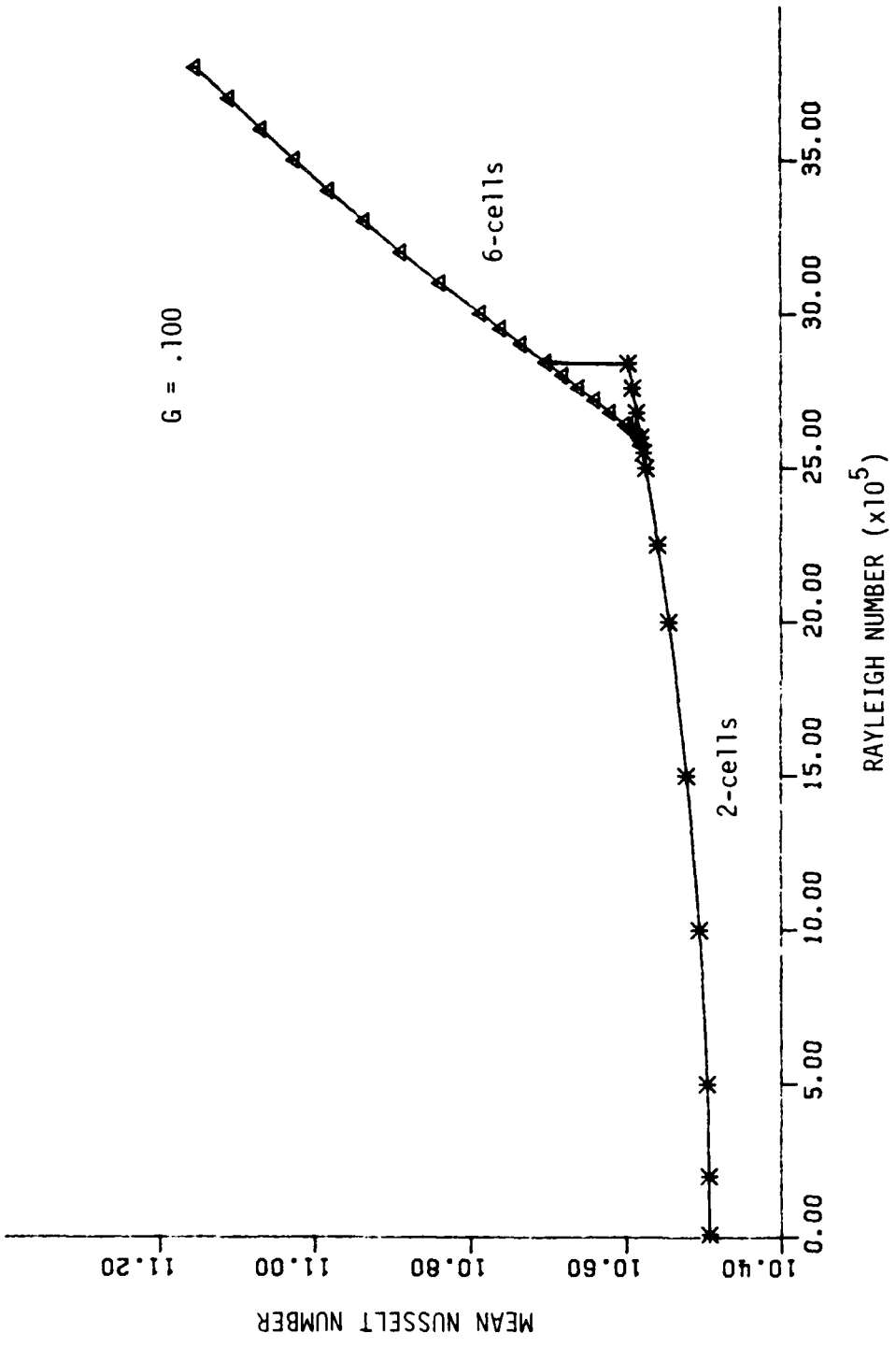

Figure 6.4. Hysteresis behavior of the mean Nusselt number variation with Rayleigh number for G = .100 and Pr = .706 (Ra_{TR} = 2,841,000 and Nu_{COND} = 10.4921)

than for G = .100 by an amount of approximately .052, or about a 50 percent increase.

The above occurrences may be explained as follows. As the gap decreases in size, both the viscous effects and the restraining influence of the geometry become more significant for a given value of Rayleigh number, thus suppressing natural convective fluid motion within the annulus. This has several ramifications. First, because of the fluid motion hindrance, a higher transitional Rayleigh number is needed to trigger the instability for G = .100, compared to that for G = .200. Secondly, once the multicellular instability results, related hysteresis effects persist longer for G = .100 due to suppressed fluid motion changes. Hence, a greater Rayleigh number range for the hysteresis loop of this gap occurs. Thirdly, suppressed convective effects for G = .100 may also cause a less pronounced rise in the average Nusselt number associated with multicellular transition, compared to that for G = .200. Lastly, as the gap decreases, curvature effects diminish, resulting in a better comparison to the Bénard type of instability between horizontal parallel flat plates. This, coupled with increased viscous effects, may cause the number of cells occurring at transition to increase, i.e., a two to six cell transition for G = .100 as opposed to the two to four cell transition with G = .200.

The results of this study seem to indicate that for $G \leq .175 \pm .015$ an initial transition from two to six cells occurs, rather than the two to four cell transition for G = .200. This statement is supported by the numerical results of Rao et al. (1985), where they graphically

depicted a six-cell flow pattern at a Rayleigh number of approximately 750,000 for G = .175. However, they did not give the Rayleigh number corresponding to the point of transition for this particular gap size. In this study, for G = .175, a transition to six-cells took place at Ra = 450,000. A typical six-cell flow pattern with related isotherms, for G = .100 and Ra = 3,600,000, is depicted in Figures 6.5 and 6.6, respectively. Notice the upright thermal plume (Figure 6.6) associated with the six-cell flow field.

For G = .100, a hysteresis behavior was also present for the average inner shear-stress versus Rayleigh number. However, these results were not plotted since the related hysteresis loop was very slight and almost indistinguishable in a graphical sense--where only a .2 percent increase in the average inner shear-stress occurred at the point of multicellular transition for G = .100.

Figures 6.7 and 6.8 indicate the effect of multicellular flow on the angular variation of the inner Nusselt number and centerline stream function, respectively, with regard to G = .100 and G = .200. To understand these effects, cell rotation must be taken into consideration. For the half-annulus cellular pattern of G = .200, the smaller secondary cell rotates counter-clockwise and extends between 165° and 180° for Ra = 900,000 (see Figure 6.3c). This rotation is responsible for the development of an inverted thermal plume near the top portion of the annulus. For the cellular pattern of G = .100 at Ra = 3,600,000, two secondary cells are present in the half-annulus. One occurs between 170° and 180° and rotates clockwise, while the other occurs between

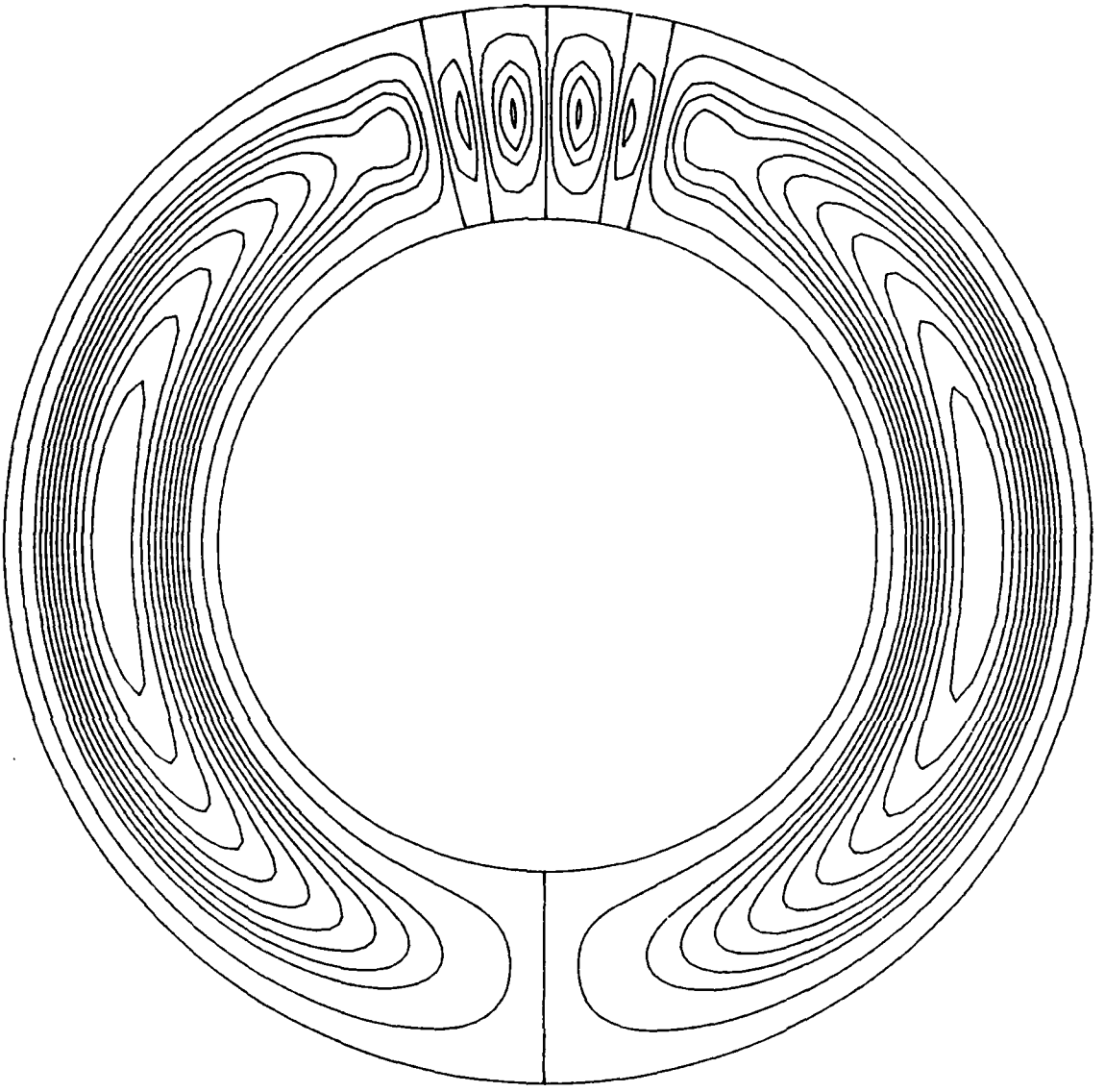

Figure 6.5. Streamlines of a six-cellular flow field at Ra = 3,600,000 for G = .100 and Pr = .706 (diameter ratio shown as 1.5 times actual size)

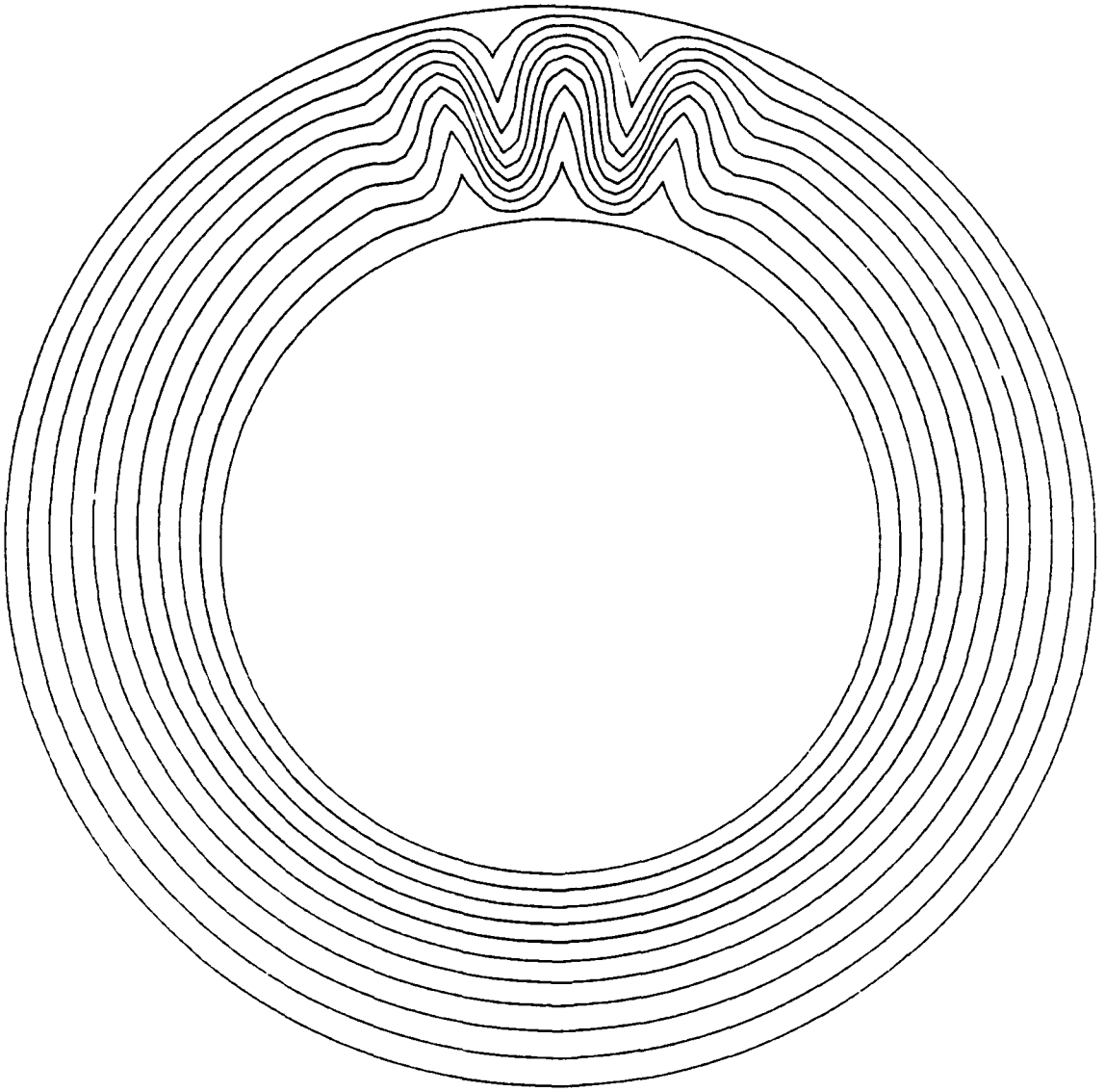

Figure 6.6. Isotherms of a six-cellular flow field at Ra = 3,600,000 for G = .100 and Pr = .706 (diameter ratio shown as 1.5 times actual size)

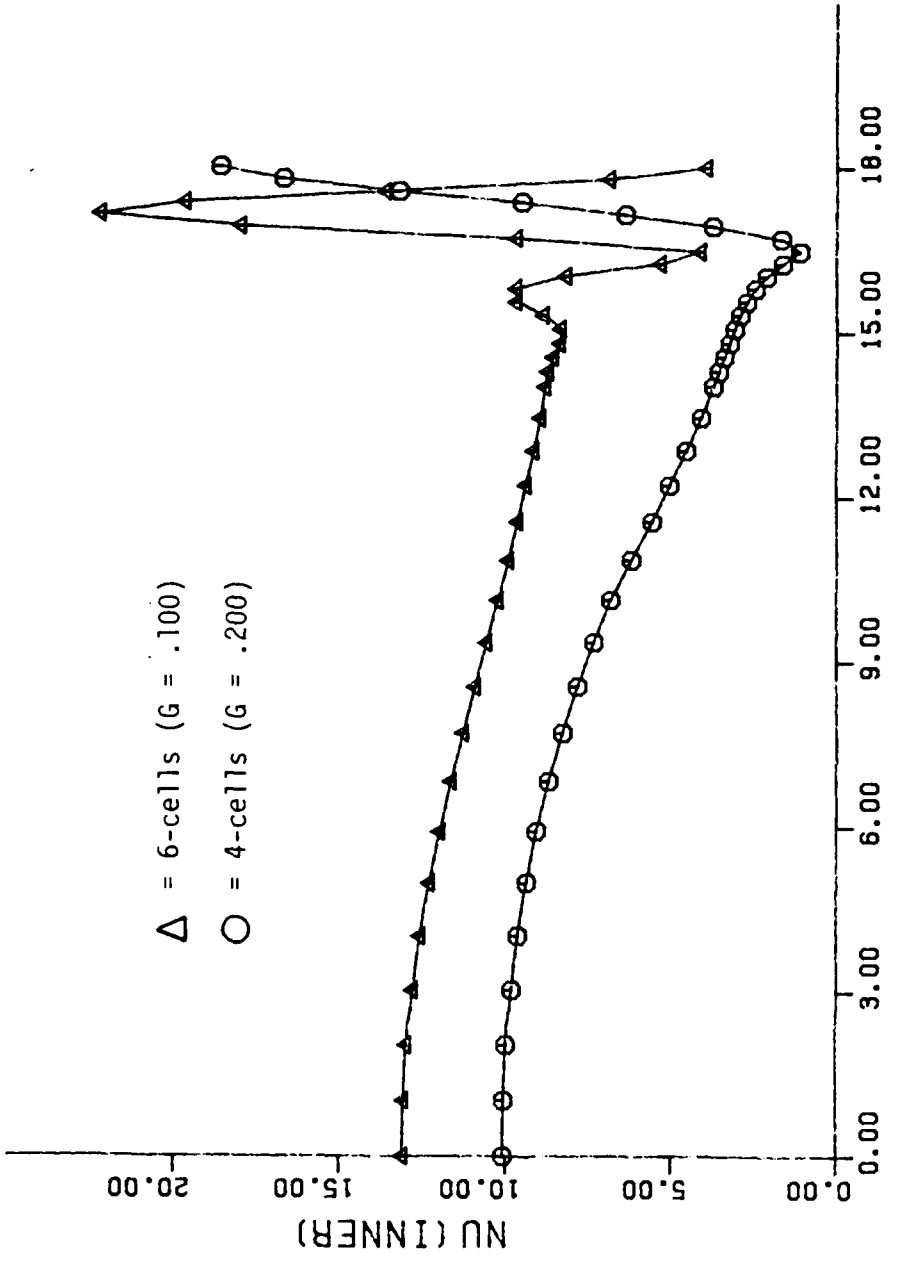

Figure 6.7. Angular variation of the inner (r=0) Nusselt number for G = .100 and .200 at Ra = 3,600,000 and 900,000, respectively

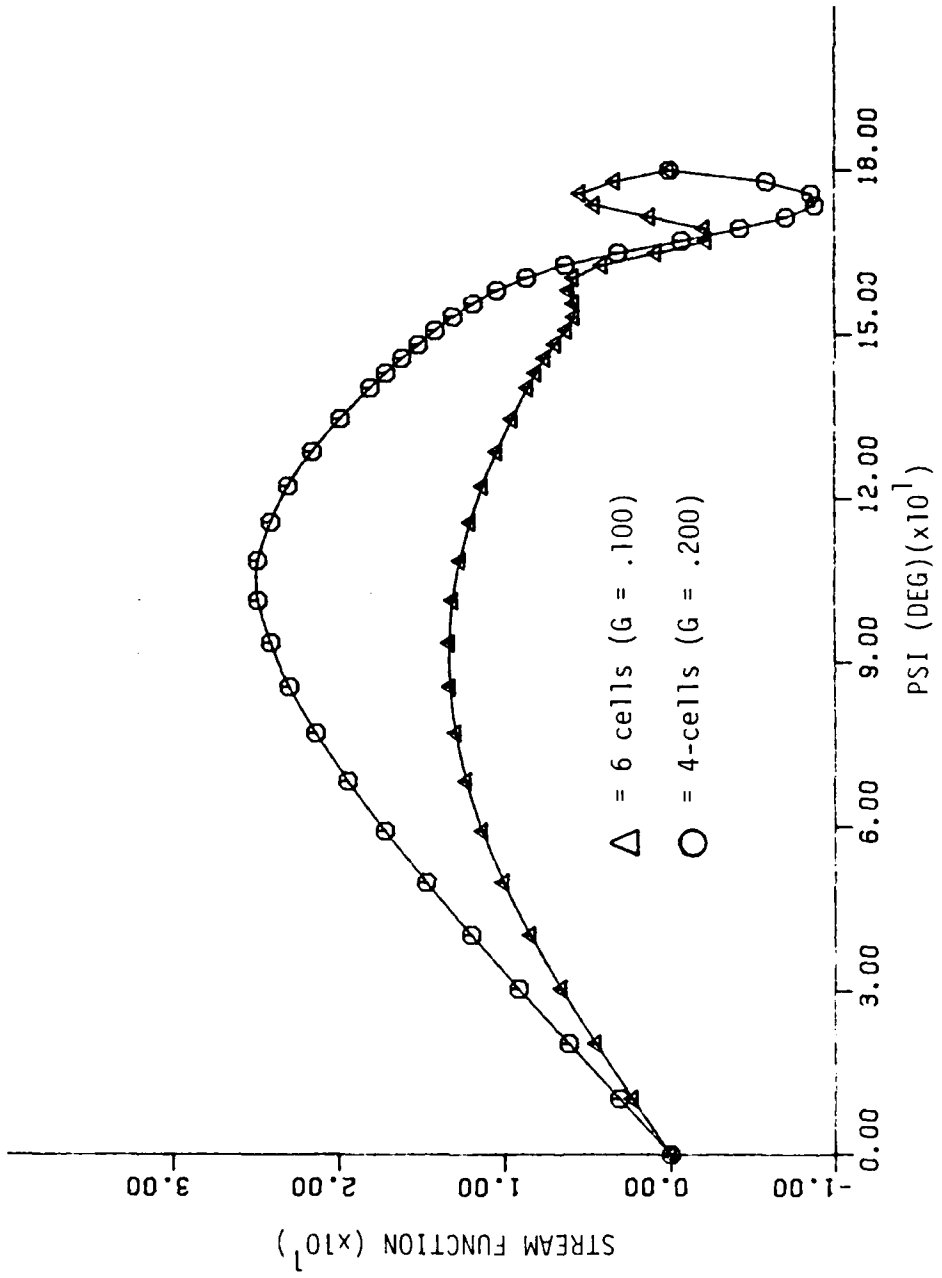

Figure 6.8. Angular variation of the center-line (r=.5) stream function for G = .100 and .200 at Ra = 3,600,000 and 900,000, respectively

165° and 170° and rotates counter-clockwise (see Figure 6.5).

Due to the inverted thermal plume for G = .200, Figure 6.7 shows a local maximum in heat transfer on the inner wall at ψ = 180° and a local minimum near ψ = 165°. In contrast, the six-cell flow pattern of G = .100 shows a local maximum in heat transfer near ψ = 170° due to the counter-clockwise rotating secondary cell, while a local minimum results at ψ = 180°. This minimum occurs because the clockwise rotating secondary cell causes an upright thermal plume near the top of the inner cylinder. Also, smaller local maximum and minimum in heat transfer result near ψ = 155° and 165°, respectively, due to the thermal response of the clockwise rotating primary cell (which bottle-necks) near ψ = 155° coupled with the counter-clockwise rotating secondary cell.

In a similar manner, the two types of multicellular flow also cause a departure of the unicellular sinusoidal-like stream function distribution between ψ = 150° and 180°. This departure is illustrated in Figure 6.8 for the four and six-cell flow patterns.

6.1.2. Analytical comparison

The analytical perturbation expressions derived in Chapter 4, from the finite-Prandtl number boundary-layer equations, were employed as convenient checks to the pretransitional results generated in the preceding numerical analysis.

The forthcoming comparison has a dual purpose: first, it is valuable in the sense that the amount of available data pertaining to local flow changes in the narrow-type gaps is extremely scarce for the

high Rayleigh number range; and second, a valid comparison will serve to support the numerical method used in this study, which in turn, supports the asymptotic analysis described in Chapter 4.

The three-term inner Nusselt number perturbation expression given in Eq. (4.54), together with the three-term expressions for vorticity and stream function given in Eq. (4.29), will be used to generate comparative data for the pretransitional 2-D Navier-Stokes numerical results. Comparisons for the inner (r = 0) Nusselt number, the inner-wall (r = 0) vorticity and the center-line (r = .5) stream function are provided in Figures 6.9-6.11, respectively.

Figure 6.9 depicts the angular variation of the inner Nusselt number using the analytical expression (4.54) with $\tilde{G} = 4.0$ and Pr = .706. It is worth noting that $\tilde{G} = 4.0$ does not correspond to a conduction-dominated flow (as with $\tilde{G} = 1.0$ or 2.0), but rather a flow subject to significant convective effects. Recalling that $\tilde{G} = Ra^{1/4}G$, four different combinations of G and Ra corresponding to $\tilde{G} = 4.0$ will be used as numerical comparisons to the analytical result. These combinations are G = .200 (Ra = 160,000), G = .150 (Ra = 505,680), G = .100 (Ra = 2,560,000) and G = .025 ($Ra = 6.554 \times 10^8$). Related results are also displayed in Figure 6.9.

The best comparison to the analytical result corresponded to G = .025. This was expected since the asymptotic analysis was tailored for the small-gap/high Rayleigh number flow regime. Therefore, the 2-D Navier-Stokes solutions do indeed converge toward the perturbation solutions as $G \to 0$. In the comparisons that follow, relative errors

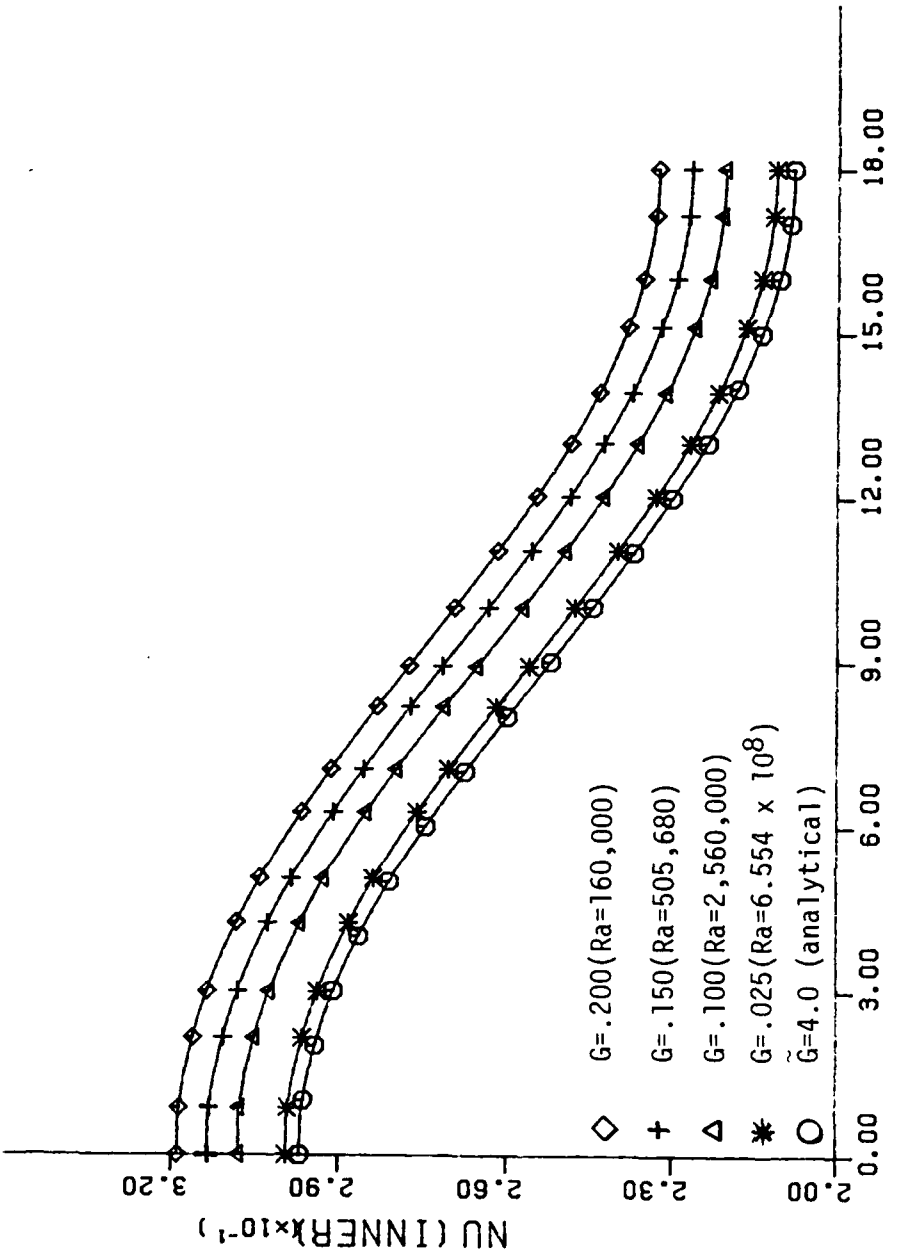

Figure 6.9. Angular variation of the inner (r=0) Nusselt number ($\div Ra^{1/4}$) for $\tilde{G} = G\,Ra^{1/4} = 4.0$ and Pr = .706: 2-D Navier-Stokes/analytical comparison

of the 2-D Navier-Stokes results with respect to the analytical results are calculated. For G = .025, a maximum error of 1.5 percent resulted near the top of the inner cylinder, ψ = 180°. The three larger size gaps also compared favorably. For G = .200, .150 and .100, maximum respective errors of 11.5, 8.5 and 6.0 percent occurred, also at ψ = 180°.

In Figure 6.10, a comparison similar to Figure 6.9 is presented. This new comparison regards the angular variation of the inner-wall vorticity for $\tilde{G}$ = 4.0 and Pr = .706. For G = .200, .100 and .025, maximum respective errors of 7.1, 3.5 and 1.0 percent resulted near ψ = 90°, or approximately the point of maximum fluid velocity.

Lastly, Figure 6.11 depicts the angular variation of the center-line stream function for $\tilde{G}$ = 4.0 and Pr = .706. This particular comparison was in very close agreement to the 2-D Navier-Stokes results, with maximum respective errors of 2.0, 1.5 and 1.0 percent for G = .200, .100 and .025.

Although the inner Nusselt number (which is proportional to the radial temperature gradient) is generally considered the least sensitive parameter of the three, it did not agree as closely as did the inner-wall vorticity and the center-line stream function comparisons. Most probably, this agreement would improve if more expansion terms are incorporated into the analytical expression for the inner Nusselt number. But overall, all three analytical comparisons agreed rather well with the 2-D Navier-Stokes results, hence supporting both the numerical and analytical work set forth in this thesis.

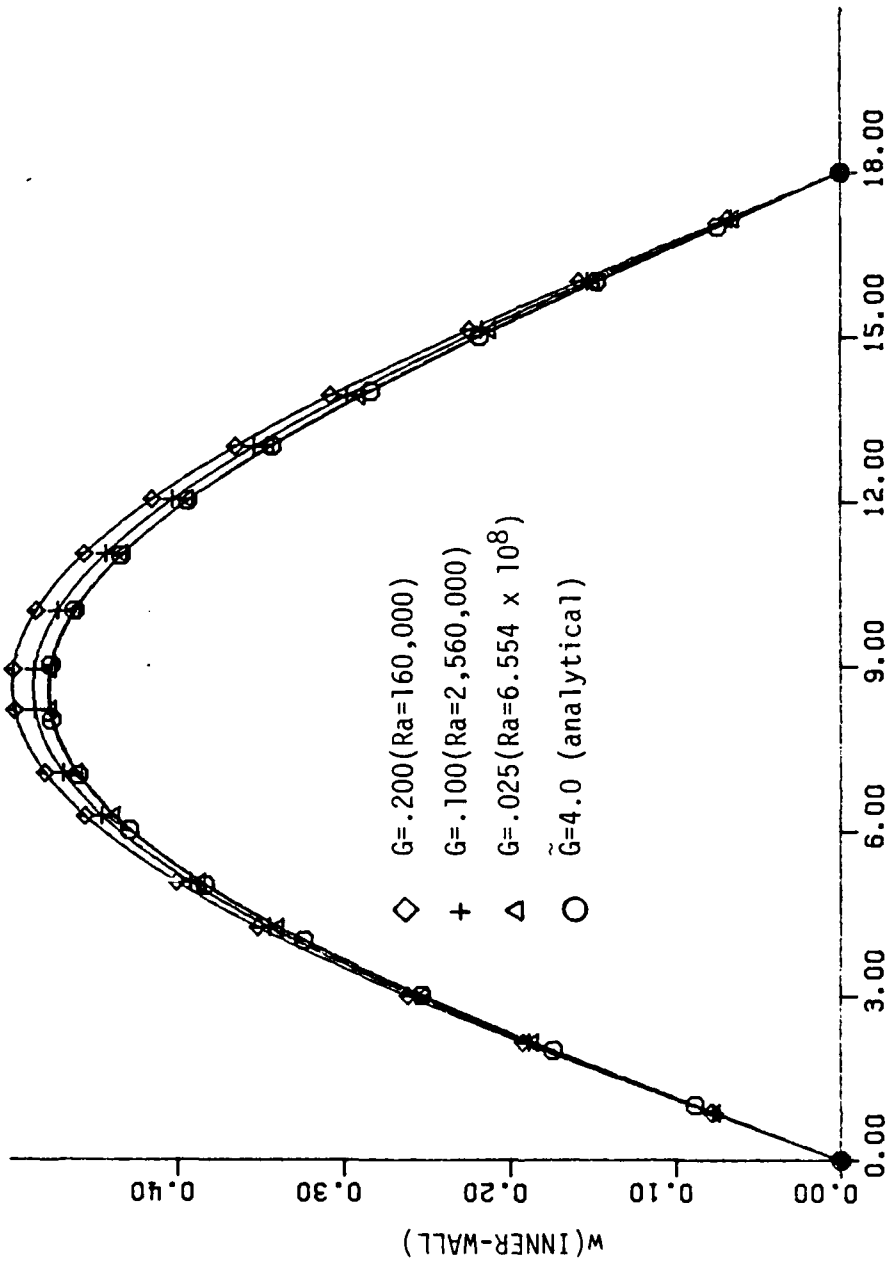

Figure 6.10. Angular variation of the inner-wall (r=0) vorticity ($\div Ra^{3/4}$) for $\tilde{G} = G\,Ra^{1/4} = 4.0$ and Pr = .706: 2-D Navier-Stokes/analytical comparison

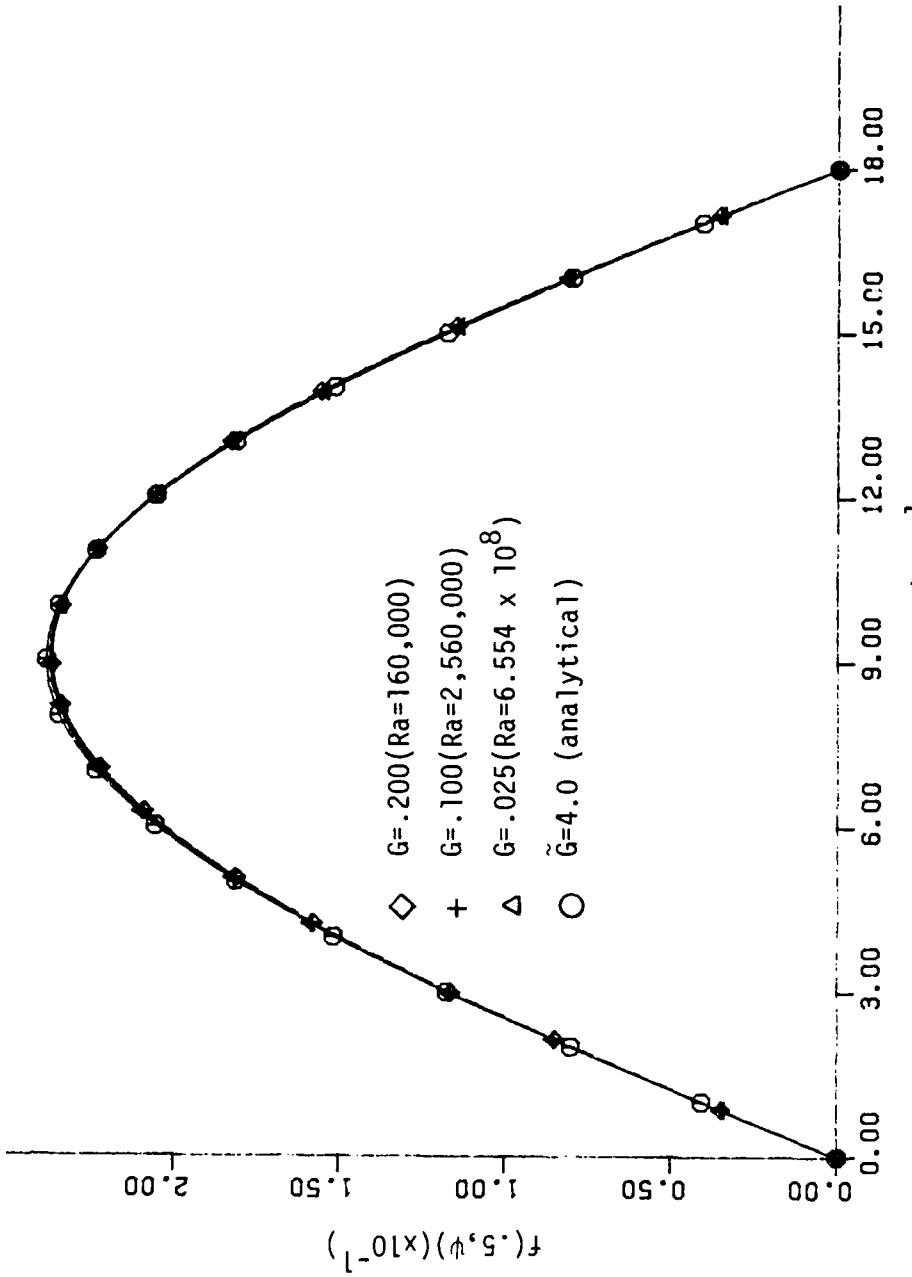

Figure 6.11. Angular variation of the center-line (r=.5) stream function ($\div Ra^{1/4}$) for $\tilde{G} = G\,Ra^{1/4} = 4.0$ and Pr = .706: 2-D Navier-Stokes/analytical comparison

In summary, the first three terms of the perturbation solution appear to be valid to within approximately 10 percent for the pretransitional cases of $G \leq .200$. Thus, quick and fairly accurate approximate solutions to the 2-D Navier-Stokes equations, in this particular range of narrow-gap widths, can be obtained from the analytical expressions derived in this study.

6.1.3. Small-gap number stability curves

As discussed in Chapter 4, previous investigators (Walton, 1980; Powe et al., 1971; Liu et al., 1962) speculated that as the narrow annular gap spacing approaches zero, a true Bénard-type instability would erupt, corresponding to a critical Rayleigh number (Ra_{b-a}) of approximately 1700. Instead, it appears from Figure 6.12 that the minimum transitional Rayleigh number approaches 2400 for G = .175. Beyond this point, the transitional Rayleigh number begins to increase substantially with decreasing gap number; where at G = .050, the thermal instability sets in at approximately $Ra_{b-a} = 4560$.

Directly related to the stability curve of Figure 6.12 is Figure 6.13, which was obtained from the relation $\tilde{G} = Ra^{1/4}G$. This new curve appears monotonic and seems to indicate that for very small gaps, the instability sets in at a near-constant value of $\tilde{G}$ equal to approximately 3.90.

All data points on the stability curve of Figure 6.12 were calculated assuming vertical symmetry for a half-annular mesh of 31 x 102 nodes, except for G = .100 and .200 where the complete annulus

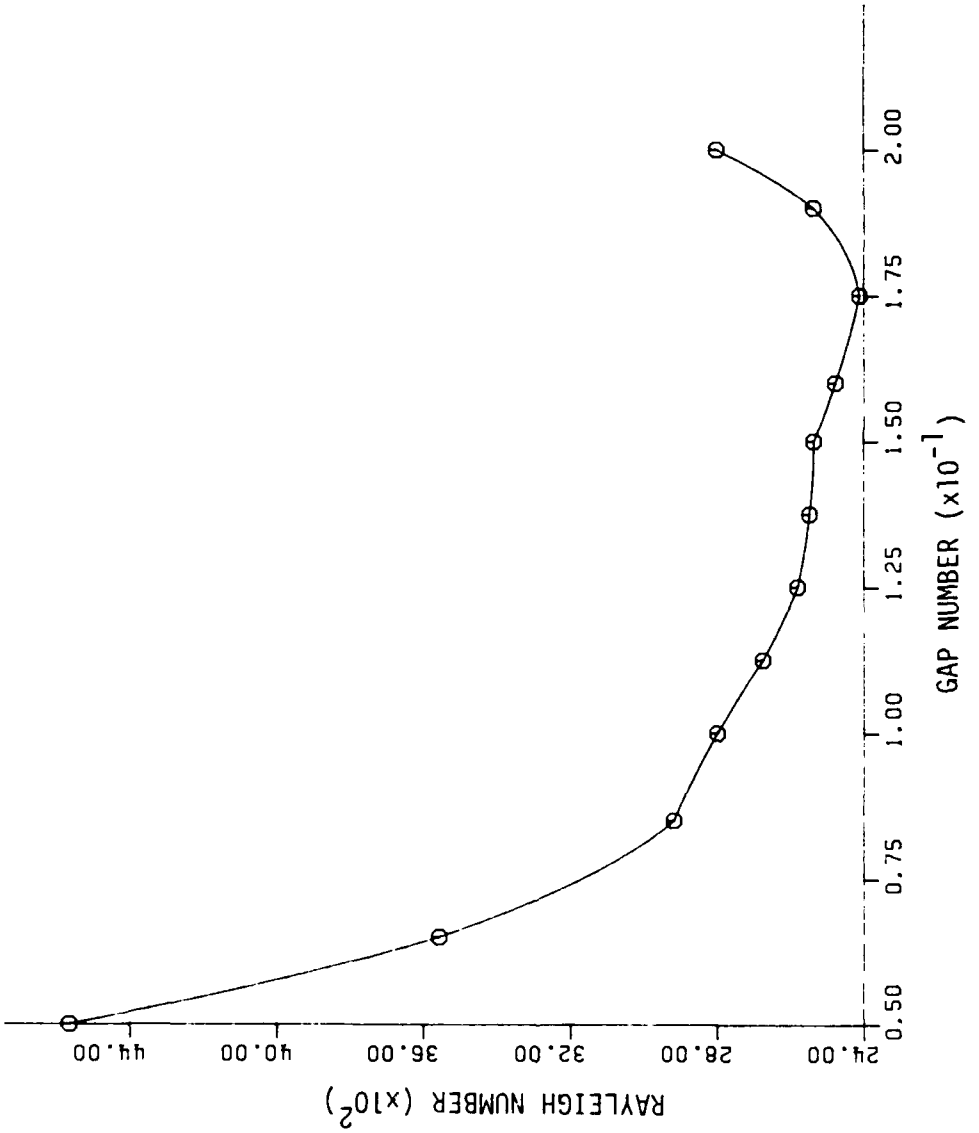

Figure 6.12. Transitional Rayleigh numbers (based on gap width, Ra_{b-a}) as a function of gap numbers (G) for Pr = .706

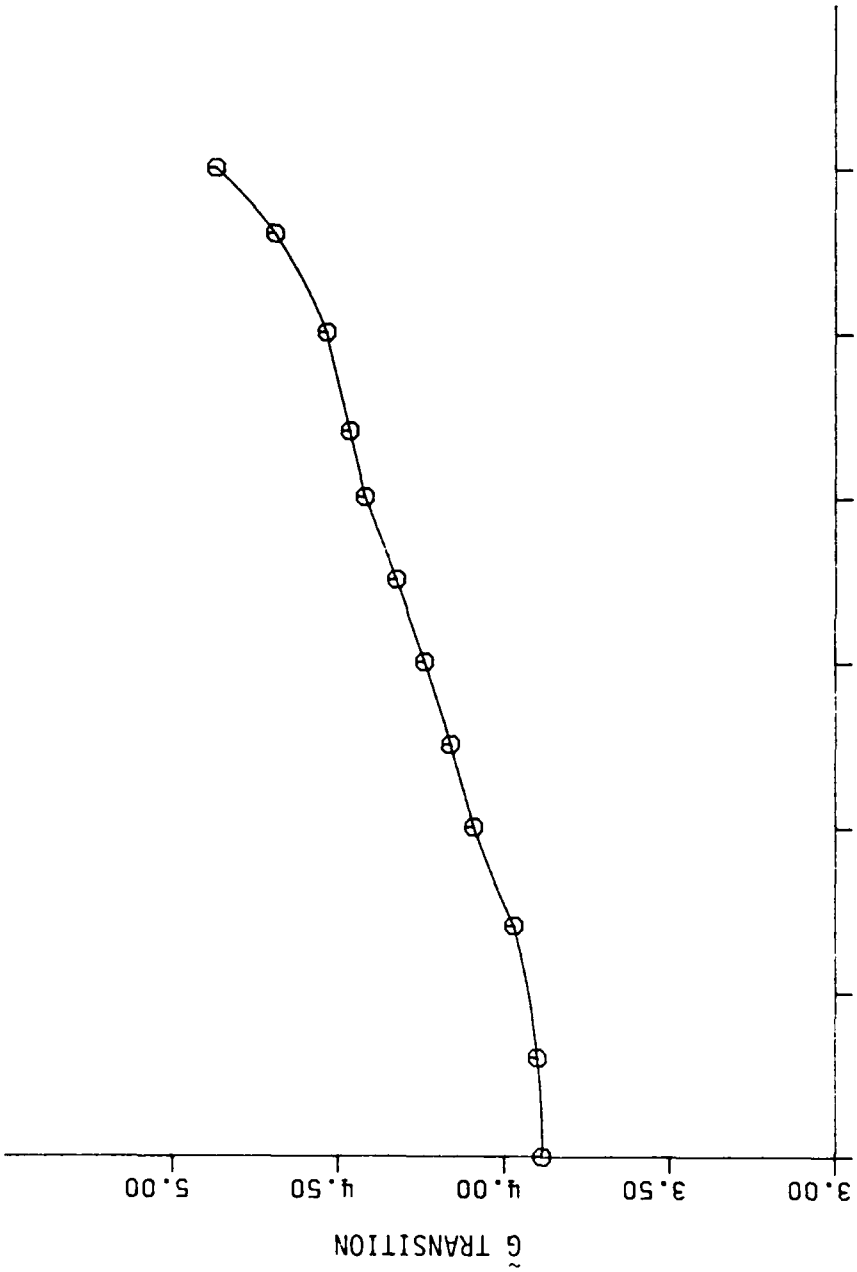

Figure 6.13. $\tilde{G}$ transitional as a function of gap numbers (G) for Pr = .706

(0 - 2π) was considered when investigating possible hysteresis behavior. The vertical symmetry assumption proved to be valid, as was discussed in Section 5.2.4. In order to obtain some type of tolerance criteria for the numerically predicted transitional Rayleigh numbers, a mesh resolution study was performed (see Appendix E) for three different size gap widths. Based on these results, it appears that the predicted transitional Rayleigh numbers are within 5 to 15 percent uncertainty. This error range seems to indicate fairly reasonable accuracy when compared to some of the larger discrepancies reported in the literature for predicting the onset of secondary motion (Elder, 1965; Powe et al., 1971; Rao et al., 1985).

Also in Appendix E is a comparison of the cellular development for G = .200 when using either a first-order upwind or a second-order central-differencing method. This comparison demonstrated that even at very high Rayleigh numbers, the first-order upwind differencing scheme could not capture multicellular flow transition. In addition, this appendix compares mean Nusselt numbers predicted numerically for G = .200 to that estimated by the correlation of Raithby and Hollands (1975), which was valid for narrow gaps in the pretransitional convective-dominated flow regimes, and also to the correlation of Kuehn and Goldstein (1980b).

6.2. Hydrodynamic Instability

Under certain conditions, an unsteady multicellular flow instability originates in the vertical sections of two-dimensional

narrow horizontal cylindrical annuli. This particular type of multicellular flow was captured numerically from the simplified governing equations derived in Section 4.5, corresponding to the high Rayleigh number/narrow-gap/small-Prandtl number limiting conditions.

The multicells apparently result because of hydrodynamic instability, and are analogous to those investigated by other researchers with regard to the vertical slot geometry, as discussed in detail in Section 2.6.

In contrast to the vertical slot studies, the multicellular flow initiated in the vertical portions of a horizontal annulus is unsteady. Results from this study seem to indicate that the initial instability behaves in a rather periodic manner. That is, the strength of the cells appears to increase and decrease with time in a cyclic fashion. Closely related to this observation is the phenomena of strange-attractors. In some systems that experience a multicellular-like flow instability, an ordered route to chaos has been reported (see Section 2.5 for specific references and related discussion). Briefly though, a typical sequence of events consists of the system first behaving in a time-periodic manner, followed by a cycle of periodic-doubling until finally, the system is stressed into chaotic-like nonperiodic motion. This present flow under study seems to have the potential to follow a similar ordered path to chaos.

The following subsections deal with a thorough discussion of both the numerical and analytical results relating to this unique type of secondary-flow instability.

6.2.1. Pr → 0 numerical solution

Assuming symmetry about the vertical center-line greatly reduced the amount of CPU-time associated with the numerical computations. This assumption was based on the detailed discussion given in Section 5.2. The above symmetry condition was proven valid in Figure 6.14a. Here, the first 832 time steps (for $\Delta\hat{t} = 1.0$) of the numerical solution to the complete annulus (31 x 202 nodes) produced the cellular cycle of the half-annulus (31 x 102 nodes) almost identically, and graphically, no notable differences could be discerned. Also, for both the full and half-annulus, the inner-wall vorticity at $\hat{t} = 832$ were compared in Figure 6.14b. The two cases were again in close agreement, to within approximately one percent error. Note that these curves are presented at this time to support the assumption of vertical symmetry. The exact nature and meaning of the cellular behavior described by these curves will be explained later in this section. Therefore, for the results that follow, a half-annulus mesh of 31 radial nodes and 102 angular nodes was employed. In general, the justification for this size mesh was due to proper resolution of the cellular structure and also to computer power and time limitations. These considerations are again discussed in more detail in Section 5.2.

Steady-state results were obtained up to a $\hat{G}$ value of 5.1. Then, at $\hat{G} = 5.2$, a seven-cell unsteady instability set in at a $\hat{t}$ value of approximately 30.0. Note that the converged steady-state results for $\hat{G} = 5.1$ were used as initial conditions to start the $\hat{G} = 5.2$ case. Prior to the seven-cell development, the instability first occurs near

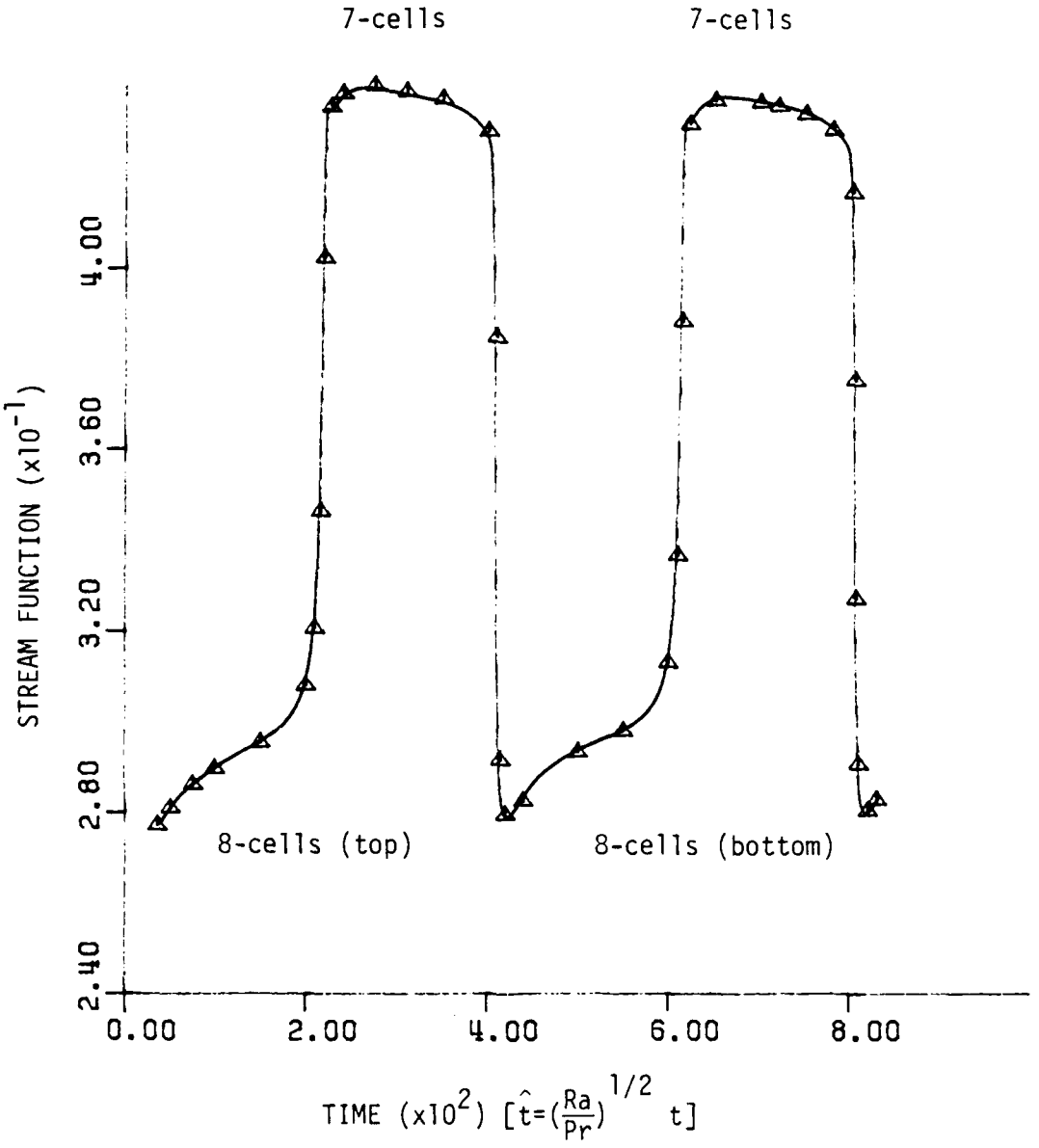

Figure 6.14a. Time-dependence of the stream function at r = .5/ ψ = 90° for $\hat{G}$ = 5.2. Full versus half-annulus comparison. Δ = full-annulus, ——— = half-annulus

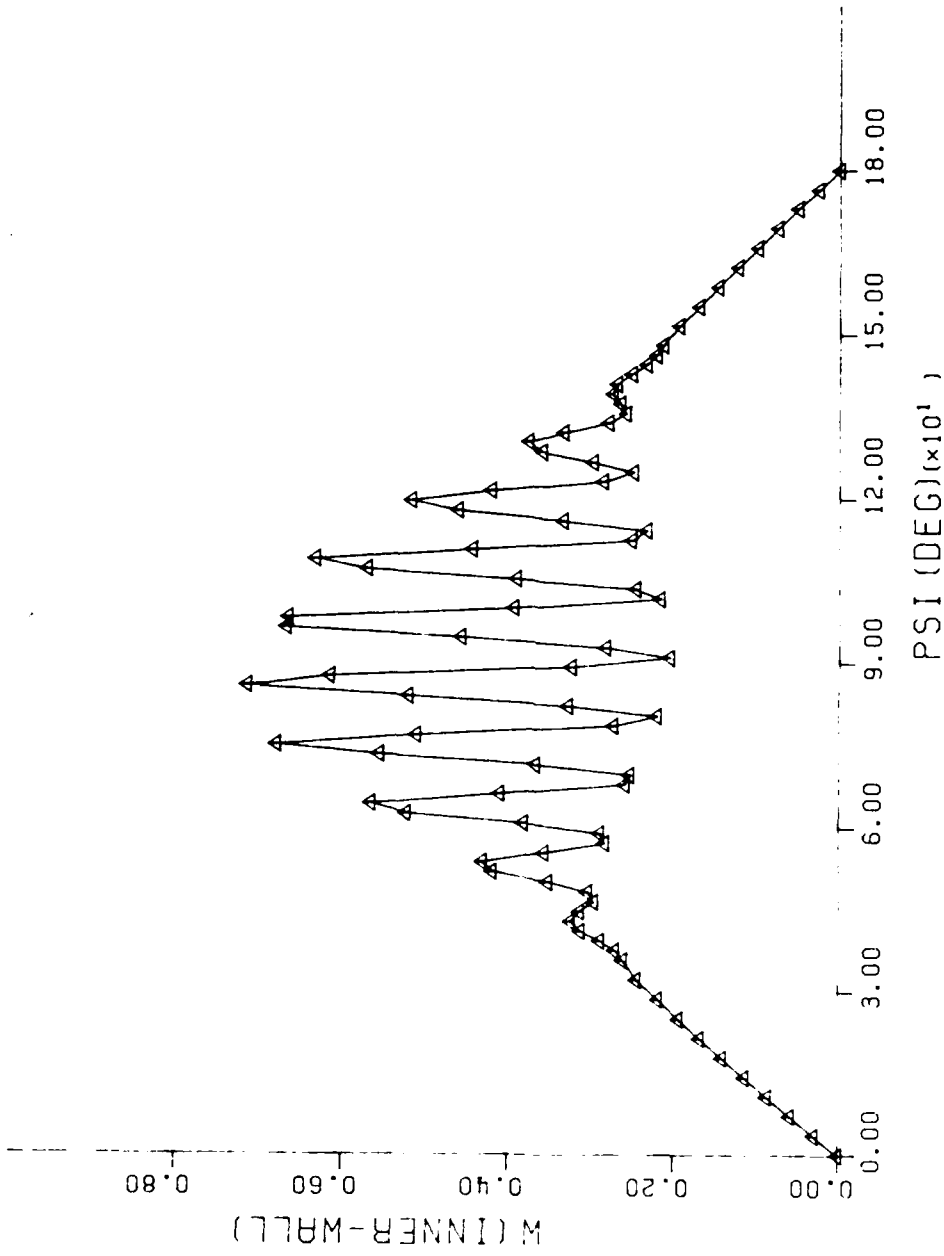

Figure 6.14b. Angular variation of the inner-wall vorticity at $\hat{G} = 5.2$ for $\hat{t} = 832.0$ Full versus half-annulus comparison. Δ = full-annulus, ——— = half-annulus

ψ = 90°, where the maximum buoyancy force causes the most rapid rising and falling of the fluid, as illustrated in Figure 6.15a. Also in Figure 6.15b, the cellular pattern is displayed at a time slightly beyond the initial development stage. The cellular instability then grew until the relatively stable seven-cell pattern resulted at $\hat{t}$ = 30.0. The initial seven-cell solution encompassed an arc of about 80 degrees near the vertical portion of the annulus (see Figure 6.16).

It is important to note that this multicellular flow instability was preserved with both finer and coarser mesh sizes, as evidenced by the data in Table 6.1. The coarser mesh, 31 x 72, could not resolve the smaller cells near the top and bottom portion of the vertical section, thus resulting in only five cells for the initial instability. The other three mesh sizes indicate that the instability sets in as a six or seven-cellular flow pattern. This result was in close agreement with that reported by Lee and Korpela (1983) for their vertical slot geometry.

Table 6.1. Mesh resolution comparison

Mesh size	$\hat{G}$ transitional	Geometry	Cells	Convergence constraint	Precision
31 x 72	5.7	half-annulus	5	1×10^{-6}	single
31 x 102	5.2	half-annulus	7	1×10^{-6}	single
41 x 132	4.9	half-annulus	7	1×10^{-8}	double
31 x 162	5.2	full-annulus	6	1×10^{-6}	single

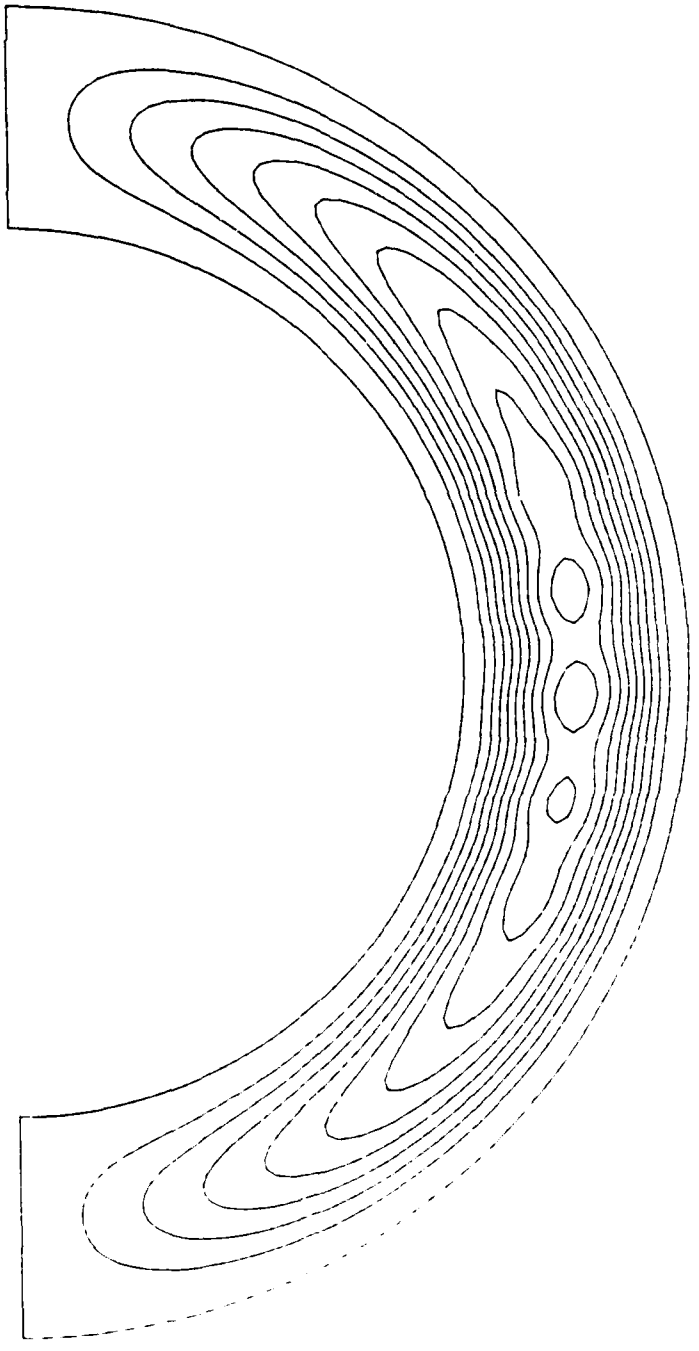

Figure 6.15a. Streamlines of an initial development stage for the onset of hydrodynamic instability at $\hat{G} = 5.2$ and $\hat{t} = 21.0$ (diameter ratio = 1.5)

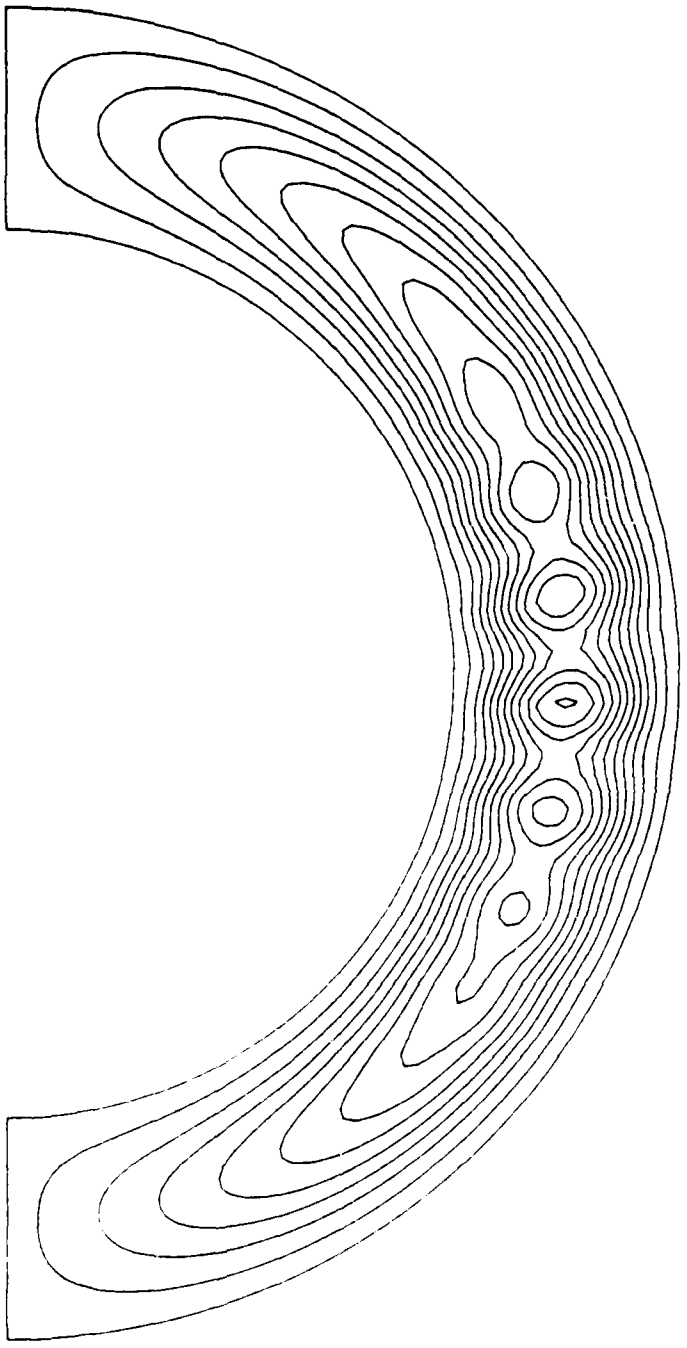

Figure 6.15b. Streamlines of the cellular instability slightly beyond the initial development stage for $\hat{G} = 5.2$ and $\hat{t} = 25.0$ (diameter ratio = 1.5)

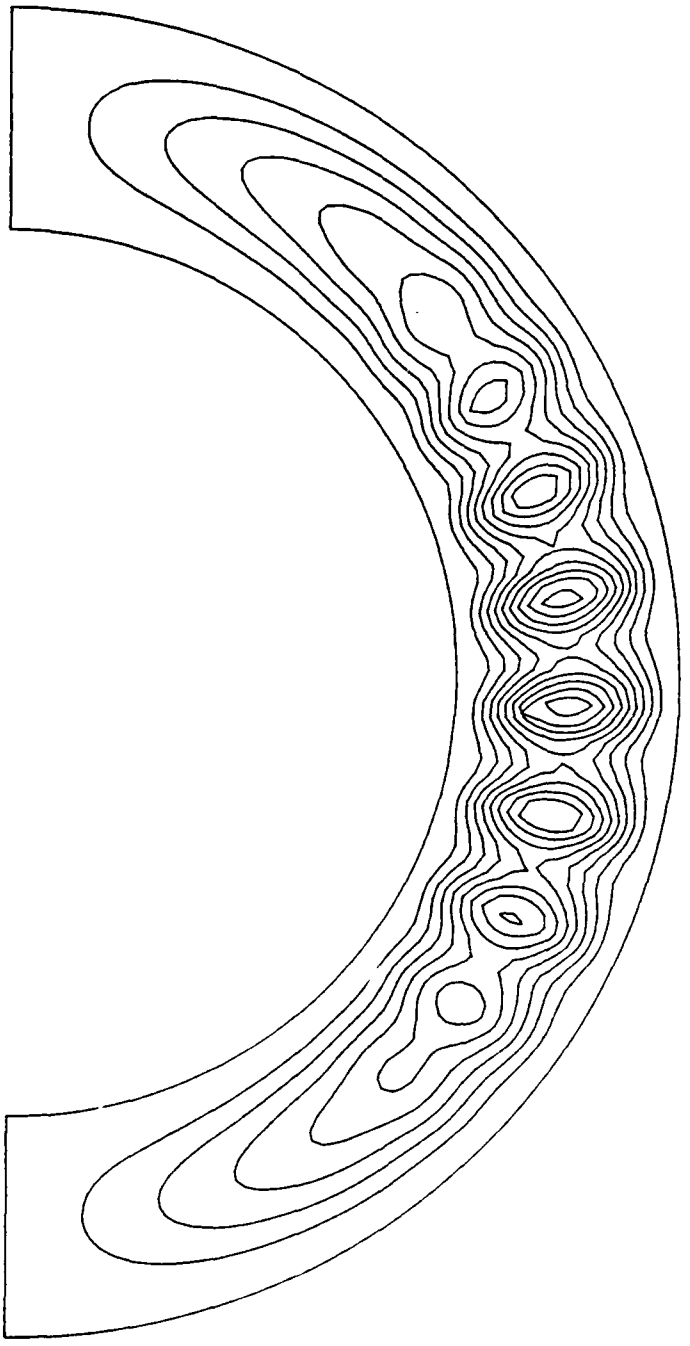

Figure 6.16. Streamlines of the initial seven-cellular flow field for $\hat{G}$ = 5.2 and $\hat{t}$ = 35.0 (diameter ratio = 1.5)

They claimed that a six-cellular flow pattern initially appeared at Gr_{b-a} = 8000 for a Prandtl number very near zero (see Section 2.6). This Grashof number of 8000 compared favorably with the transitional value of this study, where $\hat{G}$ = 5.2 translated to a Grashof number (based on gap width) of 7855. Furthermore, transitional values of 7880 and 7932 were predicted analytically by Vest and Arpaci (1969) and Korpela et al. (1973), respectively, for a similar vertical slot geometry.

Lee and Korpela (1983) also reported a wavenumber of 2.80 associated with the six-cellular flow pattern in their narrow vertical slot. They defined the wavenumber as $2\pi/Z$, where Z represented the center-point distance between two adjacent cells. When this study's initial seven-cellular state at $\hat{t}$ = 35.0 was compared to their narrow vertical slot geometry (aspect ratio = 15), the wavenumber was determined to be approximately 2.60--a good correlation.

However, as previously mentioned, the cellular flow within the vertical slot geometry was steady, whereas in this study, the multicellular flow at $\hat{G}$ = 5.2 seemed to vacillate periodically about the seven-cell state. That is, upon increasing $\hat{t}$, a cyclic pattern resulted: an additional eighth cell formed on top of the 80° arc, reverted back to seven cells, then an additional eighth cell formed on the bottom of the 80° arc, and again, reverted back to seven cells, forming an 8-7-8-7 cellular pattern (see Figure 6.17). In the seven-cell formation, the stronger cells appeared near ψ = 90° (see Figures 6.16 and 6.18). The remaining cells successively decreased in strength (in approximate proportion to sin ψ) as they proceeded away

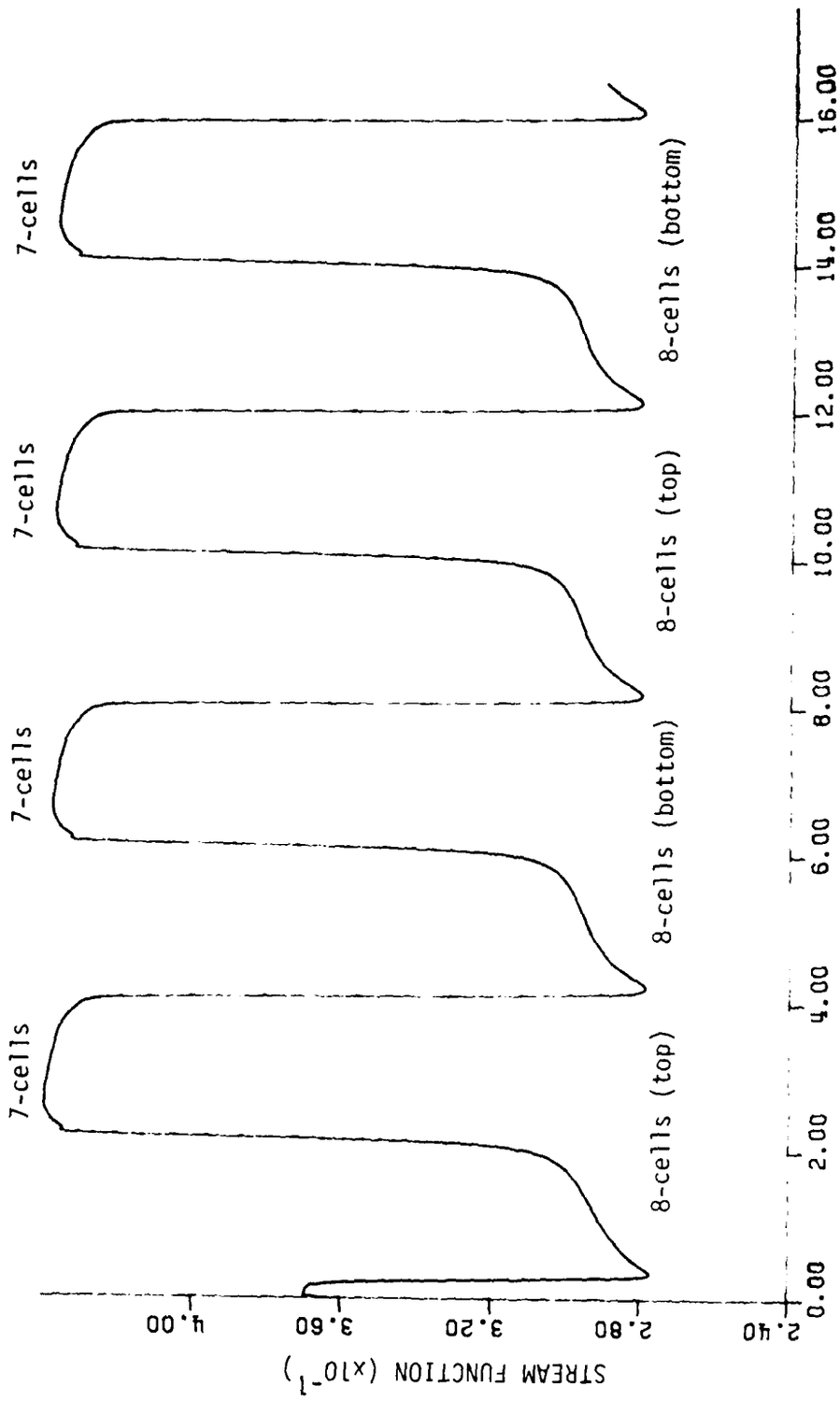

Figure 6.17. Time-dependence of the stream function at r = .5/ψ = 90° for the half-annulus at $\hat{G}$ = 5.2

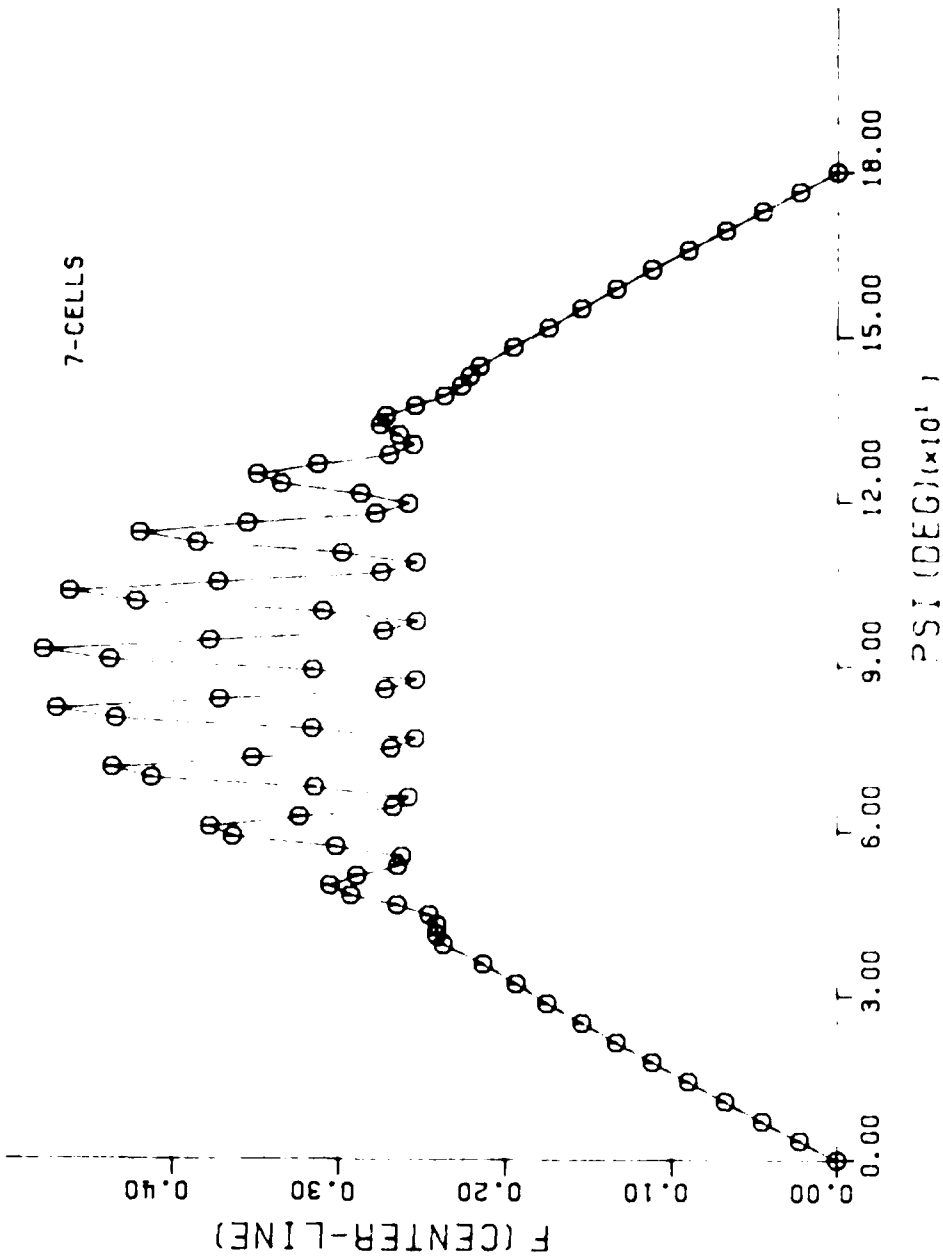

Figure 6.18. Angular variation of the 7-cell center-line stream function (r=.5) at t = 1060.

from the 90° point.

At the start of the cellular cycle, the seven cells weakened (the maximum stream function decreased) as the eighth cell formed on top (see Figure 6.19). Then, the eight-cell pattern grew in strength until the two larger cells near 90° merged into one with the maximum stream function shifting upward to 92°, thus forming an upward-shifted seven cellular flow pattern. Similarly, these seven cells then weakened as the eighth cell formed on the bottom portion of the chain of cells (see Figure 6.20). Again, the eight-cell pattern grew in strength until the two larger cells merged into one with the maximum stream function shifting downwards now to 87°, thus forming a downward-shifted seven-cellular flow pattern completing the 8-7-8-7 cycle. A cyclic behavior of the average inner shear-stress also accompanied this changing cellular pattern. Table 6.2 outlines a typical cycle. (Note that these relationships would repeat for subsequent cycles.)

Table 6.2. Characteristics of the 8-7-8-7- cellular cycle

Cell structure	t	Average inner shear-stress	Maximum stream function location	Maximum stream function value
8-top	85.0	.23722	87°	.4506
7-top	280.0	.23644	92°	.4815
8-bottom	350.0	.237247	82°	.4501
7-bottom	680.0	.23627	87°	.4824

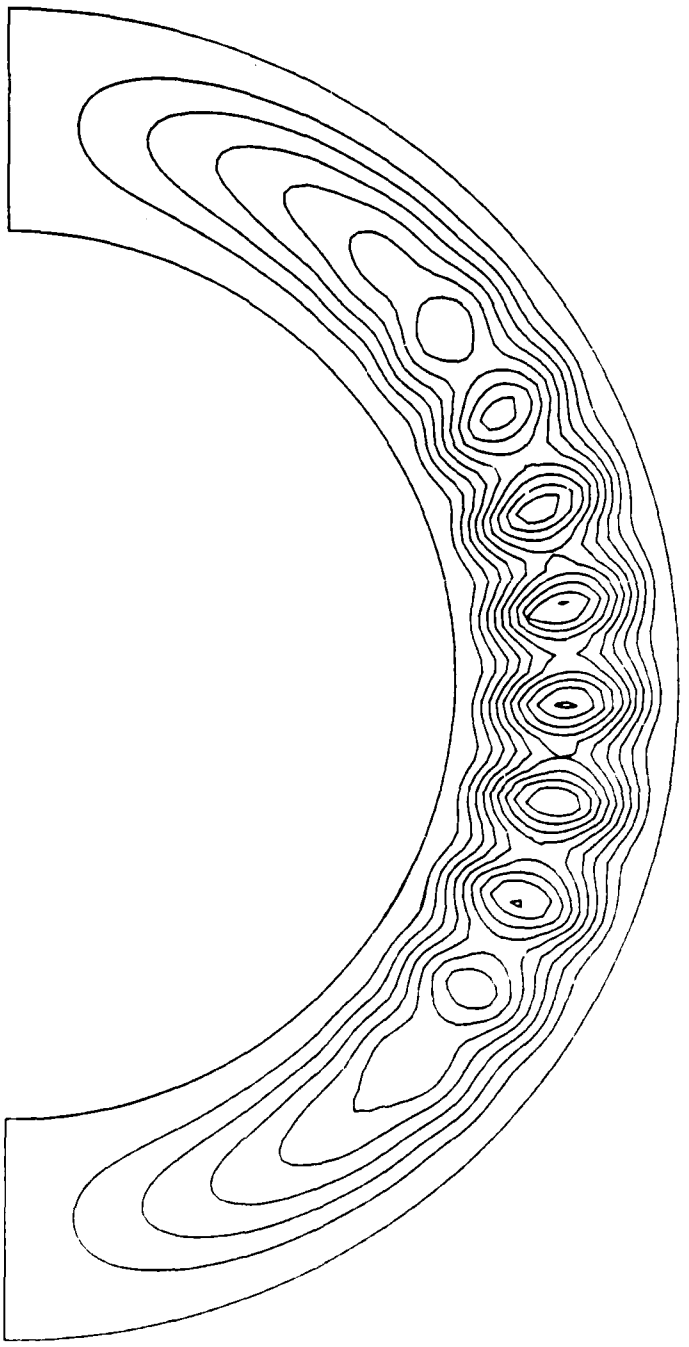

Figure 6.19. Streamlines of an upward-shifted eight cellular flow field (eight-cells-top) for $\hat{G} = 5.2$ and $\hat{t} = 1782.0$ (diameter ratio = 1.5)

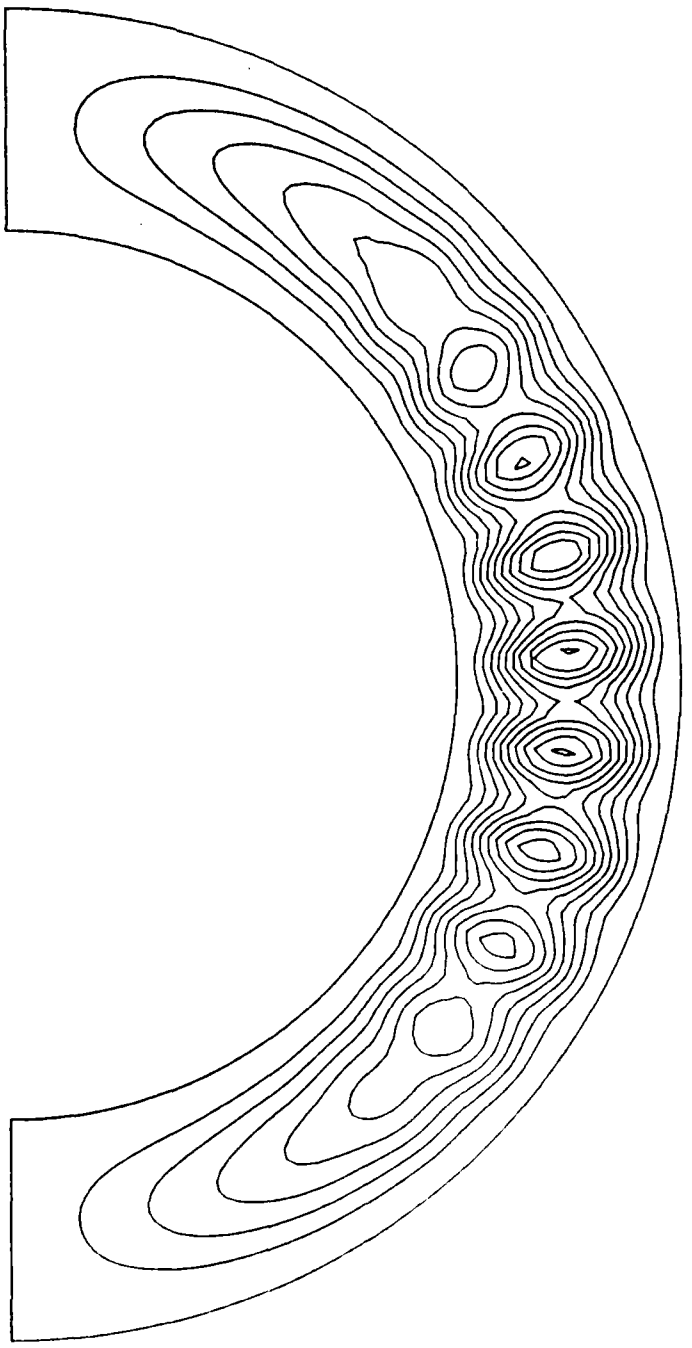

Figure 6.20. Streamlines of a downward-shifted eight cellular flow field (eight-cells-bottom) for $\hat{G}$ = 5.2 and $\hat{t}$ = 1182.0 (diameter ratio = 1.5)

This table, along with the particular nature of the cellular activity, seems to imply a potential energy exchange in the 8-7-8-7 cellular cycle. That is, the most potential energy seems to be stored within the seven-cell formation, corresponding to a minimum average shear-stress and a larger maximum stream function. It then appears that some of the potential energy is released and is converted to shear energy which aids in the creation of an eighth-cell. This then causes a rise in the average inner shear-stress and a corresponding decrease in the maximum stream function.

The strength of the stream function at $\Psi = 90°/r = .5$ behaved in a square-wave-like time-periodic fashion, as clearly illustrated in Figure 6.17. The period of this cyclic pattern was approximately 800 time ($\hat{t}$) units.

The fact that the cellular behavior at $\hat{G} = 5.2$ is unsteady can be supported by the work of Thomas and Vahl Davis (1970). They observed a multicellular flow, similar to that reported by Elder (1965) and Lee and Korpela (1983), in narrow vertical cylindrical annuli (see Section 2.6). Even though they were only interested in predicting the onset of this multicellular flow, they did report that the flow was unsteady and attributed this unsteadiness to curvature effects.

Figure 6.21 displays the vorticity distribution at the inner cylinder wall for both unicellular and multicellular flows. The unicellular steady-state result, for $\hat{G} = 5.1$, behaved in a sinusoidal manner with the maximum vorticity occurring near $\Psi = 90°$. Then, due to the multicellular instability at $\hat{G} = 5.2$, the vorticity distribution

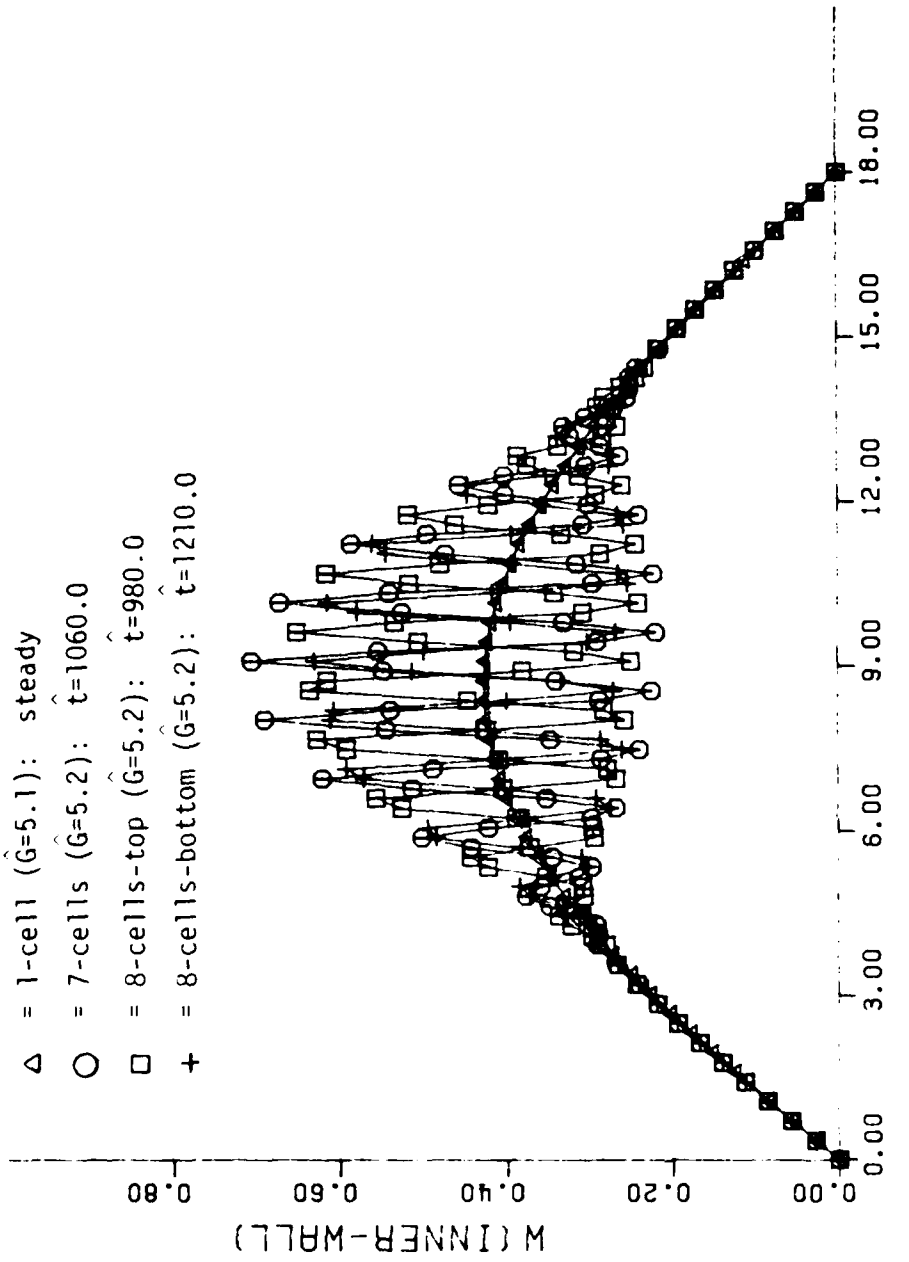

Figure 6.21. Angular variation of the inner-wall vorticity for various cellular patterns

was clearly disturbed and behaved in an intense oscillatory manner near the vertical portion of the half-annulus. This extremely wavy vorticity pattern shifted only slightly as the number of cells made the transition from eight-cells-top, to seven-cells, to eight-cells-top. The seven-cell solution experienced the strongest variation in wall vorticity. For individual comparison, the four curves plotted in Figure 6.21 are depicted separately in Figures 6.22 through 6.25.

To examine the change in cellular behavior with $\hat{G}$, the value $\hat{G}$ = 5.5 was calculated using the $\hat{G}$ = 5.2 seven-cellular terminal state at $\hat{t}$ = 35.0. Figure 6.26a displays the time variation of the stream function at $\psi = 90°/r = .5$, using a constant time step. Up to $\hat{t}$ = 400, a hint of double-periodicity seems to be present, but afterwards, the flow seems to become aperiodic, resembling the onset of chaotic motion. The multicellular pattern was similar to that of $\hat{G}$ = 5.2, except in this case, the cellular flow seemed to oscillate between nine, ten and eleven cells. The maximum stream function, occurring near $\psi = 90°$, was greatest for the nine-cell structure, least for the eleven-cell structure. A typical eleven-cell pattern is shown in Figure 6.26b. Also, in general, the cellular motion at $\hat{G}$ = 5.5 was similar to that experienced with $\hat{G}$ = 5.2.

The preceding results show that a multicellular hydrodynamic instability is indeed probable in the vertical sections of narrow horizontal annuli. It appears that this instability arises because of the coupling of the nonlinear terms with the buoyancy term.

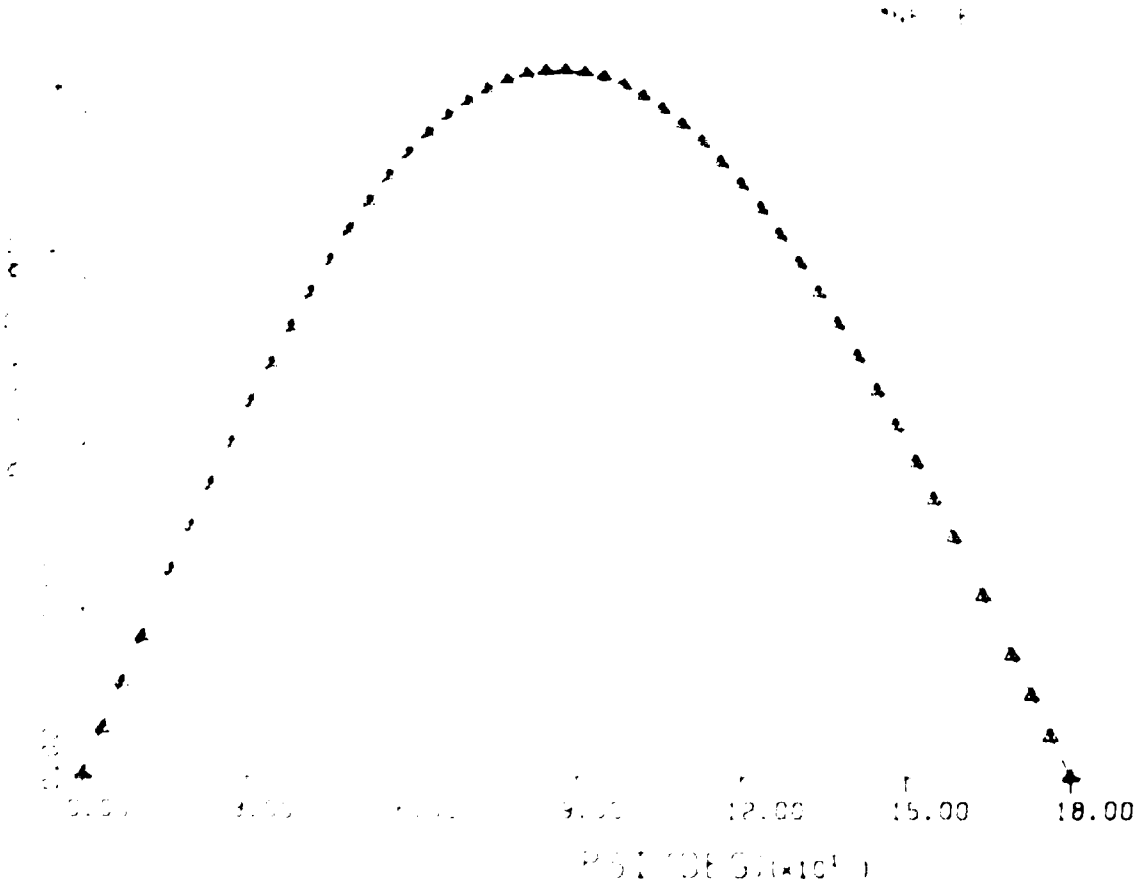

Figure [illegible]. Angular variation of the one cell steady state inner-wall vorticity for G = 5.1

AD-A186 113 THE NUMERICAL AND ANALYTICAL STUDY OF BIFURCATION AND MULTICELLULAR FLOW..(U) AIR FORCE INST OF TECH WRIGHT-PATTERSON AFB OH D B FANT 1987 3/3

UNCLASSIFIED AFIT/CI/NR-87-134D F/G 20/13 NL

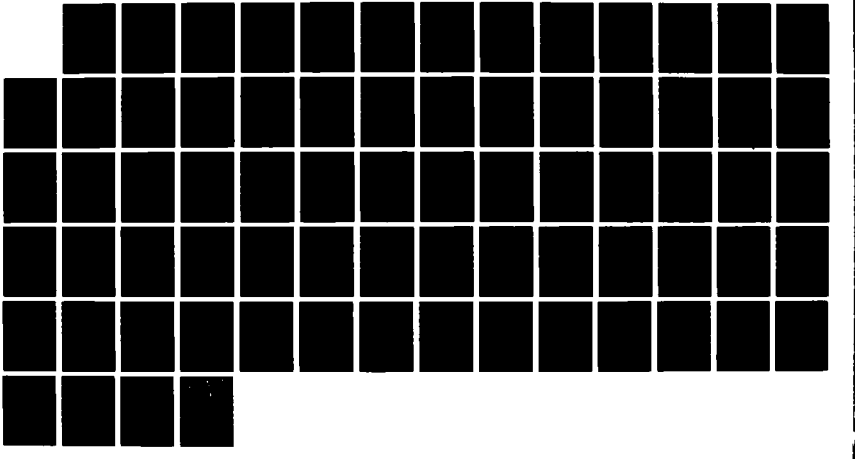

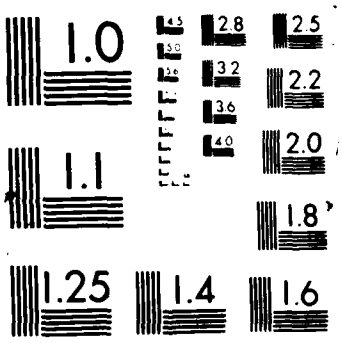
1.0
1.1
1.25
1.4
1.6
1.8
2.0
2.2
2.5
2.8
3.2
3.6
4.0

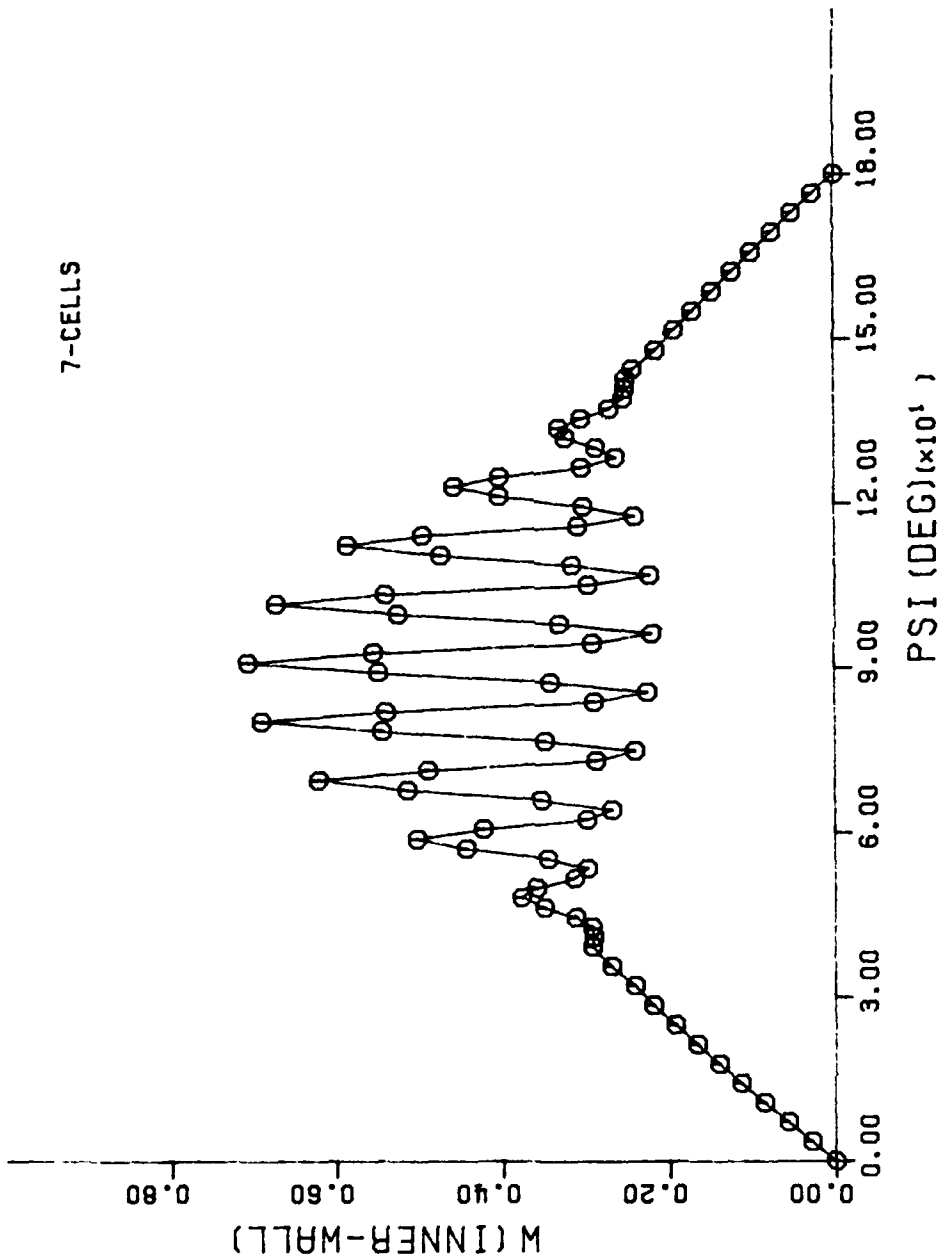

Figure 6.23. Angular variation of the 7-cell inner-wall vorticity for $\hat{G} = 5.2$ and $\hat{t} = 1060.0$

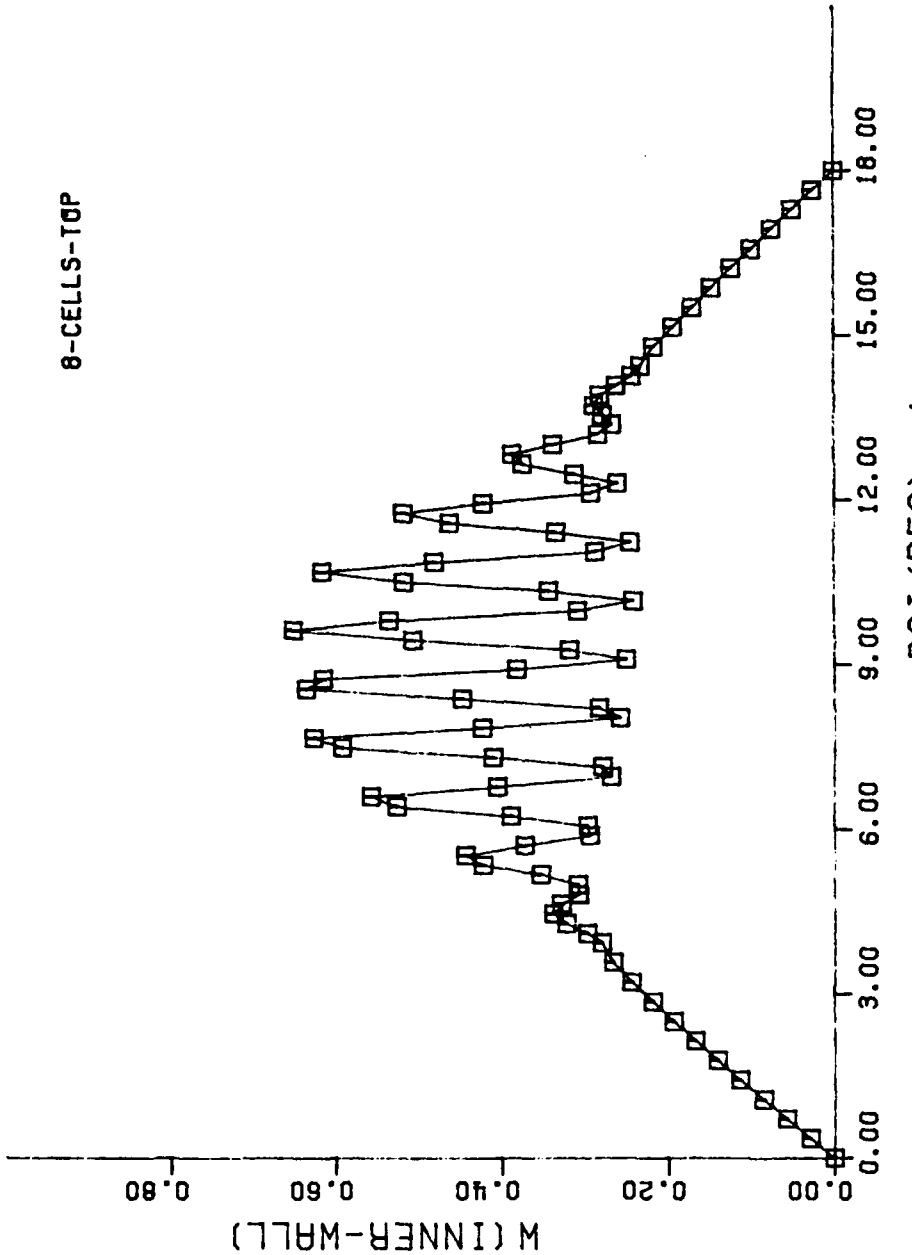

Figure 6.24. Angular variation of the 8-cell-top inner-wall vorticity for $\hat{G} = 5.2$ and $\hat{t} = 980.0$

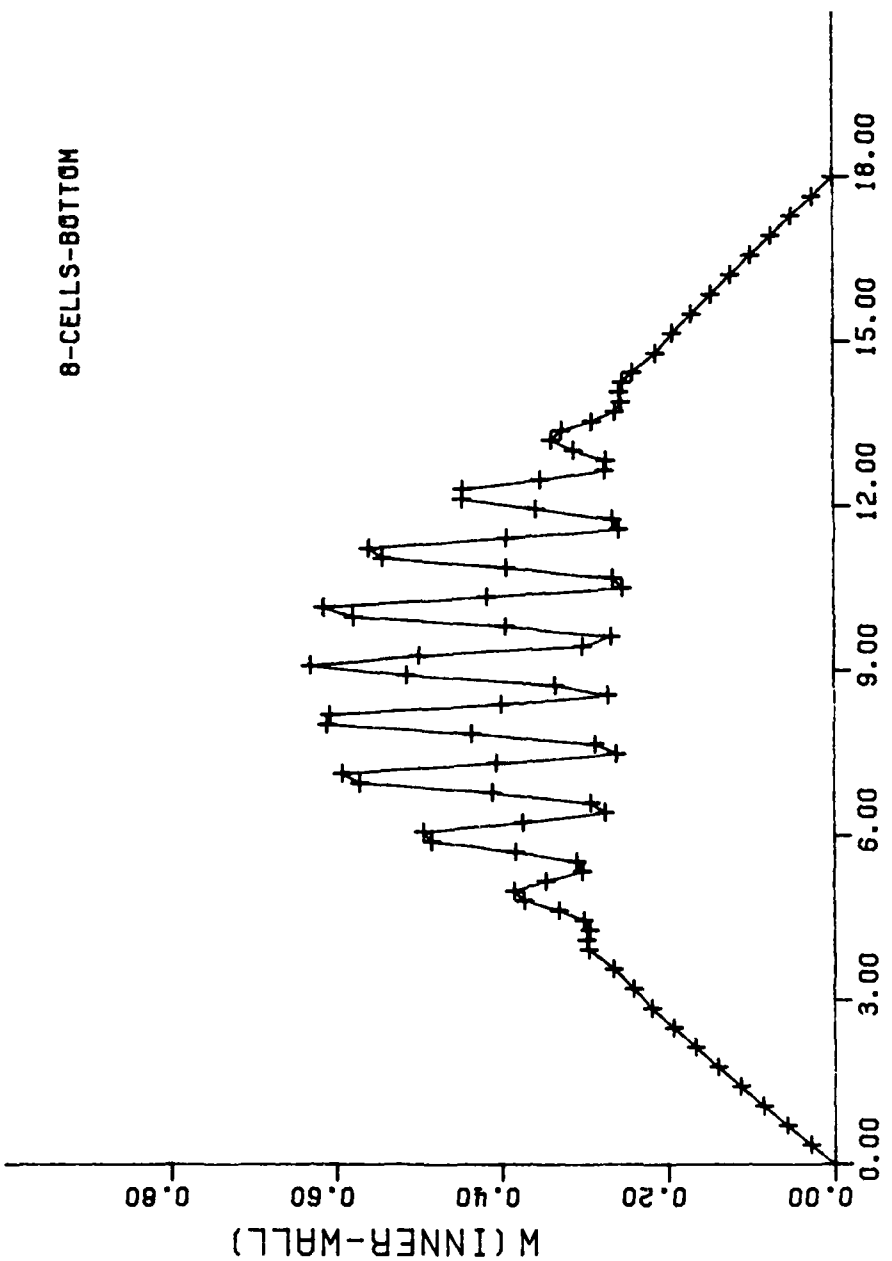

Figure 6.25. Angular variation of the 8-cell-bottom inner-wall vorticity for $\hat{G} = 5.2$ and $\hat{t} = 1210.0$

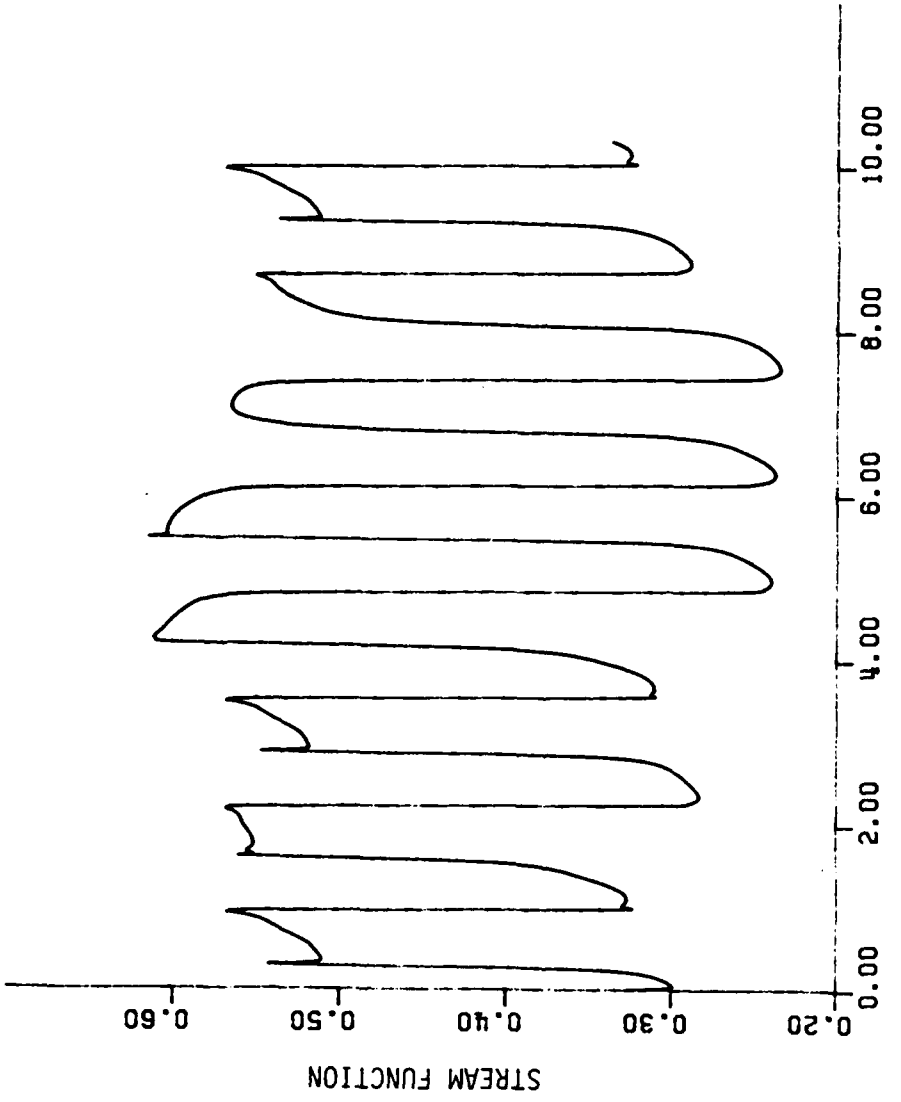

Figure 6.26a. Time-dependence of the stream function at r=.5/ψ = 90° for the half-annulus at $\hat{G}$ = 5.5

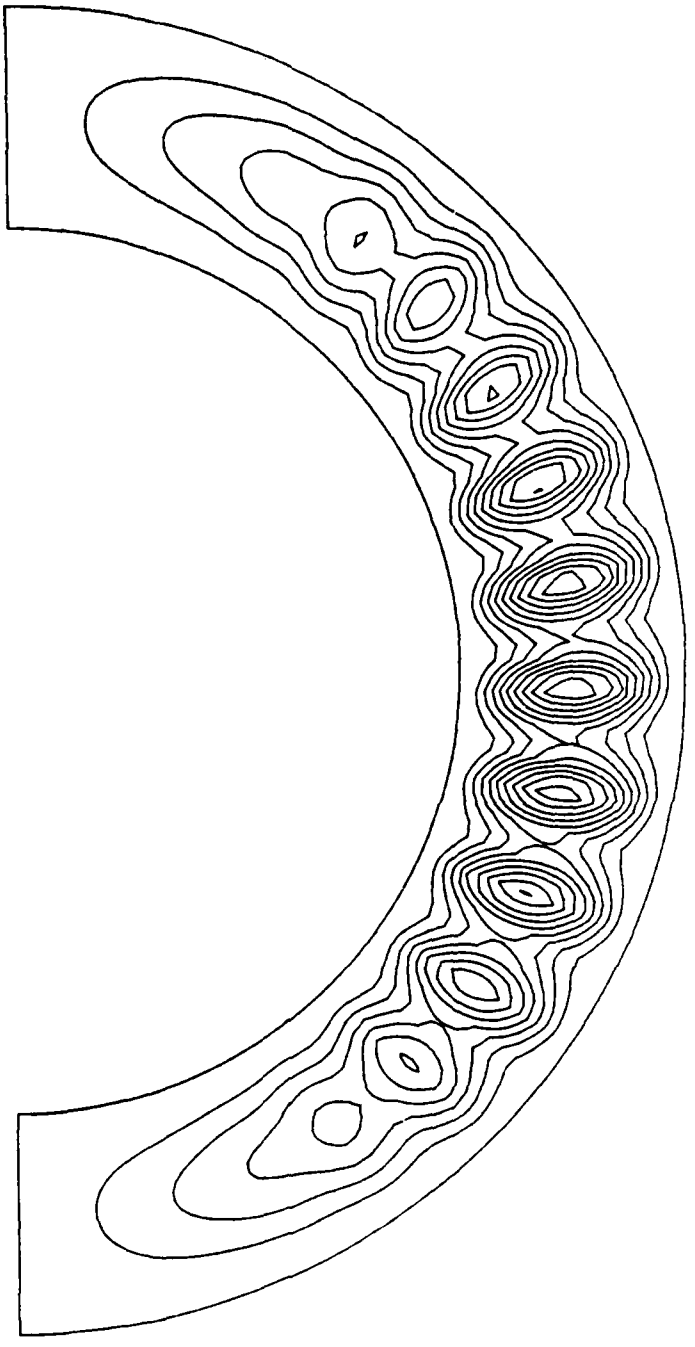

Figure 6.26b. Streamlines of an eleven-cellular flow field for $\hat{G} = 5.5$ and $\hat{t} = 1031.0$ (diameter ratio = 1.5)

$-\hat{G} \sin \psi$, in the vorticity equation. Considering this statement together with the fact that periodicity is lost for $\hat{G} = 5.5$, one might infer that the effects of the nonlinear terms become more and more pronounced as $\hat{G}$ increases.

Based on this reasoning, it is anticipated that for some intermediate value of $\hat{G}$ between 5.2 and 5.5, the possibility of an emerging doubly-periodic solution is likely, thus causing the system to make a further transition on its ordered path to chaos.

6.2.2. Pr → 0 perturbative solution

To verify the Pr → 0 perturbative expansion solution, the analytical results will be compared to related numerical results for the pretransitional case $\hat{G} = 5.1$. As discussed in Section 4.6, only F_1 and W_1 (as given in Eqs. (4.93) and (4.94), respectively) appear to be significant prior to the onset of multicellular flow. This claim will now be tested in the following comparisons.

An analytical expression for the inner wall vorticity was found by evaluating W_1 at $r = 0$ for $\hat{G} = 5.1$:

$$W_{inner} = .425 \sin \psi \quad .$$

A comparison to the numerical result at $\hat{G} = 5.1$ is given in Figure 6.27. The largest deviations occurred near $\psi = 45$ and 135°, corresponding to relative errors of nearly five percent. At the point of maximum vorticity, $\psi = 90°$, the error was only about .1 percent.

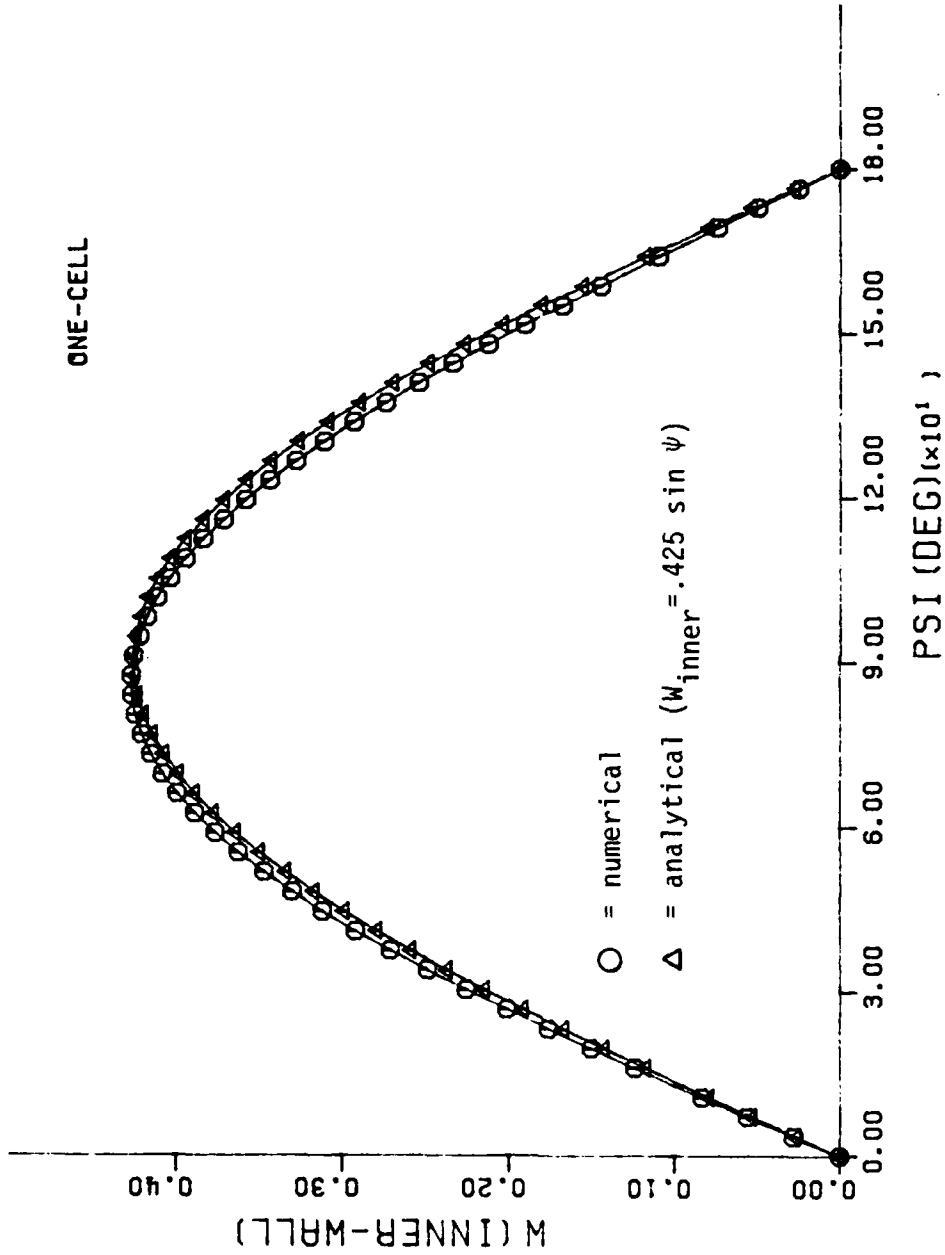

Figure 6.27. Angular variation of the steady-state inner-wall vorticity for $\hat{G}$ = 5.1

Similarly, an analytical expression for the vorticity at the horizontal center-line was obtained by evaluating W_1 at $\psi = 90°$ and $\hat{G} = 5.1$:

$$W_{90°} = 2.55\ (r^2 - r + \frac{1}{6}) \quad .$$

This result was compared to the numerical result in Figure 6.28. The vorticity was positive near the walls of the annulus, $.81 \leq r \leq .19$, signifying the boundary-layer region. It became negative within the center portion of the annulus, representing the inviscid-core region. A maximum error of approximately 3.5 percent occurred near the switching point, where the vorticity changed from positive to negative. The maximum vorticity occurred at the walls, $r = 0$ and 1, and took on a value of approximately .425. For $r = .5$, the vorticity reached a minimum at -.2125.

The analytical expression for stream function at $\psi = 90°$ and $\hat{G} = 5.1$ is given by:

$$F_{90°} = 5.527125\ r^2\ (r - 1)^2 \quad .$$

Figure 6.29 displays its comparison to the numerical result. A maximum error of about one percent occurred at $r = .5$, where the stream function reached its maximum value of approximately .346.

The above results indicate that the pretransitional flow field ($\hat{G} \leq 5.1$) can be adequately represented by the first-term expansions

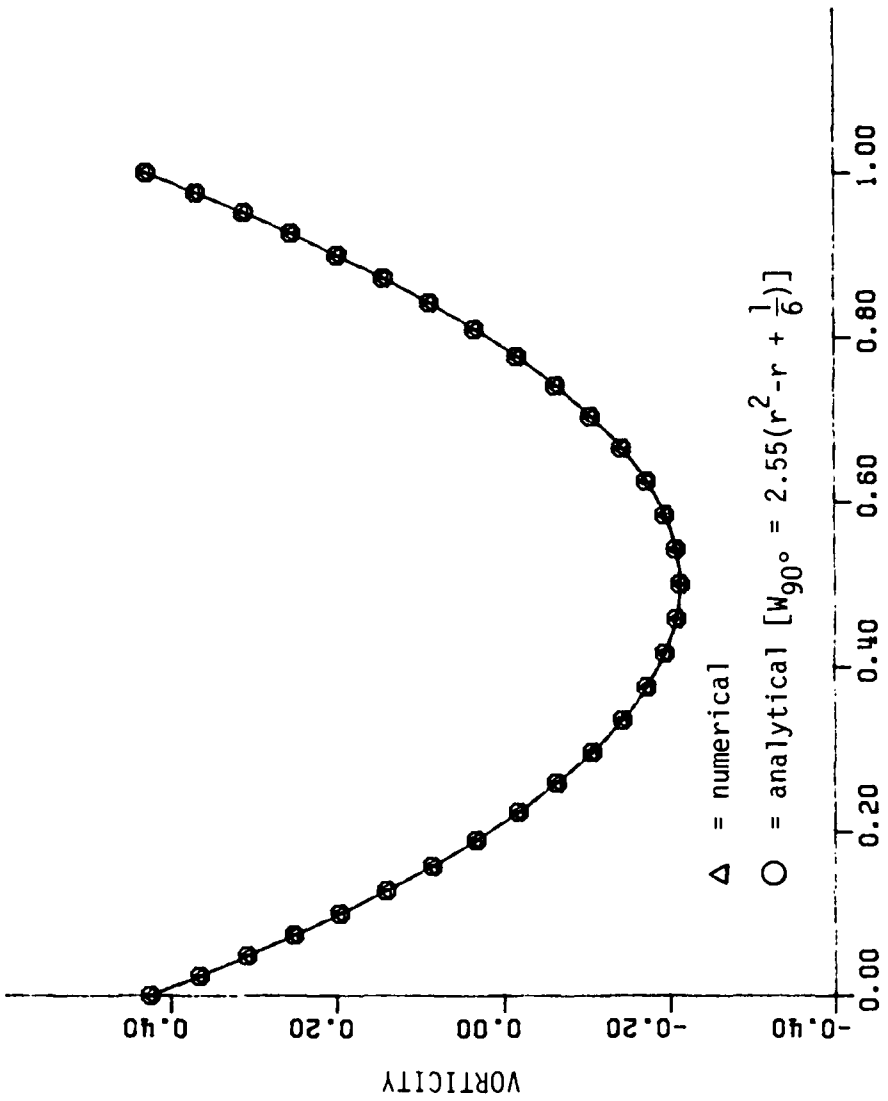

Figure 6.28. Radial variation of the vorticity at 90° for $\hat{G} = 5.1$

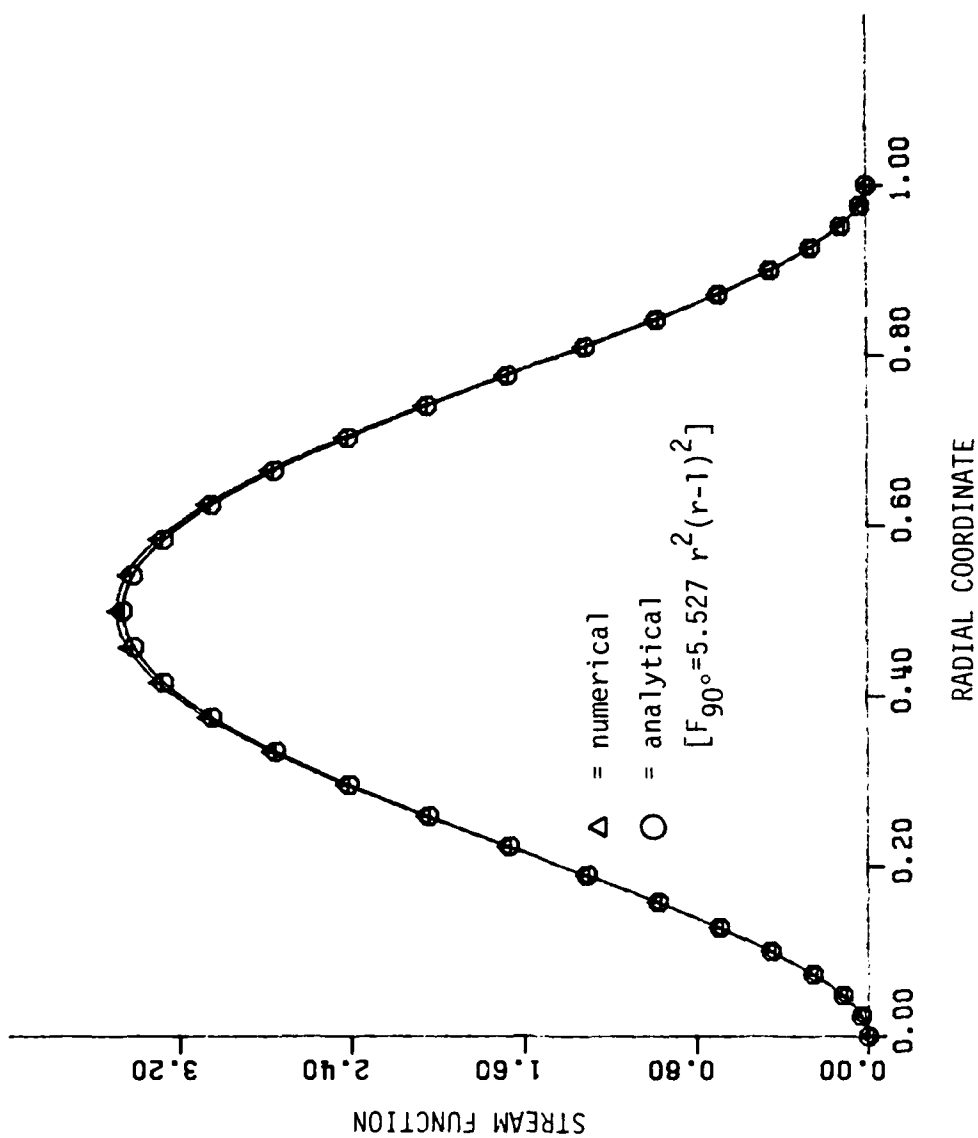

Figure 6.29. Radial variation of the stream function at 90° for $\hat{G}$ = 5.1

(W_1 and F_1) of the perturbation solution, which do not account for nonlinear effects. That is, the problem appears to be linear and steady up to $\hat{G} = 5.1$. This suggests that the full nonlinear influence only becomes evident just prior to and beyond the point of instability. For this case, the nonlinear effects appear to come into play for $\hat{G} \geq 5.2$.

Figure 6.30 was generated in order to show how the $Pr \to 0$ perturbative solution breaks down as the Prandtl number increases. Using the relationship $\tilde{G} = \hat{G}\, Pr^{1/4}$, two numerical results corresponding to $Pr = .7$ and 2.0 were compared to the analytical solution for $\hat{G} = 4.0$. Surprisingly, for Prandtl numbers as large as 2.0, the comparison between the analytical and numerical results was fairly close. For $Pr = .7$ and 2.0, respective maximum errors of 3.5 and 10.5 percent occurred near $\psi = 140°$. Thus, for air, the use of $Pr \to 0$ expansions should provide for relatively good estimates of the local flow variables, at least for the pretransitional cases.

The finite-Prandtl number perturbative solution of Eq. (4.29) can also be used to obtain analytical results for small Prandtl number cases. Using the three-term perturbative solution (F_1, F_2 and F_3), all of the important physics can be taken into account, including the first effects of nonlinearity through F_2 and F_3. For liquid mercury, $Pr = .02$, a six-cellular counter-rotating flow was encountered at $\tilde{G} = 3.5$. In the complete annulus, the large kidney-shaped cells maintained themselves near $\psi = 90$ and 270°, while two smaller counter-rotating cells formed first at the bottom, then at the top portions of the annulus - $\psi = 0$ and 180°. This multicellular flow pattern was more fully developed for

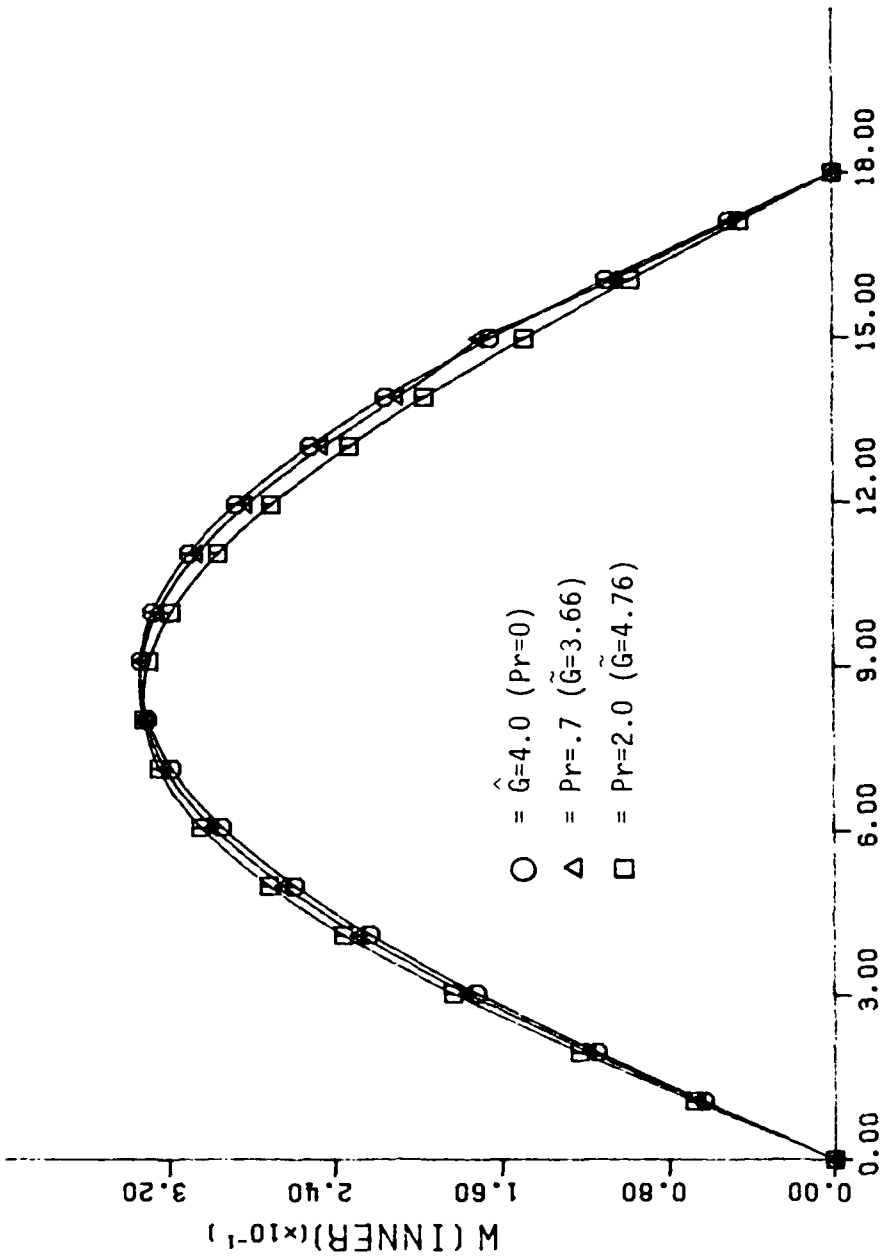

Figure 6.30. Angular variation of the inner-wall vorticity for $\hat{G} = 4.0 = Pr^{-1/4}\,\tilde{G}$ and $W = Pr^{3/4}\,\tilde{w}$

$\tilde{G}$ = 4.0, and is depicted in Figure 6.31. This particular flow pattern was very similar to that observed by Mack and Bishop (1968) and Huetz and Petit (1974) for a larger gap width, G = 1, and Pr = .02. They graphically depicted the multicellular behavior at Ra = 300, but mentioned that it initially occurred (analytically) at a lower value of Rayleigh number. In addition, the presence and shape of the secondary cells for G = 1 and Pr = .02 were confirmed by the numerical experiments of Charrier-Mojtabi et al. (1979), where they reported a similar type of multicellular flow that began to develop near Ra = 300.

Using the relation $\tilde{G} = Ra^{1/4}G$, $\tilde{G}$ = 4.0 translates into a Rayleigh number of 256 for G = 1.0, thus reaffirming the results described above. Note also that Huetz and Petit (1974) claimed that the bottom cell developed first. However, when the finite-Prandtl number boundary-layer equations were solved numerically for Pr = .02 (thus incorporating the full effects of nonlinearity), a multicellular flow field resembling that described with the Pr → 0 numerical solution resulted in the vertical section of the half-annulus at $\tilde{G}$ = 1.92 ($\hat{G}$ = 5.106).

From these results, one might conclude that the effects of the boundary-layer are less significant in the larger size gaps, thus creating a weakly nonlinear instability as originally reported by Mack and Bishop (1968). But for the narrow-gap widths, the boundary-layer effects are much more dominant, thus creating stronger nonlinear interactions which trigger the hydrodynamic type of instability as described in this study for the small-gap/small-Prandtl number limiting conditions. These results are discussed further in Appendix B.

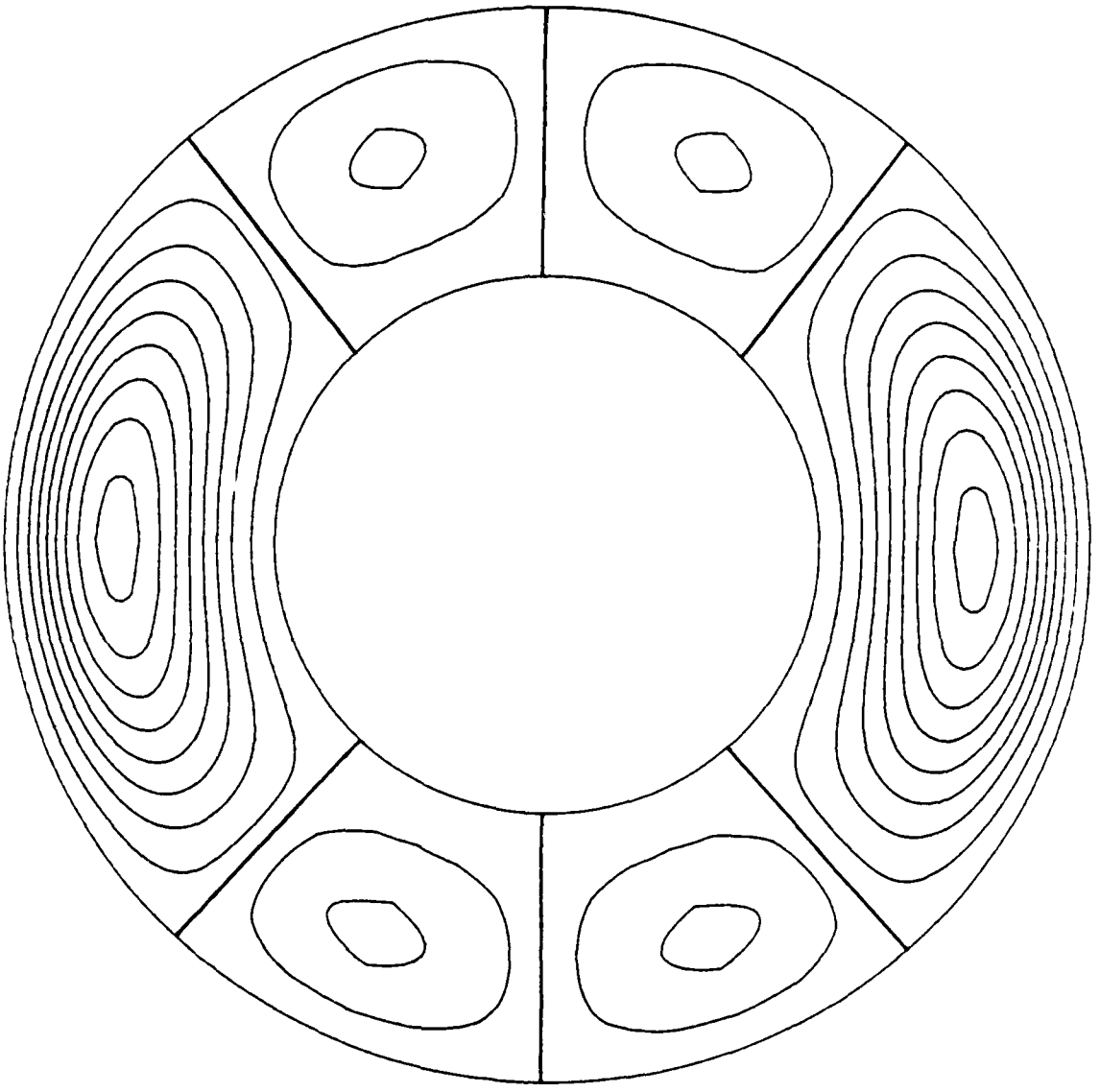

Figure 6.31. Streamlines of the steady six-cellular perturbation solution corresponding to Pr = .02 and $\tilde{G}$ = 4.0 (diameter ratio = 2.0)

6.2.3. Small-Prandtl number stability curves

In order to obtain a more universal relationship for predicting multicellular flow instability with regard to small-Prandtl number fluids in the narrow horizontal annuli, the following derivation was considered.

It was shown in Chapter 4 that

$$\tilde{G} = Ra^{1/4} G = Pr^{1/4} \hat{G} \quad , \tag{6.1}$$

but since $Ra = Gr_a \cdot Pr$, Eq. (6.1) becomes (after some manipulation):

$$Gr_a = \left(\frac{\hat{G}}{G}\right)^4 \tag{6.2}$$

where Gr_a is the Grashof number based on the inner cylinder radius. Then, using the relation

$$Gr_{b-a} = Gr_a \, G^3 \quad ,$$

one obtains:

$$Gr_{b-a} = \frac{\hat{G}^4}{G} \tag{6.3}$$

where Gr_{b-a} now represents the Grashof number based on the gap width. For $Pr = 0$, the transition to multicellular flow occurred at $\hat{G} = 5.2$. Using this result transforms Eq. (6.3) into a universal relation which

is inversely proportional to the gap number, G:

$$Gr_{b-a} = \frac{731}{G} \quad . \tag{6.4a}$$

This relationship is plotted for various values of G in Figure 6.32. Note that the transitional value of $Gr_{b-a} = 8000$, as predicted in this study and by Lee and Korpela (1983), corresponds to a gap number of approximately G = .10. Also, the shape of the stability curve seems to make sense, since for the vertical slot studies it was reported by Lee and Korpela (1983) and Elder (1965) that as the gap width increased, the transition to turbulence occurred sooner. Similarly, in this study, it was shown for very small-gap widths (for air) that as the gap number decreased, the transitional Rayleigh number for multicellular flow increased. The above statements indicate that as gap width decreases, the onset of instability is suppressed. Thus, the stress parameter $\hat{G}$ or Rayleigh number, must increase accordingly in order to trigger the respective hydrodynamic or thermal instability. Qualitatively, the shape of the stability curve in Figure 6.12 for Pr = .706 (in the small-gap limit) is similar to that in Figure 6.32 for Pr = 0. Also, for thermal instability, the following relation holds:

$$Gr_{b-a} = \frac{\tilde{G}^4}{G \cdot Pr}$$

where for air in the small-gap limit, Pr = .706 and $\tilde{G}_{TR} = 4.0$, hence:

$$Gr_{b-a}\Big|_{air} = \frac{363}{G} \quad . \tag{6.4b}$$

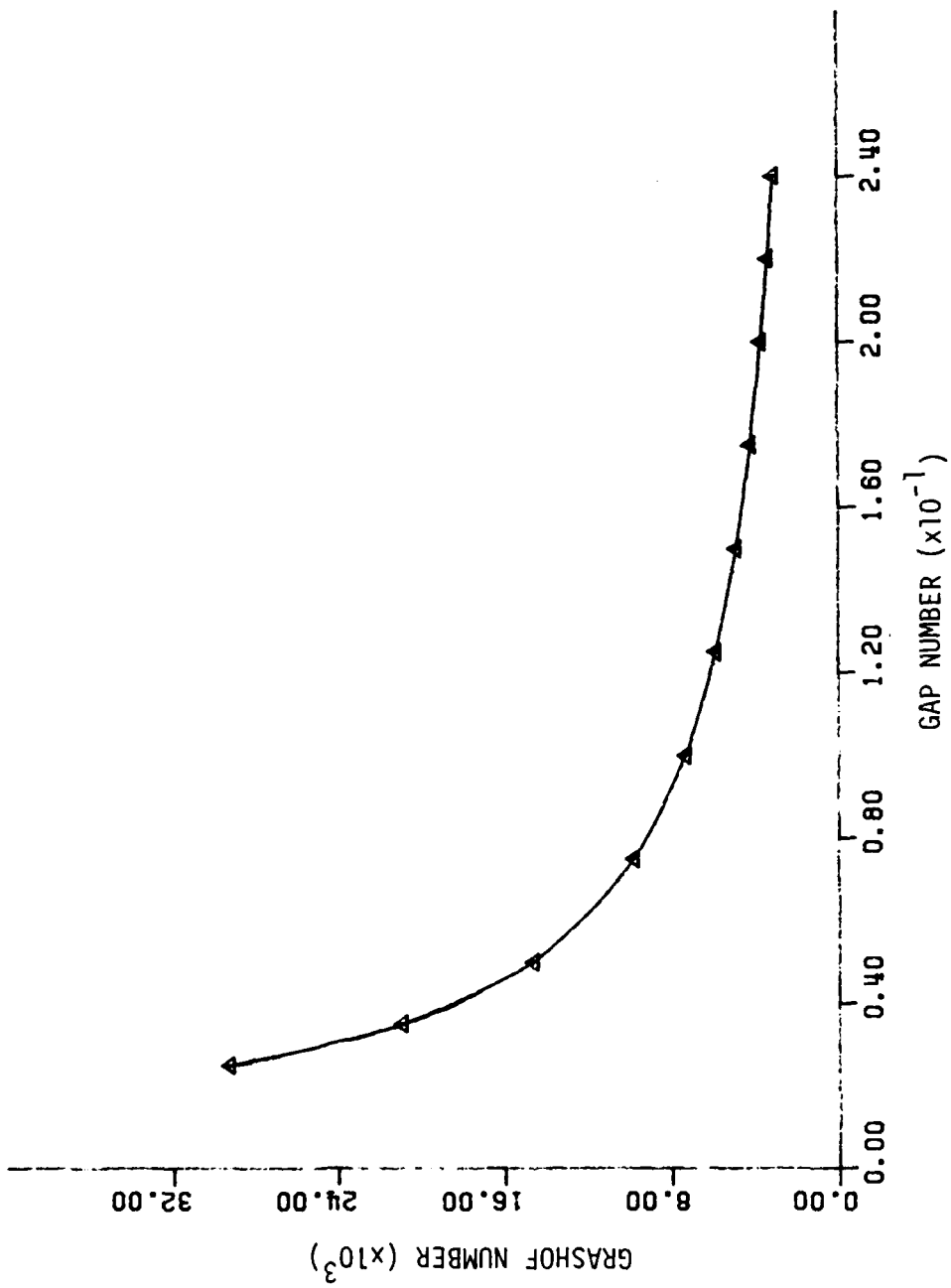

Figure 6.32. Zero-Prandtl number stability curve: Grashof number (based on gap width, Gr_{b-a}) as a function of gap number

This relationship is very similar to that for hydrodynamic instability (Pr = 0), except the proportionality constant differs by a factor of two.

Taking the above approach a step further, one can also determine a stability curve based on finite-Prandtl number by using the relation $\tilde{G} = 5.2\ Pr^{1/4}$, where $\hat{G} = 5.2$ again represents the transitional value for Pr = 0. The new stability curve is shown in Figure 6.33. These analytical predictions were compared against numerically predicted transitional values of $\tilde{G}$ (obtained from the finite-Prandtl number boundary-layer equations) for four different small-Prandtl number fluids (see Table 6.3).

Table 6.3 indicates that for small-Prandtl numbers, the relationship $\tilde{G} = 5.2\ Pr^{1/4}$ appears to be valid for predicting the transitional $\tilde{G}$ associated with hydrodynamic instability in the vertical sections of narrow annuli. For Pr = .02, an initial seven-cell unsteady flow field, resembling that of Pr = 0, was obtained at $\tilde{G} = 1.92$.

Table 6.3. Numerical predictions of $\tilde{G}$ transitional as a function of Prandtl number

Prandtl number	$\tilde{G}$ (transitional)	$\hat{G}(= \tilde{G} \cdot Pr^{-1/4})$
.02	1.92	5.106
.2	3.42	5.114
.3	3.80	5.135
.35	3.99	5.187

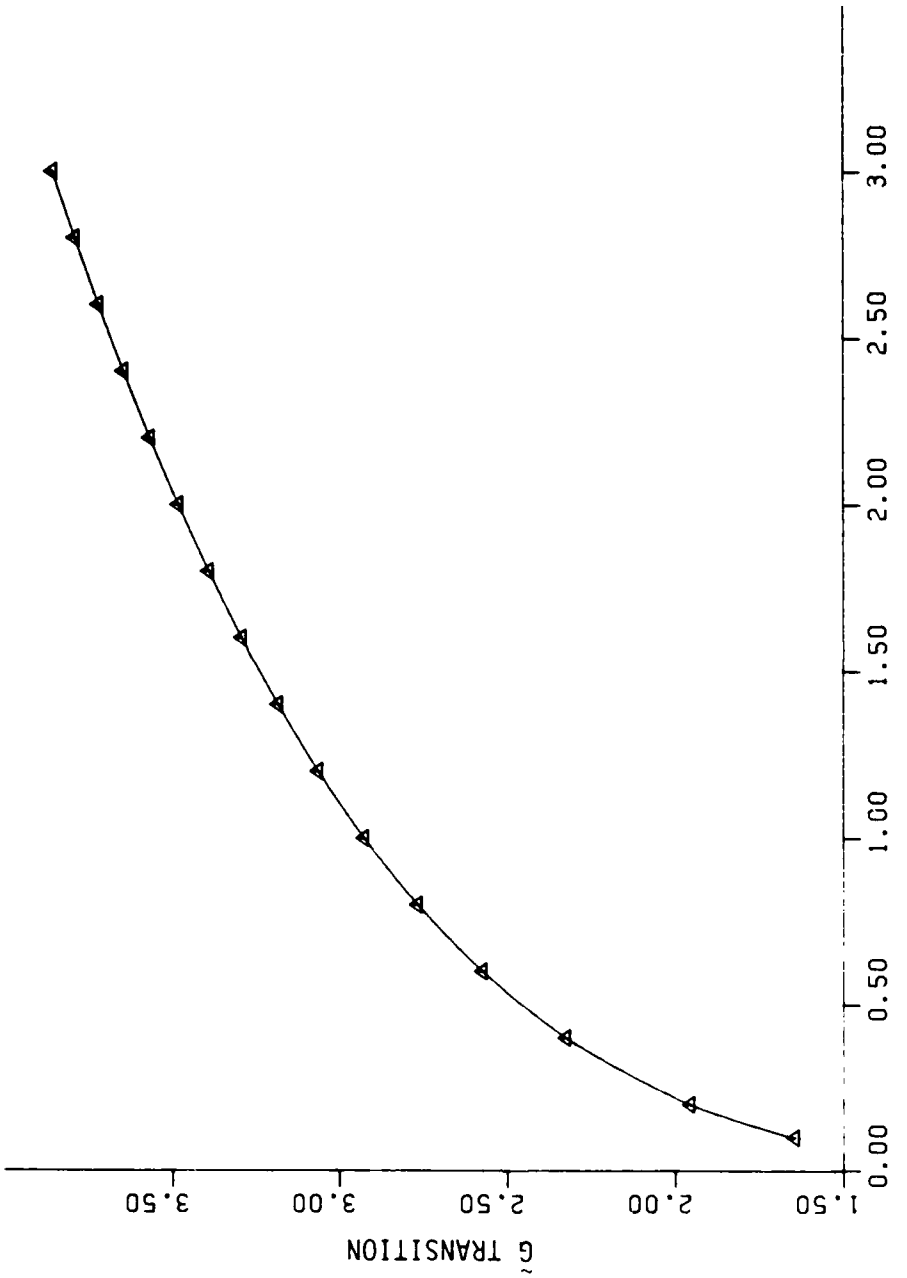

Figure 6.33. Finite-Prandtl number stability curve: $\tilde{G}$ transitional ($\tilde{G}_{TR} = 5.2\ Pr^{1/4}$) as a function of Prandtl number

However, for Pr = .35 (at $\tilde{G}$ = 3.99), an interesting change occurred--only a six-cell pattern resulted (see Figure 6.34) and the solution achieved a steady-state condition similar to that reported for the cellular instability between narrow vertical slots. Also, at Pr = .35, the isotherms were no longer perfectly concentric as with the Pr = 0 solution. Instead, they responded quite closely with the fluid motion (see Figure 6.35).

From these results, it appears that the same type of hydrodynamic instability as for Pr = 0 extends to at least Pr = .35. But, the nature of the multicellular flow has changed from seven-cells unsteady for Pr = .02 to six-cells steady with Pr = .35. Perhaps, though, if one stresses the Pr = .35 case past $\tilde{G}$ = 3.99, an unsteady cellular motion may ensue. Note that for Pr = .2 and .3, the cellular flow field was not resolved; only the point of instability was determined.

The two stability curves described above should provide for simple and convenient comparisons to future related studies of narrow horizontal annuli (especially experimental ones). Note that the curve in Figure 6.33 could easily be extended for comparison to data in the larger Prandtl number range, thus, eventually establishing an acceptance band on this asymptotically generated stability curve.

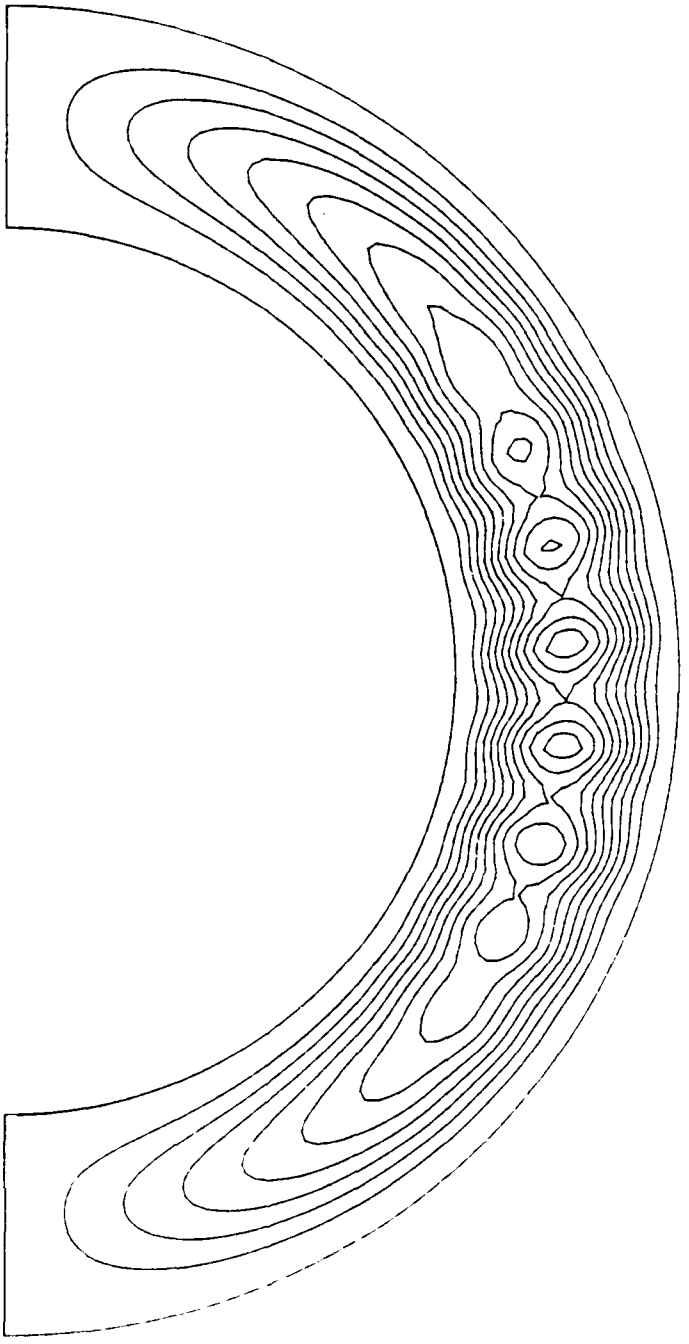

Figure 6.34. Streamlines of the steady six-cellular flow field for Pr = .35 at $\tilde{G}$ = 3.99 (diameter ratio = 1.5)

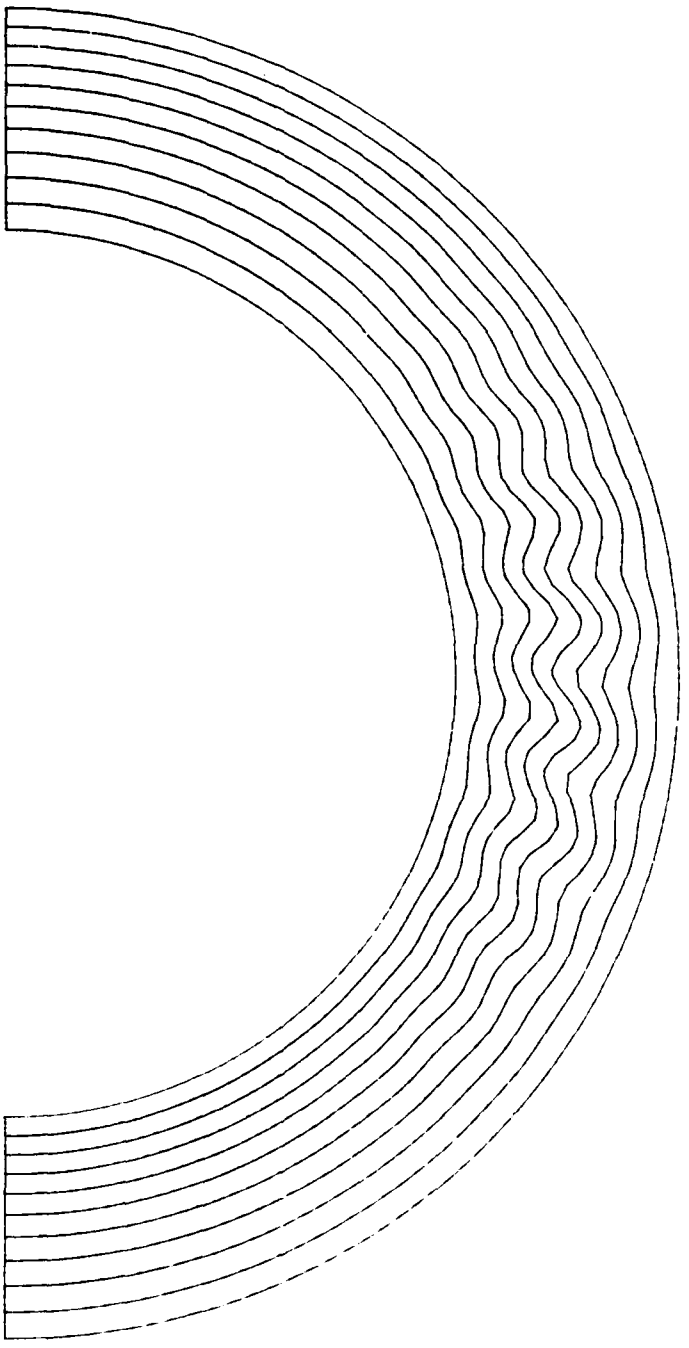

Figure 6.35. Isotherms of the steady six-cellular flow field for Pr = .35 at $\tilde{G}$ = 3.99 (diameter ratio = 1.5)

7. CONCLUSIONS

Numerical solutions of the 2-D Navier-Stokes equations yielded steady laminar multicellular flow for air near the top portions of narrow horizontal isothermal concentric cylinders. It was shown that hysteresis behavior exists for G = .100 and .200, with regard to sudden changes in the mean Nusselt number and average shear-stress as the Rayleigh number was slowly increased and then decreased past the multicellular transition point. Also, for G less than approximately .175, the results for air indicate that the transitional Rayleigh number increases as the gap number decreases. The minimum transitional Rayleigh number occurred at Ra_{b-a} = 2400 for G = .175.

In performing this multicellular flow study, first-order upwind differencing of the nonlinear convective terms proved inadequate. In relation to the pretransitional flow field cases, the first-order method was in good agreement with the results obtained from the second-order central-differenced numerical scheme. However, for the higher Rayleigh number flow regimes, the artificial viscosity associated with the first-order differencing of the nonlinear convective terms suppressed the development of secondary counter-rotating cells. Thus, it appears that at least second-order accuracy is needed to properly capture multicellular flow behavior. Moreover, multicellular flow resolution is also strongly dependent upon mesh size. That is, coarse meshes frequently failed to resolve the multicells, while finer meshes would sometimes result in asymmetric cellular patterns

when not enough nodes were concentrated in the thermal plume region for air.

A high Rayleigh number/small-gap asymptotic expansion theory was constructed which simplified the 2-D Navier-Stokes equations into Cartesian-like boundary-layer equations. Analytical perturbative solutions to these equations were obtained and the results compared favorably with the pretransitional numerical data generated in the 2-D Navier-Stokes hysteresis study of this thesis. For the limit as $\tilde{G} \to 0$, the boundary-layer equations reduced to viscous-dominated Stokes-flow equations, as shown in Chapter 4. This implies that for either $Ra \to 0$ or $G \to 0$, a conductive-dominated flow results.

In addition, simplified limiting equations for $Pr \to 0$ and $Pr \to \infty$ were obtained from the finite-Prandtl number boundary-layer equations. In the $Pr \to \infty$ limit, only the nonlinear terms in the energy equation remained and the vorticity equation reduced to a Stokes-flow equation, suggesting the possibility of a Bénard-type thermal instability, as seen with air near the top portion of narrow annuli. In direct contrast, the energy equation decoupled from the vorticity equation and reduced to simply $T = 1-r$ for the limit as $Pr \to 0$. Thus, only the nonlinear terms in the vorticity equation came into play, suggesting a source of hydrodynamic instability.

When the $Pr \to 0$ equations were solved numerically, an unsteady time-periodic multicellular instability developed (at $\hat{G} = 5.2$) in the vertical portions of a narrow horizontal annulus. Both the wavenumber and the transitional Grashof number (based on gap width) of the

initial seven-cellular instability compared favorably with the steady six-cellular instability experienced in a narrow vertical slot of aspect ratio equal to 15, as studied by Vest and Arpaci (1969) and Lee and Korpela (1983).

Upon increasing time, cyclic changes in the multicellular flow pattern resulted for $\hat{G} = 5.2$, forming an 8-7-8-7 repetitive cellular behavior. However, this periodic flow pattern was lost when $\hat{G}$ was increased from 5.2 to 5.5, resulting in a seemingly chaotic cellular behavior between nine, ten and eleven cells.

Also, the $Pr \to 0$ analytical pretransitional solutions were in good agreement with the numerical results up to $\hat{G} = 5.1$. Based on this comparison, the $Pr \to 0$ problem appeared linear and steady prior to the point of instability.

Moreover, a universal relationship for small-Prandtl number fluids,

$$Gr_{b-a} = \frac{731}{G} \quad ,$$

was suggested as a simple guide for predicting the onset of hydrodynamic instability between narrow vertical slot-like geometries.

Figure 6.13 shows that for air (Pr = .706) in very narrow-gap widths ($G < .075$), thermal instability sets in near $\tilde{G} = 3.90$. But for Pr = 0, hydrodynamic instability sets in at $\hat{G} = 5.2$, which corresponds to a $\tilde{G}$ of approximately 4.8 for air when using the analytical relation $\tilde{G} = 5.2\ Pr^{1/4}$. This difference in $\tilde{G}$ indicates that the mechanism which

triggers the instability for air is different than that for Pr = 0 (as previously discussed), and is probably largely due to the nonlinear terms in the energy equation being coupled with the buoyancy term $\cos \psi \frac{\partial T}{\partial \psi}$ in the 2-D Navier-Stokes equations (see Appendix B). Considering the above, competing effects of both thermal and hydrodynamic instability may result for Prandtl numbers between zero and .706.

In order to more fully support and study the nature of the unsteady multicellular instability described in this research effort, an experimental analysis of a narrow horizontal annulus filled with liquid mercury (Pr = .02) is recommended as a possible follow-up project. Also, numerical solutions relating to $\hat{G}$ = 5.3 or 5.4 should be carried out to determine if a doubly-periodic cellular behavior does indeed precede the chaotic state noted at $\hat{G}$ = 5.5, as suggested in the 'ordered path to chaos' scenario described by Ruelle and Takens (1971).

In addition, the energy spectrum of the fluid motion at $\hat{G}$ = 5.2 and 5.5 could be calculated in order to reveal any type of spectral broadening (or fundamental frequencies) associated with flow changes from time-periodic to chaotic-like behavior.

Lastly, the Pr $\rightarrow \infty$ boundary-layer equations should be solved numerically to determine the nature of any cellular instability that might develop. In the same spirit, the limiting 2-D Navier-Stokes equations derived in Appendix B should also be further investigated numerically for different size gap widths.

In closing, since natural convective flow instabilities generally develop slowly, especially in narrow horizontal annuli where the geometry itself limits the number of degrees of freedom, a more thorough investigation of laminar flow transition can be undertaken. Also, it has been conjectured that the transition to chaos in a system with many degrees of freedom (such as a fluid flow at large Reynolds numbers) is not qualitatively different from the transition to chaos in a system with a few degrees of freedom (Jensen, 1987). Thus, it is hoped that further study of simple geometries, such as described in this thesis, will lead to a deeper understanding of the nonlinear processes involved in the mysterious, yet ever-present dynamics of fluid flow instability phenomena.

8. REFERENCES

Abbott, M. R. 1964. A numerical method for solving the equations of natural convection in a narrow concentric cylindrical annulus with a horizontal axis. Quart. J. Mech. and Applied Math. 17: 471-481.

Arakawa, A. 1966. Computational design of a long-term numerical integration of the equations of fluid motion: Two dimensional incompressible flow. J. Comp. Phys. 1:119-143.

Arpaci, V. S. and P. S. Larsen. 1984. Convection heat transfer. Prentice-Hall, Inc., Englewood Cliffs, New Jersey.

Astill, K. N., H. Leong and R. Martorana. 1979. A numerical solution for natural convection in concentric spherical annuli. R-1028. The Charles Stark Draper Laboratory, Inc., Cambridge, MA.

Benjamin, T. B. 1978. Bifurcation phenomena in steady flows of a viscous fluid. Proc. R. Soc. London, Ser. A, 359:1-26.

Benjamin, T. B. and T. Mullin. 1982. Notes on the multiplicity of flows in the Taylor experiment. J. Fluid Mech. 121:219-230.

Bird, R. B., W. E. Stewart and E. N. Lightfoot. 1960. Transport phenomena. John Wiley & Sons, Inc., New York.

Bishop, E. H. and C. T. Carley. 1966. Photographic studies of natural convection between concentric cylinders. Proc. Heat Trans. Mech. Inst. 63-78.

Bishop, E. H., R. S. Kolflat, L. R. Mack and J. A. Scanlan. 1964. Convective heat transfer between concentric spheres. Proc. Heat Trans. Mech. Inst. 69-80.

Bishop, E. H., L. R. Mack and J. A. Scanlan. 1966. Heat transfer by natural convection between concentric spheres. Int. J. Heat Mass Trans. 9:649-662.

Bishop, E. H., C. T. Carley and R. E. Powe. 1968. Natural convective oscillatory flow in cylindrical annuli. J. Heat and Mass Trans. 11:1741-1752.

Boyd, R. D. 1981. A unified theory for correlating steady laminar natural convective heat transfer data for horizontal annuli. Int. J. Heat Mass Trans. 24(9):1545-1548.

Brandstäter, A., J. Swift, H. L. Swinney and A. Wolf. 1983. Low-dimensional chaos in a hydrodynamic system. Phys. Rev. Letters 51(b):1442-1445.

Busse, F. H. and R. M. Clever. 1981. An asymptotic model of two-dimensional convection in the limit of low Prandtl number. J. Fluid Mech. 102:75-83.

Caltagirone, J. P., M. Combarnous and A. Mojtabi. 1979. Natural convection between two concentric spheres: Transition towards a multicellular flow. Proc. of the First Int. Conf. on Numerical Methods in Thermal Problems, Pineridge, Swansea, U.K.

Chand, J. and D. Vir. 1980. Natural convection heat transfer from horizontal cylinders. IE (I) J.-CH. 60:34-40.

Chandrashekar, B., P. Vasseur and T. Hung Nguyen. 1984. Natural convection in a heat generating fluid bound by two horizontal concentric cylinders. The Can. J. Chem. Eng. 62:482-489.

Charrier-Mojtabi, M. C., A. Mojtabi and J. P. Caltagirone. 1979. Numerical solution of a flow due to natural convection in horizontal cylindrical annulus. ASME J. Heat Trans. 101:171-173.

Cho, C. H., K. S. Chang and K. H. Park. 1982. Numerical simulation of natural convection in concentric and eccentric horizontal cylindrical annuli. ASME J. Heat Trans. 104:624-630.

Choi, I. G. and S. A. Korpela. 1980. Stability of the conduction regime of natural convection in a tall vertical annulus. J. Fluid Mech. 99:725-738.

Chou, F. C. and G. J. Huang. 1984. Combined free and forced laminar convection in horizontal rectangular channels for high ReRa. The Can. J. Chem. Eng. 62:830-836.

Clausing, A. M. and S. N. Kempka. 1981. The influences of property variations on natural convection from vertical surfaces. ASME J. Heat Trans. 103:609-612.

Clever, R. M. and F. H. Busse. 1981. Low-Prandtl-number convection in a layer heated from below. J. Fluid Mech. 102:61-74.

Cliffe, K. A. 1983. Numerical calculations of two-cell and single-cell Taylor flows. J. Fluid Mech. 135:219-233.

Coles, D. 1965. Transition in circular Covette flow. J. Fluid Mech. 21:385-425.

Crawford, L. and R. Lemlich. 1962. Natural convection in horizontal concentric cylindrical annuli. I&EC Fund. 1(4):260-264.

Currie, I. G. 1974. Fundamental mechanics of fluids. McGraw-Hill, Inc., New York.

Custer, J. R. and E. J. Shaughnessy. 1977a. Thermoconvective motion of low Prandtl number fluids within a horizontal cylindrical annulus. ASME J. Heat Trans. 99:596-602.

Custer, J. R. and E. J. Shaughnessy. 1977b. Natural convection in liquid metals in an enclosure. ASME J. Heat Trans. 99:675-676.

Daniels, P. G. and P. M. Eagles. 1983. Slender channel theory in flow between two cylinders. J. Eng. Math. 17:125-147.

Eagles, P. M. 1974. On the torque of wavy vortices. J. Fluid Mech. 62(1):1-9.

Edelson, E. 1986. The ubiquity of nonlinearity. MOSAIC 17(3):10-17.

Elder, J. W. 1965. Laminar free convection in a vertical slot. J. Fluid Mech. 23(1):77-98.

Elder, J. W. 1966. Numerical experiments with free convection in a vertical slot. J. Fluid Mech. 24(4):823-843.

Farouk, B. and S. I. Güceri. 1982. Laminar and turbulent natural convection in the annulus between horizontal concentric cylinders. ASME J. Heat Trans. 104:631-636.

Fasel, H. 1976. Investigation of the stability of boundary layers by a finite-difference model of the Navier-Stokes equations. J. Fluid Mech. 78(2):355-383.

Fife, P. C. and D. D. Joseph. 1969. Existence of convective solutions of the generalized Bénard problem which are analytic in their norm. Arch. Rational Mech. Anal. 33:116-138.

Gebhart, B. 1962. Effects of viscous dissipation in natural convection. J. Fluid Mech. 14:225-232.

Giglio, M., S. Musazzi and V. Perini. 1981. Transition to chaotic behavior via a reproducible sequence of period-doubling bifurcations. Phys. Rev. Letters 47(4):243-246.

Gill, A. E. 1966. The boundary-layer regime for convection in a rectangular cavity. J. Fluid Mech. 26(3):515-536.

Goldstein, S. 1948. On laminar boundary-layer flow near a position of separation. Quart. J. Mech. and Applied Math. 1:43-69.

Gray, D. and A. Giorgini. 1976. The validity of the Boussinesq approximation for liquids and gases. Int. J. Heat Mass Trans. 19:545-551.

Grebogi, C., E. Ott and J. A. Yorke. 1983. Are three-frequency quasiperiodic orbits to be expected in typical nonlinear dynamical systems? Phys. Rev. Letters 51(5):339-342.

Grigull, U. and W. Hauf. 1966. Natural convection in horizontal cylindrical annuli. Proc. of the Third Int. Heat Trans. Conf., Am. Inst. Chem. Engrs., New York.

Guckenheimer, J. 1986. Strange attractors in fluids: Another view. Ann. Rev. Fluid Mech. 18:15-31.

Hessami, M. A., A. Pollard and R. D. Rowe. 1984. Numerical calculation of natural convective heat transfer between horizontal concentric isothermal cylinders-effects of the variation of the fluid properties. ASME J. Heat Trans. 106:668-671.

Hessami, M. A., A. Pollard, R. D. Rowe and D. W. Rtuh. 1985. A study of free convective heat transfer in a horizontal annulus with a large radii ratio. ASME J. Heat Trans. 107:603-610.

Hodnett, P. F. 1973. Natural convection between horizontal heated concentric circular cylinders. J. Applied Math. and Phys. 24:507-516.

Holmes, P. J. and F. C. Moon. 1983. Strange attractors and chaos in nonlinear mechanics. J. Applied Mech. 50:1021-1032.

Horne, R. N. and M. J. O'Sullivan. 1974. Oscillatory convection in a porous medium heated from below. J. Fluid Mech. 66(2):339-352.

Huetz, J. and J. P. Petit. 1974. Natural and mixed convection in concentric annular spaces-experimental and theoretical results for liquid metals. Proc. of the Fifth Int. Heat Trans. Conf., Tokyo, Japan.

Ingham, D. B. 1981. Heat transfer by natural convection between spheres and cylinders. Num. Heat Trans. 4:53-67.

Itoh, M., T. Fujita, N. Nishiwaki and M. Hirata. 1970. A new method of correlating heat-transfer coefficients for natural convection in horizontal cylindrical annuli. Int. J. Heat Mass Trans. 13:1364-1368.

Jacobs, D. A. H. 1973. A corrected upwind differencing scheme using a strongly implicit solution procedure. Pages 84-98 in Proc. of the Int. Conf. on Num. Methods in Fluid Dynamics, Univ. of Southampton, Southampton, England.

Jeffreys, H. 1927. Some cases of instability in fluid motion. Proc. R. Soc. London, Ser. A. 118:195-208.

Jensen, R. V. 1987. Classical chaos. Amer. Sci. 75:168-181.

Jischke, M. C. and M. Farshchi. 1980. Boundary layer regime for laminar free convection between horizontal circular cylinders. ASME J. Heat Trans. 102:228-235.

Kassinos, A. 1986. Melting in rectangular geometries in the presence of subcooling and density change effects. M.S. Thesis. Iowa State University, Ames, IA.

Keller, H. B. 1977. Numerical solutions of bifurcation and nonlinear eigenvalue problems. Pages 359-384 in P. H. Rabinowitz, ed. Applications of bifurcation theory. Academic Press, New York.

Kolodner, P., R. W. Walden, A. Passner and C. M. Surko. 1986. Rayleigh-Benard convection in an intermediate-aspect-ratio rectangular container. J. Fluid Mech. 163:195-226.

Korpela, S. A. 1974. A study on the effect of Prandtl number on the stability of the conduction regime of natural convection in an inclined slot. Int. J. Heat Mass Trans. 17:215-222.

Korpela, S. A., D. Gözüm and C. B. Baxi. 1973. On the stability of the conduction regime of natural convection in a vertical slot. Int. J. Heat Mass Trans. 16:1683-1690.

Kuehn, T. H. and R. J. Goldstein. 1976a. An experimental and theoretical study of natural convection in the annulus between horizontal concentric cylinders. J. Fluid Mech. 74(4):695-719.

Kuehn, T. H. and R. J. Goldstein. 1976b. Correlating equations for natural convection heat transfer between horizontal circular cylinders. Int. J. Heat Mass Trans. 19:1127-1134.

Kuehn, T. H. and R. J. Goldstein. 1978. An experimental study of natural convection heat transfer in concentric and eccentric horizontal cylindrical annuli. ASME J. Heat Trans. 100:635-640.

Kuehn, T. H. and R. J. Goldstein. 1980a. Numerical solution to the Navier-Stokes equations for laminar natural convection about a horizontal isothermal circular cylinder. Int. J. Heat Mass Trans. 23:971-979.

Kuehn, T. H. and R. J. Goldstein. 1980b. A parametric study of Prandtl number and diameter ratio effects on natural convection heat transfer in horizontal cylindrical annuli. ASME J. Heat Trans. 102:768-770.

Kuiken, H. K. and Z. Rotem. 1971. Asymptotic solution for plume at very large and small Prandtl numbers. J. Fluid Mech. 45(3): 585-600.

Kuo, H. P., S. A. Korpela, A. Chait and P. S. Marcus. 1986. Stability of natural convection in a shallow cavity. Proc. of the Eighth Int. Heat Trans. Conf., San Francisco, CA 4:1539-1544.

Lanford, O. E. III. 1982. The strange attractor theory of turbulence. Ann. Rev. Fluid Mech. 14:347-364.

Lee, T. S. 1984. Numerical experiments with laminar fluid convection between concentric and eccentric heated rotating cylinders. Num. Heat Trans. 7:77-87.

Lee, Y. and S. A. Korpela. 1983. Multicellular natural convection in a vertical slot. J. Fluid Mech. 126:91-121.

Liang, S. F., A. Vidal and A. Acrivos. 1969. Buoyancy-driven convection in cylindrical geometries. J. Fluid Mech. 36(2):239-256.

Lis, J. 1966. Experimental investigation of natural convection heat transfer in simple and obstructed horizontal annuli. Proc. of the Third Int. Heat Trans. Conf., Chicago, IL.

Liu, C., W. K. Mueller and F. Landis. 1962. Natural convection heat transfer in long horizontal cylindrical annuli. ASME Int. Devel. in Heat Trans., Proc. of the 1961-1962 Int. Heat Trans. Conf., University of Colorado and London, England.

Lorenz, E. 1963. Deterministic nonperiodic flow. J. of Atmos. Sci. 20:130-141.

McAdams, W. H. 1954. Heat Transmission. 3rd ed. McGraw-Hill, New York.

McLaughlin, J. B. and P. C. Martin. 1975. Transition to turbulence in a statically stressed fluid system. Phys. Rev. A. 12(1): 186-203.

Mack, L. R. and E. H. Bishop. 1968. Natural convection between horizontal concentric cylinders for low Rayleigh numbers. Quart. J. Mech. and Applied Math. 21(2):223-241.

Mack, L. R. and H. C. Hardee. 1968. Natural convection between concentric spheres at low Rayleigh numbers. Int. J. Heat Mass Trans. 11:387-396.

Mahony, D. N., R. Kumar and E. H. Bishop. 1985. Numerical investigation of variable property effects on laminar natural convection of gases between two horizontal isothermal cylinders. ASME Nat'l. Heat Trans. Conf., Denver, CO. 85-HT-23.

Marcus, P. S. 1981. Effects of truncation in modal representations of thermal convection. J. Fluid Mech. 103:241-255.

Mittai, R. C. and P. K. Sharma. 1985. A one-parameter family of LAD methods for the steady-state Navier-Stokes equations. Comp. & Fluids 13(4):507-511.

Nandakumar, K. and J. H. Masliyah. 1982. Bifurcation in steady laminar flow through curved tubes. J. Fluid Mech. 119:475-490.

Nandakumar, K., J. H. Masliyah and H. Law. 1985. Bifurcation in steady laminar mixed convection flow in horizontal ducts. J. Fluid Mech. 152:145-161.

Newhouse, S., D. Ruelle and F. Takens. 1978. Occurrence of strange axiom A attractors near quasi periodic flows on T^m, $m \geq 3$. Commun. Math. Phys. 64:35-40.

Ohring, S. 1986. Calculations of self-excited impinging jet flow. J. Fluid Mech. 163:69-98.

Orszag, S. A. and L. C. Kells. 1980. Transition to turbulence in plane Poiseville and plane Covette flow. J. Fluid Mech. 96(1): 159-205.

Orszag, S. A. and A. T. Patera. 1983. Secondary instability of wall-bounded shear flows. J. Fluid Mech. 128:347-385.

Ozoe, H., K. Fujii, T. Shibata and H. Kuriyama. 1985. Three-dimensional numerical analysis of natural convection in a spherical annulus. Num. Heat Trans. 8:383-406.

Panton, R. L. 1984. Incompressible flow. John Wiley & Sons, Inc., New York.

Pepper, D. W. and S. D. Harris. 1977. Numerical simulation of natural convection in closed containers by a fully implicit method. ASME J. Fluids Eng. 99:649-656.

Powe, R. E. 1974. Bounding effects on the heat loss by free convection from spheres and cylinders. ASME J. Heat Trans. 96(4): 558-560.

Powe, R. E. and R. M. Comfort. 1978. Numerical solution of two-dimensional natural convection in enclosed spaces. ASME Winter Annual Meeting, San Francisco, CA. 78-WA-HT-11.

Powe, R. E., C. T. Carley and E. H. Bishop. 1969. Free convective flow patterns in cylindrical annuli. ASME J. Heat Trans. 91(3): 310-314.

Powe, R. E., C. T. Carley and S. L. Carruth. 1971. A numerical solution for natural convection in cylindrical annuli. ASME J. Heat Trans. 93:210-220.

Proctor, M. R. E. 1977. Inertial convection at low Prandtl number. J. Fluid Mech. 82(1):97-114.

Projahn, U., H. Rieger and H. Beer. 1981. Numerical analysis of laminar natural convection between concentric and eccentric cylinders. Num. Heat Trans. 4:131-146.

Prusa, J. 1983. A spatial Stefan problem modified by melting around a horizontal heated cylinder. Ph.D. Dissertation. University of Illinois at Urbana-Champaign, Urbana, IL.

Prusa, J. and L. S. Yao. 1983. Natural convection heat transfer between eccentric horizontal cylinders. ASME J. Heat Trans. 105:108-116.

Quon, C. 1972. High Rayleigh number convection in an enclosure - A numerical study. The Phys. of Fluids 15(1):12-19.

Rabinowitz, P. H. 1968. Existence and nonuniqueness of rectangular solutions of the Bénard problem. Arch. Rational Mech. Anal. 29: 32-57.

Raithby, G. D. 1976. A critical evaluation of upstream differencing applied to problems involving fluid flow. Computer Methods in Applied Mech. and Eng. 9:75-103.

Raithby, G. D. and G. T. Hollands. 1975. A general method of obtaining approximate solutions to laminar and turbulent free convection problems. Pages 265-315 in T. F. Irvine, Jr. and J. P. Hartnett, eds. Advances in heat transfer. Vol. 11. Academic Press, New York.

Rao, Y., Y. Miki, K. Fukada, Y. Takata and S. Hasegawa. 1985. Flow patterns of natural convection in horizontal cylindrical annuli. Int. J. Heat Mass Trans. 28(3):705-714.

Ratzel, A. C., C. E. Hickox and D. K. Gartling. 1979. Techniques for reducing thermal conduction and natural convection heat losses in annular receiver geometries. ASME J. Heat Trans. 101:108-113.

Reynolds, W. C. and M. C. Potter. 1967. Finite-amplitude instability of parallel shear flows. J. Fluid Mech. 27(3):465-492.

Roache, P. J. 1976. Computational fluid dynamics. Hermosa Publishers, Albuquerque, New Mexico.

Robbins, K. A. 1979. Periodic solutions and bifurcation structure at high R in the Lorenz model. SIAM J. Applied Math. 36(3):457-472.

Rotem, Z. 1972. Conjugate free convection from horizontal conducting circular cylinders. Int. J. Heat Mass Trans. 15:1679-1693.

Rotem, Z. and L. Claassen. 1969. Natural convection above unconfined horizontal surfaces. J. Fluid Mech. 38(1):173-192.

Rudraiah, N. and T. Musuoka. 1982. Asymptotic analysis of natural convection through horizontal porous layer. Int. J. Eng. Sci. 1:27-39.

Rudraigh, N. and S. B. Rao. 1982. Nonlinear cellular convection and heat transport in a porous medium. Applied Sci. Research 39:21-43.

Ruelle, D. and F. Takens. 1971. On the nature of turbulence. Commun. Math. Phys. 20:167-192.

Sande, E. van de and B. J. G. Hamer. 1979. Steady and transient natural convection in enclosures between horizontal circular cylinders (constant heat flux). Int. J. Heat Mass Trans. 22:361-370.

Scanlan, J. A., E. H. Bishop and R. E. Powe. 1970. Natural convection heat transfer between concentric spheres. Int. J. Heat Mass Trans. 13:1857-1872.

Seki, N., S. Fukusako and H. Inaba. 1978. Visual observation of natural convective flow in a narrow vertical cavity. J. Fluid Mech. 84(4):695-704.

Sen, P. K., D. Venkateswarlu and S. Maji. 1985. On the stability of pipe-Poiseville flow to finite-amplitude axisymmetric and non-axisymmetric disturbances. J. Fluid Mech. 158:289-316.

Solov'ev, S. V. and A. S. Lyalikov. 1979. Natural convective heat exchange between isothermal concentric spheres. Inzhenero-Fizicheskii Zhurnal. 36(5):807-813.

Southwell, R. V. 1946. Relaxation methods in theoretical physics. Oxford University Press, New York.

Spalding, D. B. 1972. A novel finite difference formulation for differential expressions involving both first and second derivatives. Int. J. for Num. Methods in Eng. 4:551-559.

Sparrow, E. M. and J. L. Gregg. 1958. The variable fluid-property problem in free convection. ASME J. Heat Trans. 80:879-886.

Sreenivasan, K. R. and P. J. Strykowski. 1984. On analogies between turbulence in open flows and chaotic dynamical systems. Pages 191-196 in T. Tatsumi, ed. Turbulence and chaotic phenomena in fluids. Elsevier Science Publishers, B.V. (North-Holland).

Stewart, J. T. 1977. Bifurcation theory in nonlinear hydrodynamic stability. Pages 127-147 in P. H. Rabinowitz, ed. Applications of bifurcation theory. Academic Press, New York.

Stewartson, K. and J. T. Stuart. 1971. A non-linear instability theory for a wave system in plane Poiseuille flow. J. Fluid Mech. 48(3):529-545.

Stuart, J. T. 1960. On the non-linear mechanics of wave disturbances in stable and unstable parallel flows. J. Fluid Mech. 9:353-370.

Thomas, R. W. and Vahl Davis, G. de. 1970. Natural convection in annular and rectangular cavities - a numerical study. Proc. of the Fourth Int. Heat Trans. Conf., Paris, France, NC2.4.

Tsui, Y. T. and B. Tremblay. 1984. On transient natural convection heat transfer in the annulus between concentric, horizontal cylinders with isothermal surfaces. Int. J. Heat Mass Trans. 27(1):103-111.

Tuann, S. and M. D. Olson. 1978. Review of computing methods for recirculating flows. J. Comp. Phys. 29:1-19.

Vahl Davis, G. de and G. D. Mallinson. 1975. A note on natural convection in a vertical slot. J. Fluid Mech. 72(1):87-93.

Vahl Davis, G. de and G. D. Mallinson. 1976. An evaluation of upwind and central difference approximations by a study of recirculating flow. Comp. and Fluids 4:29-43.

Vahl Davis, G. de and R. W. Thomas. 1969. Natural convection between concentric vertical cylinders. Phys. Fluids Suppl. II:198-207.

Vest, C. M. and V. S. Arpaci. 1969. Stability of natural convection in a vertical slot. J. Fluid Mech. 36(1):1-15.

Wacholder, E., S. Kaizerman and E. Elias. 1982. Numerical analysis of the stability and transient behavior of natural convection loops. Int. J. Eng. Sci. 20(11):1235-1254.

Walton, I. C. 1980. The stability of free convection in a horizontal cylindrical annulus. Quart. J. Mech. and Applied Math. 33(2): 125-139.

Warrington, R. O., Jr. and R. E. Powe. 1985. The transfer of heat by natural convection between bodies and their enclosures. Int. J. Heat Mass Trans. 28(2):319-330.

Weinstein, H. G., H. L. Stone and T. V. Kwan. 1970. Simultaneous solution of multiphase reservoir flow equations. Soc. of Petroleum Eng. Journal, June:99-110.

Wirtz, R. A. and L. H. Liu. 1975. Numerical experiments on the onset of layered convection in a narrow slot containing a stably stratified fluid. Int. J. Heat Mass Trans. 18:1299-1305.

Yao, L. S. 1980. Analysis of heat transfer in slightly eccentric annuli. ASME J. Heat Trans. 102:279-284.

Yao, L. S. and F. F. Chen. 1980. Effects of natural convection in the melted region around a heated horizontal cylinder. ASME J. Heat Trans. 667-672.

Yin, S. H., R. E. Powe, J. A. Scanlan and E. H. Bishop. 1973. Natural convection flow patterns in spherical annuli. Int. J. Heat Mass Trans. 16:1785-1795.

9. ACKNOWLEDGMENTS

I wish to thank the Air Force, through AFIT sponsorship under Dr. Peter J. Torvik, for allowing me the valuable time and opportunity to pursue this advanced degree. I would like to thank my major professor, Dr. Joseph M. Prusa, for his suggestions and many hours of help with the numerical method and the writing of this thesis; Dr. Alric P. Rothmayer for introducing me to perturbation methods and greatly helping with the asymptotic analysis; Dr. Bruce R. Munson for his helpful assistance in analyzing numerical results; and thanks to Dr. William J. Cook and Dr. Leroy D. Sturges for their supportive discussion. I would also like to express my thanks to Dr. Richard H. Pletcher and Dr. George H. Junkhan for providing EVAX and Perkin-Elmer computer time; Adonis Kassinos for his graphics routine and help with the contour plots; and my sincere appreciation to Barbara Dubberke for typing this manuscript.

I would especially like to thank my wife, Ellen, for her love, patience and understanding when for the last two years, I have devoted more time to this thesis than to her. But most of all, I wish to thank my parents -- for they taught me how to live, to hope and to dream. To them, I dedicate this work.

10. APPENDIX A: ANALYTICAL COEFFICIENTS

The perturbative coefficients corresponding to the analytical solution of the finite-Prandtl number boundary-layer equations, (4.39) - (4.46), are listed below. Note again that all of the coefficients (A2 through H4) are functions of r only.

$$A2 = \frac{-r^9}{7560} + \frac{r^8}{1680} + \frac{-r^7}{1260} + \frac{r^4}{720} + \frac{-r^3}{690} + \frac{r^2}{2520}$$

$$B2 = \frac{r^9}{1512} + \frac{-r^8}{336} + \frac{r^7}{180} + \frac{-r^6}{180} + \frac{r^5}{360} + \frac{-r^3}{1512} + \frac{r^2}{5040}$$

$$C2 = \frac{-r^7}{105} + \frac{r^6}{30} + \frac{-r^5}{30} + \frac{r^2}{60} + \frac{-r}{115} + \frac{1}{1260}$$

$$D2 = \frac{r^7}{21} + \frac{-r^6}{6} + \frac{7r^5}{30} + \frac{-r^4}{6} + \frac{r^3}{18} + \frac{-r}{252} + \frac{1}{2520}$$

$$E2 = \frac{-r^{11}}{415800} + \frac{r^{10}}{75600} + \frac{-r^9}{45360} + \frac{r^6}{10800} + \frac{-r^5}{6900} + \frac{r^4}{15120} + \frac{-r}{387701}$$

$$F2 = \frac{r^{11}}{83160} + \frac{-r^{10}}{15120} + \frac{r^9}{6480} + \frac{-r^8}{5040} + \frac{r^7}{7560} + \frac{-r^5}{15120} + \frac{r^4}{30240} + \frac{-r}{997934}$$

$$G2 = \frac{-6r^{11}}{55} + \frac{3r^{10}}{5} + \frac{-23}{18} r^9 + \frac{5}{4} r^8 + \frac{-10}{21} r^7 + \frac{r^6}{30} + \frac{-r^5}{10} + \frac{r^4}{12} + \frac{-r}{277}$$

$$H2 = \frac{-4r^{11}}{55} + \frac{2}{5} r^{10} + \frac{-5}{6} r^9 + \frac{3}{4} r^8 + \frac{-5}{21} r^7 + \frac{2}{15} r^6 + \frac{-3}{10} r^5 + \frac{r^4}{6} + \frac{-r}{171}$$

$$A3 = \frac{r^{14}}{458640} + \frac{-r^{13}}{65520} + \frac{71r^{12}}{1163200} + \frac{-r^{11}}{17325} + \frac{r^{10}}{32400} + \frac{r^{9}}{90720} + \frac{-r^{8}}{38640}$$
$$+ \frac{4r^{7}}{152145} + \frac{-r^{6}}{37950} + \frac{r^{5}}{75600} + \frac{-r^{3}}{4695894} + \frac{-r^{2}}{1178430}$$

$$B3 = \frac{-r^{14}}{91728} + \frac{r^{13}}{13104} + \frac{-383r^{12}}{1663200} + \frac{3r^{11}}{7700} + \frac{-r^{10}}{2493} + \frac{23r^{9}}{90720} + \frac{-r^{8}}{10584}$$
$$+ \frac{r^{7}}{40740} + \frac{-r^{6}}{75600} + \frac{r^{5}}{151200} + \frac{-r^{3}}{1257992} + \frac{r^{2}}{5034689}$$

$$C3 = \frac{-r^{14}}{8255520} + \frac{r^{13}}{1179360} + \frac{-r^{12}}{439560} + \frac{r^{11}}{369600} + \frac{-r^{10}}{907200} + \frac{r^{9}}{1088640}$$
$$+ \frac{-r^{8}}{241920} + \frac{r^{7}}{162960} + \frac{-r^{6}}{248400} + \frac{r^{5}}{907200} + \frac{-r^{3}}{5865883}$$
$$+ \frac{r^{2}}{8519738}$$

$$D3 = \frac{r^{14}}{1651104} + \frac{-r^{13}}{235872} + \frac{r^{12}}{76680} + \frac{-r^{11}}{43200} + \frac{83r^{10}}{3230640} + \frac{-19r^{9}}{1088640}$$
$$+ \frac{r^{8}}{181440} + \frac{r^{7}}{795480} + \frac{-r^{6}}{544320} + \frac{r^{5}}{1814400} + \frac{r^{3}}{3724001}$$
$$+ \frac{-r^{2}}{4020927}$$

$$E3 = \frac{r^{14}}{9.0811 \times 10^{8}} + \frac{-r^{13}}{1.2973 \times 10^{8}} + \frac{r^{12}}{59875200} + \frac{-r^{9}}{5443200} + \frac{r^{8}}{2318400}$$
$$+ \frac{-r^{7}}{3175200} + \frac{r^{4}}{9304824} + \frac{-r^{3}}{26554595} + \frac{-r^{2}}{79473251}$$

$$F3 = \frac{-r^{14}}{1.8162 \times 10^{8}} + \frac{r^{13}}{25945920} + \frac{-r^{12}}{8553600} + \frac{r^{11}}{4989600} + \frac{-r^{10}}{5443200}$$

$$+ \frac{r^{8}}{5080320} + \frac{-r^{7}}{6350400} + \frac{r^{4}}{23950428} + \frac{r^{3}}{7.353 \times 10^{11}}$$

$$+ \frac{-r^{2}}{71688776}$$

$$G3 = \frac{r^{14}}{20020} + \frac{-r^{9}}{2860} + \frac{23r^{12}}{23760} + \frac{-r^{11}}{792} + \frac{r^{10}}{1512} + \frac{-r^{9}}{15120} + \frac{r^{8}}{3360} + \frac{-r^{7}}{2520}$$

$$+ \frac{r^{4}}{6648} + \frac{-r^{3}}{4656794} + \frac{-r^{2}}{19259}$$

$$H3 = \frac{r^{14}}{30030} + \frac{-r^{13}}{4290} + \frac{r^{12}}{1584} + \frac{-r^{11}}{1320} + \frac{r^{10}}{3024} + \frac{-r^{9}}{3780} + \frac{r^{8}}{1120} + \frac{-r^{7}}{1260}$$

$$+ \frac{r^{4}}{4104} + \frac{-r^{3}}{3172589} + \frac{-r^{2}}{12102}$$

$$A4 = \frac{r^{12}}{2520} + \frac{-r^{11}}{420} + \frac{71r^{10}}{12600} + \frac{-2r^{9}}{315} + \frac{r^{8}}{360} + \frac{r^{7}}{1260} + \frac{-r^{6}}{690} + \frac{8r^{5}}{7245} + \frac{-r^{4}}{1265}$$

$$+ \frac{r^{3}}{3780} + \frac{-r}{782649} + \frac{-1}{589215}$$

$$B4 = \frac{-r^{12}}{504} + \frac{r^{11}}{84} + \frac{-383r^{10}}{12600} + \frac{3r^{9}}{70} + \frac{-r^{8}}{27.7} + \frac{23r^{7}}{1260} + \frac{-r^{6}}{189} + \frac{r^{5}}{970} + \frac{-r^{4}}{2520}$$

$$+ \frac{r^{3}}{7560} + \frac{-r}{209665} + \frac{1}{2517345}$$

$$C4 = \frac{-r^{12}}{45360} + \frac{r^{11}}{7560} + \frac{-r^{10}}{3330} + \frac{r^{9}}{3360} + \frac{-r^{8}}{10080} + \frac{r^{7}}{15120} + \frac{-r^{6}}{4320} + \frac{r^{5}}{3880}$$

$$+ \frac{-r^{4}}{8280} + \frac{r^{3}}{45360} + \frac{-r}{977647} + \frac{1}{4259869}$$

$$D4 = \frac{r^{12}}{9072} + \frac{-r^{11}}{1512} + \frac{11r^{10}}{6390} + \frac{-11r^{9}}{4320} + \frac{83r^{8}}{35896} + \frac{-19r^{7}}{15120} + \frac{r^{6}}{3240} + \frac{r^{5}}{18940}$$

$$+ \frac{-r^{4}}{18144} + \frac{r^{3}}{90720} + \frac{r}{620785} + \frac{-1}{2010245}$$

$$E4 = \frac{r^{12}}{4989600} + \frac{-r^{11}}{831600} + \frac{r^{10}}{453600} + \frac{-r^{7}}{75600} + \frac{r^{6}}{41400} + \frac{-r^{5}}{75600} + \frac{r^{2}}{775402}$$

$$+ \frac{-r}{4425766} + \frac{-1}{39736626}$$

$$F4 = \frac{-r^{12}}{997920} + \frac{r^{11}}{166320} + \frac{-r^{10}}{64800} + \frac{r^{9}}{45360} + \frac{-r^{8}}{60480} + \frac{r^{6}}{90720} + \frac{-r^{5}}{151200}$$

$$+ \frac{r^{2}}{1995869} + \frac{r}{1.2255 \times 10^{11}} + \frac{-1}{35844388}$$

$$G4 = \frac{r^{12}}{110} + \frac{-3r^{11}}{55} + \frac{23r^{10}}{180} + \frac{-5r^{9}}{36} + \frac{5r^{8}}{84} + \frac{-r^{7}}{210} + \frac{r^{6}}{60} + \frac{-r^{5}}{60} + \frac{r^{2}}{554}$$

$$+ \frac{-r}{776133} + \frac{-1}{9629}$$

$$H4 = \frac{r^{12}}{165} + \frac{-2r^{11}}{55} + \frac{r^{10}}{12} + \frac{-r^{9}}{12} + \frac{5r^{8}}{168} + \frac{-2r^{7}}{105} + \frac{r^{6}}{20} + \frac{-r^{5}}{30} + \frac{r^{2}}{342}$$

$$+ \frac{-r}{528765} + \frac{-1}{6051}$$

11. APPENDIX B: LIMITING CONDITIONS OF THE 2-D NAVIER-STOKES EQUATIONS

Since the simplified boundary-layer equations of Chapter 4 (in the limits of $Pr \to 0$ and $Pr \to \infty$) applied only to the narrow-gap/high Rayleigh number regime, the effects of small and large Prandtl number on arbitrary gap size and Rayleigh number could not be explored. To consider these effects, the 2-D Navier-Stokes equations of Chapter 3 must be employed. This appendage will derive these limiting equations, and will explain the important features and differences of both approaches.

11.1. The $Pr \to 0$ Equations

In the limit as $Pr \to 0$, *the thermal-energy equation of* (3.1a) becomes:

$$\frac{\partial^2 T}{\partial r^2} + \left(r + \frac{1}{G}\right)^{-1} \frac{\partial T}{\partial r} + \left(r + \frac{1}{G}\right)^{-2} \frac{\partial^2 T}{\partial \psi^2} = 0 \qquad (11.1)$$

subject to the following boundary conditions (assuming symmetry):

$$T(0, \psi) = 1 \qquad (11.2a)$$

$$T(1, \psi) = 0 \qquad (11.2b)$$

$$\frac{\partial T}{\partial \psi}(r, \psi = 0, \pi) = 0 \quad . \qquad (11.2c)$$

Given Eqs. (11.2a-c), the solution to Eq. (11.1) is

$$T = 1 - \frac{\ell n(1 + G\cdot r)}{\ell n\ (1 + G)} \tag{11.3}$$

which is simply the steady-state conduction solution for the concentric cylindrical annulus. Because Eq. (11.3) is independent of ψ, one gets:

$$\frac{\partial T}{\partial \psi} = 0 \tag{11.4}$$

and

$$\frac{\partial T}{\partial r} = \frac{-G}{(1 + G\cdot r)\ell n(1 + G)} \quad . \tag{11.5}$$

Hence, for the limit as $Pr \to 0$, the buoyancy term, $\sim\cos\psi \frac{\partial T}{\partial \psi}$ in Eq. (3.1b), reduces to zero, whereas $\sin\psi \frac{\partial T}{\partial r}$ becomes:

$$\sin\psi \frac{\partial T}{\partial r} = \frac{-G \sin\psi}{(1 + G\cdot r)\ell n(1 + G)} \quad . \tag{11.6}$$

Thus, the energy equation has again decoupled itself from the vorticity equation.

Now, in the limit as $G \to \infty$, Eq. (11.6) vanishes (or approaches zero from the negative side). But as $G \to 0$, Eq. (11.6) simplifies to:

$$\sin\psi \left.\frac{\partial T}{\partial r}\right|_{G\to 0} = -\sin\psi \quad . \tag{11.7}$$

Therefore, $\sin \psi \frac{\partial T}{\partial r}$ achieves its maximum absolute value at $\psi = 90$ and $270°$ for $G \to 0$, thus duplicating the $Pr \to 0$ condition described in Chapter 4 in which a hydrodynamic (or shear-flow) instability is probable for the narrow-size gap widths.

From the above results, one may deduce that as $G \to 0$, the shearing influence of the inner and outer boundary-layers is strong enough to cause hydrodynamic instability to originate near the points of maximum velocity, or at $\psi = 90$ and $270°$. In contrast, as gap size increases, the shearing influence of the boundary-layers is less destabilizing since the buoyancy-induced velocities are reduced. However, at high enough Grashof numbers within the inviscid core, a thermal-like multicellular instability develops near the upper and lower portions of the annulus ($\psi = 0$ and $180°$), where smaller counter-rotating cells have been reported (Mack and Bishop, 1968; Huetz and Petit, 1974; Charrier-Mojtabi et al., 1979) (also see Subsection 6.2.2 and Figure 6.31).

After factoring out the Prandtl number dependency in the vorticity equation of (3.1b) and using the results of Eqs. (11.4) and (11.5), the governing equations for the $Pr \to 0$ limit become:

Vorticity:

$$G^2 \frac{\partial w}{\partial t} + \left(r + \frac{1}{G}\right)^{-1} \left(\frac{\partial f}{\partial r}\frac{\partial w}{\partial \psi} - \frac{\partial f}{\partial \psi}\frac{\partial w}{\partial r}\right)$$

$$= \frac{\partial^2 w}{\partial r^2} + \left(r + \frac{1}{G}\right)^{-1} \frac{\partial w}{\partial r} + \left(r + \frac{1}{G}\right)^{-2} \frac{\partial^2 w}{\partial \psi^2}$$

$$+ G(Gr) \left\{\frac{-G \sin \psi}{(1 + G \cdot r)\ell n(1 + G)}\right\} \qquad (11.8a)$$

Stream Function:

$$\frac{\partial^2 f}{\partial r^2} + \left(r + \frac{1}{G}\right)^{-1} \frac{\partial f}{\partial r} + \left(r + \frac{1}{G}\right)^{-2} \frac{\partial^2 f}{\partial \psi^2} = G^2 \,, \tag{11.8b}$$

with boundary conditions:

$$f(0, \psi) = f(1, \psi) = 0 \tag{11.8c}$$

and

$$w(r = 0, 1; \psi) = \frac{1}{G^2} \frac{\partial^2 f}{\partial r^2}\bigg|_{r=0,1} \,. \tag{11.8d}$$

Consistent with the $Pr \to 0$ result discussed in Chapter 4, the nonlinear terms in the vorticity (momentum) equation remain and the energy equation decouples and reduces to the simple conduction solution. Importantly, though, the equations given in (11.8) are valid for arbitrary gap and Grashof number, thus enabling one to further investigate the various effects of each parameter.

11.2. The $Pr \to \infty$ Equations

For the boundary-layer equations of Chapter 4, in the limit as $Pr \to \infty$, specific expansions were derived in order to retain all of the important physics. Using the same rationale (see Eq. (4.102)), the following expansions will be adopted for this more general approach:

$$w = Pr^{-1}\,\hat{W} + O(Pr^{-2})$$

$$f = Pr^{-1}\,\hat{F} + O(Pr^{-2}) \qquad (11.9)$$

$$T = \hat{T} + O(Pr^{-1}) \quad .$$

Then, in the $Pr \to \infty$ limit, Eqs. (3.1a-e) simplify to:

Thermal Energy:

$$G^2\,\frac{\partial \hat{T}}{\partial \hat{t}} + \left(r + \frac{1}{G}\right)^{-1}\left(\frac{\partial \hat{F}}{\partial r}\,\frac{\partial \hat{T}}{\partial \psi} - \frac{\partial \hat{F}}{\partial \psi}\,\frac{\partial \hat{T}}{\partial r}\right) = \frac{\partial^2 \hat{T}}{\partial r^2} + \left(r + \frac{1}{G}\right)^{-1}\frac{\partial \hat{T}}{\partial r}$$

$$+ \left(r + \frac{1}{G}\right)^{-2}\frac{\partial^2 \hat{T}}{\partial \psi^2} \qquad (11.10a)$$

(where $\hat{t} = Pr^{-1}t$)

Vorticity:

$$\frac{\partial^2 \hat{W}}{\partial r^2} + \left(r + \frac{1}{G}\right)^{-1}\frac{\partial \hat{W}}{\partial r} + \left(r + \frac{1}{G}\right)^{-2}\frac{\partial^2 \hat{W}}{\partial \psi^2}$$

$$+ G(Ra)\left(\sin\psi\,\frac{\partial \hat{T}}{\partial r} + \frac{\cos\psi}{r + \frac{1}{G}}\,\frac{\partial \hat{T}}{\partial \psi}\right) = 0 \qquad (11.10b)$$

Stream Function:

$$\frac{\partial^2 \hat{F}}{\partial r^2} + \left(r + \frac{1}{G}\right)^{-1}\frac{\partial \hat{F}}{\partial r} + \left(r + \frac{1}{G}\right)^{-2}\frac{\partial^2 \hat{F}}{\partial \psi^2} = G^2\hat{W} \qquad (11.10c)$$

with boundary conditions:

$$\hat{T}(0, \psi) = 1; \; \hat{T}(1, \psi) = 0 \tag{11.10d}$$

$$\hat{F}(0, \psi) = \hat{F}(1, \psi) = 0 \tag{11.10e}$$

$$\hat{W}(r = 0, 1; \psi) = \frac{1}{G^2} \frac{\partial^2 \hat{F}}{\partial r^2}\bigg|_{r=0,1} . \tag{11.10f}$$

In the above equations, only the nonlinear terms in the thermal-energy equation remain and the Prandtl number dependency has again vanished. However, both buoyancy terms are retained in the Stokes-like vorticity equation, and Eqs. (11.10a-f) are also valid for arbitrary gap and Rayleigh number.

As $Pr \to \infty$, the thermal-energy diffuses much more slowly than for $Pr \to 0$; hence, the radial temperature gradient, $\frac{\partial T}{\partial r}$, tends toward its minimum in the former case and approaches its maximum in the latter. This implies that as $Pr \to \infty$, the tendency of a hydrodynamic instability to originate near the vertical portion of the annulus is reduced, since the term $\sin \psi \frac{\partial T}{\partial r}$ is rot as strong as in the $Pr \to 0$ case. This statement is further supported by the results of Lee and Korpela (1983). They found that as Prandtl number increased, the width of the vertical slot had to be decreased (or aspect ratio increased) in order to trigger the multicellular instability more readily seen in the smaller Prandtl number fluids.

Furthermore, regardless of the flow, only concentric isotherms result for $Pr \to 0$. However, the isotherms are significantly influenced by the flow field for $Pr \to \infty$, thus causing the angular temperature gradient $\frac{\partial T}{\partial \psi}$ to be of much more importance. This behavior is especially true for the thermal plume region near the top of the inner cylinder ($\psi = 180°$), whereas near the bottom of the annulus ($\psi = 0°$), $\frac{\partial T}{\partial \psi}$ is minimal for flow fields in this larger Prandtl number range. Then, since cos ψ is -1 at $\psi = 180°$ and zero at $\psi = 90°$, and because $\frac{\partial T}{\partial \psi}$ is most significant in the vicinity of $\psi = 180°$, the buoyancy term cos $\psi \frac{\partial T}{\partial \psi}$ reaches its absolute maximum near $\psi = 180°$, where sin $\psi \frac{\partial T}{\partial r}$ tends to zero.

From the above discussion, the following conclusions can be drawn. Due to the nonlinear terms in the energy equation being coupled with the buoyancy term cos $\psi \frac{\partial T}{\partial \psi}$, a thermal-type multicellular flow instability near the top of narrow annuli may occur for large Prandtl number fluids. Whereas, for $Pr \to 0$, a hydrodynamic instability is probable near the vertical portions of narrow annuli, due to the nonlinear terms in the vorticity equation being coupled with the buoyancy term sin $\psi \frac{\partial T}{\partial r}$, as previously shown in Chapter 4.

12. APPENDIX C: E^n VERSUS E^{n+1} FORMULATION

As discussed in Chapter 5, a correction term was added to the first-order upwind-differenced representations of both the streamwise (angular) and transverse (radial) convective terms. This was done in order to gain second-order central-differencing accuracy while avoiding the stability problems of spurious wiggles at high Rayleigh numbers, associated with ordinary central-differencing of the nonlinear terms.

For the 2-D Navier-Stokes equations, the correction term (E) in Eqs. (5.6a-f) was evaluated at the old-time level E^n, as opposed to the new-time level E^{n+1}, for a truly implicit method. This particular change seemed to further aid in stabilizing the numerical method for highly convective flows, and also significantly reduced the total number of iterations required for convergence to a steady-state solution, as will be shown in Section 12.2.

To show that this substitution (E^n for E^{n+1}) does not affect the formal accuracy of the numerical method, a formal truncation-error analysis was performed on the governing set of equations as written in (5.4) and (5.6). The basic procedure and final results are given in the following section.

12.1. E^n Truncation - Error Analysis

Using the E^n formulation, the general finite-difference equation for ϕ = T, w or f can be written as:

$$C_0\phi_0^{n+1} = \frac{(\Delta 2)\tilde{\Delta}\, G^2}{\tau}\,\phi_0^n + C_1\phi_1^{n+1} + C_2\phi_2^{n+1} + C_3\phi_3^{n+1}$$

$$+ C_4\phi_4^{n+1} + E^n + S^{n+1} \qquad (12.1)$$

where the nodal point locations are depicted in Figure 5.1 and the symbols and coefficients are as described in Eqs. (5.5) and (5.6). In general, E^n is a function of ϕ_0^n, ϕ_1^n, ϕ_2^n, ϕ_3^n and ϕ_4^n, as shown in Eq. (5.6g). To properly show the truncation-error of this scheme, the coefficients in Eq. (12.1) are first written in terms of Taylor-series expansions about node zero (at the new-time level):

$$\phi_0^n = \phi_0^{n+1} - \phi_t\Big|_0^{n+1}\Delta t + \frac{1}{2}\,\phi_{tt}\Big|_0^{n+1}\Delta t^2 - \frac{1}{6}\,\phi_{ttt}\Big|_0^{n+1}\Delta t^3$$

$$+ O(\Delta t)^4 \qquad (12.2a)$$

$$\phi_1^{n+1} = \phi_0^{n+1} + \phi_r\Big|_0^{n+1} h_f + \frac{1}{2}\,\phi_{rr}\Big|_0^{n+1} h_f^2 + \frac{1}{6}\,\phi_{rrr}\Big|_0^{n+1} h_f^3$$

$$+ O(h_f)^4 \qquad (12.2b)$$

$$\phi_2^{n+2} = \phi_0^{n+1} + \phi_\psi\Big|_0^{n+1} k_f + \frac{1}{2}\,\phi_{\psi\psi}\Big|_0^{n+1} k_f^2 + \frac{1}{6}\,\phi_{\psi\psi\psi}\Big|_0^{n+1} k_f^3$$

$$+ O(k_f)^4 \qquad (12.2c)$$

$$\phi_3^{n+1} = \phi_0^{n+1} - \phi_r \Big|_0^{n+1} h_b + \frac{1}{2}\phi_{rr} \Big|_0^{n+1} h_b^2 - \frac{1}{6}\phi_{rrr} \Big|_0^{n+1} h_b^3$$

$$+ O(h_b)^4 \qquad (12.2d)$$

$$\phi_4^{n+1} = \phi_0^{n+1} - \phi_\psi \Big|_0^{n+1} k_b + \frac{1}{2}\phi_{\psi\psi} \Big|_0^{n+1} k_b^2 - \frac{1}{6}\phi_{\psi\psi\psi} \Big|_0^{n+1} k_b^3$$

$$+ O(k_b)^4 \quad . \qquad (12.2e)$$

The remaining terms in E^n, ϕ_1^n, ϕ_2^n, ϕ_3^n and ϕ_4^n, are represented by double Taylor-series expansions; for example:

$$\phi_1^n = \phi_0^{n+1} - \phi_t \Big|_0^{n+1} \Delta t + \frac{1}{2}\phi_{tt} \Big|_0^{n+1} \Delta t^2 + \phi_r \Big|_0^{n+1} h_f$$

$$+ \frac{1}{2}\phi_{rr} \Big|_0^{n+1} h_f^2 + \phi_{rt} \Big|_0^{n+1} \Delta t\, h_f + \frac{1}{6}\phi_{rrr} \Big|_0^{n+1} h_f^3$$

$$- \frac{1}{2}\phi_{rrt} \Big|_0^{n+1} \Delta t\, h_f^2 + \frac{1}{2}\phi_{ttr} \Big|_0^{n+1} \Delta t^2 h_f - \frac{1}{6}\phi_{ttt} \Big|_0^{n+1} \Delta t^3$$

$$+ O(\Delta t)^4 + O(h_f)^4 \qquad (12.2f)$$

and similarly for ϕ_2^n, ϕ_3^n and ϕ_4^n.

Considering the stream function equation, the appropriate expansions of Eq. (12.2) are substituted into Eq. (12.1), resulting in the following simplified expression:

$$\phi_{rr}\Big|_0^{n+1} + \left(r + \frac{1}{G}\right)^{-2} \phi_{\psi\psi}\Big|_0^{n+1} + 2\lambda\phi_r\Big|_0^{n+1} - G^2\, w_0^{n+1}$$

$$+ (TE)_f = 0 \qquad (12.3)$$

where $(TE)_f$ signifies the stream function truncation-error and is given by:

$$(TE)_f = O[\Delta t(h_f - h_b),\ h_f - h_b,\ k_f - k_b,\ h_f^2,\ h_b^2,$$

$$\Delta t^3,\ k_f^3,\ k_b^3] \quad .$$

Note that for the stream function equation, both the unsteady and streamwise convective terms are absent, as shown in Eqs. (5.4) and (5.5). Thus, Eq. (12.3) recovers the proper differential equation, and $(TE)_f$ identifies that the formal accuracy of the differencing method is not altered when replacing E^{n+1} with E^n in the stream function equation.

In a similar manner, the energy equation simplifies to:

$$-\Delta 2\ \tilde{\Delta}\ G^2\ \phi_t \Big|_0^{n+1} + \Delta 2\ \phi_{rr} \Big|_0^{n+1} + \frac{\Delta 2}{(r + \frac{1}{G})^2}\ \phi_{\psi\psi} \Big|_0^{n+1}$$

$$+ 2\lambda\ \phi_r \Big|_0^{n+1} + 2\mu\ \phi_\psi \Big|_0^{n+1} + (TE)_T = 0 \qquad (12.4)$$

where the thermal-energy equation truncation-error is given by:

$$(TE)_T = O[\Delta t(h_f - h_b),\ \Delta t(k_f - k_b),\ \Delta t,\ h_f - h_b,\ k_f - k_b,$$

$$h_f^2,\ h_b^2,\ k_f^2,\ k_b^2] \ .$$

Hence, the original energy equation is recovered and the formal accuracy of the method is not sacrified. Likewise, the vorticity truncation-error is of the same order as the energy equation.

To compare the differences of the two formulations, several test cases were performed and are discussed in the next section.

12.2. Numerical Comparison of E^n Versus E^{n+1}

For the test cases that follow, steady-state results were obtained by using a time-step of 5×10^{-4} carried out to $t = .150$. Also, the $0 - 2\pi$ program was used with a mesh size of 31 x 102 nodes. For the pretransitional cases compared below, the gap size was $G = .200$ and

Table 12.1. Pretransition comparison of E^n versus E^{n+1}

Rayleigh number	E^n iterations	E^{n+1} iterations	Convergence criteria
100,000	4585	4585	1×10^{-6}
250,000	6126	6550	1×10^{-6}
350,000	9520	10590	1×10^{-6}

the initial conditions were zero (see Table 12.1). At Ra = 100,000, the flow field was conduction-dominated and the number of iterations for convergence was the same for both formulations. But when the flow became convective-dominated at Ra = 350,000, the E^n formulation improved the convergence rate by approximately 10 percent. For these three pretransitional comparisons, both methods produced exactly the same average Nusselt numbers and shear-stresses.

However, checking one of the hysteresis loop calculations for G = .200, a marked improvement could be seen in the number of iterations saved for the four-cellular initial condition (Ra = 900,000), used to start the Ra = 350,000 test case. The results are summarized in Table 12.2. In this case, the convergence rate of the E^n method was approximately 25 percent faster than the E^{n+1} approach. For the E^{n+1} method, the two cells began to bottle-neck (local minimum stream functions resulted) near ψ = 170 and 190°, but never split apart to form the four-cellular counter-rotating pattern. But, when the E^{n+1}

Table 12.2. Multicellular flow comparison of E^n versus E^{n+1}

	Rayleigh number	Iteration number	Convergence criteria	Cellular structure
E^n	350,000	5850	1×10^{-6}	4-cells
E^{n+1}	350,000	7790	1×10^{-6}	2-cells

method was repeated with a convergence constraint of 7.5×10^{-7}, the 4-cell pattern was achieved. Therefore, it appears that as the E^{n+1} convergence constraint is reduced, its calculations compare more favorably to those of E^n for multicellular flows.

Thus, the E^n method has both speed and accuracy advantages when multicellular flow is experienced. This is most probably due to added stability, since E^n is always constant when iterating on flow variable calculations for a new time-step. Also, a relaxation strategy is not necessary when using the E^n formulation. For these reasons, the E^n approach was used in the 2-D Navier-Stokes numerical scheme.

13. APPENDIX D: HEA TRANSFER AND SHEAR STRESS RELATIONS

13.1. Dimensionless Nusselt Numbers

The local heat transfer rates along the heated inner cylinder wall and the cooled outer cylinder wall are calculated from first principles. For the inner and outer cylinders, these local rates are given by:

$$q_i = -k \left.\frac{\partial \bar{T}}{\partial \bar{r}}\right|_{\bar{r}=a} \tag{13.1}$$

$$q_0 = -k \left.\frac{\partial \bar{T}}{\partial \bar{r}}\right|_{\bar{r}=b} \tag{13.2}$$

where a, b are the radii of the inner and outer cylinders, respectively. Using the definition of Nusselt number based on the inner cylinder radius, Eqs. (13.1) and (13.2) can be nondimensionalized to yield the following expressions:

$$Nu_i = \frac{a\, q_i}{k(T_i - T_o)} = -\frac{1}{G} \left.\frac{\partial T}{\partial r}\right|_{r=0} \tag{13.3}$$

$$Nu_0 = \frac{a\, q_0}{k(T_i - T_o)} = -\frac{1}{G} \left.\frac{\partial T}{\partial r}\right|_{r=1} . \tag{13.4}$$

The average heat transfer rates can be found by simply integrating the local radial temperature gradients along the inner and outer cylinder walls:

$$\overline{Nu}_i = - \frac{1}{2\pi G} \int_0^{2\pi} \left. \frac{\partial T}{\partial r} \right|_{r=0} d\psi \qquad (13.5)$$

$$\overline{Nu}_0 = \frac{-1}{2\pi G} \int_0^{2\pi} \left. \frac{\partial T}{\partial r} \right|_{r=1} d\psi \; . \qquad (13.6)$$

Note that when symmetry is assumed, the integrations are carried out for only the half-annulus, or from 0 to π. Numerically, the integrations of (13.5) and (13.6) are approximated by using a second-order trapezoidal rule with variable increments, thus preserving the formal second-order accuracy of the numerical method. Also note that since there are no internal heat-generating sources (or sinks), the inner and outer average Nusselt numbers should equal each other upon reaching steady state, i.e., $\overline{Nu}_i = \overline{Nu}_0$.

13.2. Dimensionless Shear Stresses

Also from first principles, the local shear stresses at the inner and outer cylinder walls are defined as:

$$\tau_i = - \mu \left. \frac{\partial \bar{v}}{\partial \bar{r}} \right|_{\bar{r}=a} \qquad (13.7)$$

$$\tau_0 = - \mu \left. \frac{\partial \bar{v}}{\partial \bar{r}} \right|_{\bar{r}=b} \qquad (13.8)$$

where μ is the dynamic viscosity coefficient and $\frac{\partial \bar{v}}{\partial \bar{r}}$ is the radial gradient of the tangential velocity component. Expressing $\bar{v}$ in terms

of the stream function and then, nondimensionalizing yields the following relations for the local shear stresses:

$$\gamma_i = \frac{\tau_i a^2}{\mu \nu} = -\frac{1}{G^2} \frac{\partial^2 f}{\partial r^2}\bigg|_{r=0} \tag{13.9}$$

$$\gamma_0 = \frac{\tau_0 a^2}{\mu \nu} = -\frac{1}{G^2} \frac{\partial^2 f}{\partial r^2}\bigg|_{r=1} \quad . \tag{13.10}$$

The average shear stresses can also be obtained by integrating the local values along the inner and outer cylinders:

$$\gamma_i = \frac{-1}{2\pi G^2} \int_0^{2\pi} \frac{\partial^2 f}{\partial r^2}\bigg|_{r=0} d\psi \tag{13.11}$$

$$\gamma_0 = \frac{-1}{2\pi G^2} \int_0^{2\pi} \frac{\partial^2 f}{\partial r^2}\bigg|_{r=1} d\psi \quad . \tag{13.12}$$

Again, the integrations were carried out numerically by using a second-order trapezoidal rule with variable increments.

13.3. Heat Transfer and Shear Stress Finite-Difference Expressions

In order to numerically approximate the local and average Nusselt numbers as given in Eqs. (13.3) - (13.6), finite-difference expressions for the radial temperature gradient on the inner and outer cylinder walls must first be obtained. To do this, a second-order polynomial curve fit was employed:

$$T_{i,j}^{n+1} = a_j^{n+1} + b_j^{n+1} \Delta r_i + c_j^{n+1} \Delta r_i^2 \quad . \tag{13.13}$$

Using the inner cylinder boundary condition, $T_{1,j}^{n+1} = 1$, the following equations can be written:

$$T_{1,j}^{n+1} = a_j^{n+1} = 1 \text{ for all } j \tag{13.14a}$$

$$T_{2,j}^{n+1} = 1 + b_j^{n+1} \Delta r_2 + c_j^{n+1} \Delta r_2^2 \tag{13.14b}$$

$$T_{3,j}^{n+1} = 1 + b_j^{n+1} (\Delta r_2 + \Delta r_3) + c_j^{n+1} (\Delta r_2 + \Delta r_3)^2 \tag{13.14c}$$

where $\Delta r_1 = 0$ and $\Delta r_i = r_i - r_{i-1}$ for $i = 2, 3$. Note that $i = 1$ corresponds to the inner cylinder wall at $r = 0$ and $i = 2, 3$ represent consecutive nodal points in the positive radial direction. Then, since

$$\left.\frac{\partial T}{\partial r}\right|_{1,j}^{n+1} = b_j^{n+1} \quad ,$$

one obtains, after some algebra, the following expression for the inner local Nusselt number:

$$Nu_i = \frac{1 + c_j^{n+1} \Delta r_2^2 - T_{2,j}^{n+1}}{G \cdot \Delta r_2} \tag{13.15}$$

where

$$c_j^{n+1} = \frac{T_{3,j}^{n+1} - 1 + \left(\frac{\Delta r_2 + \Delta r_3}{\Delta r_2}\right)\left(1 - T_{2,j}^{n+1}\right)}{(\Delta r_2 + \Delta r_3)^2 \left(1 - \frac{\Delta r_2}{\Delta r_2 + \Delta r_3}\right)} \quad .$$

Similarly, using the outer wall boundary condition, $T_{NR,j}^{n+1} = 0$, the expression for the outer local Nusselt number becomes:

$$Nu_0 = \frac{T_{NR1,j}^{n+1} \left(\frac{\Delta r_{NR} + \Delta r_{NR1}}{\Delta r_{NR}}\right)^2 - T_{NR2,j}^{n+1}}{G(\Delta r_{NR} + \Delta r_{NR1})\left(\frac{\Delta r_{NR} + \Delta r_{NR1}}{\Delta r_{NR}} - 1\right)} \tag{13.16}$$

where

$$\Delta r_{NR} = r_{NR} - r_{NR1}$$

$$\Delta r_{NR1} = r_{NR1} - r_{NR2}$$

and i = NR corresponds to the outer cylinder wall at r = 1, while i = NR1, NR2 represent consecutive nodal points in the negative radial direction.

In the same fashion, a similar polynomial fit as in Eq. (13.13) can also be used for the stream function in order to obtain expressions for the inner and outer local shear stresses. Employing

the boundary conditions

$$f_{1,j}^{n+1} = f_{NR,j}^{n+1} = 0 \quad ,$$

Eqs. (13.9) and (13.10) can be cast into the following algebraic representations:

$$\gamma_i = \frac{-2\ (f_{3,j}^{n+1} - \frac{\Delta r_2 + \Delta r_3}{\Delta r_2} f_{2,j}^{n+1})}{G^2(\Delta r_1 + \Delta r_2)^2(1 - \frac{\Delta r_2}{\Delta r_2 + \Delta r_3})} \tag{13.17}$$

and

$$\gamma_0 = \frac{-2\ (f_{NR2,j}^{n+1} - \frac{\Delta r_{NR} + \Delta r_{NR1}}{\Delta r_{NR}} f_{NR1,j}^{n+1})}{G^2(\Delta r_{NR} + \Delta r_{NR1})^2(1 - \frac{\Delta r_{NR}}{\Delta r_{NR} + \Delta r_{NR1}})} \quad . \tag{13.18}$$

The above relations are valid for the 2-D Navier-Stokes equations as used in this study. However, these relations can also be used with the finite and zero-Prandtl number boundary-layer equations by simply substituting the appropriate related variables for temperature, stream function and gap number. Also, since a second-degree polynomial curve fit was used, the Nusselt number expressions are typically of second-order accuracy for uniform increments, while the shear stress expressions are of first-order accuracy.

14. APPENDIX E: TRUNCATION-ERROR STUDY

This appendix investigates the effect of truncation error on the numerical solution to the 2-D Navier-Stokes equations. Work begins with the comparison of first-order upwind differencing versus second-order central differencing of the nonlinear convective terms in the 2-D Navier-Stokes equations. Then, a mesh resolution study for three different size gap widths is conducted to gain an idea of the uncertainty involved in the numerically predicted transitional Rayleigh numbers of Section 6.1. Lastly, two correlations for the mean Nusselt number are compared to related numerical results with respect to an annulus of diameter ratio 1.200.

14.1. Upwind Versus Central - Differencing

In Figure 14.1, the two different schemes are compared for a pretransitional Rayleigh number of 300,000. The complete annulus was considered with G = .200 and a mesh size of 31 x 102 nodes. The upwind scheme was employed by setting the correction term (E^n) to zero in Eq. (5.6g). The first-order upwind method compared rather well to the central-differencing scheme in this case, with maximum relative errors of 2-3 percent occurring near $\Psi = 180°$ and $\Psi = 0°$, respectively. Hence, for the pretransitional cases, the first-order upwind-differencing method should yield fairly accurate numerical results.

However, for Ra = 1,000,000 (well beyond the point of multicellular transition as predicted with the central-differencing scheme), the

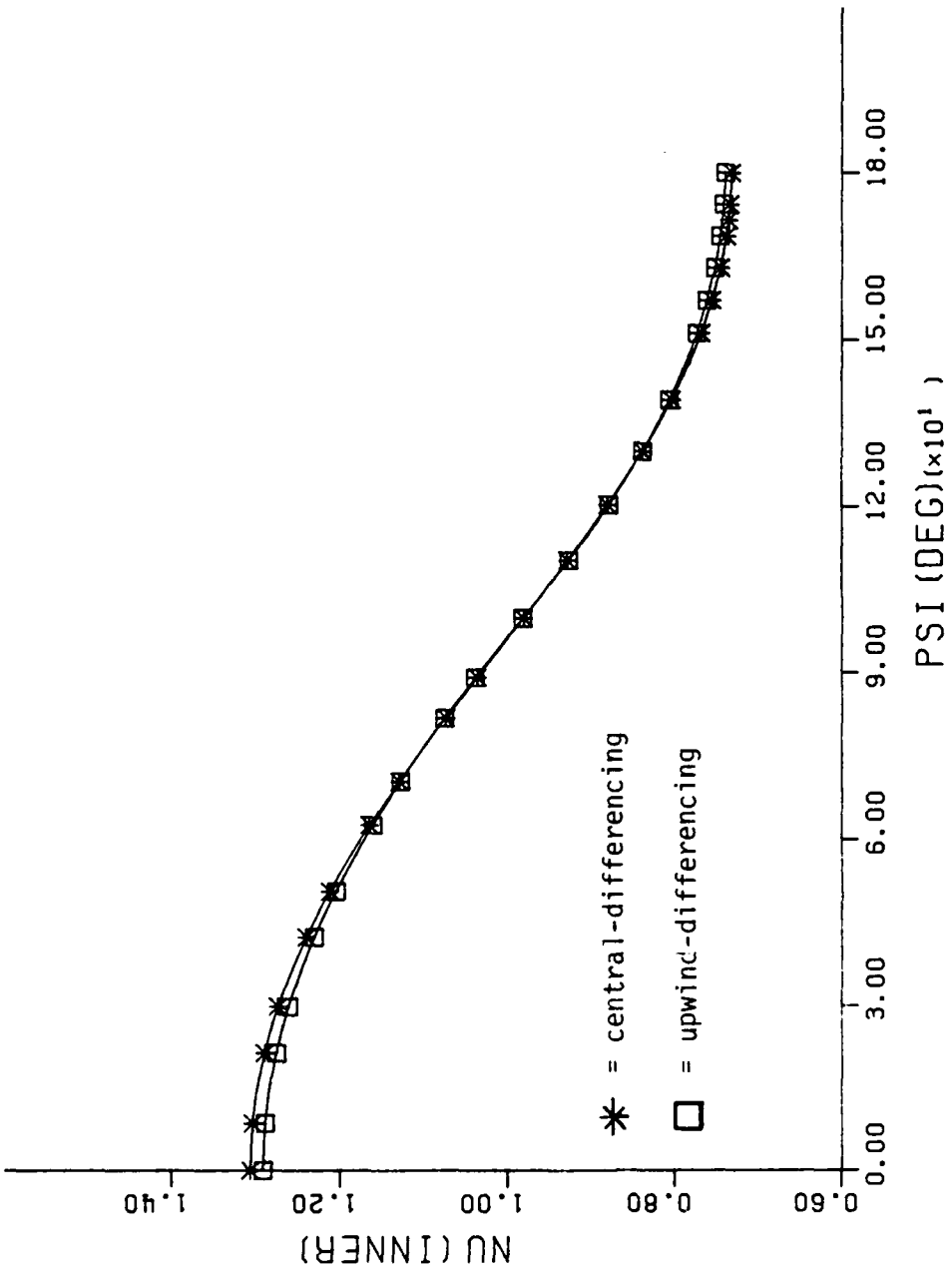

Figure 14.1. Angular variation of the inner Nusselt number ($\div Nu_{COND}$) at Ra = 300,000 for G = .200 and Pr = .706 (Nu_{COND} = 5.4836)

first-order upwind method was not able to resolve the multicellular flow field, as indicated in Figure 14.2. This was most likely due to artificial viscosity effects associated with first-order upwind-differencing schemes. Thus, it appears that at least second-order accuracy is needed to capture multicellular flow transition.

14.2. Mesh Resolution Study

This study examines three different gap widths with a mesh of 31 x 102 nodes for both the complete and half-annulus. Thus, the number of angular nodes in the half-annulus is approximately doubled compared to that in the full-annulus.

For the half-annulus, vertical center-line symmetry was assumed. This assumption was proven valid by the symmetric multicellular flow patterns shown in Figures 6.3c and 6.5 for G = .200 and .100, respectively. In Figure 14.3, the angular variation of the inner-wall vorticity is plotted for the full and half-annulus at Ra = 2,500,000 and G = .100. The results of the half-annulus mesh are nearly identical to those of the full-annulus, within one percent relative error for this pretransitional case. These results provide confidence that the half-annular calculations are indeed valid.

Considering the above symmetry discussion, the following study was performed (note: the convergence constraint was 1×10^{-6} for all test cases shown below in Table 14.1).

Based on the results of this table, it appears that the numerically predicted transitional Rayleigh numbers (associated with the full-annulus

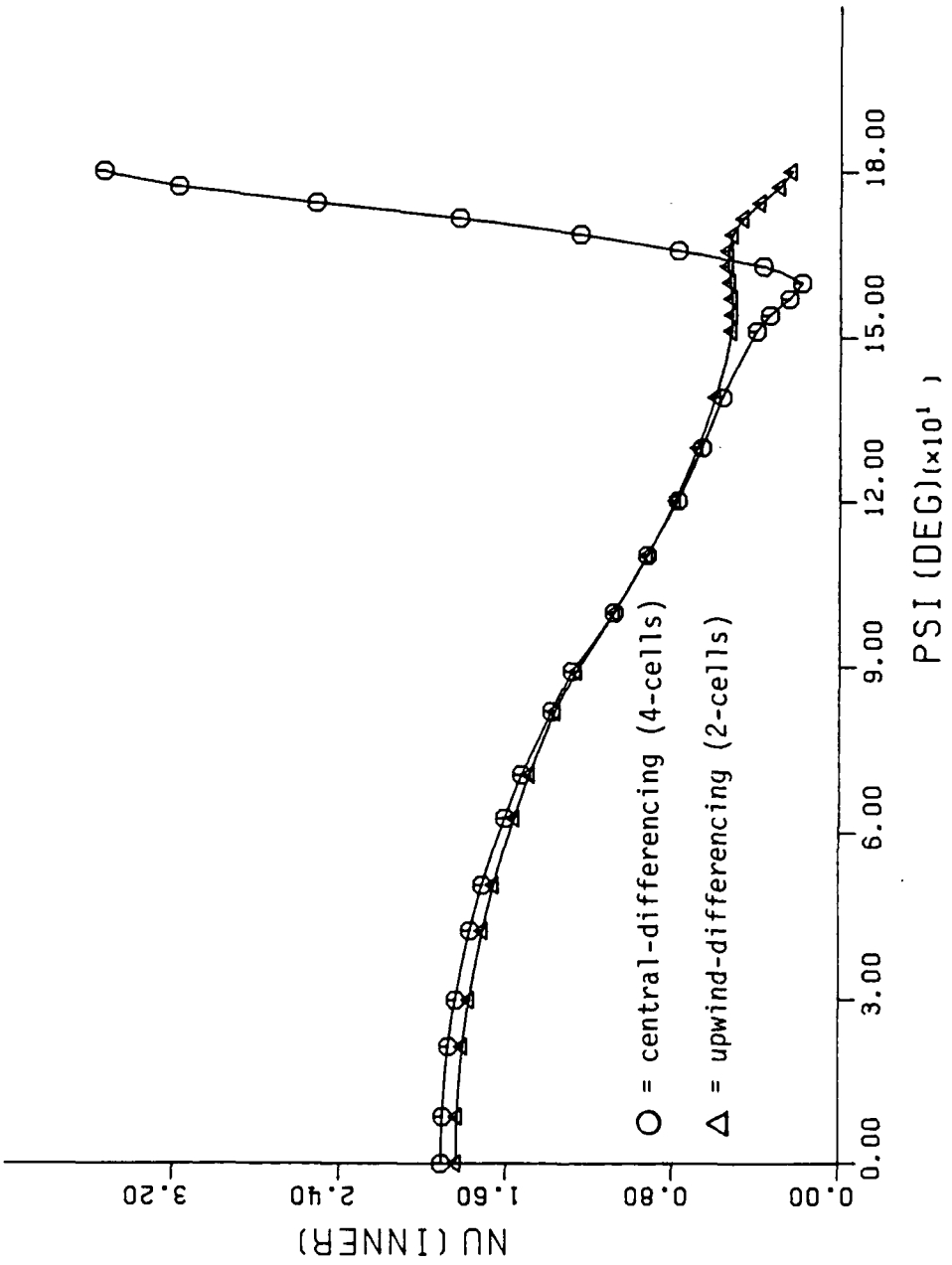

Figure 14.2. Angular variation of the inner Nusselt number ($\div$ Nu_{COND}) at Ra = 1,000,000 for G = .200 and Pr = .706 (Nu_{COND} = 5.4836)

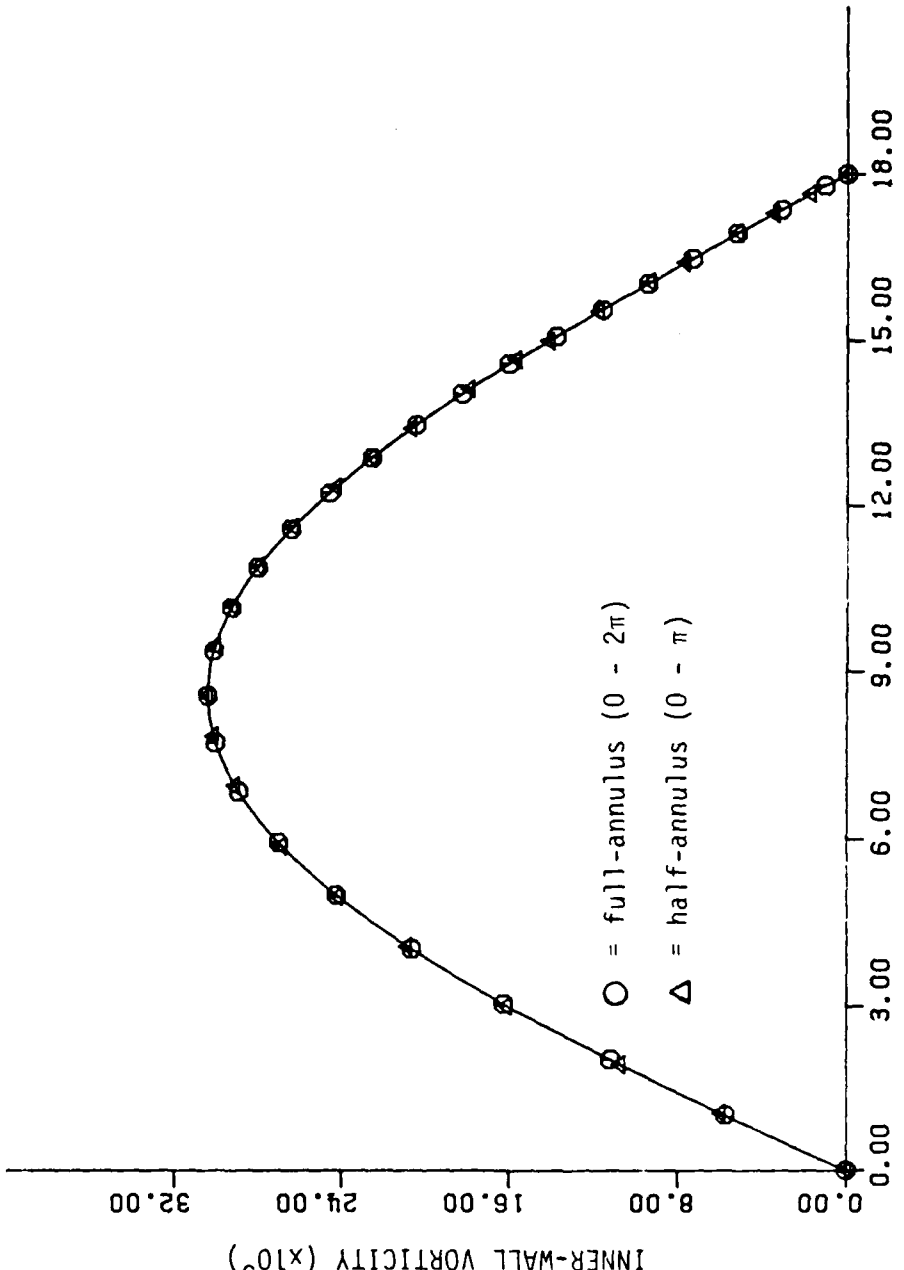

Figure 14.3. Angular variation of the inner-wall vorticity at Ra = 2,500,000 for G = .100 and Pr = .706

Table 14.1. Mesh resolution comparison

G	Mesh size	Geometry	Ra_{TR}	Ra_{b-a}	Percent relative error
.100	31 x 102	full-annulus	2,840,000	2840	} 4.4
.100	31 x 102	half-annulus	2,720,000	2720	
.150	31 x 102	full-annulus	810,000	2730	} 7.7
.150	31 x 102	half-annulus	751,000	2535	
.200	31 x 102	full-annulus	350,000	2800	}14.75
.200	31 x 102	half-annulus	305,000	2440	

mesh) are within 5-15 percent uncertainty. This uncertainty tends to decrease with decreasing gap size. In addition, the transitional Rayleigh numbers predicted with the half-annulus mesh (used mostly in generating the small-gap stability curve of Figure 6.12) are probably within five percent uncertainty.

It should also be noted that when a 21 x 48 full-annulus mesh was used for G = .100 and .200, the transition to multicells did not occur. Therefore, the ability to capture multicellular flow transition appears to be very sensitive to first-order upwind-differencing and mesh coarseness.

14.3. Mean Nusselt Number Correlations

In this section, two correlations for the mean Nusselt number are compared to this study's pretransitional numerical results for G = .200 and Pr = .706, with a full-annulus mesh of 31 x 102 node. The empirical correlations used are those of Raithby and Hollands (1975) and Kuehn and Goldstein (1980b), outlined in Eqs. (2.14) and (2.19), respectively.

In Figure 14.4, the above two correlations were used to obtain mean Nusselt numbers within 2.5 percent relative error of those obtained numerically - for a range of Rayleigh numbers between 275,000 and 350,000. This comparison is fairly good, considering these correlations are fitted to within 10-15 percent uncertainty of the experimental data.

A much more convincing measure of the accuracy of the numerical method was given in Section 6.1. There, it was shown that 2-D Navier-Stokes pretransitional numerical results (of local flow variables) converged to related analytical perturbation results in the limit as $G \to 0$ and $Ra \to \infty$. Note that local flow variable data for narrow gap widths could not be found in the literature, hence reinforcing the importance of a valid analytical solution comparison.

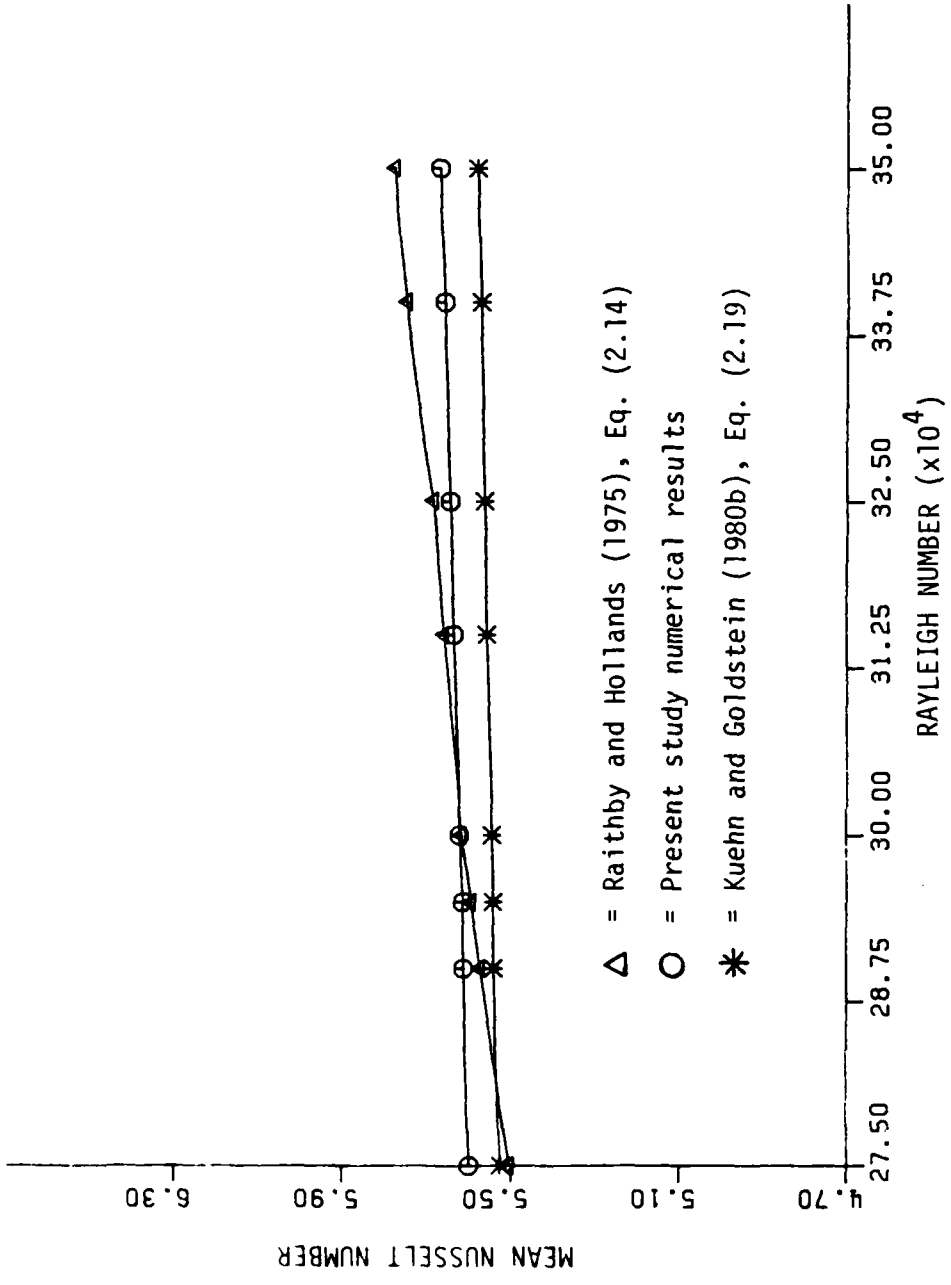

Figure 14.4. Mean Nusselt number variation as a function of Rayleigh number for G = .200 and Pr = .706

END

12-87

DTIC